HAL open science

Adhesion test and stripping process of paint using Shock Produced by LaserPlasma : Application to Aeronautical parts in Al alloys and CFRP

Selen Unaldi

▶ To cite this version:

Selen Unaldi. Adhesion test and stripping process of paint using Shock Produced by LaserPlasma : Application to Aeronautical parts in Al alloys and CFRP. Mechanics of materials [physics.class-ph]. HESAM Université, 2022. English. NNT : 2022HESAE059 . tel-04050325

HAL Id: tel-04050325

https://pastel.hal.science/tel-04050325

Submitted on 29 Mar 2023

HAL is a multi-disciplinary open access archive for the deposit and dissemination of scientific research documents, whether they are published or not. The documents may come from teaching and research institutions in France or abroad, or from public or private research centers.

L'archive ouverte pluridisciplinaire **HAL**, est destinée au dépôt et à la diffusion de documents scientifiques de niveau recherche, publiés ou non, émanant des établissements d'enseignement et de recherche français ou étrangers, des laboratoires publics ou privés.

HESAM UNIVERSITÉ

Arts et Métiers Sciences et Technologies

ÉCOLE DOCTORALE SCIENCES ET MÉTIERS DE L'INGÉNIEUR
Laboratoire PIMM - Campus de Paris

THÈSE

présentée par : **Selen ÜNALDI**

soutenu le 6 Décembre 2022

pour obtenir le grade de : **Docteur d'HESAM Université**
préparée à : **École Nationale Supérieure d'Arts et Métiers**
spécialité : **Mécanique-Matériaux**

Test d'adhérence et procédé de décapage de la peinture par choc laser : Application aux pièces aéronautiques en alliages d'aluminium et CFRP

Thèse dirigée par :
M. Laurent BERTHE

Et co-encadrée par :
M. Emmanuel Richaud et M. Matthieu Gervais

Jury

M. Nazih Mechbal	Prof, PIMM, ENSAM	Président
M. Laurent VIDEAU	Dir de recherche, DAM, DIF, CEA	Rapporteur
Mme Dominique DEBARNOT	MdC, IMMM, Le Mans Université	Rapporteuse
M. Laurent BERTHE	Dir de recherche, PIMM, ENSAM	Examinateur
M. Emmanuel RICHAUD	Prof, PIMM, ENSAM	Examinateur
M. Matthieu GERVAIS	MdC, PIMM, ENSAM	Examinateur
Mme Ana MARQUES	Asist Prof, Univ. of Lisbon	Examinatrice
M. Konstantinos TSERPES	Associate Prof, LTSM-UPAT, Univ. of Patras	Examinateur
Mme Alexandra KARANIKA	Dr, Hellenic Aerospace Industry	Invitée
Mme Flora CHAPALAIN	Ing, AIRBUS Opérations, Toulouse	Invitée

T H È S E

There exists a field, beyond all notions of right and wrong.
I will meet you there
Rumi

Acknowledgements

First of all, I would like to thank my supervisor, Laurent Berthe. We started our journey for my master thesis with you and you opened all the doors for me to continue my path. You always believed in me and helped me to push further! As I told you 9865 times, you are not just my supervisor anymore, you are one of the main part of my family. Since I finished now, finally I can tell you "merci pour tout!". I would also like to thank my co-supervisor Emmanuel Richaud. Manu, thanks a lot for helping me to dive into the chemistry world! Thanks a lot for all the valuable discussions we had both at the lab and at Fufu! I'm so lucky that I had a co-supervisor like you. I will continue to disturb you with my whatsapp stickers, no escape sorry! Lastly, I want to thank my second co-supervisor Matthieu Gervais for his support during my PhD.

The work conducted during my PhD was under the framework of VULCAN project. I can not skip to thank the project manager of the project, Alexandra Karanika. Alexandra, many thanks for all the help and the support that you provided during the project. Also, thanks a lot for becoming a really good friend!

A big thanks to all the jury members of my thesis: Nazih Mechbal, Laurent Videau, Dominique Debarnot, Ana Marques, Konstantinos Tserpes, Alexandra Karanika and Flora Chapalain. More specifically to (the reporters) Laurent Videau and Dominique Debarnot. Laurent, I was really honoured that you accepted to be part of the jury. Dominique, it was a pleasure to meet with you and to present my work to you. Huge thanks to the president of my jury and the director of our lab, Nazih Mechbal. In addition to the jury members, I also want to thank to Romain Ecault (my future colleague) for our valuable discussions!

This work would not have been possible to be completed without the dream team. Thank you Max (Maxime Guerbois) for being there whenever we need each other and thank you for being such an amazing friend! Coco (Corentin Le Bras), my kucuk kedi, I hope you will "uslu dur"! Je vais essayer d'améliorer mon français pour avoir une bonne conversation avec toi, promise. Marine (Marine Scius Bertrand), thanks a lot for being

there for me! Mo, mo, mo (Mohammad Ayad)... You know without you it wouldn't have been possible to finish what we've dreamed of (front face paint stripping :D). You know that you are not just a colleague to me, you became a little brother (les Toulousains). Ines (Ines SMA), thank you for being the best intern ever! You are now far more than an intern, super close friend of mine! I am sure you will do great with your thesis! Lastly, thanks a lot Yannou for being the magic!

Un grand merci à tous les doctorants : Gwénaelle (Gwénaelle Chebil) and Lucas FF (quoi-ffeur- Lucas Fournet-Fayard), my top South France slangs teachers, Klauss (Julien Daligault), my baby pie with his amazing heart, Julien (Juju-Julien Rodrigues da Silva), my smoko! I will miss our smoko times and your positive energy a lot!, Pierre (Pierre Hebrard), best drawer! (see you soon racoon), Lucas (Lucas Lapostolle), my bébé boi, I know that you will be a great scientist! Romain (Delannoy), our aged epoxy friendhood will be aged as well I hope! Sara (Sara Zanchi), grazie mille per tutto! Thank you so much for being my rock and providing me infinite amount of croissants.

I would like to thank my friends: İrem, Mert, Selim, Merve, Ümido (I will continue in Turkish a bit here). İrem'im, her şey için çok teşekkür ederim, sen olmasan yapabilir miydim bilmiyorum, iyi ki varsın. Mert bebeğim, Ibiza kaçamağımız olmasa ve "HALA" ile tanışmasak bu tez bitmezdi. Her ihtiyacım olduğunda yanımda olduğun için teşekkürler, seni çok çok seviyorum! Bütün desteğin için teşekkürler Selim'im, bitanesin. Son olarak, fizikçilerime de teşekkürü bir borç bilirim. Ümido'm, Dublin'de kendimi kontrol edemiyorum dinlemek için gün sayıyorum, Mervi'm, artık hunharca yakınız, çat kapı Barcelona'ya gelip seni darlayabileceğim. Hepinize bana katlanabildiğiniz için kocaman teşekkürler!

I would also like to thank my family who always encouraged me. Hope I was able to make you proud! I would like to thank to my granparents, especially my grandmother whom I dedicated my thesis. Anneanneciğim sana bütün emeklerin için sonsuz minnettarım. Umarım benimle gurur duyuyorsundur, seni çok seviyorum.

I would also like to thank Viktor (in Swedish). Tack så mycket för allt! Utan dig var det inte möjligt att avsluta det, tack för att du älskar mig villkorslöst.

Abstract

Laser stripping is a process which typically includes different forms of ablation phenomena. The presented work investigates a mechanical stripping process using high pressure laser-induced shock waves in a confined regime. Power density is studied as a parameter for selective Laser Paint Stripping Process (LPSP) on specimens and for paint adhesion relations. A flashlamp-pumped Nd:YAG lasers with fixed spot size (4mm) is shot on single layer epoxy and several layers of polymeric paint applied on AA 2024-T3 (Aluminium), AL-Li 2060 and CFRP based substrates. After laser treatment, samples are investigated with optical microscopy, profilometer and chemical analysis (FTIR, DSC & TGA). The results show that selective laser stripping is possible between different layers of external aircraft coatings and without any visual damage on the substrate material. In addition, paint stripping is developed from the paint side of specimens with the usage of thermal layer for single layer of epoxy coating. In parallel to the experimental work, a numerical model has been developed to explain the background of the physical mechanisms and to evaluate the detailed stress analysis and interfacial failure simulation both for the laser stripping from the substrate side and the paint side applications. The work covers the background and specifications for the laser paint stripping. Afterwards, samples, tools and lasers are presented. In the third part of the manuscript, behavior of aluminum based materials, aluminum tape, epoxy primers, polyurethane top coats and CFRP under laser shock loading is conducted. In the fourth part, laser paint adhesion tests are demonstrated as function of different coatings' layer thickness, specimen thickness, surface treatment, layer type, substrate type and thermal ageing. The common process window is defined by sub-grouping the tested specimens for paint stripping applications in chapter 5 which is directly linked with the applied adhesion tests. In addition, stripping rates are evaluated for different laser technologies. Development of laser paint stripping is optimized from the painted side of specimens via numerical work. Eventually, large stripping zones are created with the overlapped spots.

Keywords: laser paint stripping, adhesion tests, laser shock processes, epoxy under high strain rate, process optimization

Résumé

Le décapage au laser est un procédé qui repose généralement sur différentes phénomènes d'ablation. Le travail présenté étudie un procédé de décapage mécanique utilisant des ondes de choc à haute pression induites par laser dans un régime confiné. Le paramètre clé étudié pour le décapage laser de la peinture (LPSP) sur des échantillons et pour les relations d'adhésion est la densité de puissance. Un laser Nd :YAG pompé par une lampe flash avec un diamètre de tâche focale (4mm) focalisé durant quelques nano secondes sur une couche unique d'époxy et plusieurs couches de polymère. Couche d'époxy et plusieurs couches de peinture polymérique appliquées sur AA 2024-T3 (Aluminium), AL-Li 2060 et des substrats à base de CFRP. Des caractérisations par microscopie optique, profilomètre et analyse chimique (FTIR, DSC & TGA) sont réalisées après traitement laser. Les résultats montrent que le décapage sélectif au laser est possible entre différentes couches de revêtements externes d'aéronefs et sans aucun dommage visuel. De plus, le décapage de la peinture est développé du côté de la peinture des spécimens avec l'utilisation d'une couche de protecteur thermique. Parallèlement au travail expérimental, un modèle numérique a été développé pour expliquer les mécanismes derrière ce phénomène. Pour expliquer le contexte des mécanismes physiques et pour évaluer l'analyse détaillée des contraintes et la simulation des défaillances interfaciales pour les applications de décapage laser du côté du substrat et du côté de la peinture. Le travail réalisé ici concerne le contexte et les spécifications du décapage laser de la peinture. Ensuite, les échantillons, les outils et les lasers seront présentés. Dans la troisième partie du manuscrit, le comportement de matériaux sous choc au laser sera présenté : d'aluminium, du ruban adhésif aluminium, des primaires époxy, des couches de finition en polyuréthane et du CFRP. Dans la quatrième partie, des tests d'adhésion de peinture au laser sont réalisés en fonction de différents paramètres : épaisseur des couches de différents revêtements, épaisseur de l'échantillon, du traitement de surface, du type de couche, du type de substrat et du vieillissement thermique. La fenêtre de procédé commune est définie en sous-groupement des échantillons testés pour les applications de décapage de peinture dans le chapitre 5. Ce chapitre est directement liée aux applications des tests d'adhésion. En outre, les taux de décapage seront évalués pour différentes technologies

laser. Le développement du décapage de la peinture par laser est optimisé à partir de du côté peint des échantillons par le biais d'un travail numérique. A l'issu de ces travaux, le décapage est réalisé sur de grandes zones avec les spots superposés.

Mots-clés : décapage de peinture au laser, tests d'adhérence, procédés de chocs laser, époxy sous taux de déformation élevé, optimisation du procédé

Contents

List of Figures ix

List of Tables xv

1 Context and State of Art 1

1.1 Context . . . 5

1.1.1 Paint Usage in the Industry . . . 5

1.1.2 Choice of Base Materials in Industry . . . 8

1.1.3 Need of Paint Stripping & Paint Adhesion Tests . . . 10

1.1.4 Clean Sky 2 VULCAN Project . . . 11

1.2 Paint Adhesion Tests . . . 12

1.3 LASer Adhesion Tests (LASAT) . . . 14

1.3.1 Historical Evaluation . . . 14

1.3.2 Physical Principle . . . 15

1.4 Application: Laser Paint Stripping Process (LPSP) . . . 29

1.5 Other Laser Shock Based Applications . . . 31

1.6 PhD Objectives . . . 33

2 Samples, Tools and Lasers 35

2.1 Samples . . . 37

2.1.1 Aluminium Based Samples . . . 37

2.1.2 Composite Based Samples . . . 39

2.1.3 Aged Samples . . . 40

2.1.4 Coating Layers . . . 40

2.2 Material Characterization and Physico-Chemical Analysis . . . 42

2.2.1 Profilometer . . . 42

2.2.2 Optical Microscopy . . . 43

2.2.3 Fourier Transfrom Infrared Spectroscopy (FTIR) . . . 43

2.2.4 Differential Scanning Calorimetry (DSC) . . . 44

2.2.5 Thermogravimetric Analysis (TGA) . . . 45

2.2.6 Micro Indentation Tester 45
2.3 Laser 46
2.3.1 Héphaïstos Facility 46
2.3.2 Monarque Facility 47
2.3.3 Energy Optimization at Hephaistos 47
2.3.4 Laser Spot Optimization at Hephaistos 48
2.3.5 Temporal Profile 49
2.4 Velocity Interferometer System for Any Reflector (VISAR) 50
2.4.1 Physical Principle 50
2.4.2 Experimental Set-up 50
2.5 Numerical Methods 52
2.5.1 Multidimensional Model 52
2.5.2 Material Model 53
2.5.3 Spatial and Temporal Pressure Profiles 56
2.6 Summary of Used Samples 58
2.6.1 AA 2024 - T3 Based Samples 58
2.6.2 AL-Li 2060 - T8 E30 Based Samples 59
2.6.3 CFRP Based Samples 59
2.7 Summary of Used Experimental Tools 60

3 Materials Under Shock **61**
3.1 Behavior of Aluminum based materials under laser shock 63
3.1.1 Characterization via VISAR 64
3.1.2 Comparison of VISAR and Numerical Simulations 72
3.2 Bi-layer Aluminium Adhesive Tape for laser shock application 74
3.2.1 Dynamic response of bi-layer adhesive tape 76
3.2.2 Coupling of Experimental and Numerical Work 77
3.3 Behavior of Epoxy and Polyurethane Coatings under laser shock loading 80
3.3.1 AA 2024 + Epoxy Primer 81
3.3.2 AA 2024 + Epoxy Primer + Top Coat 89
3.4 High strain rate response of CFRP under laser shock loading 91
3.4.1 Sample Properties 91
3.4.2 Characterization via VISAR 91

4 Laser Paint Adhesion Tests **98**
4.1 Effect of Layer Thickness 100
4.1.1 AA 2024-T3 + Epoxy 101
4.1.2 AA 2024-T3 + Epoxy + Top Coat 110
4.2 Effect of Specimen Thickness, Surface Treatment and Layer Type 113
4.2.1 AA 2024-T3 + Epoxy 113
4.2.2 AL-Li 2060 T8 E30 + External Aircraft Coatings 114

4.3 Effect of Substrate Type 116
4.3.1 AA 2024-T3 + External Aircraft Coatings 116
4.3.2 CFRP + External Aircraft Coatings 119
4.4 Effect of Thermal Ageing 120
4.4.1 Physico-Chemical Analysis 120
4.4.2 Laser Adhesion Tests and Post-Mortem Analysis 123
4.4.3 Numerical Analysis and Validation 124

5 Development of Laser Paint Stripping **132**
5.1 Development of Laser Paint Stripping from the Substrate Side of Specimens via mono impact 136
5.2 Validation of Laser Paint Stripping from the Painted Side of Specimens 138
5.3 Optimization of Laser Paint Stripping from the Painted Side of Specimens 140
5.4 Large Stripped Zones 141

Appendices

A Appendix 1 **169**
A.1 Background of Surface Treatments 169
A.1.1 Chemical Etching 170
A.1.2 Anodizing 170
A.1.3 Sol-Gel Treatment 172

B Appendix 2 **173**
B.1 Hugoniot & Shock Polar 173
B.1.1 Hugoniot Curve 173
B.1.2 Shock Polar 174

List of Figures

1.1 Schematic of basic aircraft layers [8]. 6
1.2 Latest Airbus A380. Retrieved from: https://twitter.com/calloing 6
1.3 Main reactions during cross-linking [10]. 7
1.4 Polyurethane formation. Retrieved from: http://polymerdatabase.com. . . 7
1.5 Boeing, 777-300, ANA Airways, Japan. Retrieved from: https://www.airplane-pictures.net 8
1.6 Evolution of mechanical properties for aircraft fuselage [8]. 9
1.7 Total weight attributed by composites vs years of first flight [25]. 10
1.8 Main involved partners for the Clean Sky 2 VULCAN project. 11
1.9 Schematic of the process. 15
1.10 WDM (Warm Dense Medium) for the worked range of confined plasmas. . 17
1.11 Configurations of with and without confinement. 18
1.12 Generated pressure as a function of the laser intensity for a direct ablation, water confined ablation and glass confined ablation [60]. 19
1.13 Obtained pressure values as function of applied power density versus used different confinements [64]. 20
1.14 Evaluation of P_2 /P_1 as function of delay and intensity [65]. 20
1.15 Spatial repartition of the laser intensity on beam A (a) before DOE were included in the experimental setup and (b) after DOE were included in the experimental setup [47]. 21
1.16 Space-time diagram with two layers material with an acoustic impedances Z_A and Z_A in case first material has a bigger impedance (Z_A) than the second material impedance (Z_B) (shock in solid red line, release in dashed blue lines) [44]. 23
1.17 (a) Space-time diagram with two layers material with an acoustic impedances Z_A and Z_A in case first material has a smaller impedance (Z_A) than the second material impedance (Z_B) (shock in solid red line, release in dashed blue lines) [44]. 23

1.18 1D Time/position diagram in case of a three-layer target – (a) No interfacial debonding and (b) Debonding at B-C interface (impedance mismatch is neglected) [44]. 24
1.19 Space-time diagrams for mono impact configuration with different pulse durations. 25
1.20 Space-time diagrams for double impact configuration with different delays between pulses. 26
1.21 Space-time diagrams for symmetrical impact configuration with different delays between pulses durations. 27
1.22 Representation of the 2D mechanisms for a short loading duration of shock wave over a limited surface. Radioss numerical simulation of pressure evolution for various time steps are shown: (a) t = 0.01μs, (b) t = 0.018μs, (c) t = 0.1μs, (d) t = 0.15μs after laser loading (laser loading according to the pressure profile of laser pulse with λ = 1.06μm, τ= 5 ns used at various intensities) for a 1 mm thick aluminum target on a spot size of 2mm diameter [73]. 28
1.23 The history of laser cleaning/stripping development [76, 77]. 29
1.24 (a) Mono impact application from specimen side and and (b) Mono impact application from paint side. 31
1.25 Residual Stress Profiles for Laser Peening vs Shot Peening for two Titanium alloys. Retrieved from: https://www.lsptechnologies.com 32

2.1 Target configuration for pure aluminum specimen. 37
2.2 Different paint configurations for AA 2024-T3 specimen. 37
2.3 Different paint configurations for Al-Li 2060 T8 E30 specimen. 38
2.4 Schematic ply directions of the CFRP (on the left) and scanning electron microscope image of used CFRP with its plies and interplies (on the right). . . 39
2.5 Schematic description of CFRP based specimens with/without external aircraft coatings. 39
2.6 The painting schema for thermally aged specimens. 40
2.7 Specimens peened with (a) an without (b) protective coatings, respectively [103]. 40
2.8 Ion sputter JFC-1100 and deposited gold layer thickness as function of operation time,respectively [105]. 41
2.9 PVD operating principle diagram [109]. 42
2.10 3M-431 tape. Retrieved from: https://www.3m.com 42
2.11 Profilometer's tip and tray. 43
2.12 Surface analysis after laser impact on AA 2024 + Epoxy with microscope, on the left. In the middle, microscope itself and on the right cross-section cut of an AA 2024 + External Aircraft Coating Layers. 43
2.13 Principle of FTIR. 44
2.14 Principle of DSC. 44

2.15 TGA Process Scheme. 45
2.16 Micro Indentation Tester at PIMM, ENSAM. 46
2.17 Gaïa HP Laser at PIMM. 46
2.18 Monarque facility at RESCOLL. 47
2.19 Energy optimization for laser energy for one beam (Beam A) with a correction of 9.2%, approximately at Hephaistos, PIMM. 48
2.20 Comparison of spatial shapes for 4 mm spot size, without & with DOE. . . 48
2.21 Pulse duration measurements at Hephaistos, PIMM for different energy values [49]. 49
2.22 Pulse duration measurement at Monarque, RESCOLL. 49
2.23 Schematic representation of the experimental set-up at PIMM. 50
2.24 Schematic description of the followed methodology. 52
2.25 2D axisymmetric model with pressure loading and back face velocity measurement position [129]. 53
2.26 Spatial distribution for normalized intensity profile for 4 mm spot for SP1, SP2 and SP3 [129]. 56
2.27 The pressure profile as a function of time [49]. 57

3.1 Schematic description of the followed methodology. 63
3.2 Pure Aluminum target with the VISAR diagnostic. 64
3.3 Experimentally obtained back face velocity curves at different power densities for pure aluminum. 65
3.4 Given VISAR signal at 2 GW/cm^2 with the elastic precursor velocity V_F and corresponding peaks. 66
3.5 AA 2024 - T3 with the VISAR diagnostic. 67
3.6 Experimentally obtained back face velocity curves at different power densities for AA 2024-T3. 68
3.7 Given VISAR signal at 2.8 GW/cm^2 with elastic precursor velocity V_F at 110 m/s. 69
3.8 AL-Li 2060-T8 with the VISAR diagnostic. 69
3.9 Experimentally obtained back face velocity curves at different power densities for AL-Li 2060-T8. 70
3.10 AL-Li specimen with its elastic precursor velocity at 4.79 GW/cm^2. 71
3.11 Experimentally and numerically obtained back face velocity curves at different power densities for pure aluminum. 72
3.12 Axial compression and tension stress level σ_{yy} (blue and red arrows accordingly) during the wave propagation through the target thickness (horizontal axis) and during the laser shock with the associated BFV profile under 3.3 GW/cm^2 power density and 3 mm focal spot [129]. 73
3.13 Experimentally and numerically obtained back face velocity curves at different power densities for AA 2024-T3. 74

3.14 Tensile or shear modulus as a function of applied temperature (T) or strain rate ($\dot{\epsilon}$), influence of applied pressure on glass transition or frontier between glassy state and rubbery state. T_g and τ_g are the glass transition in terms of temperature and characteristic time, respectively [145]. 75
3.15 Pure aluminum + aluminum tape configuration with the VISAR diagnostic. 76
3.16 Experimentally obtained back face velocity curves at different power densities for pure aluminum + aluminum tape. 77
3.17 Validation of the Simulated BFV for the taped Pure Aluminum for the applied power densities of 0.5 GW/cm^2 and 4 GW/cm^2, respectively. 78
3.18 Cross section cuts for (a) reference sample without any applied laser impact and (b) after applied 1 GW/cm^2. 78
3.19 Axial compression and tension stress level σ_{yy} (blue and red colors respectively) during the wave propagation through pure aluminum + adhesive tape (horizontal axis) with an applied laser shock loading of 1.8 GW/cm^2 for different glue thickness (26 µm, 50 µm, 80 µm, 110 µm, 140 µm and 200 µm) represented as a, b, c, d, e, and f accordingly. 79
3.20 Specimen configurations with different layer architectures. 80
3.21 Specimen configurations with the applied laser impact. 81
3.22 Experimentally obtained back face velocity curves at different power densities for RES1 + aluminum tape. 82
3.23 Experimentally obtained back face velocity curves at different power densities for HAI1 + aluminum tape. 83
3.24 Experimentally obtained back face velocity curves at different power densities for RES2 + gold coat. 84
3.25 RES2 and RES1 specimen configurations with the applied laser impact. . . 85
3.26 Experimental and numerical comparison at 2.3 GW/cm^2. 86
3.27 Experimentally obtained back face velocity curves at different power densities for RES1 + aluminum coat. 87
3.28 Maximum axial tensile stress for epoxy and glue interfaces as function of applied power densities. 88
3.29 Space-time diagrams at 0.43 GW/cm^2 and 3 GW/cm^2. 88
3.30 RES3 specimen with the applied laser and VISAR configuration. 89
3.31 Experimentally obtained back face velocity curves at different power densities for RES3 + aluminum tape. 90
3.32 Ply directions for used CFRP type. 91
3.33 Obtained signals via VISAR at 0.52 GW/cm^2. 92
3.34 Obtained signals via VISAR at 0.24 GW/cm^2. 92

4.1 Painting Architecture provided by RESCOLL: (**a**) Chemically etched AA 2024 T3 substrate with Epoxy Primer (CA 7049), (**b**) Chemically etched AA 2024 T3 substrate with Epoxy Primer (CA 7049) & Polyurethane Top Coat (CA 8800). 100

4.2 Schematic representation of specimens. 101
4.3 Representation of thickness measurements on sample A, B and C. 101
4.4 Applied impact and sample configuration. 102
4.5 Sample A, B and C, respectively with after applied laser impacts and corresponding microscope images. 103
4.6 Sample A, B and C, respectively within stripping, partial stripping, debonding and no-stripping ranges. 103
4.7 Specimen architecture with aluminum base material, epoxy and gold coating. 104
4.8 Back face velocity comparison of VISAR and simulation at 2.3 GW/cm^2 for AA 2024 -T3 + Epoxy (25 μm). 105
4.9 Representative damage ring and complete stripping patterns for Sample A. 105
4.10 Obtained maximum axial stress at the center and at the edge of the focal spot as function of applied power density by numerical work. 106
4.11 Numerically obtained various stages of shock wave propagation for sample A at 1 GW/cm^2. 108
4.12 Various stages of shock wave propagation for sample C. 108
4.13 σ_{yy} as function of applied pressure for sample A. 109
4.14 Sample configuration of epoxy primer and polyurethane top-coat (PU). . . 110
4.15 Sample with a typical range of thicknesses for epoxy primer and polyurethane top-coat (PU). 111
4.16 Zone Definition on sample 1 as a representative. 111
4.17 The representation of remained thickness versus the total thickness as function of stripping threshold. 112
4.18 Obtained depth profiles for different power density values and different type of epoxies. 114
4.19 Samples' configuration with their respective surface treatments. 115
4.20 Sample S and M, respectively within stripping, debonding and no-stripping ranges. 115
4.21 Configuration for AA 2024-T3 and CFRP based specimens, respectively. . . 116
4.22 Figure on the right is the cross-section cut of AA 2024-T3 CAA + EAC under the optical microscope. The figure left is the zoom-out of the cross section to demonstrate the thickness variation for the clear coat layer. 116
4.23 Close-Up Optical Microscope Analysis of surfaces after laser impulsion for Sample F, respective power density values. 117
4.24 FTIR spectra for the epoxy 37035A. 118
4.25 Comparison of FTIR Spectras. 118
4.26 CFRP + external aircraft coatings with their respective thickness. 119
4.27 CFRP based sample after applied laser impacts at 1.11 GW/cm^2, 3.23 GW/cm^2 and 6.71 GW/cm^2 with their corresponding microscope images, respectively. 119
4.28 Aged and non-aged samples with a change in color observed with ageing. . 120
4.29 FTIR Analysis for AA 2024-T3+Epoxy. 121

4.30 DSC results for AA 2024-T3+Epoxy Primer sample. 122
4.31 TGA results for AA 2024-T3 + Epoxy Primer sample. 122
4.32 Comparison of applied laser impacts on Aged (120°C for 3 weeks) and Non aged Samples. 123
4.33 Impact configuration for validation tests. 124
4.34 Evolution of Young's modulus as function of ageing time. 125
4.35 Flexural storage modulus (1Hz) against temperature for the unoxidized and aged samples [158]. 126
4.36 VISAR signals and numerical comparison of back face velocities for non-aged samples. 127
4.37 Stress distribution along the epoxy-aluminum interface. 127

5.1 Overview of the process within different specimens. 136
5.2 Stripping rate for AA 2024 + EAC for different laser technologies. 137
5.3 Stripping rate for CFRP + EAC for different laser technologies. 138
5.4 Stripped target and validated experimental and numerical signals at 3 GW/cm^2. 139
5.5 σ_{yy} values as function of time for glue and epoxy interfaces, respectively. . 139
5.6 σ_{yy} values as function of time for glue and epoxy interfaces, respectively. . 141
5.7 Specimen's Architecture. 142
5.8 Zone Definition on sample labeled as 1 as a representative. 142
5.9 Neutral Salt Spray Test: (a) T = 0 (the specimen before any operation), (b) T = 1012h (the sample after 1012 hours of neutral spray application), (c) T = 2500h (the sample after 2500 hours of neutral spray application). 143

A.1 Idealized anodic oxide structures. 171
A.2 Preparation of sol-gel method. 172

B.1 Hugoniot Curve. 173
B.2 Shock Polar Graph. 174

List of Tables

1.1 Summary of some qualitative adhesion testing methods [31]. 13
1.2 Summary of some quantitative adhesion testing methods [31]. 14

2.1 AA 2024 - T3's mechanical properties and parameters used for Johnson-Cook equation [133, 129]. 54
2.2 Pure Aluminum's mechanical properties and parameters used for Johnson-Cook equation [133, 129]. 54
2.3 Acrylic's mechanical properties and parameters which used for Steinberg material model [135]. 55
2.4 Epoxy's mechanical properties and parameters which used for Steinberg material model [136, 137]. 55
2.5 Used Grüneisen mechanical parameters for pure aluminum [139]. 55
2.6 Used Grüneisen mechanical parameters for AA 2024-T3 [139]. 55
2.7 Used Grüneisen mechanical parameters for acrylic [135]. 56
2.8 Used Grüneisen mechanical parameters for epoxy [136, 137]. 56
2.9 Summary of samples based on AA 2024-T3. 58
2.10 Summary of samples based on AL-Li 2060 - T8 E30 Based Samples. 59
2.11 Summary of samples based on CFRP Based Samples. 59
2.12 Summary of used experimental tools. 60

3.1 Summary of used focal spot, applied impact type and power densities on samples. 64
3.2 Origin of pure aluminum BFV profiles peaks [129]. 66
3.3 Summary of used and calculated parameters for P_{HEL} - Pure Aluminum [133]. 67
3.4 Summary of used focal spot, applied impact type and power densities on samples. 68
3.5 Summary of used and calculated parameters for P_{HEL} - AA 2024 - T3 [133]. 68
3.6 Summary of used focal spot, applied impact type and power densities on samples. 70
3.7 Summary of used and calculated parameters for P_{HEL} - AL- Li [133, 142]. . 71

3.8 Summary of calculated P_{HEL} values for different types of aluminum specimens. 71
3.9 Summary of used focal spot, applied impact type and power densities on samples. 76
3.10 Summary of used focal spot, applied impact type and power densities on sample RES1. 82
3.11 Summary of used focal spot, applied impact type and power densities on sample HAI1. 83
3.12 Summary of used focal spot, applied impact type and power densities on sample RES2. 84
3.13 Summary of used focal spot, applied impact type and the power density on sample RES2. 85
3.14 Summary of used focal spot, applied impact type and power densities on sample RES1. 86
3.15 Summary of the used power densities, $\sigma_{yy,epoxy}$ and $\sigma_{yy,glue}$ for sample RES1. 87
3.16 Summary of used focal spot, applied impact type and power densities on sample RES3. 90
3.17 Summary of calculated P_{HEL} values for different types of aluminum specimens. 93
3.18 Summary of obtained results. 93

4.1 Categorization of each sample with their respective base material, surface treatment and thickness. 101
4.2 Thickness specification of each sample before laser operations. 110
4.3 Remaining thickness as function of total thickness of specimens after laser stripping operations. 112
4.4 Categorization of each sample with the thickness of each layer, respectively. CAA refers to Chromic Acid Anodization & CE is for Chemical Etching. . . 113

5.1 Summary of paint stripping parameters as function of different configurations. 134
5.2 Stripping Rates for different laser technologies and for different specimens. 137
5.3 Required power density for paint stripping, $\sigma_{yy,epoxy}$ and $\sigma_{yy,glue}$ for sample different glue thicknesses. 140

A.1 Summary of Surface Treatments on Aluminum Alloys. 169
A.2 DC- and AC-Electrochemical Surface Treatments Prior to Adhesive Bonding. 170

1

Context and State of Art

Introduction

Paint stripping is an essential process in the aeronautical industry since aircrafts need restoration, maintenance and routine inspection during their life time. In the 1970s, the Air Force Logistics Command began inspecting alternative stripping methods to reduce the environmental drawbacks caused by the hazardous chemicals and waste disposed from the chemical stripping process. They found that plastic media blasting and laser stripping are the most applicable techniques due to the environmental concerns. Although plastic media blasting was found as a replacement to chemical stripping, there were still limitations for how it could be used. Due to high amounts of dust produced while operating plastic media blasting, sensitive components and machinery of the airplanes should be covered and protected requiring careful maintenance work both during blasting and after stripping operations. In addition, since plastic media blasting is not complete selective stripping process and in many cases damages the substrate surface, laser stripping appeared as the most promising technique. Environmental friendliness, lower investment costs and the monitorable aspects of laser stripping process makes the application more favorable for industrial applications.

Aircrafts are painted with several layers to guarantee their protection. A primer can be applied for corrosion protection and for better adhesion between the substrate and the top coat. On top of the primer layer, a polyurethane top coat is applied both for aesthetics and a protection from external environmental attacks.

Laser paint stripping is common in the literature, however most research is focused on the paint ablation as a result of thermal effects as explained by Jasim et. al. This work presents a new stripping process which is based on spallation phenomena produced by shock wave propagation via laser-plasma interaction both from the substrate and the coating side of specimens. This technique can be used for thin coatings via pure mechanical effects which is applied on a stack of AA 2024-T3, AL-Li 2060 and CFRP specimens.

Thanks to the sensitivity of the laser stripping procedure, it opened us up a new perspective of laser paint adhesion test with the same methodology. Specimens are investigated to see the effect of coatings' thickness, specimen thickness, surface treatment, coating type, substrate type and thermal ageing. Hence, laser paint adhesion test can be an innovative tool for paint adhesion test domain. The obtained results focus on the capability of the process to control. Moreover, mechanical, chemical and interface properties are studied to understand the origin of the adhesive failure for different layer configurations. In addition, specific stripping phenomena is considered (damage ring and the effect of thermal ageing) and compared with modeling via LS-DYNA software for a single epoxy layer samples.

The work is based on the European Project of Clean Sky 2, VULCAN (deVelopment of a Universal seLeCtive stripping solution for Aircraft coatiNgs). The project aims at developing an industrial laser stripping process which is able to selectively remove the top coat of an aircraft paint system, layer by layer and with an accuracy of 1 μm. The VULCAN project's objective is to go beyond traditional laser stripping methods by using laser shock with the involved partners (RESCOLL, HELLENIC AEROSPACE INDUSTRY, AKZO NOBEL) in order to fulfill all requirements of aerospace industry that are:

- Development of a dry stripping process
- Environmental friendliness: no use of chemicals, reduction of produced hazardous wastes, limited worker exposure to toxic and hazardous substances, reduction of hazardous material disposal costs
- Selective/controlled stripping of a thin layer without affecting the surface treatment or the primer

Introduction FR

Le décapage de la peinture est un processus essentiel dans l'industrie aéronautique, car les avions doivent être restaurés, entretenus et inspectés régulièrement au cours de leur vie. Dans les années 1970, le commandement logistique de l'armée de l'air a commencé à étudier d'autres méthodes de décapage afin de réduire les inconvénients environnementaux causés par les produits chimiques dangereux et les déchets rejetés par le processus de décapage chimique. Il s'est avéré que le décapage au moyen d'un support plastique et le décapage au laser étaient les techniques les plus applicables en raison des préoccupations environnementales. Bien que le décapage sur support plastique ait été considéré comme une solution de remplacement du décapage chimique, son utilisation reste limitée. En raison des grandes quantités de poussière produites lors de l'utilisation du décapage sur support plastique, les composants et les machines sensibles des avions doivent être couverts et protégés, ce qui nécessite un travail de maintenance minutieux pendant et après les opérations de décapage. En outre, le décapage au jet de plastique n'étant pas un processus de décapage sélectif complet et endommageant dans de nombreux cas la surface du substrat (AA 2024-T3), le décapage au laser est apparu comme la technique la plus prometteuse. Le respect de l'environnement, les faibles coûts d'investissement et les aspects contrôlables du processus de décapage au laser rendent l'application plus favorable pour les applications industrielles.

Les avions sont peints avec plusieurs couches pour garantir leur protection. Un apprêt peut être appliqué pour la protection contre la corrosion et pour une meilleure adhérence entre le substrat et la couche de finition. Par-dessus la couche d'apprêt, une couche de finition en polyuréthane est appliquée pour l'esthétique et la protection contre les agressions extérieures.

Le décapage de peinture par laser est courant dans la littérature, mais la plupart des recherches se concentrent sur l'ablation de la peinture en raison des effets thermiques, comme l'expliquent Jasim et al. Ce travail présente un nouveau procédé de décapage qui est basé sur les phénomènes de decollement produits par la propagation d'ondes de choc via l'interaction laser-plasma à la fois du côté du substrat et du côté du revêtement des échantillons. Cette technique peut être utilisée pour des revêtements minces via des effets mécaniques purs. Elle est appliquée sur un empilement d'éprouvettes en AA 2024-T3, AL-Li 2060 et CFRP. La sensibilité du procédé de décapage au laser, permet d'ouvrir de nouvelles perspectives de test d'adhésion de peinture au laser avec la même méthodologie. Les essais sont menés pour étudier l'effet de l'épaisseur des revêtements, de l'épaisseur du spécimen, du traitement de surface, du type de revêtement, du type de substrat et du vieillissement thermique. Par conséquent, le test d'adhésion des peintures par laser peut être un outil innovant dans le domaine des tests d'adhésion des peintures. Les résultats obtenus mettent l'accent sur la capacité du processus à être contrôlé. De

plus, les propriétés mécaniques, chimiques et d'interface ont été étudiées pour comprendre l'origine de la défaillance de l'adhésif pour différentes configurations de couches. De plus, des phénomènes de décapage spécifiques sont observés (anneau de dommage et effet du vieillissement thermique) et comparés à la modélisation via le logiciel LS-DYNA pour des échantillons à une seule couche d'époxy.

Ce travail est réalisé dans le cadre du projet européen Clean Sky 2, VULCAN (deVelopment of a Universal seLeCtive stripping solution for Aircraft coatiNgs). Le projet vise à développer un procédé industriel de décapage laser capable d'enlever sélectivement la couche supérieure d'un système de peinture d'avion, couche par couche et avec une précision de 1 μm. L'objectif du projet VULCAN est d'aller au-delà des méthodes traditionnelles de décapage laser en utilisant le choc laser. Des partenaires industriels ont été impliqués dans le projet (RESCOLL, HELLENIC AEROSPACE INDUSTRY, AKZO NOBEL) afin de répondre à toutes les exigences de l'industrie aérospatiale qui sont :

- Développement d'un procédé de décapage à sec
- Respect de l'environnement : aucune utilisation de produits chimiques, réduction des déchets dangereux produits, exposition limitée des travailleurs aux substances toxiques et dangereuses, réduction des coûts d'élimination des matières dangereuses
- Décapage sélectif/contrôlé d'une fine couche sans affecter le traitement de surface ou l'apprêt

1.1 Context

1.1.1 Paint Usage in the Industry

There are different areas for paint usage such as marine, automobile and aerospace. For example, for marine applications, corrosion resistance and anti-fouling properties are the main priorities. However, anti-fouling coatings include Tributyltin (TBT) which is a toxic substrate that threatens the sea life [1]. While the automotive sector has the most advanced and automated coating technologies, they are also subject to many different challenges during their life cycle such as heat and humidity [2]. For the aircraft coatings which is the subject of this study, it is known that the paint should protect the aircrafts from environmental effects and corrosion [3], such as sunlight, volcanic activity, dust, lightning strike which all can affect the aircraft's coatings lifetime. For example, between 1992-1995 it was observed that aircraft coatings only had half of their life cycle as a result of the volcanic eruption of Pinatubo that released approximately 20.000.000 tons of sulphuric acid aerosol in to the stratosphere (the altitude aircrafts can fly) [3].

Paint is a general term which includes all the coated layers such as primers, base/top coats and/or clear coats that are based on polymer technologies. Before any paint application, surface treatment might be applied for corrosion protection and promote paint adhesion on substrates [4]. The most used surface treatment is anodizing. For aluminum substrates, during the anodizing process, the natural oxide on aluminum itself becomes thicker via electrolytic method. There are mainly two types of anodizing methods that are dominant for aeronautics: chromic acid and sulphuric acid anodization. Hence the chromic acid anodizing has thinner layers and less damaging effects on fatigue characteristics, it's more preferable in the sector [5]. However, due to environmental concerns (toxicity), Cr-free surface treatments are in development for the aeronautics industry. For the Cr-free surface treatments, sol-gel is the most investigated replacement (see appendix A for more detail) [6]. On top of surface treatment, primer layer is applied (see figure 1.1).

The main function of the primer is to improve the level of adhesion between layers and protecting the substrate from corrosion. In general, primers for aircrafts are made of epoxy components while top coats or base + clear coat configurations consist of polyurethane. The role of a top coat in aeronautical applications is to resist external environmental attacks [7].

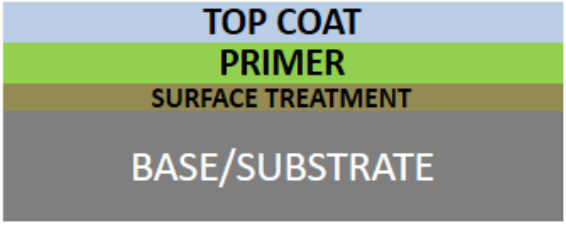

Figure 1.1: Schematic of basic aircraft layers [8].

Primer/Epoxy

Epoxy resins were first developed by Paul Schlack in 1934 with an obtained patent. In the following years, Pierre Castan and Sylvan Greenlee concluded the invesigations on this revolutionary product [9]. The epoxy resin usage covers a wide range of applications such as primer part of planes, as in airframe part in figure 1.2, cars or even mobile phone cases [9].

Figure 1.2: Latest Airbus A380. Retrieved from: https://twitter.com/calloing

Epoxy is very popular in the field of aeronautics with the advantage of having a conventional mechanical fixing, a low structural weight and good sealing capacity [10, 11].

The epoxy used for the painting of an aircraft is called epoxy resin network. It's due to the fact that the polymer is made from an epoxy monomer and a hardener to form the network. The monomer is mainly bisphenol A diglycidyl ether which is known as DGEBA. Diamines or anhydrides are mainly used as hardeners [12, 13]. Also, amine could be used as a hardener and makes it possible to obtain a three-dimensional network. The latter is the result of a polyaddition reaction (see figure 1.3). This reaction is the most common one and is exothermic in nature, so heat is released during its evolution [10].

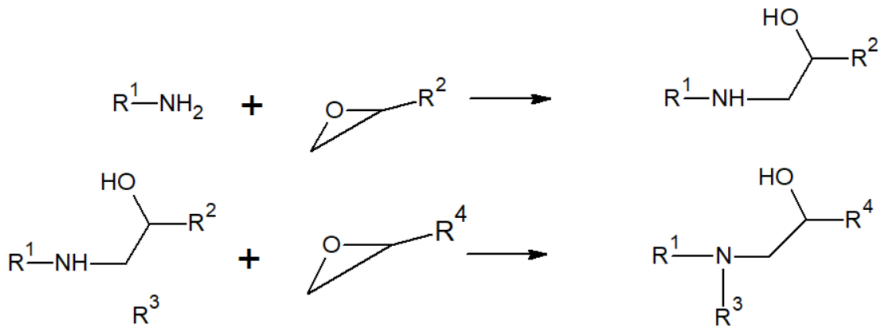

Figure 1.3: Main reactions during cross-linking [10].

During the addition reaction, the epoxy resin hardens since there is a presence of hardener. The reaction of both components gives a cross-linked network. The properties of the epoxy can be controlled with thinners, modifiers, nature of epoxy prepolymer and hardener [13].

During the operation time of aircrafts, different ageing phenomenas can be observed which might lead to a paint failure. Thermal ageing is the one of them which is studied during this work for epoxy primer coatings on top of aluminum substrates (see 4.4). To analyze the mechanical and chemical behavior of an epoxy and an epoxy/aluminum interface at high temperatures, degradation phenomena has a huge importance [14, 15]. With the presence of the oxygen, epoxy oxidation can occur. Created oxidation phenomena during the thermal ageing phenomena affects the epoxy's properties, particularly failure properties [10].

Top Coat/Polyurethane

The origin of polyurethanes date back to 1937 as a replacement of a rubber. Due to its versatility, it has been used not just as an elastic rubber but also in many different areas such as safe coatings for metals, wood and aeronautical applications (see figure 1.5) thanks to its durability, toughness and excellent chemical resistance.

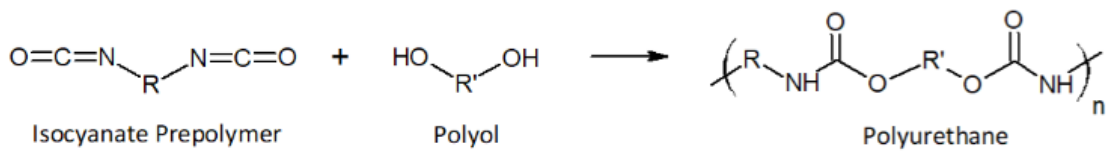

Figure 1.4: Polyurethane formation. Retrieved from: http://polymerdatabase.com.

The reaction between polyisocyanate and polyol creates urethane groups as shown in figure 1.4 [16, 17]. Characteristics of polyurethanes like softness, hardness or flexibility, depend on both polyol and the isocyanate parts. However, in general, the main function

Figure 1.5: Boeing, 777-300, ANA Airways, Japan. Retrieved from: https://www.airplane-pictures.net

of isocyanate is on curing properties of polyurethane and polyols to create elastic polymers [18, 19].

In addition, there might be additional components for a desired polyurethane products such as plasticizers (to decrease the hardness) or pigments (for aesthetic purposes) [20].

1.1.2 Choice of Base Materials in Industry

Since the aircraft structure consists of different parts, each of them experience different loading profiles (tension, compression, shear, constant load, fluctuating loads) and environmental constraints during takeoff, in flight and during landing. By taking into account all of these, there are many different designs and material criterias for aeronautics industry [21, 22]. Apart from design aspects, there are also environmental concerns, especially with the kerosene consumption. For instance, using composite structures instead of metals can reduce the total weight of the aircraft and eventually, it results in less kerosene consumption [23].

Even though composite structures are being used in modern commercial aircrafts, aluminum alloys are still the main choice. In addition, the usage of titanium alloys has increased in commerical airlines, like landing gear assembly of the Boeing 777 [21, 24]. Hence aluminium alloys and composite based materials are aimed by the thesis, the focus

will be around them.

Aluminum Alloys

For aluminum alloys 2XXX, 6XXX, 7XXX and 8XXX are mainly used in the airframe structures. In this work, the used material from this family is AA 2024-T3. It's known that 2XXX alloys used when the damage tolerance is the main concern [8]. T3 subset represents the further modification of the properties (strength,hardness). In addition to the mentioned AA 2024 alloy family, AL-Li alloys seem to have a good corrosion resistance and comparable or better strength. The study also includes AL-Li 2060 T8E30 alloys. As one can see from figure 1.6, for fuselage applications, the specific strength and specific toughness are quite higher for 2060-T8X than 2024-T3 which are highlighted/framed in figure 1.6 [8].

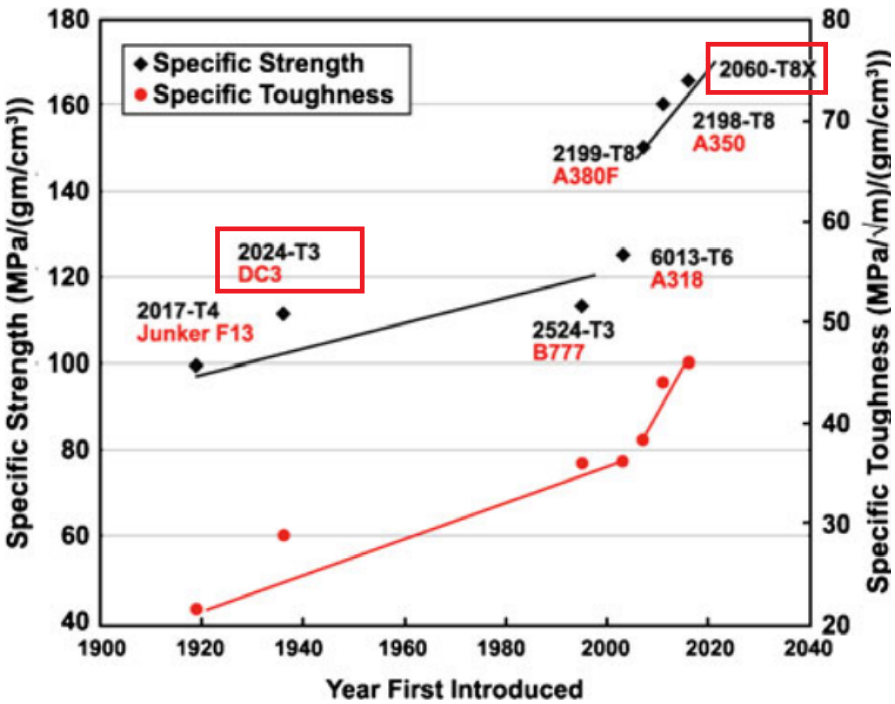

Figure 1.6: Evolution of mechanical properties for aircraft fuselage [8].

Composite Materials

In addition to their light weight, composites also increase aircrafts' structural robustness (higher strength, fatigue resistance, toughness, damage tolerance, corrosion resistance). Airbus was the pioneer of using complete composite for a tail part of A320 in 1988. In addition, the latest Airbus A350XWB has 53% of composites by weight (see figure 1.7) [25].

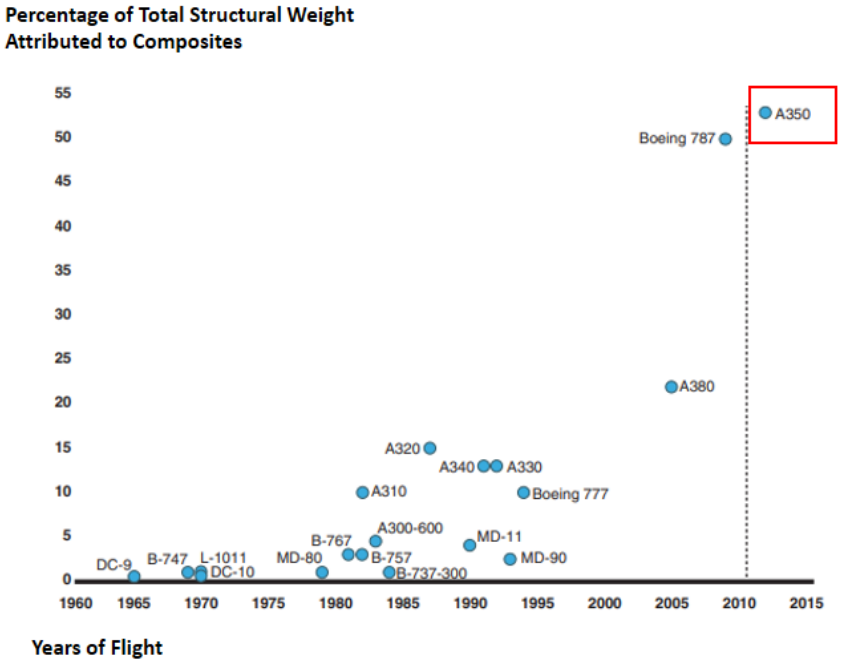

Figure 1.7: Total weight attributed by composites vs years of first flight [25].

1.1.3 Need of Paint Stripping & Paint Adhesion Tests

Paint stripping has an essential role which on average, need to be repeated, once every 4 years since aircrafts need restoration, maintenance and routine inspection [26, 27]. In the 1970s, the Air Force Logistics Command started to inspect alternative stripping methods to reduce the environmental drawbacks caused by the hazardous chemicals and waste disposed from the chemical stripping process. They found that plastic media blasting and laser stripping are the most applicable techniques mostly due to the environmental concerns. Environmental friendliness, lower investment costs and the monitorable aspects of laser stripping process make the application more favorable for industrial applications [28, 29].

Adhesion is an important phenomena for coatings mostly because of their durability dependance (since adhesion levels define the removal conditions) and corrosion protection. Some coatings provide better adhesion which is due to the differences in the stability of the adhesional interactions between paint films and substrates.

Moreover, coatings such as epoxy primer can have chemical changes due to their reactive properties which can affect the curing or leads to oxidation that might eventually affect the paint adhesion [30, 31]. By considering all different phenomenas affecting paint health might lead to paint failure which should be investigated regularly during the life time of an aircraft.

1.1.4 Clean Sky 2 VULCAN Project

VULCAN (deVelopment of a Universal seLeCtive stripping solution for Aircraft coatiNgs) project aims at developing an industrial laser stripping process which is able to selectively remove layer by layer the top coat of a an aircraft paint system, with an accuracy of 1 μm.

The VULCAN project's objective is to go beyond traditional laser stripping methods by using laser shock with the involved partners (figure 1.8) in order to fulfill all requirements of aerospace industry that are:

- Development of a dry stripping process

- Environmental friendliness: no use of chemicals, reduction of produced hazardous wastes, limited worker exposure to toxic and hazardous substances, reduction of hazardous material disposal costs

- Universal solution that can be applied on metallic and composite substrates

- Selective/controlled stripping of a thin layer

Figure 1.8: Main involved partners for the Clean Sky 2 VULCAN project.

There are three major scenarios according to the project's work flow description

- Clear + base coat (top coat) stripping then repaint with clear and base coat (Scenario 1A)
- Clear + base coat (top coat) stripping then repaint with clear coat + base coat + primer (Scenario 1B)
- Clear, base coat and primer stripping then repaint with clear coat + base coat + primer (Scenario 2)

In addition to the investigation of laser paint stripping capability, the main scientific issue appeared as laser paint adhesion tests for different configurations. The goal was to achieve different types of interfaces' separation via optimization of laser parameters. Influence of paint properties for defining common process windows as function of applied power densities was analyzed. In addition, epoxy primer integrity (after laser paint adhesion tests) is studied.

1.2 Paint Adhesion Tests

Adhesion can be defined as the phase when two surfaces are held in contact by forces. These forces can be electrostatic, chemical-bonding or van der Waals' forces. Experimentally, adhesion can be measured as function of forces and as function of work or energy. In terms of forces, it can be measured by extracting the maximum force to separate two layers/surfaces. In terms of work or energy, it can be described as the work/energy to split off the layers [32].

The performance of the adhesion depends on the differences in stability of the adhesional interaction between paint films and substrates. In order to better understand that phenomena, there are different methods in the literature. Some of the most well known ones are explained below which are divided as qualitative and quantitative [32, 31].

Scotch Tape Test

By placing the pressure sensitive tape on top of coating and removing it quickly is the basic definition for the method [33]. Since the test is extremely qualitative, it's not possible to extract numerical data from it but it is useful for screening poor adhesive behaviors [31].

Abrasion Test

The abrasion tests date back to 1930s not as an adhesion test method but as a durability test. After realization of adhesion dependence of abrasion, it has also become a tool for adhesion testing. However, by including the drawbacks of this method such as coating stripping during testing, it is far from giving realistic results [31].

METHOD QUALITATIVE	ADVANTAGES	DISADVANTAGES	WORKING PRINCIPLE
Scotch Tape	Inexpensive and quick Easy observation on coating and substrate due to different environmental effects	Choosing the right testing method is difficult Need of cleaning surface at least 3 times Qualitative Results	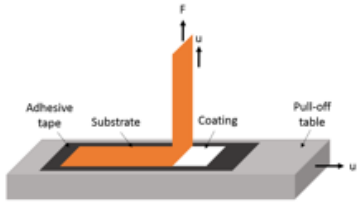 Retrieved from: https://www.mvm.kit.edu/english/697_5102.php, March 2022.
Abrasion Test	Not only for adhesion also to check durability of coatings	It includes burnishing and stripping during the operation -> which affects adhesion levels Qualitative Results	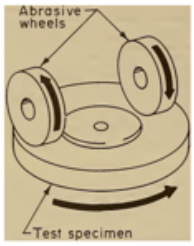 Retrieved from: https://www.911metallurgist.com/taber-abraser-test/, March 2022.

Table 1.1: Summary of some qualitative adhesion testing methods [31].

Pull-off Test

Pull-off test is based on the attached pulling device which pulls the coated layer in the perpendicular direction. The most important part for this test is the alignment of attached pulling device to create homogeneous loading within the specimens [31].

Ultracentrifuge Tests

In order to have a proper pull-off test measurement, there is a need of adhesive usage to attach the pull off device on the coating. However, for the ultracentrifuge test, the sample can be placed in a rotor which has a high speed without any adhesive usage. With the help of centrifugal force, coating removal occurs [31].

Scratch Tests

Scratch test and indentation tests will be explained together since they both use the same phenomena. For both cases, a fine tip used within the coating with gradually increasing load. This test has been studied first by Heavens and Collins to observe the adhesion levels of thin metallic films on glass [34, 31].

METHOD QUANTITATIVE	ADVANTAGES	DISADVANTAGES	WORKING PRINCIPLE
Pull-off Test	Easy access of direct indication of adhesion strength	Need of adhesive for a pull off device Difficulty of pull off device alignment for a homogenous loading	 Retrieved from: http://dfdinstruments.com/astm-d4541-iso-4624/, March 2022
Ultra centrifuge Test	No need to have an extra adhesive unlike pull off test	Complicated set up	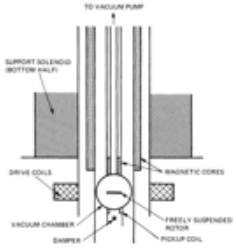 From Handbook of Thin Film Technology. Copyright (1970) McGraw-Hill Book Company.
Scratch Test	Opportunity to test areas which are too small for other methods Measurement of wide range of adhesion strengths	Obtained results can be affected by the indenter and the coating	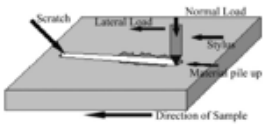 From Journal of Polymer Science Part B: Polymer Physics 2003; 41(6):623–36.

Table 1.2: Summary of some quantitative adhesion testing methods [31].

Although there are a lot of different adhesion methods as mentioned above, none of them provide easy implementation during the manufacturing or they need specific sample preparation which is why laser adhesion test appears as a promising method [35].

1.3 LASer Adhesion Tests (LASAT)

1.3.1 Historical Evaluation

After the first laser was built in 1960 by Maiman [36], scientists gained a whole new perspective for how to deeper investigate different materials [37, 38]. In 1978, Vossen has developed the adhesion bond strength of a film for the first time [39]. In the following years, Yuan and Gupta measured the interface tensile stress [40, 41] which since then has been known as LASAT (Laser Adhesion Test) throughout the literature. In the 2000s, many PhD works are developed around the adhesion tests such as C. Bolis [35], S. Barradas [42], E. Gay [43], R. Ecault [44], D. Courapied [45], S. Bardy [46], M. Sagnard [47] and M. Scius Bertrand [48, 49]. C. Bolis specifically focused on the adhesion behavior of pure copper and electrolytic-deposited nickel [35]. Experimental and numerical works

are coupled to investigate the adhesion strength and created damage thresholds via shock waves. S. Barradas followed the similar experimental and numerical approaches for cold-sprayed systems [42]. E. Gay specifically concentrated on the loading duration influence for adhesion tests [43]. R. Ecault focused on mono impact configuration to screen a weak bond structure with an adherence level of 20% of a reference bond under the framework of ENCOMB (2011-2014) project [44]. M. Sagnard concluded that weak bond threshold has been increased up to 80% with the usage of symmetrical impact (ComboNDT 2014-2018) [47]. D. Courapied focused on the usage of double pulses for adhesion tests [45]. S. Bardy worked on different joint assemblies (Al/Al, TA6V4/composite) both numerically and experimentally during his thesis. M. Scius Bertrand investigated controlled damage within composite specimens during her thesis [49].

The body of literature is rich but mostly focused on weak bond detection. This thesis instead examines the adhesion test that results in coating/paint breakaway and exfoliation which has the same physical phenomena as conventional LASAT.

1.3.2 Physical Principle

Fundamentally, laser adhesion test technique is based on a created tensile stresses at the desired depths/interfaces via shock waves [50] produced by laser plasma on a specimen. In order to generate the plasma on a target, a high power laser source (1-40 J) focuses on to the specimen through focal lens and diffractive optical element (DOE) with a water or solid transparent confinement (see figure 1.9) [51, 52]. For laser-shock applications, a water confinement regime is preferred for many years. Compared to the direct ablation regime (without any confinement), generated pressure on the target is two times longer and four times higher with the water confinement [53, 52].

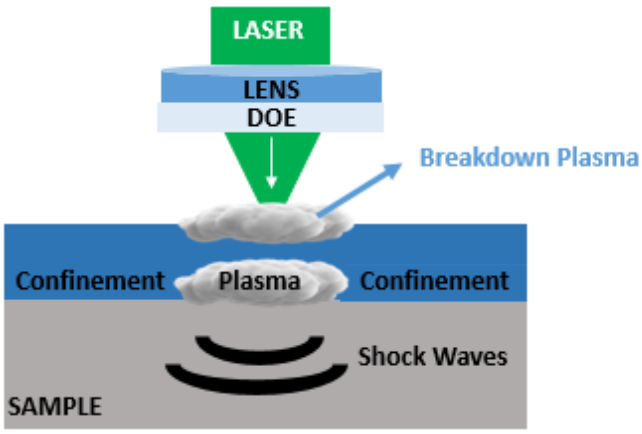

Figure 1.9: Schematic of the process.

Since the induced pressure is correlatable with the applied power density / intensity (see section 1.3.2.2), the power density calculation has a great importance in the field which can be calculated via following formula:

$$I(GW/cm^2) = \frac{E(J)}{S(cm^2) \times \Delta t(ns)} \tag{1.1}$$

where I represents the beam intensity (power density), E is the beam energy, S is the focal surface area and Δt is the pulse duration [51]. As an alternative to power density, some researchers use the fluence (F) to define the laser irriadiation:

$$F(J/cm^2) = \frac{E(J)}{S(cm^2)} \tag{1.2}$$

1.3.2.1 Plasma Creation

In the 1920s, researchers started to work on the fundemantals of plasma physics. The dedicated work covered the effect of ionospheric plasma on long distance short-wave radio propagation and for gaseous electron tubes. In 1940s, Hannes Alfvén conducted research on hydromagnetic waves for astrophysical applications [54].

Magnetic fusion energy research has gained an importance in the beginning of 1950s in many countries including UK, USA and Russia. With the development of tokamak configuration, many more countries have joined the circle, such as France with ITER facility. In parallel, some works have been conducted on space plasmas as well, such as auroras. In the 1980s, plasma processing appeared as a manufacturing tool for small parts in electric circuits. As one can see, plasma physics has a wide range of applications both for research and industrial approaches [54].

As defined in the previously, the phenomena behind the laser adhesion test is created via the shock waves which are induced by the formed plasma on top of the target [51]. This plasma can be defined as any physical system containing charged particles, free electrons and ions with a sufficient proportion so that the behavior of the system has a collective character due to the electromagnetic interactions [55]. In addition to their collective behaviour, plasmas also have a quasineutrality characteristics which comes from the plasmas' tendency to remain electrically (almost) neutral [56]. Apart from their behaviour, plasmas can be categorized as function of their temperature and their electronic densities. By the help of these parameters, plasmas can be treated as ideal gas or with the quantum behaviour of electrons. Coupling coefficient Γ is an important parameter to define plasma behaviour which is a ratio of Coulomb energy (electrostatic potential energy) to thermal energy (kinetic energy):

$$\Gamma = \frac{E_P}{E_K} = \frac{e^2 n_e^{1/3}}{6\pi\epsilon_0 k_B T_e} \tag{1.3}$$

where e is the electron charge, ϵ_0 is the vacuum permittivity, n_e is the electronic density, k_B is the Boltzmann constant and T_e is the electronic temperature. It can be said that when $\Gamma < 1$, the kinetic part is dominant so the plasma behavior is close to an ideal gas. On the other hand, for $\Gamma > 1$ the interactions between the particles are dominant [57].

The formed (confined) plasma has a temperature of approximately 10.000 K [58] with an electron density which is around 10^{-4} g/cm^{-3} to 1 g/cm^{-3} [59]. Since the confined plasmas have a mixed behaviour according to their temperature and density range, modelling them is a complex and challenging phenomena. Sollier [60] and Bardy [46] conducted a study to precise the regime for confined plasmas via simulations with the help of ACCIC and ESTHER codes (see figure 1.10) [49].

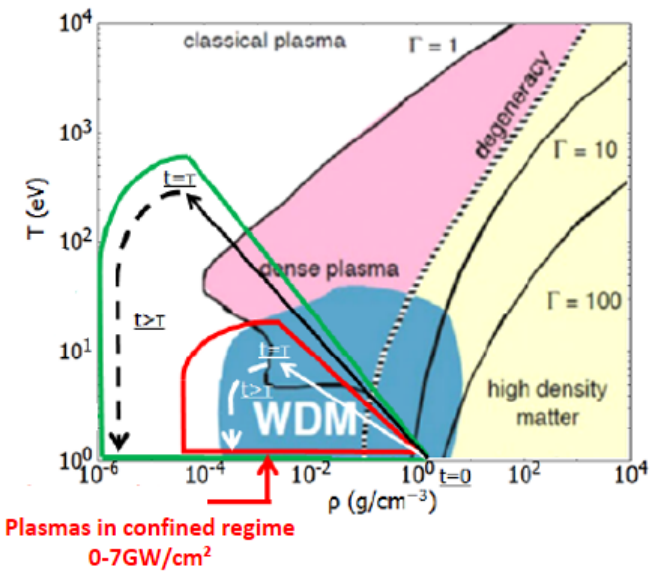

Figure 1.10: WDM (Warm Dense Medium) for the worked range of confined plasmas.

Breakdown Plasma

Although confinement structure is used for many applications, after certain threshold value, the breakdown plasma occurs in water that extracts the energy of the beam before reaching the sample which limits the process capability. Another definition of breakdown plasma might be a plasma with a sufficient electron density to act opaque towards the laser irradiation [61]. Breakdown plasma is based on avalanche and multiphoton ionization (direct ionization of the medium) phenomenas [62].

- Multiphoton ionisation (MPI) is the direct ionisation of the medium via multiphoton absorption. Basically, a photon that has higher energy than the ionization threshold, will ionize the atom which is called as photoionisation. For the case of multiphoton ionization, there is a need of multiple photons to have a sufficient energy to exceed the ionization threshold [63].

$$k(h\nu) \rightarrow e^- + A^+ \tag{1.4}$$

- Avalanche ionization is caused by accelerated electrons via laser pulse. Their kinetic energy reaches an adequate level to create an ionization. The avalanche ionization requires an initial electron (which can be generated by thermal ionization or MPI) [63].

$$e^- + h\nu + A \rightarrow 2e^- + A^+ \tag{1.5}$$

1.3.2.2 Pressure Control

In general, two main configurations might be used to generate shock waves which are direct ablation and confined regimes as demonstrated in figure 1.11. For the direct ablation, a vacuum chamber is used and for the confined regime water, glass or solid confinements are utilized to imprison the plasma [50]. The history of the invention of the confined regime goes back to 1970 when Anderholm demonstrated that by covering the generated plasma with a confinement, the applied pressure within the target becomes two times longer and four times higher [53].

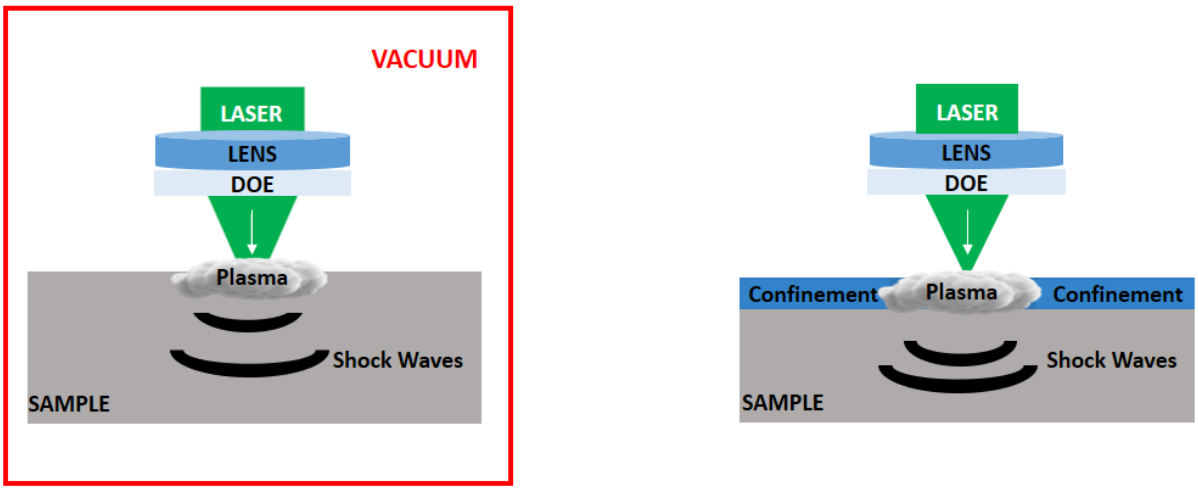

(a) Without Confinement (a) With Confinement

Figure 1.11: Configurations of with and without confinement.

In 1990, Fabbro demonstrated the relation between pressure and the intensity with the following formula [52] :

$$P(GPa) = 0.01\sqrt{\frac{\alpha}{2\alpha+3}}\sqrt{I}(GW/cm^2)\sqrt{Z_{rel}}(kg.m^{-2}.s^{-1}) \tag{1.6}$$

where P is the pressure (GPa), α devoted part for the pressure generation, I is the intensity (GW/cm^2), Z_{rel} is the relative impedance calculated via sample's and the confinement's acoustic impedance (kg.m^{-2} s^{-1}) which is:

$$Z_{rel} = 2 \times \frac{Z_{conf} \times Z_{sample}}{Z_{conf} + Z_{sample}} \tag{1.7}$$

where Z_{conf} is the confinement's acoustic impedance and Z_{sample} is the sample's acoustic impedance.

As described in figure 1.12, using a confinement, increases the applied pressure. Also, there is a huge applied pressure difference between water, glass and direct irradiation regimes for the same applied laser intensities [60].

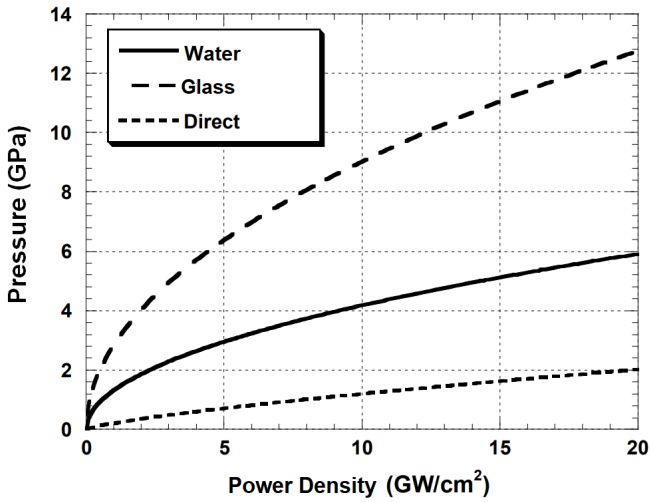

Figure 1.12: Generated pressure as a function of the laser intensity for a direct ablation, water confined ablation and glass confined ablation [60].

In addition to Fabbro Model, there are other works in the literature which correlate the pressure and intensity parameters and provide the temporal pressure profile. As Scius-Bertrand et.al. extracted from a hydrodynamic code via generic scaling laws, for water confined regime:

$$Pmax = 2.2 \times I^{0.57} \tag{1.8}$$

at 532 nm wavelength, with 7 ns Gaussian pulse. Also for 1053 nm pulse with 10-40 ns pulse duration with a top-hot pulse shape [48]:

$$Pmax = 2 \times I^{0.53} \tag{1.9}$$

On the other hand, for polymer based solid confinements as Le Bras et. al. explained, such as Acrylate or PDMS, there is no significant difference on the applied pressure in comparison with the water confinement until the breakdown where pressure values start to saturate (especially with the acrylate confinement) as shown in figure 1.13 [64].

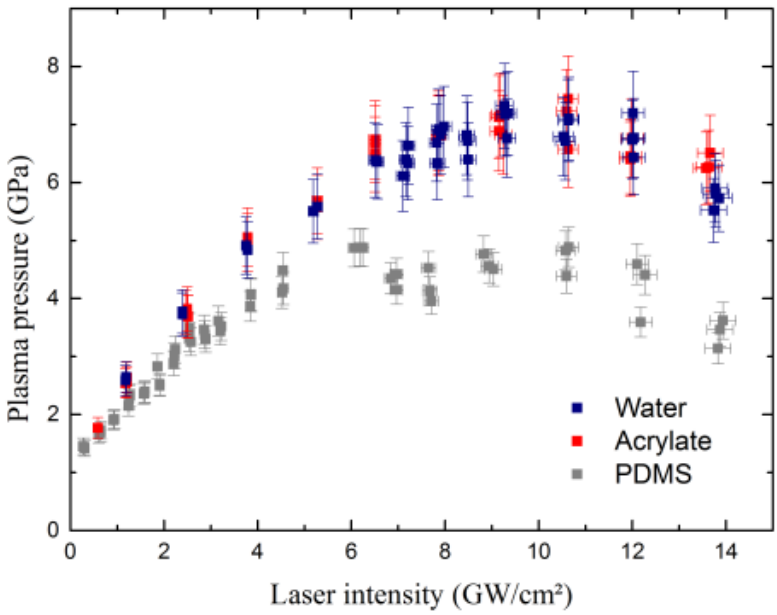

Figure 1.13: Obtained pressure values as function of applied power density versus used different confinements [64].

Apart from mono impact configuration by using one laser beam, the pressure control is also subject to double and symmetrical laser impacts. For example, for the double impact configuration, the applied pressures should be adjusted since the first pulse affects/decreases the pressure level of second applied pulse. Bardy *et al.* demonstrated the pressure ratios as function of applied delay between pulses and laser intensity (see figure 1.14) [65].

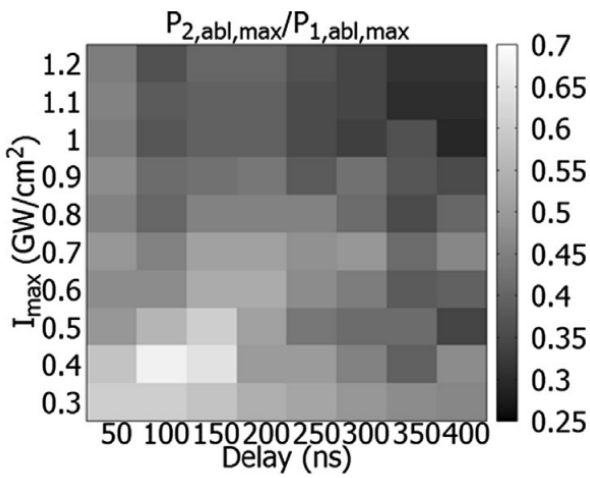

Figure 1.14: Evaluation of P_2 /P_1 as function of delay and intensity [65].

Beam Quality

In order to have smooth and homogeneous laser spot for LASAT tests, an optical element called "Diffractive Optical Element (DOE)" is used for many applications. With the help of the DOE, applied pressure can be more controllable and equal through the focal spot.

Fig. 1.15 presents the obtained camera images for focal spots with their corresponding intensity levels through the spot, respectively. From the camera images, one can say that with the usage of the DOE, more homogeneous spot is obtained (see figure 1.15b). Moreover, also via DOE, almost top-hat shaped signal is obtained with a small intensity variation, 5 %, whereas this value is up to 34 % for the one without DOE [47].

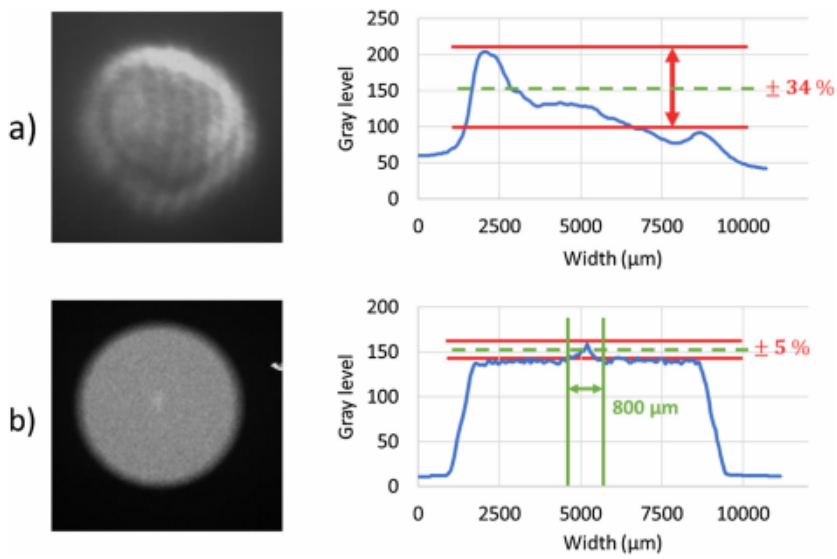

Figure 1.15: Spatial repartition of the laser intensity on beam A (a) before DOE were included in the experimental setup and (b) after DOE were included in the experimental setup [47].

1.3.2.3 Shockwave Creation & Propagation

Shock waves are defined by their **pressure** (P), **density** (ρ) and **internal energy** (E). If initial state is defined as P_0, ρ_0 and E_0 and final state is defined as P, ρ and E. During the wave propagation, material state changes from initial to final state. In order to define the material under shock, hydrodynamic approach is used. However, to better precise the behaviour of confined regimes, hydrodynamic part should be coupled with the high deformation rates ($d\epsilon/dt \simeq 10^6$ s^{-1}) for fluid behavior plus elastic approach for solid behavior. In other words, for the flow field, the known conservation of equation for mass, momentum and energy works but due to the discontinuity of shock waves, these equations are modified as:

$$\rho_0 \times U = \rho(U - u) \tag{1.10}$$

$$\sigma = \sigma_0 - \rho_0 \times U \times u \tag{1.11}$$

$$\rho_0 \times (E - E_0) = \frac{1}{2}(\sigma + \sigma_0)(1 - \frac{\rho_0}{\rho}) \tag{1.12}$$

where ρ and ρ_0 are the final and initial values of density as defined previously, U is the shock velocity, u is the particle velocity, σ and σ_0 are the total mechanical stresses in the direction of propagation before and after shock, E and E_0 are the internal energy before and after shock [66].

The Hugoniot basically formalizes the parameters of states reached by the shock. Also, it builds an equation of states for materials (EOS). At certain pressures ($< 10^5$ GPa), for a wide range of materials, the Hugoniot can be defined by a linear relationship between the particle velocity and shock velocity:

$$U = c_0 + su \tag{1.13}$$

where c_0 is the sound velocity equate the initial equilibrium bulk compressibility of the medium and s is a dimensionless material constant (see appendix B). The equation 1.13 is developed based on huge experimental data which has been collected from 1950s [66].

The shock velocity (U) depends on the material properties such as material's volumetric density (ρ) and acoustic impedance (Z). If one formulates the relation between them, it becomes:

$$U = \frac{\rho}{Z} \tag{1.14}$$

By combining equation 1.13 and 1.14 with the conservation of momentum, pressure becomes:

$$P = \rho(c_0 + su)u \tag{1.15}$$

which is known as "Shock Polar" equation. By using the very same equation, also shock polar diagrams can be sketched for pressure versus particle velocity. The figures below represent the multi-material behavior with different acoustic impedances.

$Z_A > Z_B$

When the acoustic impedance of the material A (see figure 1.16) is higher than the acoustic impedance of B, the shock wave transmitted as a shock wave from the A-B interface and reflected as a release wave within the A.

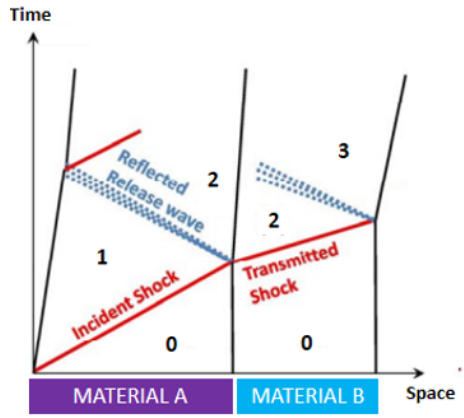

Figure 1.16: Space-time diagram with two layers material with an acoustic impedances Z_A and Z_A in case first material has a bigger impedance (Z_A) than the second material impedance (Z_B) (shock in solid red line, release in dashed blue lines) [44].

$Z_A < Z_B$

When the acoustic impedance of the material A (see figure 1.17) is lower than the acoustic impedance of B, the shock wave reflected as a shock wave within the A.

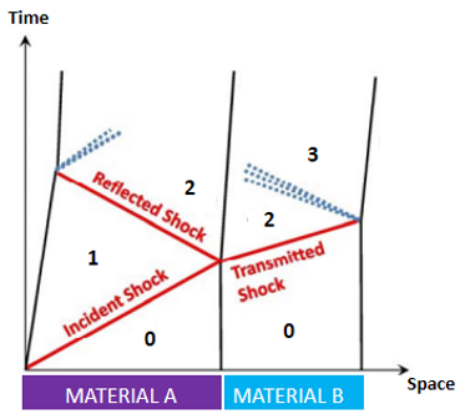

Figure 1.17: (a) Space-time diagram with two layers material with an acoustic impedances Z_A and Z_A in case first material has a smaller impedance (Z_A) than the second material impedance (Z_B) (shock in solid red line, release in dashed blue lines) [44].

Space - time graphs are also used for locating tensile stresses at the desired locations by playing with different laser parameters (pulse duration or beam configurations).

Breakaway/Stripping Phenomena via Locating the Maximum Created Tensile Stress

When the shock wave creation occurs, it travels up to the back free surface of the target and reflects as a release wave from the back free surface. Tensile stress is generated when the reflected release wave and the initial release wave cross each other [44]. When the created tensile stress reaches up to high enough values, it can lead to damage/breakaway of the material [66]. By adjusting the laser parameters (pulse duration, number of applied pulses and different laser configurations), the maximum created tensile stress can be located at the presumed localizations.

By neglecting the attenuation, if the tensile stresses created by the shock waves are lower than the failure stress of the material, no mechanical damage is obtained and waves continue to propagate within the specimens. On the other hand, for the case of damage/breakaway, the tensile stress levels which are created via shock waves are higher than the material's tensile stress. When the tensile stress creation occurs within the target, waves start to propagate within the spall with lower periods (see figure 1.18).

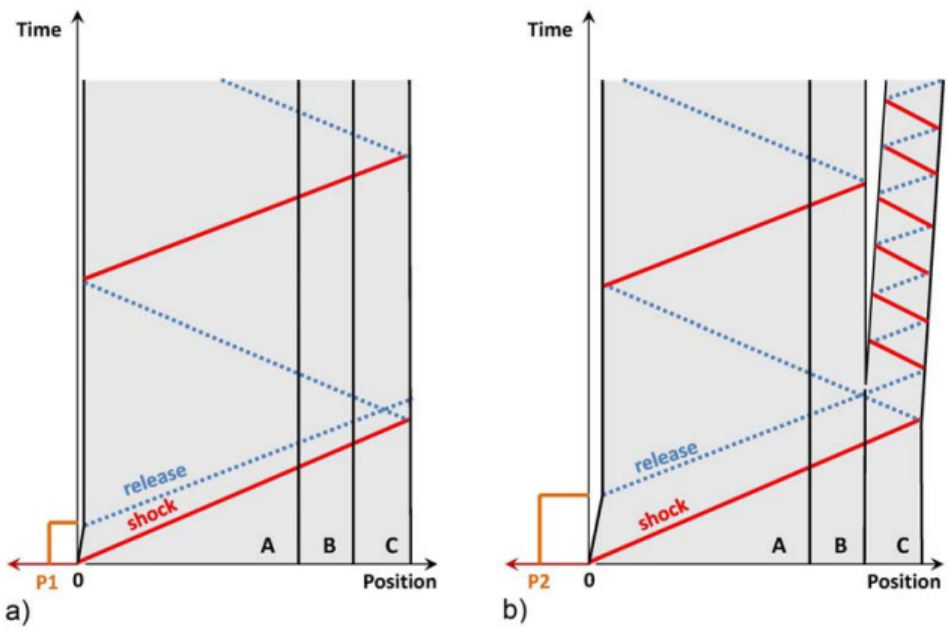

Figure 1.18: 1D Time/position diagram in case of a three-layer target – (a) No interfacial debonding and (b) Debonding at B-C interface (impedance mismatch is neglected) [44].

For both cases, spallation can be detected by post mortem and dynamic analysis [67, 68, 47, 69, 70]. For dynamic analysis, Velocity Interferometer System for Any Reflector (VISAR) can be used as explained in details in section 2.4. VISAR diagnostic gives an information about shockwave propagation within the specimen as function of velocity and time. From obtained data via VISAR, it is possible to calculate the threshold stress for an epoxy and/or polyurethane for our case. The formula to calculate the debonding strength value to strip the epoxy and /or polyurethane for that case as follows:

$$\sigma_z = \frac{1}{2} \times \rho_0 \times c_0 \times \Delta U \tag{1.16}$$

where ρ_0 is a density of the epoxy in this case, c_0 sound speed within the epoxy, ΔU is the velocity jump on the signal which is obtained experimentally [71, 44].

Mono Impact

The shock wave phenomena within materials have been subjected to many researcher's work [66]. Historically, mono impact is the most used and common method for spallation which requires the usage of one beam. However, as Ecault presented, mono impact is not precise enough to test bonds especially for composites or generalize the procedure without damaging the substrate due to the created tensile stress depth [44]. One approach was to change the pulse duration to generate tensile stresses at the desired locations.

As seen in figure 1.19, shock waves represented with solid red lines and dotted blue lines for the release waves. Created maximum tensile stress is shown with a green circle where two release waves meet (initial and reflected) as a representative 1D acoustic approach.

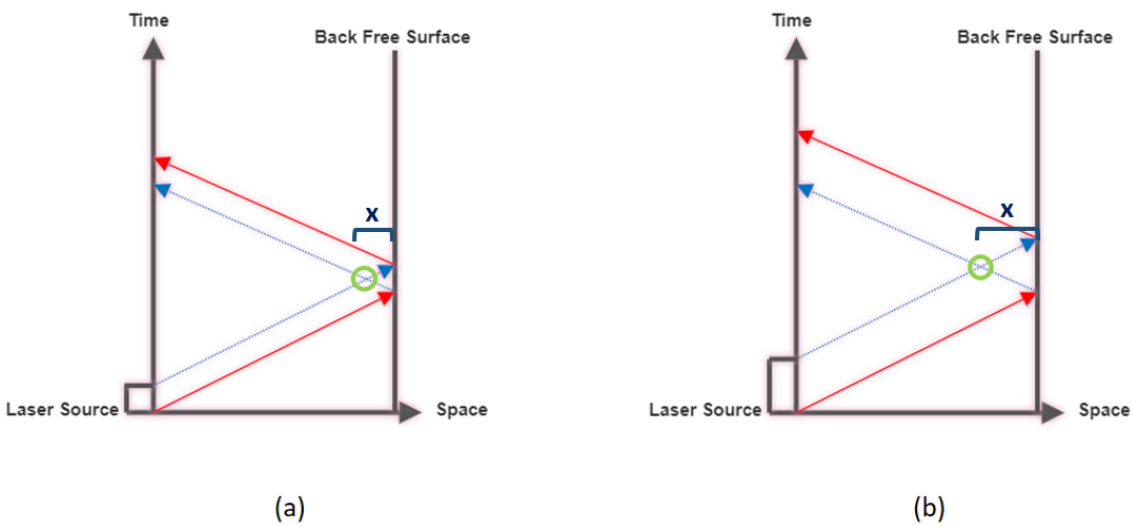

Figure 1.19: Space-time diagrams for mono impact configuration with different pulse durations.

The depth in which the maximum tensile stress occurs "x" can be calculated from the pulse duration τ and the sound velocity C_0 according to the equation 1.17:

$$x = \frac{\tau \times C_0}{2} \tag{1.17}$$

Double Impact

In order to better locate tensile stresses, some developments have been made. Using different configurations for laser impacts is one of them. For the double impact configuration, two laser pulses could be applied from the front faces of targets (figure 1.20). Compared with the mono pulse impact, tensile stress locations can be aligned at deeper positions. The main parameter for this configuration is the time delay between two pulses.

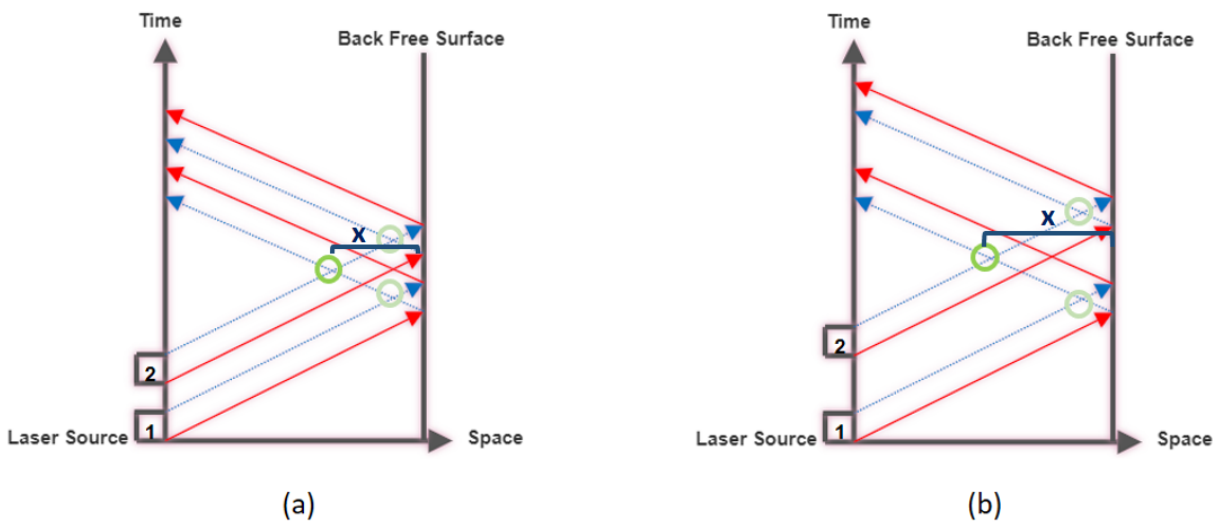

Figure 1.20: Space-time diagrams for double impact configuration with different delays between pulses.

The delay Δt, between the laser pulses of duration τ, to locate the maximum tensile stress at the desired depth/location "x" can be calculated as:

$$x = \frac{(\tau + \Delta t)C_0}{2} \tag{1.18}$$

$$\Delta t = \frac{2x}{C_0} - \tau \tag{1.19}$$

In addition to experimental approach, some numerical work also conducted. For instance, Bardy et.al. coupled experimentally obtained FSV (Free Surface Velocity) results with ESTHER WCR model. He showed that higher intensity should be used for applied second impact in order to create equal pressures for both pulses (see subsection 1.3.2.2)

[65].

Symmetrical Impact

Symmetrical Impact for spallation is first studied by Resseguier in 2001 on iron samples without having any delay between two pulses [72]. By creating shock waves from both sides of the specimen, different level of tensile stresses might occur within it. The dark green circle as in figure 1.21 is the generated highest tensile stress.

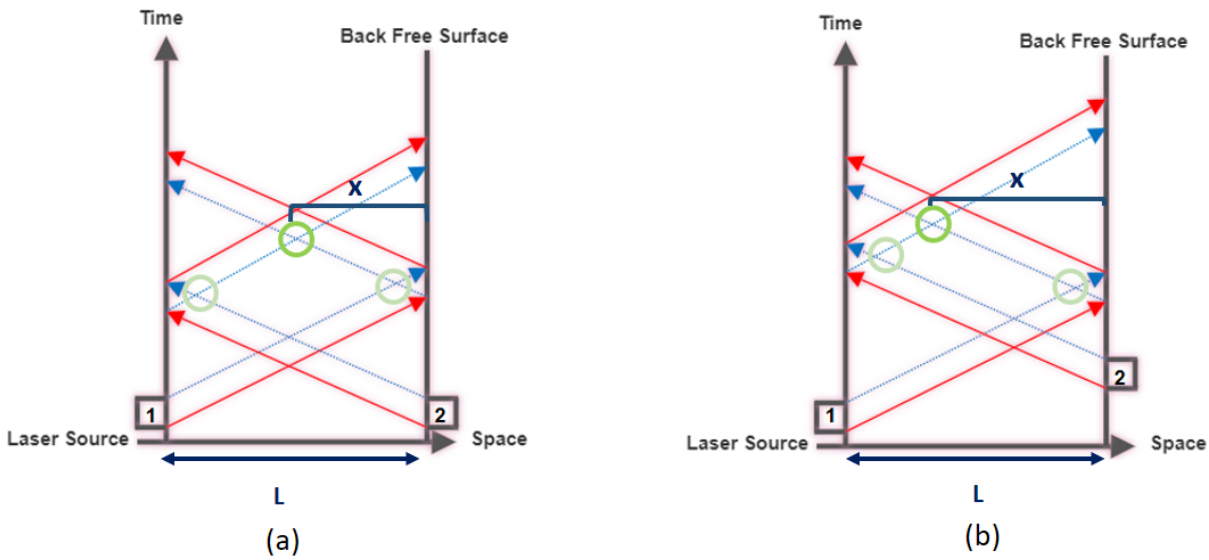

Figure 1.21: Space-time diagrams for symmetrical impact configuration with different delays between pulses durations.

The highest tensile stress location "x" might be found as function of the delay Δt applied between the laser pulses and the thickness of the target L [69]:

$$x = \frac{L - \Delta t \times C_0}{2} \tag{1.20}$$

$$\Delta t = \frac{L - 2x}{C_0} \tag{1.21}$$

1.3.2.4 Edge Effect

The created shock via plasma propagates in the axial direction. Hence, within the spot size radial compressive waves have zero pressure and they propagate until the back face of the specimens and then they become release waves. The main phenomena which creates the edge effect is the spherical propagation of this wave from the edge of the spot. If these release waves cross each other, they can create a tensile stresses as well (see figure 1.22) [73]. Material also can be damaged just by the edge effect which makes it an important phenomena for laser adhesion and laser stripping applications.

This effect is related with the used material thickness (L) to used spot size ratio (r). In his work, Cuq-Lelandais [74] divides target thickness into 3 main categories as thick, medium and thin. Then he categorized these 3 targets as function of L/r:

- Quasi 1D regime (L/r<0.25): This regime is characterized by the presence of over-traction at the edge of impact resulting from the superposition of 1D and 2D tractions.

- Mixed regime (0.25<L/r<0.65): This is the intermediate case of transition between the two previous configurations. This regime is characterized by the presence of two over-tractions, one in the center of the impact and the other at the edge of the impact.

- 2D regime (L/r>0.65): The shock wave is completely affected by 2D effects. The greater the L/r ratio the more the shock wave will be attenuated by the 2D effects [45].

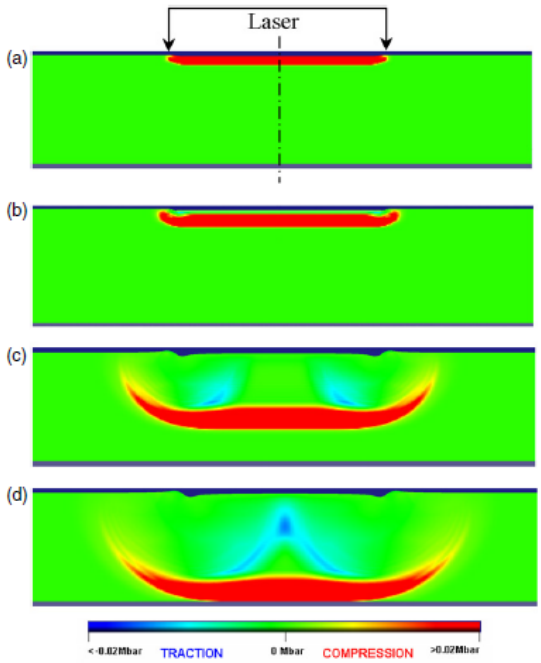

Figure 1.22: Representation of the 2D mechanisms for a short loading duration of shock wave over a limited surface. Radioss numerical simulation of pressure evolution for various time steps are shown: (a) t = 0.01μs, (b) t = 0.018μs, (c) t = 0.1μs, (d) t = 0.15μs after laser loading (laser loading according to the pressure profile of laser pulse with λ = 1.06μm, τ= 5 ns used at various intensities) for a 1 mm thick aluminum target on a spot size of 2mm diameter [73].

1.4 Application: Laser Paint Stripping Process (LPSP)

For industrial applications, there are various types of paint stripping methods. Main methods can be classified as chemical stripping, plastic media blasting and laser paint stripping. Chemical stripping is a method which utilizes different chemical solutions (such as methylene chloride) to strip aircraft coatings [75]. Since it involves the usage of chemicals and the treatment of waste chemical disposed after the operation, it does not appear as the most environmental friendly method [28]. The plastic media blasting was found replaceable by the chemical stripping but there were still limitations on the use of it. Studies showed that the increase of roughness might occur within the surfaces of specimens after the plastic media blasting operation [76]. The laser stripping appeared as a promising method due to its high precision and pollution-free characteristics.

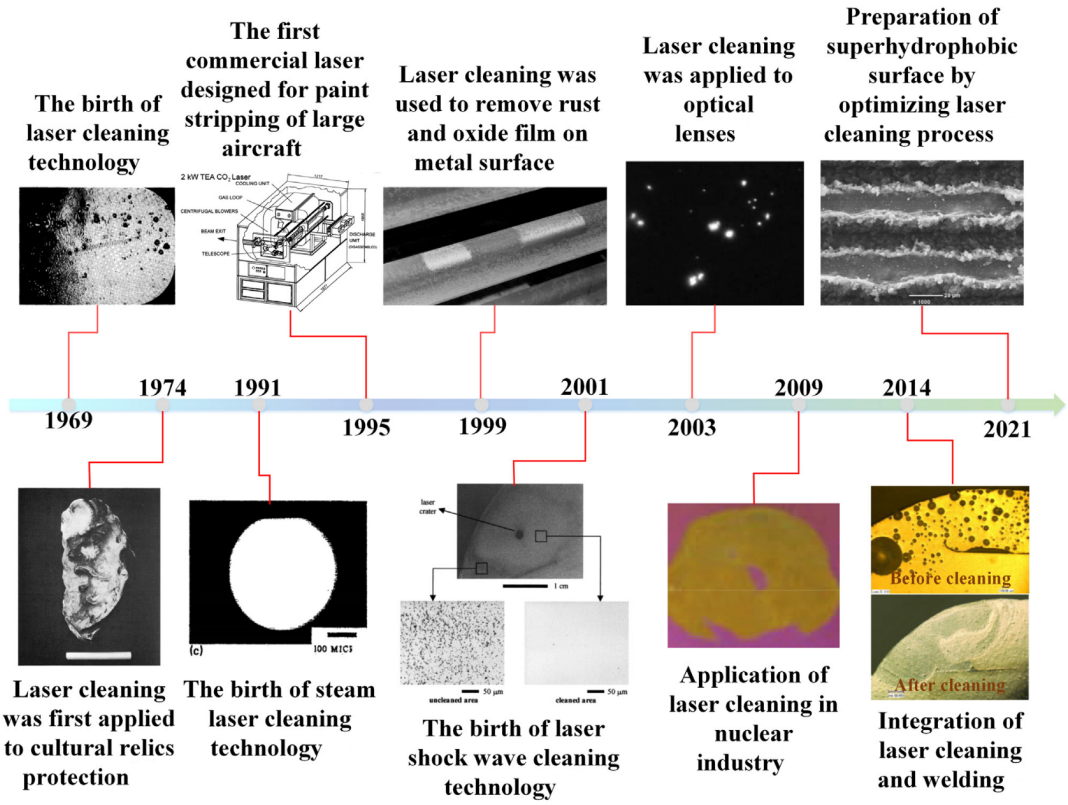

Figure 1.23: The history of laser cleaning/stripping development [76, 77].

Figure 1.23 demonstrates the development history of laser cleaning/stripping. In 1969, Bedair [78] first started to develop laser stripping via ruby Q-switched laser with a power density of 30 MW/cm^2. Moreover, A. L. Schawlow worked on laser cleaning by using a ruby-pulsed laser in order to strip black pigments from paper. His purpose was based on cleaning the surface of silicon contaminants by keeping the substrate health [79]. Afterwards, in 1974, the technology started to be used in cultural relics protection. Asmus [80] utilized a laser to strip the crusts on the surface of the stone cultural relics in Venice. Asmus et al. also investigated the possibility of using laser technology to remove

lime layers of a painting by Leonardo da Vinci. Several undesirable outcomes thought to be due to the irradiation. However, it was concluded that there was a promising laser technology with the need of further research. In 1991, Imen [81] developed a new laser-assisted particle removal technology which was based on a laser light absorptivity of a thin film on the surface of the substrate. In 1993, the Foundation for Research and Technology Hellas (FORTH) started to conduct researches about laser cleaning applications. These studies covered laser cleaning of surfaces, analysis of medium and pigments, imaging techniques for structural diagnostics and authentication techniques [82].

In 1995, Urenco proposed the first commercial CO_2 laser with an average power of more than 2 kW for aircraft paint stripping applications [83]. In 1998, Cooper [84] published the first book dedicated to laser cleaning processes. Even though the main focus of the book is on sculptures, mainly stone and metal, it also includes a chapter which is dedicated to development of laser cleaning of paintings. In 1999, Daurelio [85] developed the Nd: YAG portable laser light source in order to strip oxide layers, rust and dust of raw materials (steel, aluminum, copper, and their alloys) used in railway industry. In 2001, Lee [86] investigated that a laser-induced air plasma shock wave could strip tiny particles from surfaces. This stripping method was called as "laser shock wave cleaning". In 2003, Kane [87] used three different lasers to clean glass surfaces by using a single pulse laser. In 2009, Zhou [88] developed a laser cleaning system for tokamak mirrors. In 2014, Alshaer [89] utilized a short-pulse laser to clean the surface of automotive aluminum alloy parts. In 2021, Martinez [90] optimized the femtosecond laser cleaning process to produce layered micro and nano structures. In recent years, the high-power pulsed nanosecond laser cleaning/stripping technology is studied broadly especially for coatings on the surface of metals and composite materials.

The application of laser beam from the coated side provides stripping but the depth of the process should be well controlled in order to prevent the damage of a substrate and the anticorrosion primer for aeronautical applications [91, 92]. Apart from that, thermal effects should be taken into account on the painted layers [93]. Since some processes follow the stripping pattern by tracking the intact layer after the stripping operation, change in color due to the ablation limits the process. In addition, for the case of composite based materials as a substrate, heat changes can create undesired effects within the base material [94]. This thesis presents a new stripping process which is based on spallation phenomena produced by shock wave propagation via laser-plasma interaction from the back faces of specimens (substrate side). As an alternative, for industrial purposes, we worked on developing a process that includes the usage of shock wave propagation to create the stripping via mechanical effects with the application of the beam from the painted side of the samples via ablative layer (see figure 1.24).

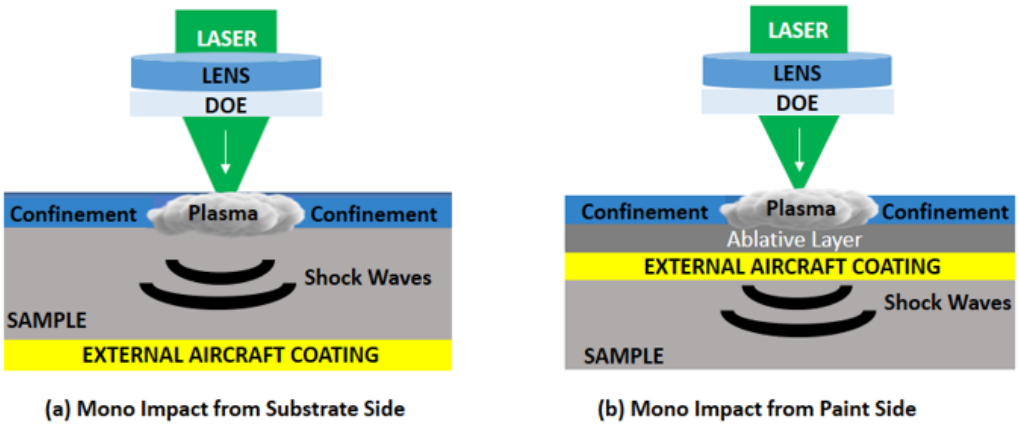

Figure 1.24: (a) Mono impact application from specimen side and and (b) Mono impact application from paint side.

1.5 Other Laser Shock Based Applications

Laser Shock Peening (LSP)

The most convenient way to increase the fatigue life is to apply a treatment in order to produce compressive residual stresses (as deep as possible) into the sample. Today, different techniques are developed to induce compressive residual stress, e.g., traditional shot peening (SP), laser shock peening (LSP), ultrasonic impact/shot peening. Among all mentioned methods, LSP actuates the deepest compressive residual stresses plus providing substantial fatigue life increase and crack growth delay (see figure 1.25). Moreover, LSP also tends to produce a better final treatment of surface and can treat complex surfaces and shapes [52].

Laser Shock Peening (LSP) originated in the late 60's and early 70's where it gained the definition of a cold working mechanical process, in which pulses hit the surface with high power intensity and as a result, shock waves are generated [95].

Experiments on materials using pulsed laser beams were first done at the Battelle Institute (Columbus, OH, USA) in between 1968 to 1981 [96]. The main samples for the experiments were aluminium and steel alloys for aerospace applications. Follow-up experiments were conducted in labs in France such as CLFA (Cooperation Laser Franco-Allemande-Arcueil Cedex), LALP (Laboratoire d'Application des Lasers de Puissance-Arcueil Cedex) and LULI (Laboratoire d'Utilisation des Lasers Intenses-Ecole Polytechnique, Palaiseau Cedex) in order to advance the industrial applicability of the process.

Until the beginning of the 1990's, attempts were made to make the industry more aware of the LSP process and its capacity for extending fatigue life in critical components. The first company supplying LSP components and equipments was the Laser Shock Peening Technologies (LSPT) in 1995 [97].

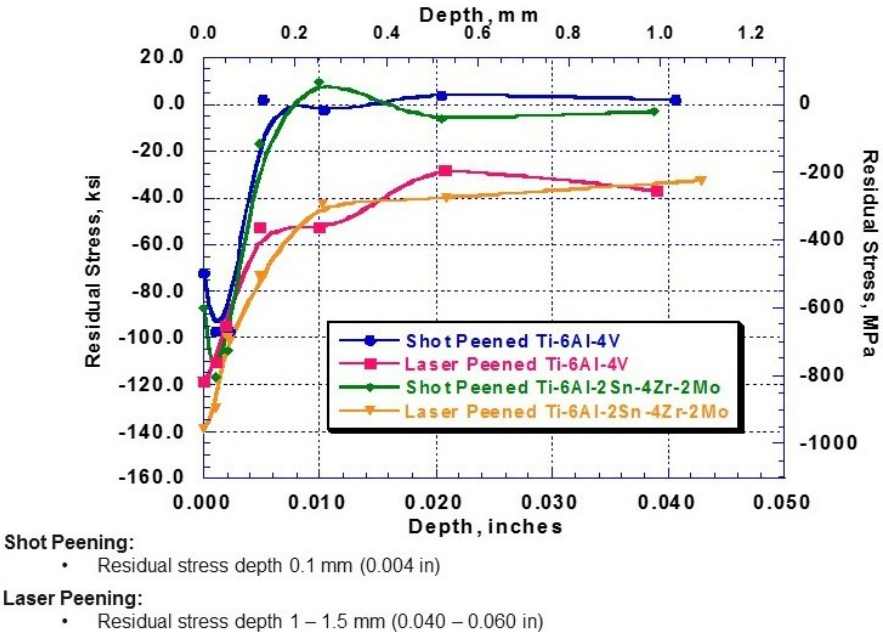

Figure 1.25: Residual Stress Profiles for Laser Peening vs Shot Peening for two Titanium alloys. Retrieved from: https://www.lsptechnologies.com

LSP gained widespread recognition internationally with the first publication in Japan in 1982 [98]. The first work characterizing the system was developed by Toshiba Corporation and was published in 1995. They started Laser Peening without Coating (LPwC) to control Stress Corrosion Cracking (SCC) in Boiling Water Reactors (BWRs). The most advanced distinction between the LSP systems present in USA and the one developed in Japan is the optical fiber utilisation to transport the laser beam into the target. In 2008 the ultra-compact LPwC system (1.5m long and 30kg) was developed, which reflects both availability and reliability due to smaller number of parts decreasing the maintenance cost of the system [99].

1.6 PhD Objectives

The main objective of this thesis is the paint adhesion tests of external aircraft coatings with its application of laser paint stripping. The physical phenomena behind the laser paint adhesion test is the usage of shock waves to create tensile stresses at the desired locations for different interface seperation while controlling the laser parameters. In addition, evaluation of primer integrity and influence of paint properties on the precision of defining common process windows as function of applied power densities are the primary investigations. The arised question is the adhesion levels dependence as function of different conditions such as different type of substrates and coatings, thickness variation of substrates and coated layers, applied surface treatments and thermal ageing impact to define the sensitivity of laser paint adhesion tests. In addition, the investigation of mechanical, chemical and interface properties are done to understand the cause of the failure mechanisms. The procedure for laser paint adhesion tests as follows:

- Pre- analysis before laser treatment
- Material characterization and comprehension of laser-matter interaction for the time of shock propagation via Velocity Interferometer for Any Reflector (VISAR) diagnostic
- Laser adhesion tests via used shock waves for different sample configurations
- Post-mortem analysis
- Parameter optimization via simulation

In addition to laser paint adhesion tests, the thesis will also include laser paint stripping application which is developed via using shock waves unlike conventional laser stripping methods that are based on paint ablation phenomena [91]. For laser paint stripping tests, the same procedure is followed as laser paint adhesion tests. Moreover, different laser technologies (PIMM & RESCOLL facilities) will be studied. The mono impact configuration is investigated both from the paint (due to it's simplicity for the industrial applications) with the usage of an ablative layer and the substrate side of specimens. The understanding of the processes occurs at the different interfaces (ablative layer/coating and coating/substrate) during the laser shots are also analysed.

Objectifs de la Thèse

L'objectif principal de cette thèse est de réaliser des tests d'adhérence de peinture sur des revêtements extérieurs d'aéronefs en appliquant le décapage au laser. Le phénomène physique qui sous-tend le test d'adhésion de la peinture au laser est l'utilisation d'ondes de choc pour créer des contraintes de traction aux endroits souhaités pour différentes séparations d'interface tout en contrôlant les paramètres du laser. En outre, l'évaluation de l'intégrité de l'apprêt et l'influence des propriétés de la peinture sur la précision de la définition des fenêtres de processus communes en fonction des densités de puissance appliquées sont les principales recherches. La question soulevée est la dépendance des niveaux d'adhésion en fonction de différentes conditions telles que les différents types de substrats et de revêtements, la variation de l'épaisseur des substrats et des couches revêtues, les traitements de surface appliqués et l'impact du vieillissement thermique pour définir la sensibilité des tests d'adhésion des peintures au laser. En outre, l'étude des propriétés mécaniques, chimiques et d'interface est effectuée pour comprendre la cause des mécanismes de défaillance. La procédure des tests d'adhésion de peinture au laser est la suivante :

- Pré-analyse avant le traitement laser
- Caractérisation du matériau et compréhension de l'interaction laser-matière au moment de la propagation du choc via le diagnostic VISAR (Velocity Interferometer for Any Reflector)
- Tests d'adhésion au laser via les ondes de choc utilisées pour différentes configurations d'échantillons
- Analyse post-mortem
- Optimisation des paramètres par simulation

En plus des tests d'adhésion de peinture par laser, la thèse comprendra également une application de décapage de peinture par laser qui est développée via l'utilisation d'ondes de chocs contrairement aux méthodes de décapage par laser conventionnelles qui sont basées sur des phénomènes d'ablation de peinture [91]. Pour les tests de décapage au laser, la même procédure est suivie que pour les tests d'adhésion de peinture au laser. De plus, différentes technologies laser (installations PIMM & RESCOLL) seront étudiées. La configuration mono impact est étudiée à la fois du côté de la peinture (en raison de sa simplicité pour les applications industrielles) avec l'utilisation d'une couche ablative et du côté du substrat des spécimens. La compréhension des processus qui se produisent aux différentes interfaces (couche ablative/revêtement et revêtement/substrat) pendant les tirs laser sont également analysés.

2

Samples, Tools and Lasers

Introduction

This chapter covers three main aspects: used samples, tools and lasers. First, the worked samples during the thesis are presented with a recap table of them. Afterwards, the utilized tools for the material characterization and physico-chemical analysis are explained which are profilometer, optical microscopy, Fourier Transform Infrared Spectroscopy (FTIR), Differential Scanning Calorimetry (DSC), Thermogravimetric Analysis (TGA) and micro indentation tester. In the final part of the chapter, the two different used lasers are presented, describing their energy optimization, laser spot optimization as well as temporal profiles. In the second part of this section, the main diagnostic used during this work is detailed which is the velocity interferometer system for any reflector (VISAR). Finally, the utilized numerical methods are explained with details on how finite element explicit solver LS-DYNA is used to model the material behavior under shock loading including used parameters and equations of state.

Introduction FR

Ce chapitre couvre trois aspects principaux : les échantillons étudiés, les caractérisations et les lasers. Tout d'abord, les échantillons travaillés au cours de la thèse sont présentés avec un tableau récapitulatif de ceux-ci. Ensuite, les outils utilisés pour la caractérisation des matériaux et l'analyse physico-chimique sont expliqués qui sont le profilomètre, la microscopie optique, la spectroscopie infrarouge à transformée de Fourier (FTIR), la calorimétrie différentielle à balayage (DSC), l'analyse thermogravimétrique (TGA) et le test de micro indentation. Dans la dernière partie du chapitre, les deux différents lasers utilisés sont présentés en décrivant leur optimisation énergétique, l'optimisation du spot laser ainsi que les profils temporels. Dans la deuxième partie de cette section, le principal diagnostic utilisé au cours de ce travail est détaillé, (VISAR). Enfin, les méthodes numériques utilisées sont expliquées avec des détails sur la façon dont le solveur explicite d'éléments finis explicite LS-DYNA est utilisé pour modéliser le comportement du matériau sous une charge de choc, y compris les paramètres et les équations d'état utilisés.

2.1 Samples

In order to test paint adhesion and laser stripping parameters, Hellenic Aerospace Industry, Akzo Nobel and RESCOLL partners prepared and painted samples for the VULCAN project. These samples can be categorized into two main groups: aluminium based and composite based targets.

2.1.1 Aluminium Based Samples

This section describes pure aluminum, AA 2024-T3 and Aluminum-Lithium based samples. Since pure aluminum is just used for the experimental alignment purposes, it's not studied as broadly as AA 2024 and Aluminum-Lithium based specimens.

Pure Aluminum

Pure aluminum (99 %) is not a specimen which is defined by the project. However, hence there is a huge set of data in the literature for this material, before each set of experiment, the validation of the Velocity Interferometer System for Any Reflector (VISAR) diagnostic (see section 2.4) is done on this target. All used specimens have 1 mm of thickness (see figure 2.1).

Figure 2.1: Target configuration for pure aluminum specimen.

AA 2024 Based Samples

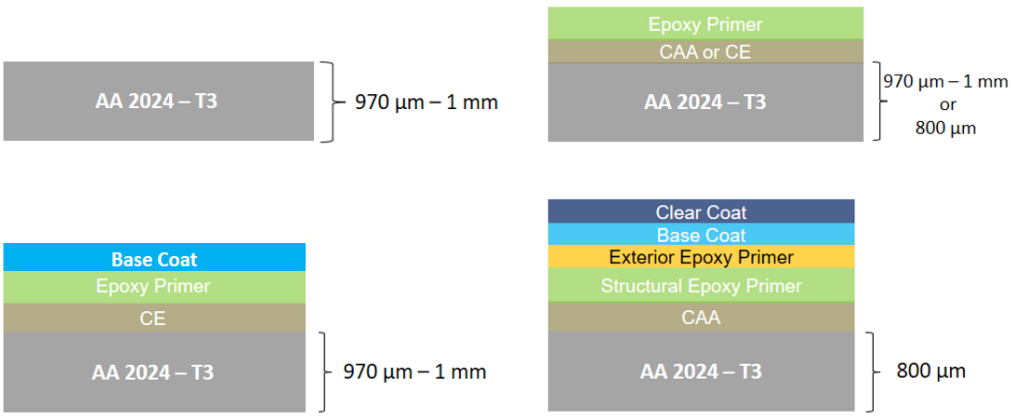

Figure 2.2: Different paint configurations for AA 2024-T3 specimen.

In general, for 2xxx series, AA 2024 is one of the most common material for the industrial usage. It is considered as an aircraft alloy because of its high strength and fatigue resistance. AA 2024 composes of 4.3-4.5% of copper, 0.5-0.6% of manganese, 1.3-1.5%

of magnesium. In addition, less than half percent of silicon, zinc, nickel, chromium, lead and bismuth are included within the alloy to prevent the low yield strength in the high stress regions [100].

For the AA 2024-T3 based samples, the set consists of AA 2024-T3 with two different substrate thicknesses which are 970 μm - 1 mm and 800 μm, epoxy primer (both for structural and exterior) thickness within the range of 18-53 μm, base/top coat of 15-123 μm and clear coat of 15-60 μm with a size of 100 mm x 100 mm and 80 mm x 125 mm for different set of specimens.

Before any paint application, surface treatment might be applied for corrosion protection and promote paint adhesion on substrates [4]. For the used specimens, the applied surface treatments for both samples are chemical etching (CE) with sulfo-ferric acid and chromic acid anodization (CAA), on different sets as shown in figure 2.2.

Due to environmental concerns (toxicity), Cr-free surface treatments are in development for the aeronautics industry. For the Cr-free surface treatments, sol-gel is the most investigated replacement which is used for the aluminum-lithium based materials for this work that will be explained in the following section.

Aluminum-Lithium Based Samples

AL-Li samples studied due to their better mechanical properties in comparison to AA 2024 as explained in figure 1.6. AL-Li 2060 sample consists of 0.75 % of lithium, 3.9 % of copper, 0.3 % of manganese, 0.85 % of magnesium, 0.2 % of silver, 0.11 % of zirconium and 0.4 % of zinc [101].

For the Aluminum-Lithium based targets, the set consists of AL-Li 2060 T8 E30 base with a substrate thickness of 2.5 mm, size of 100 mm x 100 mm. Epoxy primer on top of the base material has a thickness of 14-15 μm and top coat (a base coat in that case) is in the range of 21-22.5 μm. In addition, applied surface treatments are sol-gel and thin film sulphuric acid anodizing (TFSAA) on different sets as given in figure 2.3.

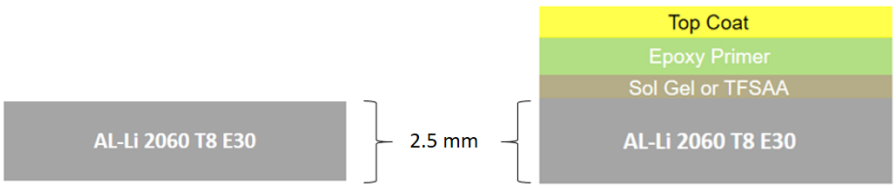

Figure 2.3: Different paint configurations for Al-Li 2060 T8 E30 specimen.

Sol-gel surface treatment emerges as an environmental friendly chromate replacement. The sol-gel method consists of simultaneous hydrolysis and condensation reactions in order to create glassy polymer networks (see Appendix A.1.3 for details) [102].

2.1.2 Composite Based Samples

In order to monitor the capacity of the process, carbon fiber reinforced polymer (CFRP) based samples are investigated as well. CFFP is a stack of plies of fibers. The epoxy matrix is Hex Ply M21. Ply directions are between 0° and 90° with an average thickness of 174 μm plus an interply of 26-30 μm (figure 2.4). The total thickness of composite samples are around 2.35-2.4 mm.

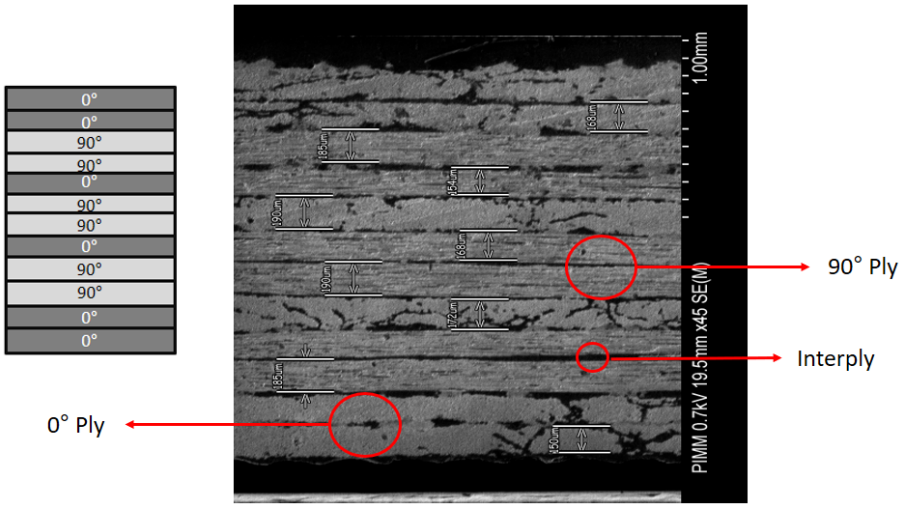

Figure 2.4: Schematic ply directions of the CFRP (on the left) and scanning electron microscope image of used CFRP with its plies and interplies (on the right).

Different sample configurations were studied as shown in figure 2.5. The structural epoxy primer thickness is within the range of 30-40 μm, the exterior primer is in between 10-25 μm, base coat of 15-60 μm and clear coat of 15-44 μm with a size of 100 mm x 100 mm.

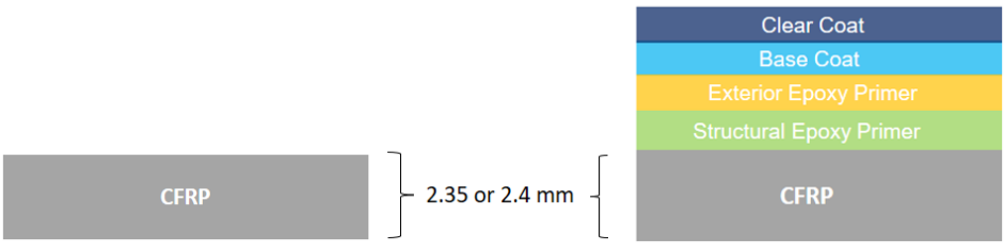

Figure 2.5: Schematic description of CFRP based specimens with/without external aircraft coatings.

2.1.3 Aged Samples

For thermal ageing procedure, only AA 2024 - T3 specimens with an epoxy primer painting architecture with chemical etching surface treatment are studied. In order to observe the effect of thermal ageing clearly, one layer (epoxy primer) based targets are studied. Hence the ageing process is broadly studied on AA 2024 targets in the literature, as a base material, AA 2024 target is used. Samples are isothermally aged in ventilated ovens which are heated at 120 °C with different durations. Plates are prepared to analyse the physico - chemical evolution and related mechanical property changes in parallel to their coating adhesion changes which were tested via laser shock.

For AA 2024 - T3 specimens, the specimen thickness is around 970 μm - 1 mm and for the epoxy primer, the thickness varies in between 40 to 50 μm from one sample to another.

Figure 2.6: The painting schema for thermally aged specimens.

2.1.4 Coating Layers

The usage of thermal layer during laser shock treatments has an important role due to created ablation effects. Created ablation can be in 1 to 5 μm depth from the surface [48]. By using thermal layer, the process becomes purely mechanical. There are several different thermal layers used in the literature such as black or aluminium tape. In Figure 2.7, an example of specimens after peening treatment is given (with and without thermal protective layer, respectively) for inconel 718 (IN718) with a Nd:Yag laser (1054 nm) with used 20 ns pulse duration [103].

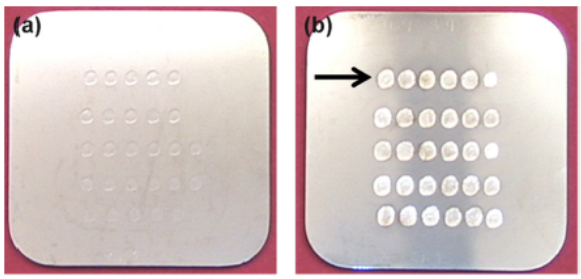

Figure 2.7: Specimens peened with (a) an without (b) protective coatings, respectively [103].

Especially, for the laser applications from paint side this layer has a great importance

since the each external aircraft layer is in μm range. In order to be sure about the created mechanical effect (without having an ablation), for the shots which are done from the paint side of specimens, different thicknesses/configurations of layers have been used.

Gold Coating

In order to obtain physical signals, samples' surfaces facing the probe laser, for VISAR experiments, should have a mirror like reflectivity. For example, for the applied laser source from the metal side of coated specimens, coated side is the part facing the probe laser. In order to have a good reflection on this side, gold coating is applied for some specific specimens with a machine called as "JFC-1100". The samples were inserted in this device under a high vacuum conditions with a sputtering of ions from the gold target to the cathode [104]. For all sets of specimens, coating operated for 2 minutes which gives 10 nm gold thickness on targets (Figure 2.8).

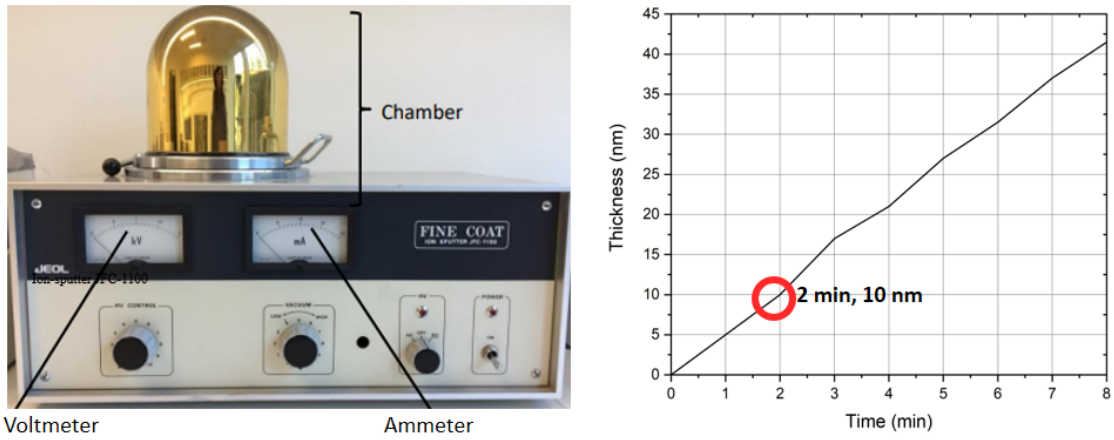

(a) Ion-sputter JFC-1100

(b) Deposited Layer Thickness as function of operation time

Figure 2.8: Ion sputter JFC-1100 and deposited gold layer thickness as function of operation time,respectively [105].

Aluminum Coating

Aluminum coating has been performed at l'Institut de Minéralogie, de Physique des Matériaux, et de Cosmochimie, Sorbonne University. The process is based on Plasma Vapor Deposition (PVD) which has main components of the targets, aluminum in our case, that will be sputtered to make the deposit, there are magnets behind the targets named as magnetron, small opening where the argon gas is introduced and a rotating and heated substrate holder directs the substrates in which the deposit is made as shown in figure 2.9, [106, 107, 108]. The coating thicknesses were 1 μm and 5 μm for VISAR experiments for reflective purposes and preventing the laser ablation effects on the surface, respectively.

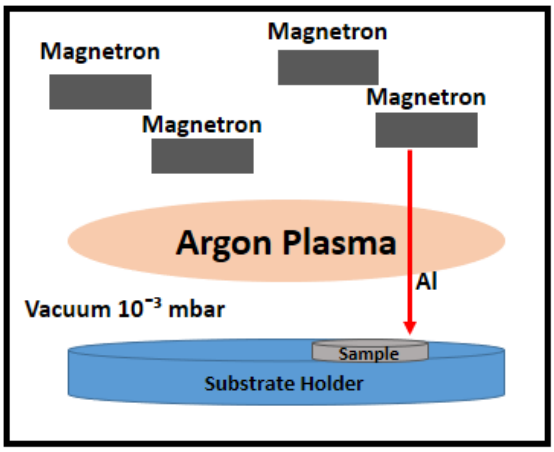

Figure 2.9: PVD operating principle diagram [109].

Pure Aluminum Tape

The used tape is composed of pure aluminum from the front face and a glue (adhesive) from the other face to ensure the adhesion with the target which is developed by 3M company with a thickness of 50 μm for the aluminum and 30 μm of glue as given in figure 2.10.

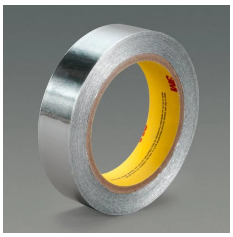

Figure 2.10: 3M-431 tape. Retrieved from: https://www.3m.com

The tape is used for the painted side impacts (epoxy in our case) to reduce the ablative effects caused by the laser.

2.2 Material Characterization and Physico-Chemical Analysis

2.2.1 Profilometer

Profilometer is an instrument which is used to determine the surface profile of a sample. With the help of a diamond tip, the device has a contact with the surface to be analysed and makes it possible to obtain the differences in depths [110]. Figure 2.11 shows this tip and the tray that function as a support. Adjustments are made with the help of a device called Dektak 150 with it's own integrated software. After laser impacts, the coatings are analyzed with respect to the stripped depth through the impacted diameter.

Figure 2.11: Profilometer's tip and tray.

2.2.2 Optical Microscopy

In order to characterize material properties such as surface analysis both before and after laser application or thickness investigation from the cross-section cut (cut-off machine Discotom-6 is used), optical microscopy is used. The used optical microscopy is ZEISS Axio Imager 2 (see Figure 2.12).

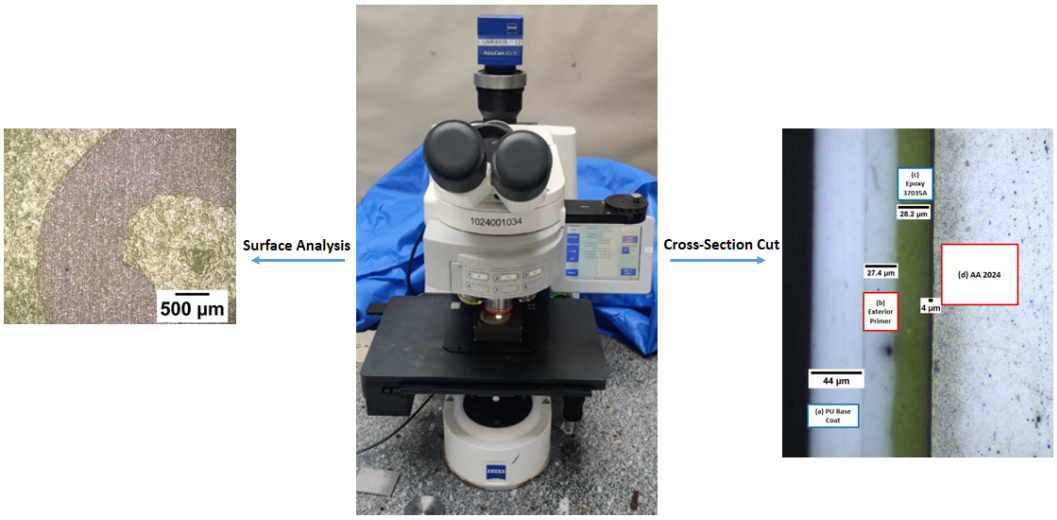

Figure 2.12: Surface analysis after laser impact on AA 2024 + Epoxy with microscope, on the left. In the middle, microscope itself and on the right cross-section cut of an AA 2024 + External Aircraft Coating Layers.

2.2.3 Fourier Transfrom Infrared Spectroscopy (FTIR)

Absorption spectroscopy is a method of physico-chemical analysis which allows the chemical species present in a solution or a solid to be determined both qualitatively and quantitatively without modifying or altering them. This functional analysis gives the identification of the chemical functions present in the molecule but not their exact position. From the signals obtained by infrared, one can attribute different frequency zones (in cm^{-1}) according to the type of bond (triple, double or single) and the function (amine, amide, carboxylic acid, carbonyl, etc.). The principle of FTIR is quite complex but a simplified diagram is presented in figure 2.13. A beam of light from a near-infrared source is directed onto an interferometer. The light passing through the interferometer is reflected

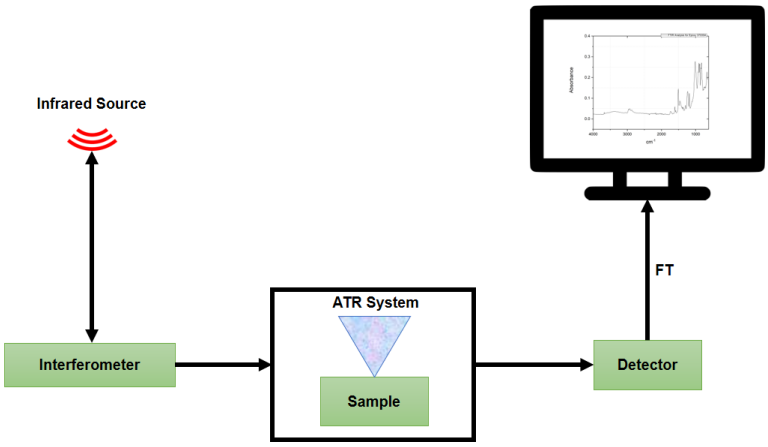

Figure 2.13: Principle of FTIR.

on the sample to be analysed, which is in contact with a crystal that allows an attenuated total reflectance (ATR). A signal is then detected and by Fourier transform, converted into a spectrum [111].

The tool used during the thesis was a Frontier 100 apparatus (Perkin Elmer) equipped with a diamond crystal and driven by spectrum software. 8 scans were collected from 650 to 4000 cm^{-1} with a resolution of 1 cm^{-1} at 1 cm^{-1} intervals. This technique was employed for analyzing the chemical changes during thermal ageing and for identifying the nature of surfaces before and after laser impacts.

2.2.4 Differential Scanning Calorimetry (DSC)

The differential scanning calorimeter is an advanced form of the differential thermal analysis (DTA) technique. During the measurement, a thermal analysis is carried out and a heat exchange difference is recorded. Figure 2.14 summarizes the general principle with the sample to be analysed and the reference cup placed in an oven. With the help of a software, the amount of the heat released or absorbed is measured and some parameters such as the glass transition temperature, the melting and crystallisation temperature, the polymerisation temperature, etc. can be accessed [10]. The apparatus used during the

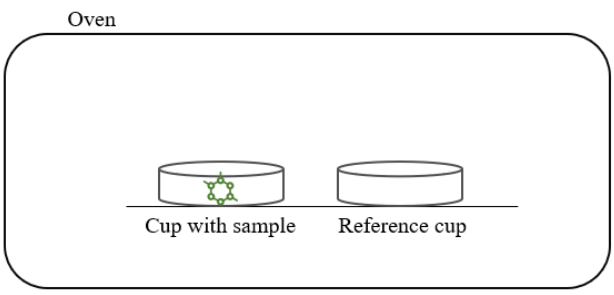

Figure 2.14: Principle of DSC.

measurements was a Q10 from TA instruments which was kept by N_2 flow as a protective inert gas. This technique was used for detecting the T_g of virgin and aged epoxies.

2.2.5 Thermogravimetric Analysis (TGA)

Thermogravimetric Analysis (TGA) is a method for monitoring the alteration of the weight against the temperature and time by certain atmospheres such as nitrogen and oxygen [112, 113, 114, 115]. Moreover, the obtained weight loss is linked to different phenomenas. TGA (Thermogravimetric Analysis) was performed using a Q500 apparatus (TA Instruments) driven by TAQ series explorer. Tested samples were placed in platinum pans and were subjected to heating ramps from room temperature to 900 °C at a 10°C min^{-1} rate under 50 ml min^{-1} nitrogen gas flow (see Figure 2.15). Results were interpreted using TA Universal Analysis software. This technique was used to quantify the

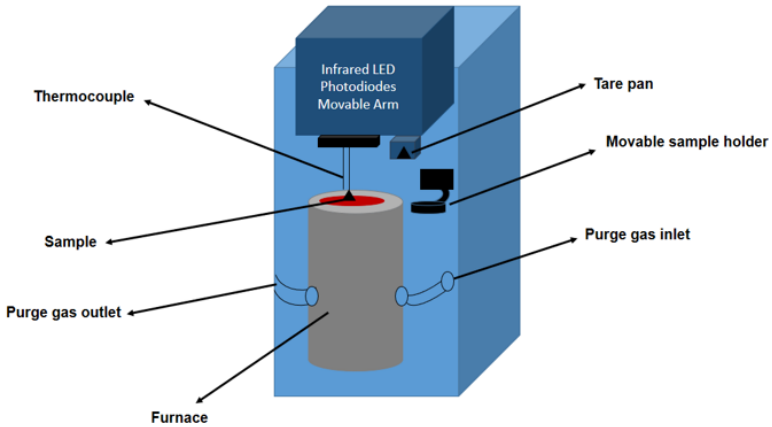

Figure 2.15: TGA Process Scheme.

level of organic component at the surface of coated AA 2024-T3 before and after thermal ageing application.

2.2.6 Micro Indentation Tester

The technique uses the registered depth of penetration of the indenter into the material and measures the applied load to determine mechanical properties such as Young's modulus [116]. As shown in figure 2.16, analyses are carried out by a CSM+ instrument at PIMM, ENSAM on AA 2024-T3 + epoxy samples from the epoxy side with a spherical tipped indenter.

A matrix of 20 intent points is created with a distance of 300 μm between each two points. The applied force on the samples was 300 mN, pause time was fixed at 15 seconds, contact force was equal to 50 μm, approach and retract speed were equal to 16 μm/min,

loading and unlaoding rates were equal to 600 mN/min. For the exploitation of the results, the method of Oliver and Pharr was used [117].

Figure 2.16: Micro Indentation Tester at PIMM, ENSAM.

2.3 Laser

2.3.1 Héphaïstos Facility

Most of the experiments were conducted at Hephaistos facility, PIMM lab, Paris, France. The used laser for the experiments is a Gaïa HP laser from THALES company, France (see figure 2.17). It is a flashlamp-pumped Nd:YAG with a Gaussian temporal profile. The laser can produce 14 Joules of energy, from two beams/channels in total (named as Beam A and Beam B), with 7 ns of pulse duration (FWHM) and 2 Hz of repetition rate at wavelength of 532 nm [118].

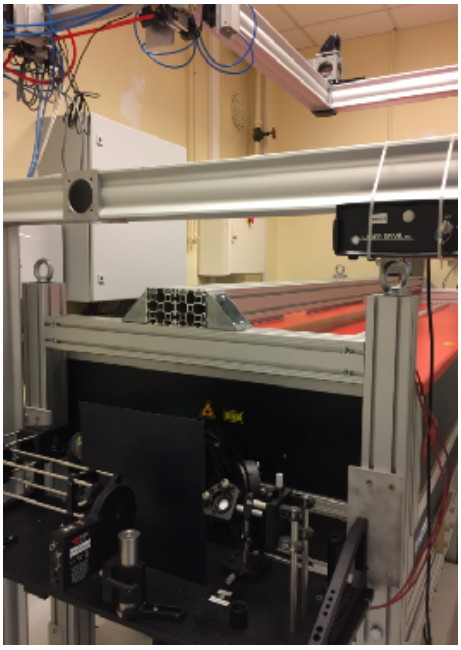

Figure 2.17: Gaïa HP Laser at PIMM.

2.3.2 Monarque Facility

Figure 2.18 shows the Monarque facility at RESCOLL, Pessac, France where some experiments were done. The platform is composed of two Rhéa lasers from THALES company. They are based on the same technology as the Gaia laser (flashlamp-pumped Nd:YAG with a Gaussian temporal profile), with the same wavelength (532 nm) and a total energy of 10 Joules but with a slightly shorter pulse duration (5 ns FWHM) and 5 Hz of repetition rate.

The same procedure was followed for laser energy and spot optimizations like the ones which are conducted at Hephaistos facility. In order to avoid from repetition, optimizations explained just once (for the Hephaistos facility).

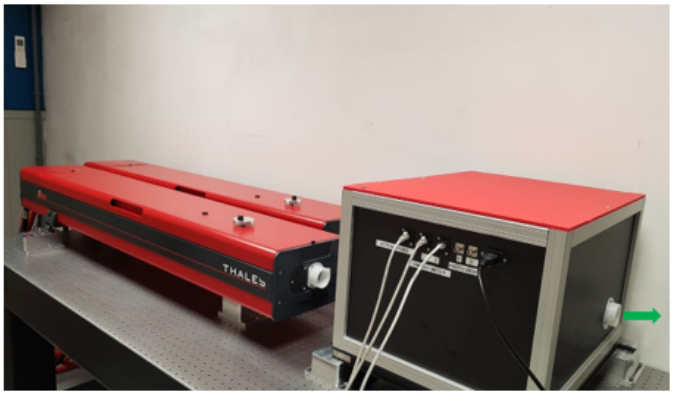

Figure 2.18: Monarque facility at RESCOLL.

2.3.3 Energy Optimization at Hephaistos

The energy output from the laser can be modified/controlled via software in the control room. The software consists of 3 main functions: Channel control, burst parameters and burst mode. Channel control allows us to control the energy output from each channel which is in between 5-100% of their energy. However, the energy output given from the software is not the exact value due to beam losses while transportation which is why energy measurement is done shot by shot and calibrated before each set of experiment using a calorimeter (QE50LP-H-MB-QED, Gentec, Québec, QC, Canada). Since the used energy is the energy obtained via calorimeter for power density calculations, it was important to obtain precise values (see figure 2.19).

For the burst parameters part in the software, there are 3 different modes: activated pulse, total pulse and number sequences. Activated pulse represents the number of pulses which will be used, total pulse is the number of pulses included in one sequence and number sequences is for the number of repetition for a pulse.

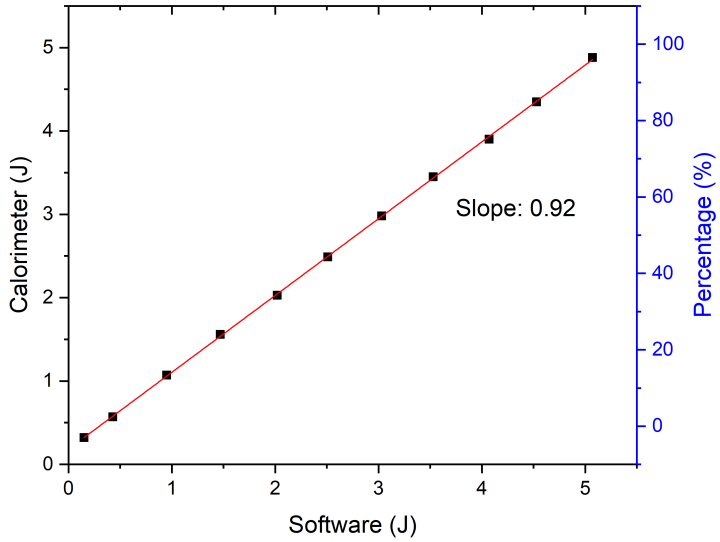

Figure 2.19: Energy optimization for laser energy for one beam (Beam A) with a correction of 9.2%, approximately at Hephaistos, PIMM.

2.3.4 Laser Spot Optimization at Hephaistos

The produced focal spots at Hephaistos, PIMM both with and without DOE (Diffractive Optical Element) obtained via camera (Camera Basler acA2040-25gm/gc, Monochrome, CMOS 1" with a Pixel Size of 5,5 μm x 5,5 μm) are represented in Fig. 2.20. As one can

(a) Without DOE (b) With DOE

Figure 2.20: Comparison of spatial shapes for 4 mm spot size, without & with DOE.

see in Fig. 2.20a, the spatial shape is not homogeneous around the focal spot which is due to diffraction effect during the beam transportation and amplification. Hence there is a strong connection between the pressure and the intensity profile, in order to apply an equal pressure through the whole focal spot on specimens, DOE is used (see Fig. 2.20b) [119].

2.3.5 Temporal Profile

Hephaistos

Figure 2.21 demonstrates the temporal profile of the beam which is measured using an avalanche photodiode with an integrator. The pulse durations of these Gaussians are determined at full width and half maximum (FWHM) which is equal to 7 ns and independent of the incident laser energy.

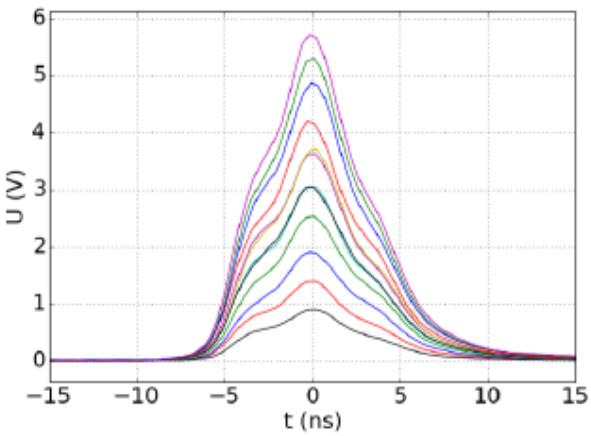

Figure 2.21: Pulse duration measurements at Hephaistos, PIMM for different energy values [49].

Monarque

As one can see from figure 2.22, the temporal profile of the beam at Monarque facility is measured with the same kind of photodiode. The measured FWHM is equal to 5 ns, which is the pulse duration of the laser in that facility.

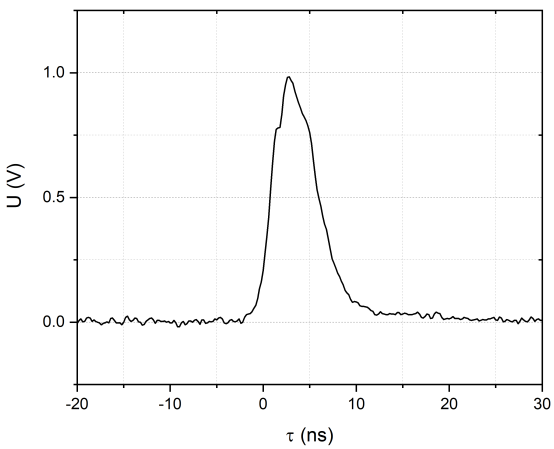

Figure 2.22: Pulse duration measurement at Monarque, RESCOLL.

2.4 Velocity Interferometer System for Any Reflector (VISAR)

2.4.1 Physical Principle

Velocity measurement is of major importance to the shock community. Extraction of material and wave velocity leads to have an information about materials under extreme conditions [120] via Velocity Interferometer System for Any Reflector (VISAR) diagnostic. In many cases, velocity is the easiest and only obtainable property in highly compressed systems unlike stress or temperature [121].

The VISAR is based on the Michelson Interferometer which is developed in the late 1960s [122]. The measured quantity is the Doppler Shift (the shock wave makes the target move) in wavelength of probe laser (VERDI) that is reflected on the back face of the accelerated target via shock wave. Therefore, the Doppler effect links the back surface velocity and the wavelength shift of the beam [121] with the following equation:

$$\lambda = \lambda_0(1 - \frac{v}{c}) \tag{2.1}$$

where λ_0 is the initial wavelength of the laser, v is the velocity of the object and c is the speed of light in vacuum.

2.4.2 Experimental Set-up

The used setup for VISAR experiments consist of two parts, which are connected via optical fiber. The first part is the probe part and the second one is an interferometer as represented in figure 2.23.

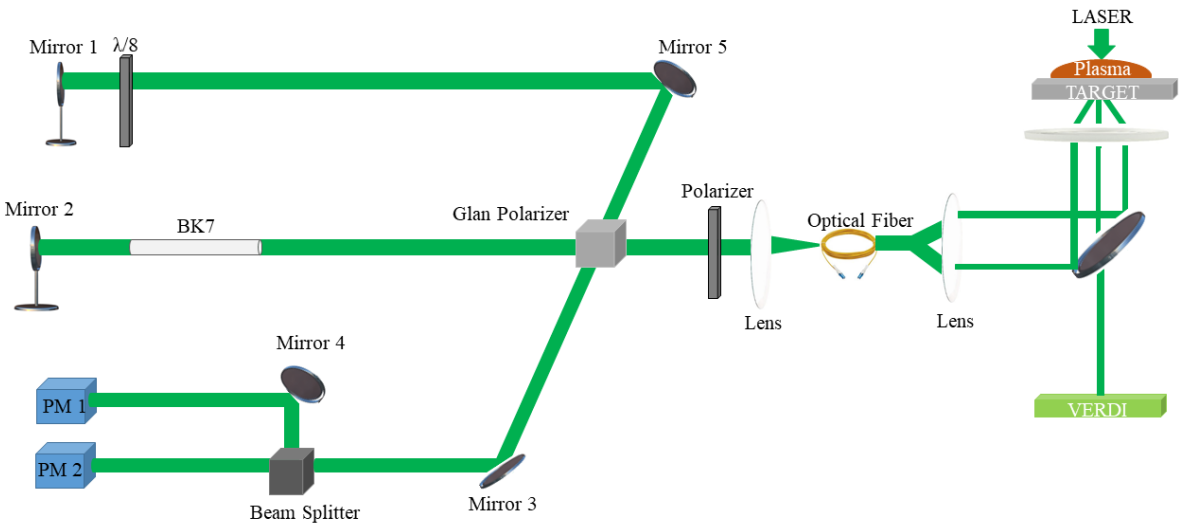

Figure 2.23: Schematic representation of the experimental set-up at PIMM.

In order to process the velocity measurements, the Doppler Shift of a monomode probe laser (Verdi - 532 nm) reflected at the rear surface of the target measured by Michelson Interferometer. For the interferometer part, the first arm is located between the Mirror

1 and a wave plate (reference branch at time t). The second arm is set between the Mirror 2 and the glan polarizer (delayed branch at t-τ). This branch also contains a crystal to apply the delay τ to the signal.

The mirror 4 guides the interference pattern into the sensors. The optical assembly formed by the polarizer and the wave plate $\lambda/8$ enables the creation of two interference phase-shifted signals with a $\pi/2$. The information of these systems detected respectively by the photo multiplier 1 (PM1) and photo multiplier 2 (PM2) via the polarizing cube splitter. The data obtained by the oscilloscope is transmitted and with the help of the software, corresponding velocity profiles can be obtained.

Fringe Factor and Velocity Relation:

The basic concept of VISAR analysis can be defined via the Doppler shift of light being reflected off of the surface of a moving object to measure the velocity profile of the object. There are two main steps for this analysis:

- Determining the fringe shift of the light reflected off of the object
- Calculating the velocity of the object based on the measured fringe shift

Velocity per fringe term, VPF, is the main parameter to obtain the free-surface velocity of the object in motion [123].

The equation for the VPF is given as:

$$VPF = \frac{\lambda}{2\tau(1+\delta)} \tag{2.2}$$

where λ is the Doppler shifted wavelength of the laser, τ is the temporal delay between the two arms of the interferometer caused by the crystal and $(1+\delta)$ is the correction term which is a function of the refraction index of the crystal and the laser wavelength [124]. VPF equation helps to provide an information about the velocity at each location in space as function of time. The Doppler shift produces light fringes in the interferometer and the number of fringes proportional to the velocity as given:

$$V = VPF * F(t) \tag{2.3}$$

where F(t) is the number of fringes.

2.5 Numerical Methods

In order to model the material behavior under shock loading, finite element explicit solver LS-DYNA has been utilized. The different material models have been used to simulate the materials' response to high strain rate in the literature [125, 126, 127]. In addition, equation of state has been inserted to relate the changes during the shock propagation like pressure, energy or density [128].

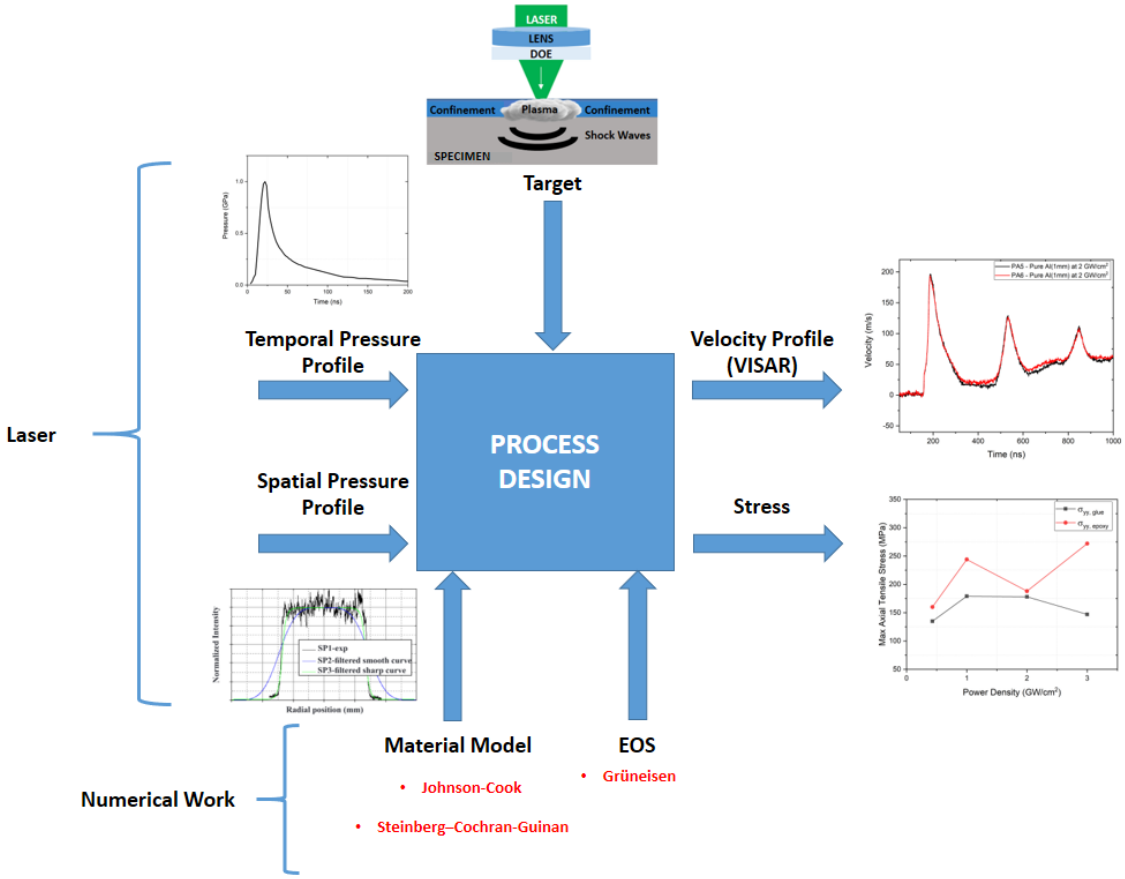

Figure 2.24: Schematic description of the followed methodology.

Figure 2.24 describes the general approach for the followed methodology. The pressure control and optimization is done via spatial and temporal pressure profiles. According to the used target for laser applications, numerical model is defined with all the related parameters. Then, the VISAR diagnostic is used to monitor and extract the experimental results. If the chosen parameters for the numerical model agrees well with the experimental results, the validation is completed and other parameters such as axial tensile stresses at the different interfaces can be extracted.

2.5.1 Multidimensional Model

2D axisymmetric model is used with a mesh size of 2 μm to model Pure Aluminum, AA 2024 - T3 and AA 2024 - T3 + Epoxy Primer with the usage of thermal coat for the

painted side applications which consists of pure aluminum (99%) and acrylic (glue). The values for the simulations were obtained from the literature since AA 2024 - T3 and pure aluminum are well-known/studied materials. For epoxy and acrylic glue, literature values were used as well but since the variety of polymers are broad, error range is higher compared to AA 2024 - T3 and pure aluminum alone.

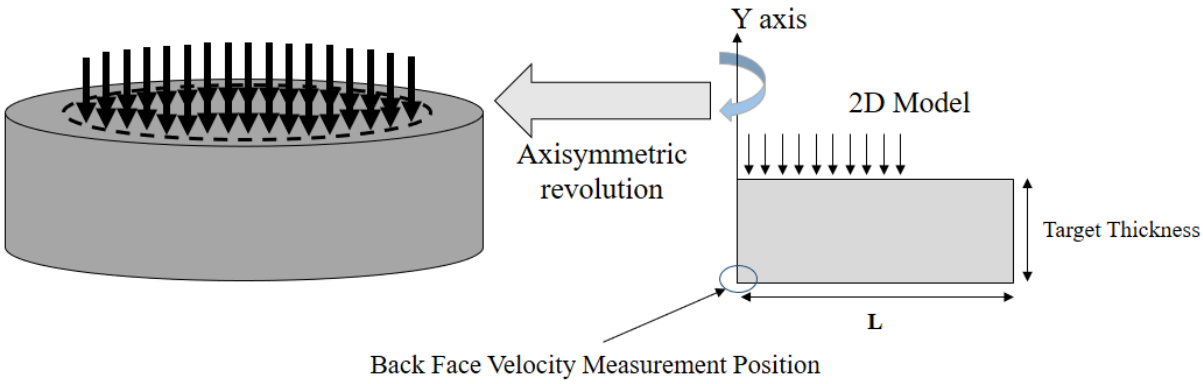

Figure 2.25: 2D axisymmetric model with pressure loading and back face velocity measurement position [129].

Figure 2.25 gives a general descriptive approach for the 2D model and the axisymmetric approach which are also explained in detail in section 3.1.2.

2.5.2 Material Model

Johnson-Cook constitutive law has been used by the community for modelling the shock wave behavior due to its strain rate, strain-hardening and temperature effects parameters. Different studies neglected thermal effects and validated numerical results by coupling them with the experimental ones [130, 131, 132]. The Johnson-Cook material model is available in LS-DYNA. During this study, MAT_JOHNSON_COOK (MAT_015) is used. The model defines a Von Mises tensile flow stress, as function of strain hardening, strain rate hardening, and thermal softening via equation 2.4:

$$\bar{\sigma}_{eq} = \left(A + B\bar{\varepsilon}_p^n\right)\left(1 + C\ln\left(\frac{\dot{\bar{\varepsilon}}_p}{\dot{\varepsilon}_0}\right)\right)\left(1 - \left(\frac{T - T_0}{T_m - T_0}\right)^m\right) \tag{2.4}$$

where the elastic limit will be calculated as function of the initial yield strength A, taking into account the strain rate sensitivity calculated by the ratio between the plastic and the reference strain rate $\dot{\bar{\varepsilon}}_p$, and $\dot{\varepsilon}_0$, respectively. B is the strain hardening modulus, C is the strain rate coefficient, n is the hardening coefficient, T_0 is the room temperature, T_{melt} is the fusion temperature and m is the thermal softening coefficient. The first part of the equation is the strain hardening effect, the second is the strain rate effect and the final part is for the stress evolution with temperature during the plastic deformation. Thermal effects are not included during this study. The used parameters for AA 2024 - T3 and pure aluminum are explained below (table 2.1 and 2.2).

Symbol	Parameter	Value	Unit (SI)
ρ	Density	2780	kg/m^3
G	Shear Modulus	28	GPa
C_P	Specific Heat Capacity	0.875	J/g°C
T_m	Melting Temperature	502	°C
T_0	Room Temperature	25	°C
A	Stress Yield limit	369	MPa
B	Strain hardening modulus	329	MPa
C	Strain Rate Coefficient	0.025	-
n	Stress hardening exponent	0.35	-

Table 2.1: AA 2024 - T3's mechanical properties and parameters used for Johnson-Cook equation [133, 129].

Symbol	Parameter	Value	Unit (SI)
ρ	Density	2698.9	kg/m^3
G	Shear Modulus	25	GPa
C_P	Specific Heat Capacity	0.9	J/g°C
T_m	Melting Temperature	660	°C
T_0	Room Temperature	25	°C
A	Stress Yield limit	90	MPa
B	Strain hardening modulus	200	MPa
C	Strain Rate Coefficient	0.035	-
n	Strain hardening exponent	0.3	-

Table 2.2: Pure Aluminum's mechanical properties and parameters used for Johnson-Cook equation [133, 129].

Since the polymer behavior is "highly engineered pressure sensitive", Steinberg–Cochran-Guinan (SCG) material model has been used to simulate the acrylic layer in the aluminium tape and epoxy primer. The material type (MAT_011) takes into account the sensitivity of the temperature and the pressure for elastic properties and yield criterion [134]. In this study, we use the elastic part of the material model with the pressure dependency, where the shear modulus G will be calculated as in equation (2.5).

$$G = G_0[1 + bpV^{1/3}] \tag{2.5}$$

where G_0 is the initial shear modulus which will increase with the increasing pressure according to the pressure sensitivity parameter b (taken as 8). "b" is the ratio of the derivative of the shear modulus with respect to pressure over the initial shear modulus ($b = \frac{1}{G_0}\frac{\partial G}{\partial P}$). V is the relative volume during the deformation under shock wave propagation.

Table 2.3 and table 2.4 give the acrylic's and epoxy's mechanical properties and parameters which used for Steinberg material model.

Symbol	Parameter	Value	Unit (SI)
ρ	Density	1180	kg/m^3
G	Shear Modulus	0.45	GPa
b	Pressure sensitivity parameter	8	GPa^{-1}

Table 2.3: Acrylic's mechanical properties and parameters which used for Steinberg material model [135].

Symbol	Parameter	Value	Unit (SI)
ρ	Density	1700	kg/m^3
G	Shear Modulus	2.5	GPa
b	Pressure sensitivity parameter	8	GPa^{-1}

Table 2.4: Epoxy's mechanical properties and parameters which used for Steinberg material model [136, 137].

2.5.2.1 Equation of State

For the high strain rate impact, the Grüneisen is a commonly used Equation of State (EOS) [138, 139] due to its accuracy for the behavior of the Hugoniot relationships under shock compression. The Grüneisen is defined in LS-DYNA (EOS_GRUNEISEN) as function of particle velocity U(u) (as given in equation 1.13) which defines different pressures for compressed and extended materials as given in the following equations accordingly:

$$p = \frac{\rho_0 C^2 \beta[1 + (1 - \frac{\gamma_0}{2})\beta - \frac{a}{2}\beta^2]}{[1 - (S_1 - 1)\beta - S_2 \frac{\beta^2}{\beta+1} - S_3 \frac{\beta^3}{(\beta+1)^2}]^2} + (\gamma_0 + a\beta)E \tag{2.6a}$$

$$p = \rho_0 C^2 \beta + (\gamma_0 + a\beta)E. \tag{2.6b}$$

Here C is the intercept of U(u) curve (value of U when u=0 [140]); S_1, S_2 and S_3 are the unitless coefficients of the slope of the U(u) curve; γ_0 is the unitless Grüneisen gamma, a is the unitless, first order volume correction to γ_0, and $\beta = \frac{\rho}{\rho_0} - 1$, E denotes the internal energy.

Used parameters to feed the equation of state for pure aluminum, AA 2024 - T3, acrylic and epoxy are given in the tables 2.5, 2.6, 2.7 and 2.8 below.

Symbol	Parameter	Value	Unit (SI)
C	Intercept of $v_s(v_p)$ curve	5328	m/s
s_1	Coefficient of $v_s(v_p)$ curve	1.338	-
γ_0	Grüneisen gamma	2	-

Table 2.5: Used Grüneisen mechanical parameters for pure aluminum [139].

Symbol	Parameter	Value	Unit (SI)
C	Intercept of $v_s(v_p)$ curve	4880	m/s
s_1	Coefficient of $v_s(v_p)$ curve	1.338	-
γ_0	Grüneisen gamma	2	-

Table 2.6: Used Grüneisen mechanical parameters for AA 2024-T3 [139].

Symbol	Parameter	Value	Unit (SI)
C	Intercept of $v_s(v_p)$ curve	1200	m/s
s_1	Coefficient of $v_s(v_p)$ curve	1.493	-
γ_0	Grüneisen gamma	1.13	-

Table 2.7: Used Grüneisen mechanical parameters for acrylic [135].

Symbol	Parameter	Value	Unit (SI)
C	Intercept of $v_s(v_p)$ curve	1400	m/s
s_1	Coefficient of $v_s(v_p)$ curve	1.493	-
γ_0	Grüneisen gamma	1.13	-

Table 2.8: Used Grüneisen mechanical parameters for epoxy [136, 137].

2.5.3 Spatial and Temporal Pressure Profiles

This part presents the source term used for simulations via laser-induced plasma pressure (temporal and spatial input).

2.5.3.1 Spatial Pressure Profile

The spatial profiles were produced via using real laser spot profiles obtained with a camera as explained in 2.3.4. The fluctuations which exist in the spatial profile might create a huge loading gradient between one element to another. These fluctuations are created due to the interferences of the laser beam after being diffracted by the DOE. To avoid this effect, we filter the experimental profile (Butterworth filter) [129].

Figure 2.26 represents the spatial distribution for normalized intensity profile for 4 mm spot size where SP1 is experimental, SP2 is the filtered smooth curve and SP3 is the filtered sharp curve.

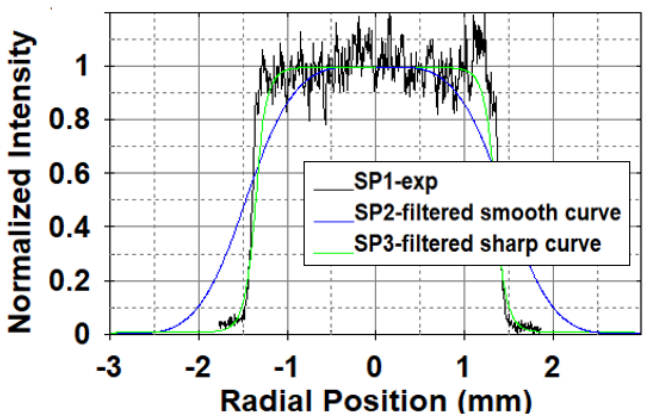

Figure 2.26: Spatial distribution for normalized intensity profile for 4 mm spot for SP1, SP2 and SP3 [129].

2.5.3.2 Temporal Pressure Profile

Temporal pressure profiles were generated from the previous works via scale law extracted from 1D ESTHER code [49]. Figure 2.27 shows a typical pressure profile generated through the code for a 7 ns Full Width half Maximum (FWHM) and for a wavelength of 532 nm.

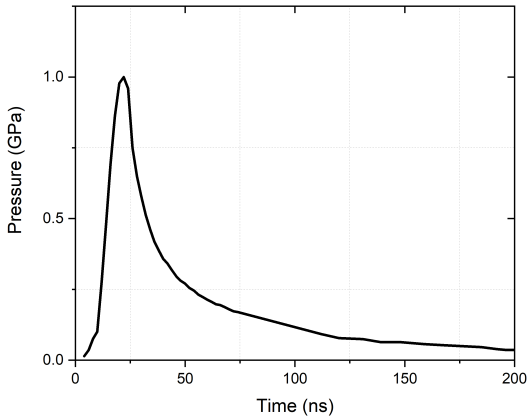

Figure 2.27: The pressure profile as a function of time [49].

2.6 Summary of Used Samples

Since pure aluminum samples are used without any coating on them, summary tables do not cover the pure aluminum target.

2.6.1 AA 2024 - T3 Based Samples

BASE MATERIAL & THICKNESS	SURFACE TREATMENT	COATING/S & THICKNESS	SAMPLE & SIZE
AA 2024 - T3 (970 µm – 1 mm)	-	-	80 mm x 125 mm
AA 2024 - T3 (970 µm – 1 mm)	Chemical Etching	- Structural Epoxy Primer CA 7049 (18 – 53µm)	80 mm x 125 mm
AA 2024 - T3 (800 µm)	Chromic Acid Anodization	- Structural Epoxy Primer 37035A (18 – 53µm)	100 mm x 100 mm
AA 2024 - T3 (970 µm – 1 mm)	Chemical Etching	- Structural Epoxy Primer CA 7049 (18 – 53µm) - Polyurethane Top Coat CA 8800 (15 – 123µm)	80 mm x 125 mm
AA 2024 - T3 (800 µm)	Chromic Acid Anodization	- Structural Epoxy Primer 37035A (18 – 53µm) - Exterior Epoxy Primer HS2121 CF (18 – 53µm) - Polyurethane Base Coat (15 – 123µm) - Polyurethane Clear Coat (15 – 60µm)	100 mm x 100 mm

Table 2.9: Summary of samples based on AA 2024-T3.

2.6.2 AL-Li 2060 - T8 E30 Based Samples

BASE MATERIAL & THICKNESS	SURFACE TREATMENT	COATING/S & THICKNESS	SAMPLE & SIZE
AL-Li 2060 - T8 E30 (2.5 mm)	-	-	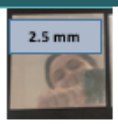 100 mm x 100 mm
AL-Li 2060 - T8 E30 (2.5 mm)	Sol Gel AC-131	- Epoxy Primer XP-371 (10– 15µm) - Polyurethane Topcoat C21 – 100 (20 – 25µm)	100 mm x 100 mm
AL-Li 2060 - T8 E30 (2.5 mm)	Thin Film Sulfuric Acid Anodizing	- Epoxy Primer XP-371 (10 – 15µm) - Polyurethane Topcoat C21 – 100 (20 – 25µm)	100 mm x 100 mm

Table 2.10: Summary of samples based on AL-Li 2060 - T8 E30 Based Samples.

2.6.3 CFRP Based Samples

BASE MATERIAL & THICKNESS	SURFACE TREATMENT	COATING/S & THICKNESS	SAMPLE & SIZE
CFRP M21 Epoxy by HEXCEL (2.35 mm)	-	-	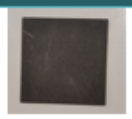 100 mm x 100 mm
CFRP M21 Epoxy by HEXCEL (2.35 mm)	-	- Structural Epoxy Primer 37045A (30 – 40µm) - Exterior Epoxy Primer HS2121 CF (10-25 µm) - Polyurethane Base Coat (15 – 60µm) - Polyurethane Clear Coat (15 – 44µm)	100 mm x 100 mm

Table 2.11: Summary of samples based on CFRP Based Samples.

2.7 Summary of Used Experimental Tools

DIAGNOSTIC	MEASUREMENT	OUTCOME
VISAR	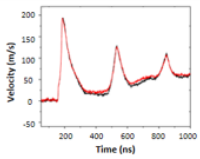	• Material characterization via back face velocity response
Optical Microscope	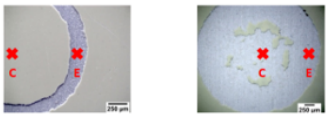	• Surface and thickness analysis before & after laser impacts
Profilometer	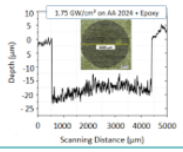	• Stripped depth of coatings through the impacted diameter (after laser impacts)
FTIR DSC TGA	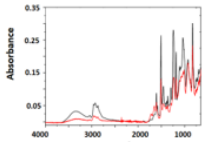 FTIR Weight Loss (%) / Stripping Treshold (GW/cm²): 10.07 / 2.77; 3.42 / -; 1.22 / 0.68 TGA Condition / Unaged / 504 h; Glass Temperature (°C) / 57 / 36 DSC	• FTIR: Chemical characterization of coatings (before & after laser) • DSC: Glass temperature evaluation • TGA: Quantification of remaining contents after laser
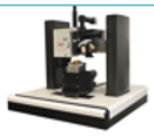 Micro Indentation Tester	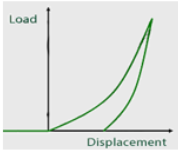	• Meaures the applied load to determine mechanical properties such as Young's Modulus

Table 2.12: Summary of used experimental tools.

3

Materials Under Shock

Introduction

This chapter begins by describing a process of substrate characterization followed by analysis of both single and several layers of paint configurations. Furthermore, process simulation for validation purposes is conducted. Finally, applications to adhesive tape under laser shock is done. The work covers of an experimental and numerical work on pure aluminum (99 %), AA 2024 -T3 and AA 2024 -T3 + Epoxy Primer. AA 2024 -T3 + Epoxy Primer + Top Coat, AL-Li 2060- T8 E30 and CFRP based specimens are just investigated via experimental work. Since the laser-shock is a complicated phenomena, we started to characterize the materials under shock via VISAR diagnostic before any laser paint adhesion and laser paint stripping tests. In addition to base materials (pure aluminum, AA 2024 - T3, AL-Li 2060- T8 E30 and CFRP), understanding of the polymer behavior (epoxy, polyurethane and acrylic in our case) is key to have conclusive results hence there is not much work on this specific subject in the literature. The monitored results are coupled with numerical work then used to optimize the parameters for laser stripping applications. The chapter is divided into 4 parts:

- Behaviour of Pure Aluminum, AA 2024-T3 and AL-Li 2060 - T8 E30 under laser shock loading
- Behaviour of Aluminum Tape under laser shock loading
- Behaviour of Epoxy and Polyurethane Coatings under laser shock loading
- Behaviour of CFRP under laser shock loading

Introduction FR

Dans ce chapitre, tout d'abord, la caractérisation du substrat est effectuée. Ensuite, des configurations à une et plusieurs couches de peinture sont analysées. En parallèle, une simulation du procédé à des fins de validation est réalisée. Enfin, les applications au ruban adhésif sous choc laser sont réalisées. Le travail couvre un travail expérimental et numérique sur de l'aluminium pur (99 %), AA 2024 -T3 et AA 2024 -T3 + Epoxy Primaire. AA 2024 -T3 + Epoxy Primaire + Top Coat, AL-Li 2060- T8 E30 et des spécimens à base de CFRP sont étudiés par le biais de travaux expérimentaux. Le choc laser étant un phénomène complexe, nous avons commencé à caractériser les matériaux sous choc par un diagnostic VISAR avant tout essai d'adhésion et de décapage de la peinture au laser. En plus des matériaux de base (aluminium pur, AA 2024 - T3, AL-Li 2060- T8 E30 et CFRP), la compréhension du comportement des polymères (époxy, polyuréthane et acrylique dans notre cas) est une clé pour avoir des résultats concluants ; il n'y a donc pas beaucoup de travaux sur ce sujet spécifique dans la littérature. Les résultats obtenus sont couplés à des travaux numériques puis utilisés pour optimiser les paramètres pour les applications de décapage laser. Le chapitre est divisé en 4 parties:

- Comportement de l'aluminium pur, AA 2024-T3 et AL-Li 2060 - T8 E30 sous charge de choc laser
- Comportement du ruban d'aluminium sous l'effet d'un choc laser
- Comportement des revêtements époxy et polyuréthane sous l'effet des chocs laser
- Comportement du CFRP sous charge de choc au laser

3.1 Behavior of Aluminum based materials under laser shock

In this section, back face velocity (BFV) profiles are extracted at different applied power densities using VISAR diagnostic (as explained in section 2.4), experimentally. Then, the loading conditions such as spatial and temporal profiles are used as an input for simulations. Eventually, numerical models are compared with the experimental results for pure aluminum and calibrated for all other different material architectures (see figure 3.1) for process optimization purposes. The obtained results are based on recently developed methodology and modelisation by Scius-Bertrand et al. [49]. In addition, correlation of experimental and numerical work is formulated on the recent works [129, 133].

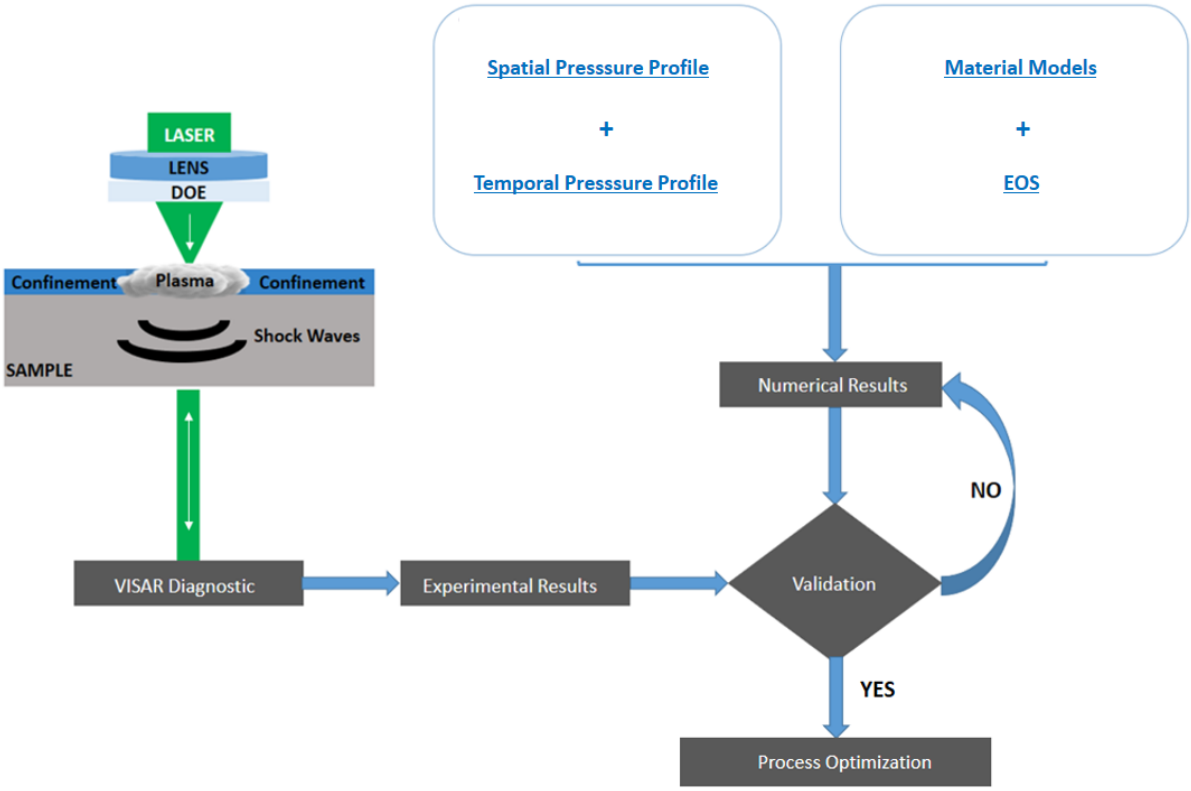

Figure 3.1: Schematic description of the followed methodology.

In the following section, first step covers the obtained experimental back face velocities for pure aluminum, AA 2024-T3 and AL-Li 2060-T8. Secondly, comparison of VISAR and numerical simulations is done for pure aluminum and AA 2024-T3 specimens to validate the material models before moving to further steps.

3.1.1 Characterization via VISAR

3.1.1.1 Pure Aluminum

Figure 3.2 represents the basic view of the laser set-up. Pure aluminum target is covered with a water confinement during the experiments. With the help of the created plasma, shock waves are induced within the specimens. The created Doppler shifts due to the acceleration of the target thanks to the shock waves are monitored with the VISAR to extract the BFV profiles.

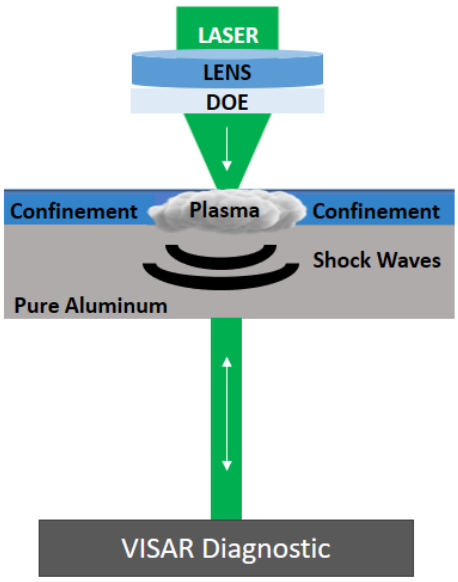

Figure 3.2: Pure Aluminum target with the VISAR diagnostic.

Experimental work is conducted on pure aluminum samples (1 mm thick) with a focal spot of 4 mm via mono impact laser configuration and within the power density range of 0.8 to 2 GW/cm^2. For simplicity, samples named as PA1, PA2, PA3, PA4, PA5 and PA6 (see table 3.1).

Sample	Focal (mm)	Impact Type	Power Density (GW/cm^2)
PA1	4	Mono	0.8
PA2	4	Mono	0.8
PA3	4	Mono	1
PA4	4	Mono	1
PA5	4	Mono	2
PA6	4	Mono	2

Table 3.1: Summary of used focal spot, applied impact type and power densities on samples.

Figure 3.3 gathers the experimentally obtained back face velocities for each different power densities. According to the curves, it can be said that all the signals are reproducible. This was the first step of the validation process before starting the simulation

approach. Since there are different material model parameters available in the literature for the numerical approach, experimental measurements of back face velocities should be completed to validate our numerical inputs.

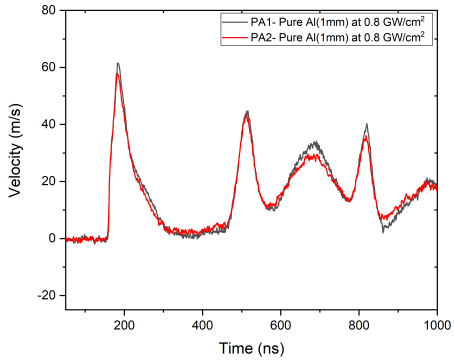

(a) 0.8 GW/cm^2 laser impact

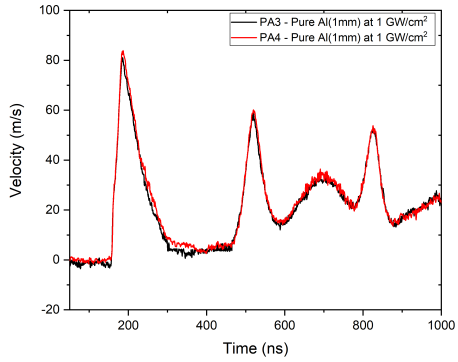

(b) 1 GW/cm^2 laser impact

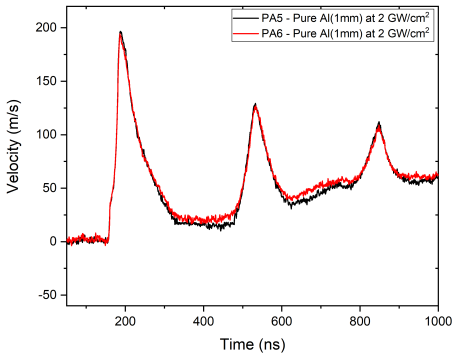

(c) 2 GW/cm^2 laser impact

Figure 3.3: Experimentally obtained back face velocity curves at different power densities for pure aluminum.

In figure 3.4, two repeated signals are presented at 2 GW/cm^2 which are named as PA5 and PA6 in table 3.1, previously. Some points are marked as "a, b, c and d" in the figure. As explained in table 3.2 , the point "a" represents the shoulder separating of a fast elastic wave from a slower plastic wave. The point "b" shows the first shock breaking out and "c" is for the second shock breaking out. Finally, the point "d" represents the third shock breaking out which corresponds to the back and forth of the second one.

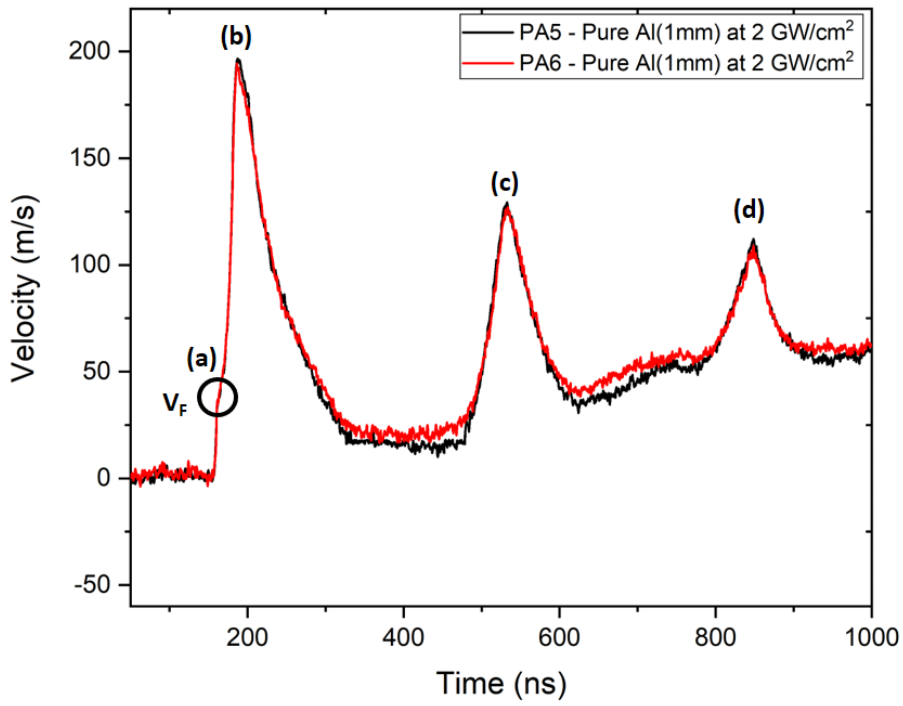

Figure 3.4: Given VISAR signal at 2 GW/cm^2 with the elastic precursor velocity V_F and corresponding peaks.

Notation	Definition
(a)	Shoulder separating the fast elastic wave from the slower plastic wave [141]
(b)	1st shock breaking out
(c)	2nd shock breaking out which corresponds to the back and forth of the first one
(d)	3rd shock breaking out which corresponds to the back and forth of the second one

Table 3.2: Origin of pure aluminum BFV profiles peaks [129].

As known, shock waves lead material to undergo plastic deformations. The point in which a material has a transition from a purely elastic state to an elastic-plastic state is named as Hugoniot elastic limit (HEL) and the value of the pressure where this transition occurs is called as "P_{HEL}". Above the HEL, the material loses most of its shear strength and starts to act like a fluid. P_{HEL} values are calculated for each aluminum target to have a conclusive result. P_{HEL} is defined via following equation [132]:

$$P_{HEL} = \frac{1}{2} \times \rho \times c_{el} \times V_F \tag{3.1}$$

where ρ is the material density, C_{el} is the elastic wave velocity given by equation (3.2), and V_F is the velocity which corresponds to the elastic precursor which is obtained

experimentally by VISAR as shown in figure 3.4.

$$C_{el} = \sqrt{\frac{E(1-\nu)}{\rho(1+\nu)(1-2\nu)}}. \tag{3.2}$$

C_{el} is calculated as 6258 m/s by inserting elastic modulus (E), ρ (density) and ν (Poisson ratio) as given in table 3.3. By placing C_{el}, ρ and V_F (35 m/s ±%16), P_{HEL} becomes 0.3 GPa (as an average).

ρ (kg/m^3)	V_F (m/s)	E (GPa)	ν	P_{HEL} (GPa)
2700	35	70	0.33	0.3

Table 3.3: Summary of used and calculated parameters for P_{HEL} - Pure Aluminum [133].

3.1.1.2 AA 2024 - T3

VISAR diagnostic is used for AA 2024-T3 specimens as well (see figure 3.5). First, the obtained BFV curves are compared for the reproducibility of the process and then, comparison of experimental results and numerical work is done, as explained previously for pure aluminum targets.

Experimental work is done on AA 2024-T3 samples (1 mm) with a focal spot of 4 mm via mono impact configuration and power density range of 0.8 to 2.8 GW/cm^2. For clarity purposes, samples named as AA1, AA2, AA3, AA4, AA5 and AA6 (see table 3.4).

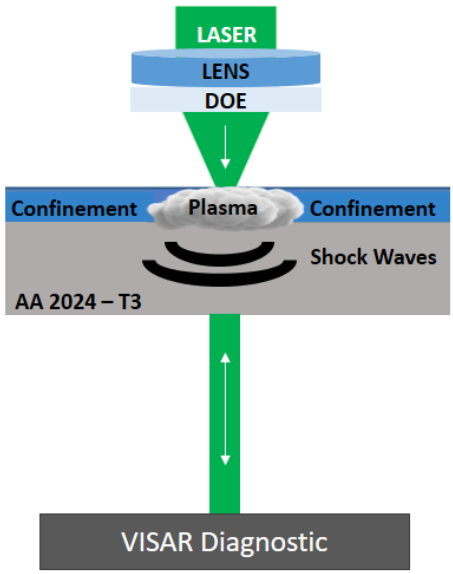

Figure 3.5: AA 2024 - T3 with the VISAR diagnostic.

Sample	Focal (mm)	Impact Type	Power Density (GW/cm^2)
AA1	4	Mono	0.8
AA2	4	Mono	0.8
AA3	4	Mono	1
AA4	4	Mono	1
AA5	4	Mono	2.8
AA6	4	Mono	2.8

Table 3.4: Summary of used focal spot, applied impact type and power densities on samples.

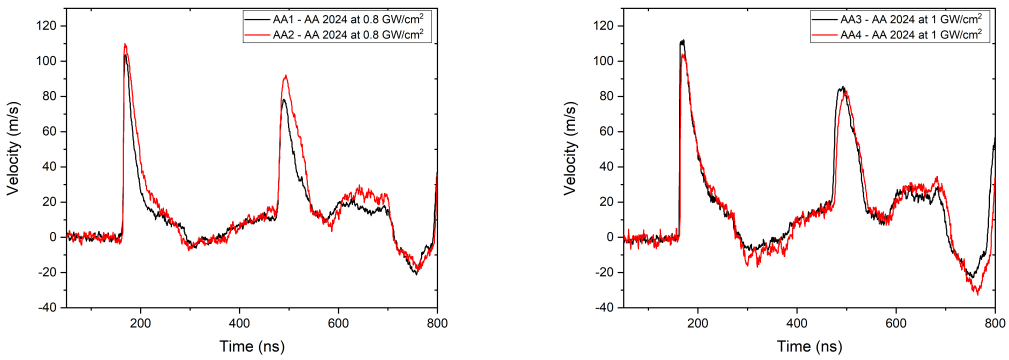

(a) 0.8 GW/cm^2 laser impact

(b) 1 GW/cm^2 laser impact

Figure 3.6: Experimentally obtained back face velocity curves at different power densities for AA 2024-T3.

In figure 3.6, the comparison between obtained experimental signals are verified for the reproducibility of the VISAR diagnostic. Obtained signals show that, the period of the signals are all well fitted. In addition, maximum velocity values are in good correlation with an error range of ±5-11 % for this set of data.

By using equation 3.1 and equation 3.2, which were explained previously for the pure aluminum, P_{HEL} is calculated for AA 2024 as well. C_{el} is found as 6162 m/s by inserting elastic modulus (E), ρ (density) and ν (Poisson ratio) as given in table 3.5. By introducing C_{el}, ρ and V_F (100 m/s± %14), as given in figure 3.7 which corresponds to the elastic precursor, P_{HEL} becomes 0.85 GPa (as an average).

ρ (kg/m^3)	V_F (m/s)	E (GPa)	ν	P_{HEL} (GPa)
2785	100	70	0.33	0.85

Table 3.5: Summary of used and calculated parameters for P_{HEL} - AA 2024 - T3 [133].

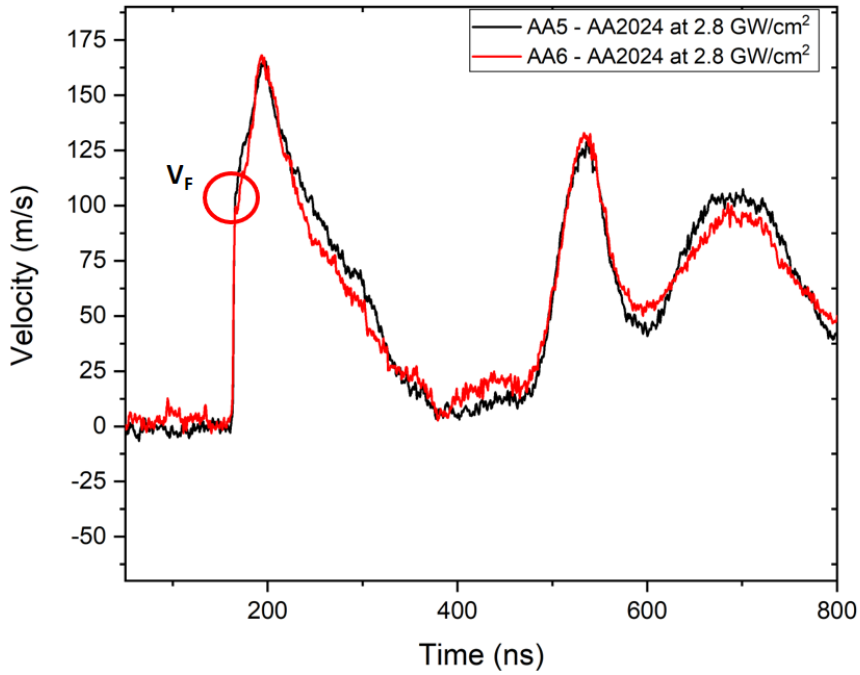

Figure 3.7: Given VISAR signal at 2.8 GW/cm^2 with elastic precursor velocity V_F at 110 m/s.

3.1.1.3 AL-Li 2060-T8

The same approach is applied as for the previous specimens. Experiments are conducted on AL-Li 2060-T8 targets (2.5 mm) with a focal spot of 4 mm by mono impact configuration and power density range of 0.98 to 2.73 GW/cm^2 via VISAR diagnostic (see figure 3.8).

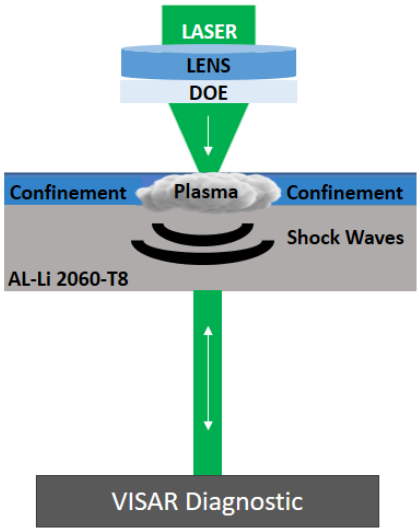

Figure 3.8: AL-Li 2060-T8 with the VISAR diagnostic.

For simplicity, samples named as AL1, AL2, AL3, AL4, AL5, AL6 (see table 3.6).

Sample	Focal (mm)	Impact Type	Power Density (GW/cm^2)
AL1	4	Mono	0.98
AL2	4	Mono	0.98
AL3	4	Mono	1.42
AL4	4	Mono	1.42
AL5	4	Mono	2.73
AL6	4	Mono	2.73

Table 3.6: Summary of used focal spot, applied impact type and power densities on samples.

Each power density is verified two times to ensure the signals' reproduciblity as done previously (see figure 3.9). Consistent signals are found with all the applied power densities. Hence this type of sample is thicker in comparison to other used aluminum substrates, the waves take longer time to travel. That phenomena can be seen from the VISAR signals clearly. For these specimens, only experimental BFV curves are studied in order to show the capacity of the VISAR diagnostic with different type of targets. No further numerical work is conducted.

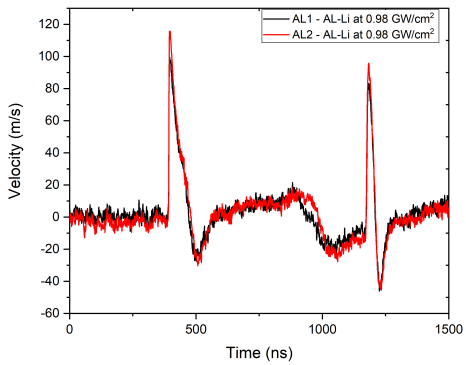

(a) 0.98 GW/cm^2 laser impact

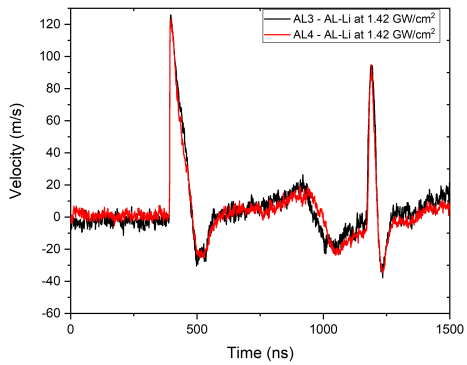

(b) 1.42 GW/cm^2 laser impact

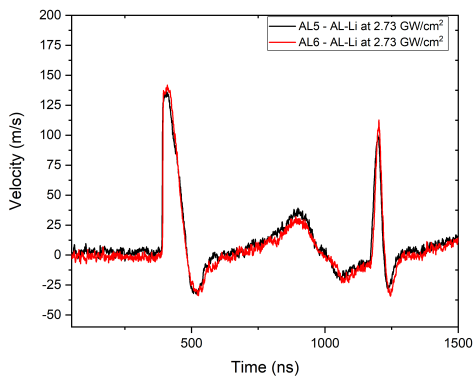

(c) 2.73 GW/cm^2 laser impact

Figure 3.9: Experimentally obtained back face velocity curves at different power densities for AL-Li 2060-T8.

After the validation of experimental signals, HEL limit is also calculated for this sample for comparison reasons. In order to see the elastic precursor, power density is increased up to 4.79 GW/cm^2 as in figure 3.10.

By using equation 3.1 and 3.2, P_{HEL} is calculated for AL-Li based sample. C_{el} is calculated as 6454 m/s, ρ (density) and ν (Poisson ratio) are as given in table 3.7. By placing C_{el}, ρ and V_F (160 m/s ±%9) as in figure 3.10, P_{HEL} becomes 1.4 GPa (as an average).

ρ (kg/m^3)	V_F (m/s)	E (GPa)	ν	P_{HEL} (GPa)
2720	160	75	0.34	1.4

Table 3.7: Summary of used and calculated parameters for P_{HEL} - AL- Li [133, 142].

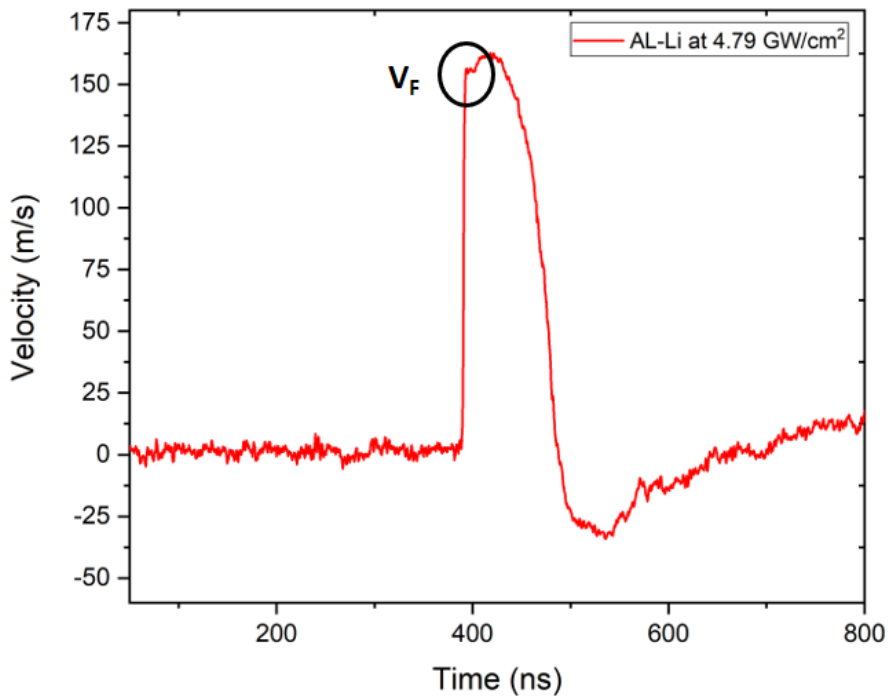

Figure 3.10: AL-Li specimen with its elastic precursor velocity at 4.79 GW/cm^2.

Obtained P_{HEL} values for pure aluminum, AA 2024-T3 and AL-Li 2060 are given in table 3.8 for comparison. According to the results, one can see that the different aluminum alloys have different behavior which is challenging for the process optimization and defining a common parameter window. However, AL-Li 2060 appears as the one which has the higher P_{HEL} that makes this base material prior for the industrial usage.

Pure Aluminum	AA 2024	AL-Li 2060
0.3 GPa	0.85 GPa	1.4 GPa

Table 3.8: Summary of calculated P_{HEL} values for different types of aluminum specimens.

3.1.2 Comparison of VISAR and Numerical Simulations

After the experimental validation of back face velocities, the same power densities used to validate the material model by using spatial and temporal profiles with a convenient material model as explained in section 2.5. The worked power densities are the same ones as in section 3.1.1 for pure aluminum and AA 2024 - T3.

3.1.2.1 Pure Aluminum

Before each set of experiment, the validation is done with pure aluminum first, since it's the most used and well-known material for the shock applications in the literature. The used power density range is as explained previously in table 3.1. Pressure loading delivered by the laser facility (spatial-temporal) is used as a control parameter for the simulation.

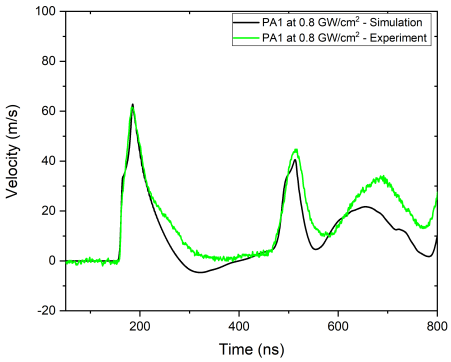

(a) 0.8 GW/cm^2 laser impact and simulation

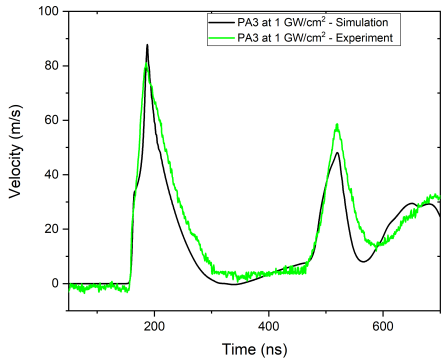

(b) 1 GW/cm^2 laser impact and simulation

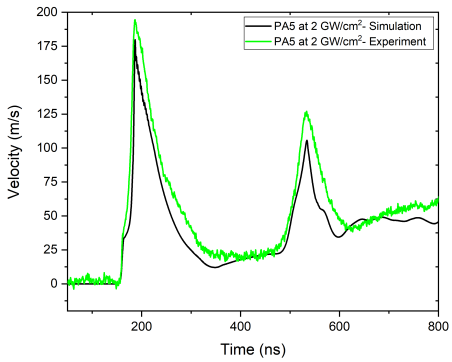

(c) 2 GW/cm^2 laser impact and simulation

Figure 3.11: Experimentally and numerically obtained back face velocity curves at different power densities for pure aluminum.

Comparison of experimental and numerical work is done as seen in figure 3.11. Obtained results show that the used material model has relatively good agreement with the experimental results.

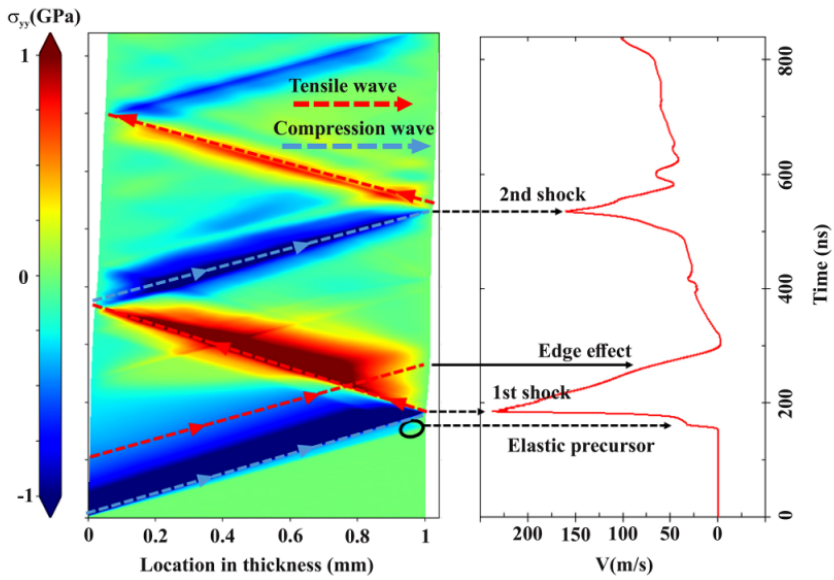

Figure 3.12: Axial compression and tension stress level σ_{yy} (blue and red arrows accordingly) during the wave propagation through the target thickness (horizontal axis) and during the laser shock with the associated BFV profile under 3.3 GW/cm^2 power density and 3 mm focal spot [129].

Figure 3.12 reveals the link between the BFV profile and the stress level σ_{yy}, which is obtained via numerical work, through the thickness of the target due to the laser shock. Furthermore, the blue arrows show the propagation of the compression waves through the plate which hit the back face and reflect as tensile waves as shown in the red arrows in figure 3.12. The signature of the elastic precursor on the back face velocity profile can be also linked to the separation of two compression waves which hit the back face, where the faster elastic one is marked by the dark circle in the X-T diagram (figure 3.12), while the plastic compression wave reaches the back face and produces the first peak of the back face velocity profile (1st Shock). The space-time diagram and the respective velocity profile are extracted from the work of Ayad et. al. In this study, the applied power density is 3.3 GW/cm^2 with 3 mm focal spot [129].

3.1.2.2 AA 2024-T3

The same approach is followed as pure aluminum for AA 2024-T3 specimens. Model validation is done for 0.8 and 1 GW/cm^2 power densities. Samples are already named as AA1 and AA3 for the power densities of 0.8 and 1 GW/cm^2, previously as in table 3.4.

After validating the loading conditions in terms of pressure profiles using the pure aluminum in figure 3.11, we compared the numerical BFV profile for AA 2024-T3 with experimental measurements as in figure 3.13 in order to test the material model parameters that are summarized previously in the section 2.5.2.

The results show that, experimental and numerical work have a good correlation within this power density range. The slight increase of the maximum velocity is observed with the increase of the power density, as expected. That validation is an important step before moving to several paint layer configurations.

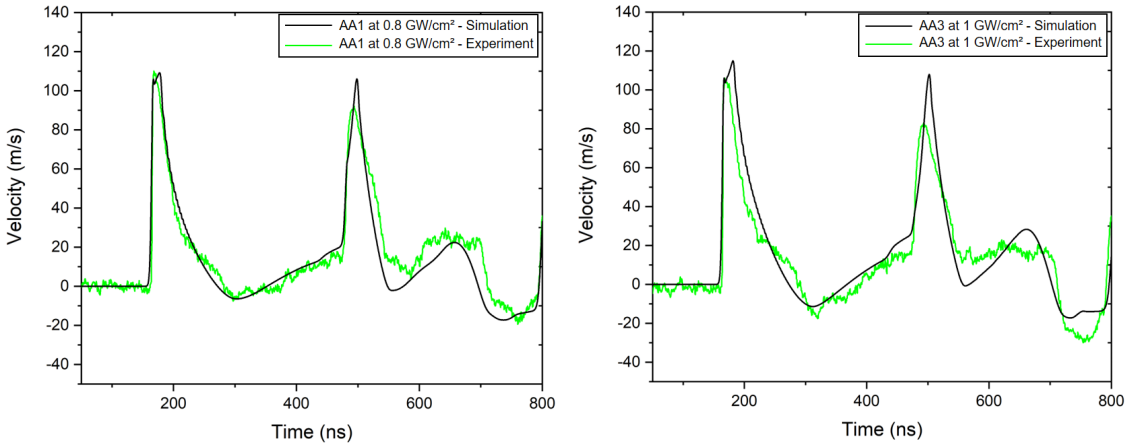

(a) 0.8 GW/cm^2 laser impact and simulation (b) 1 GW/cm^2 laser impact and simulation

Figure 3.13: Experimentally and numerically obtained back face velocity curves at different power densities for AA 2024-T3.

3.2 Bi-layer Aluminium Adhesive Tape for laser shock application

The generated shock wave by the laser is used to remove the paint from the aluminum substrate. In addition to studied paint stripping from the substrate side, for industrial applications, the laser should be applied on the paint side without burning the paint for recycling and selective stripping purposes. Therefore, a protective layer might be used on the paint side which is an aluminum tape, in our case (see figure 3.15).

The behaviour of aluminum tape is challenging to observe both experimentally and numerically. For example, the energy dissipation through the tape should be known. Since laser shock creates a high strain rate of deformation [129], elastomers might be a subject to glass transition or α transition [143]. Very recently, Le Bras et al. studied the dynamic glass transition of polycarbonate and polydimethylsiloxane under laser shock. Authors show that the dynamic glass transition of these polymers induces significant behaviour modifications. They worked both numerically and experimentally for the laser shock approach and coupled it with Dielectric Relaxation Spectroscopy (DRS) measurements to identify the limit of the rubbery and glassy behaviour of polymers under high pressure and strain rate [144].

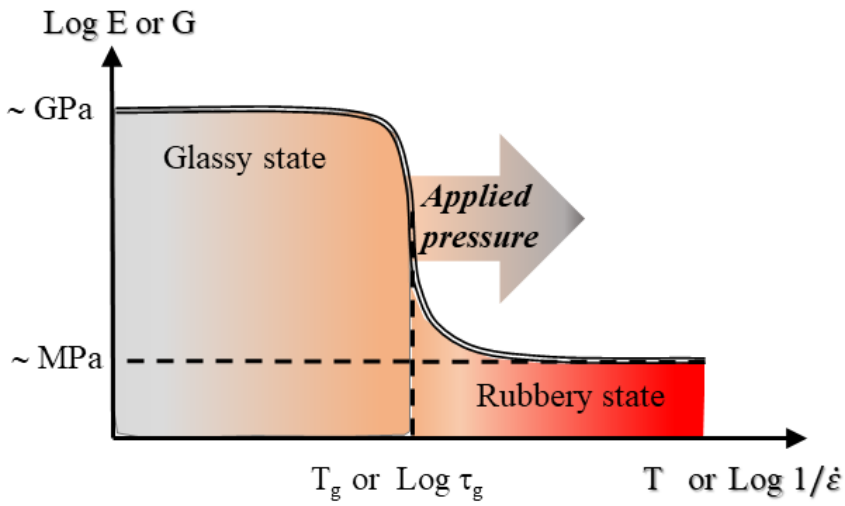

Figure 3.14: Tensile or shear modulus as a function of applied temperature (T) or strain rate ($\dot{\epsilon}$), influence of applied pressure on glass transition or frontier between glassy state and rubbery state. T_g and τ_g are the glass transition in terms of temperature and characteristic time, respectively [145].

As shown in figure 3.14, laser shock loading not only causes a shift in the glass transition by increasing the strain rate, but also by increasing the applied pressure. This influence of pressure has been highlighted by Le Bras et al. to explain the mechanical response of polymers used as solid confinement under LSP conditions [144]. As a result, materials such as acrylic that are under usual conditions in the rubbery state end up in the glassy state under conditions of high strain rate and pressure.

Since the ablative layer is needed by multi-processes (laser shock peening, laser adhesion test, laser paint stripping), different layers of the tape should be modeled. Despite the strain rate dependency of the polymers, Mulliken and Boyce used three-dimensional rate, temperature and pressure-dependent model to model the transition of yield behavior over wide range of temperatures (-140 °C to 180 °C) and strain rates ($10^{-3}s^{-1}$ to $4000s^{-1}$). Up to now, neither experiment nor simulation is done to model the glassy behavior of glue in aluminum tape by taking into account the pressure dependency under high strain rate.

In the following section, experimental BFVs for aluminum tape is first covered, followed by comparison of VISAR and numerical simulations to ensure that the material models are proper enough before optimizing the process parameters for other type of specimens. These simulations have been done on collaboration with Vanesse project. Hence the aluminum tape itself is relatively thin and includes a glue part which makes the VISAR measurement challenging due to the reflectivity reasons, these measurements are conducted with aluminum tape plus pure aluminum. Pure aluminum has the same

thickness and characteristics as previously explained.

3.2.1 Dynamic response of bi-layer adhesive tape

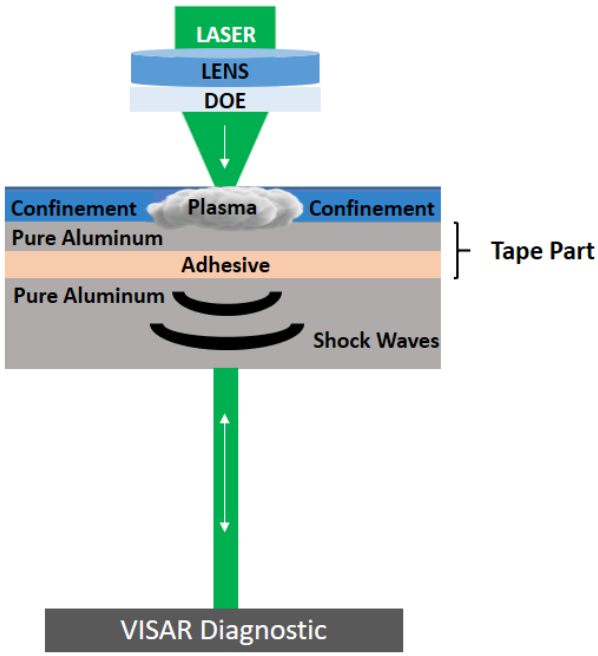

Figure 3.15: Pure aluminum + aluminum tape configuration with the VISAR diagnostic.

Experimental work is done on pure aluminum samples (1 mm) + aluminum tape (pure aluminum - 50 μm + glue - 30 μm) with a focal spot of 4 mm via mono impact configuration (see figure 3.15) by the VISAR diagnostic. Power density range is in between 0.5 to 4 GW/cm^2. For simplicity, samples named as AT1, AT2, AT3, AT4, AT5, AT6, AT7, AT8 (see table 3.9).

Sample	Focal (mm)	Impact Type	Power Density (GW/cm^2)
AT1	4	Mono	0.5
AT2	4	Mono	0.5
AT3	4	Mono	0.6
AT4	4	Mono	0.6
AT5	4	Mono	1
AT6	4	Mono	1
AT7	4	Mono	4
AT8	4	Mono	4

Table 3.9: Summary of used focal spot, applied impact type and power densities on samples.

The comparison between obtained experimental signals are verified for the reproducibility of the VISAR diagnostic (see figure 3.16). After the validation of the reproducibility, we move to the numerical model part to choose proper material model and

parameters. As one can see in figure 3.16, at 0.5 and 0.6 GW/cm^2, the reflections within the aluminum tape are more visible. Above 0.6 GW/cm^2, these reflections which look like fluctuations that become invisible.

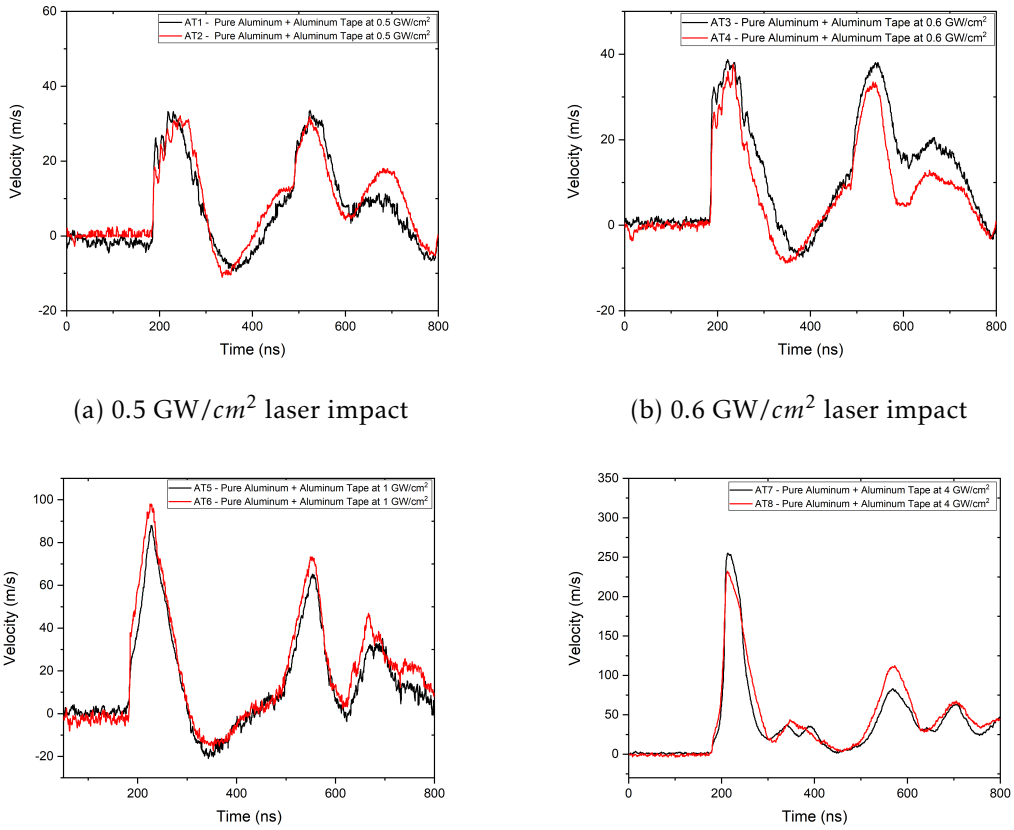

(a) 0.5 GW/cm^2 laser impact

(b) 0.6 GW/cm^2 laser impact

(c) 1 GW/cm^2 laser impact

(d) 4 GW/cm^2 laser impact

Figure 3.16: Experimentally obtained back face velocity curves at different power densities for pure aluminum + aluminum tape.

The obtained small differences for the signals which are at the same applied power densities can be explained by the multi-layered structure of the material and manual application of the adhesive tape.

3.2.2 Coupling of Experimental and Numerical Work

In this part, the conducted numerical work for 0.5 GW/cm^2 and 3 GW/cm^2 is included. Figure 3.17 shows a good correlation between the simulated BFV profile and the experimental results while taking into account the pressure sensitivity parameter ($b = 8$). The model is compared with the experimental results for the whole wave propagation.

Overall, the simulated maximum velocities show close values to the experimental results. The observed differences can be explained by the application of the adhesive tape

for each set of experiment and created sensitivity as a result of that. The debonding of the tape is observed better after 600 ns as seen in figure 3.17b.

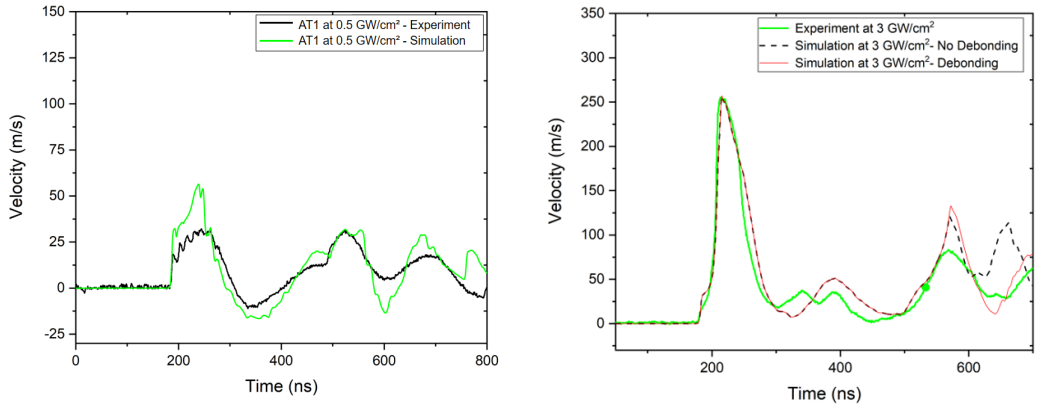

(a) 0.5 GW/cm^2 laser impact and simulation

(b) 3 GW/cm^2 laser impact and simulation

Figure 3.17: Validation of the Simulated BFV for the taped Pure Aluminum for the applied power densities of 0.5 GW/cm^2 and 4 GW/cm^2, respectively.

Figure 3.18 represents the cross-section cut off a reference sample (without any laser impact) and a sample after applied 1 GW/cm^2 power density. The part marked as "alu" is for the aluminum tape, "glue" is for the adhesive and pure aluminum is for the base material. As one can see, at 1 GW/cm^2, clear debonding is observed via optical microscope at the interface of glue and pure aluminum base material. Threshold of the interface bonding between the tape and the substrate is calibrated according to the numerous experiments. This threshold value is found as $\sigma_{yy,threshold} = 165$ MPa.

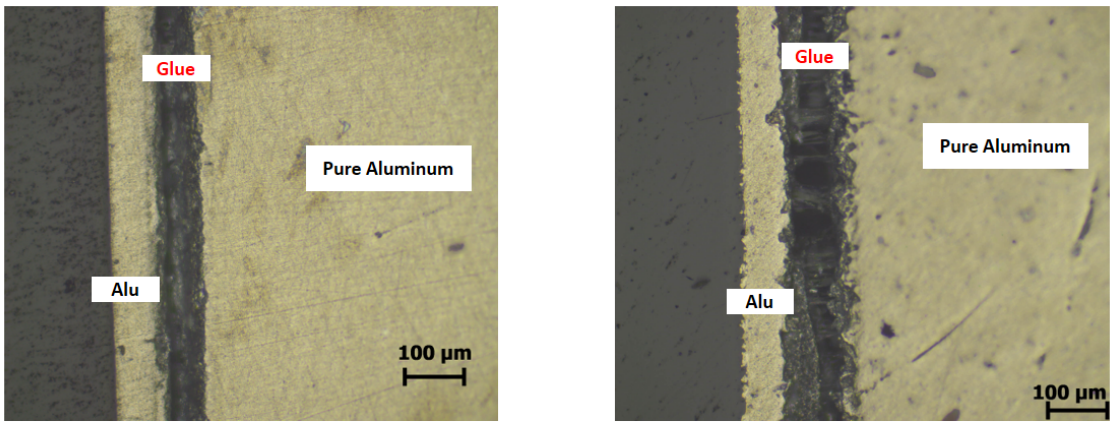

(a) Reference without any laser impact

(b) After 1 GW/cm² laser impact

Figure 3.18: Cross section cuts for (a) reference sample without any applied laser impact and (b) after applied 1 GW/cm^2.

For mono impact configuration, the maximum tensile zone in the target is usually close to the back free surface. The usage of aluminum tape changes the localization of the

maximum tensile zone due to the delay in the glue part and the reflections with the other layers. If we focus on pure aluminum target to analyze this effect, maximum tensile zone location can be modified.

The applied power density is taken constant as 1.8 GW/cm^2 to see the effect of different glue thicknesses. After that, space-time diagrams are generated as shown in Figure 3.19.

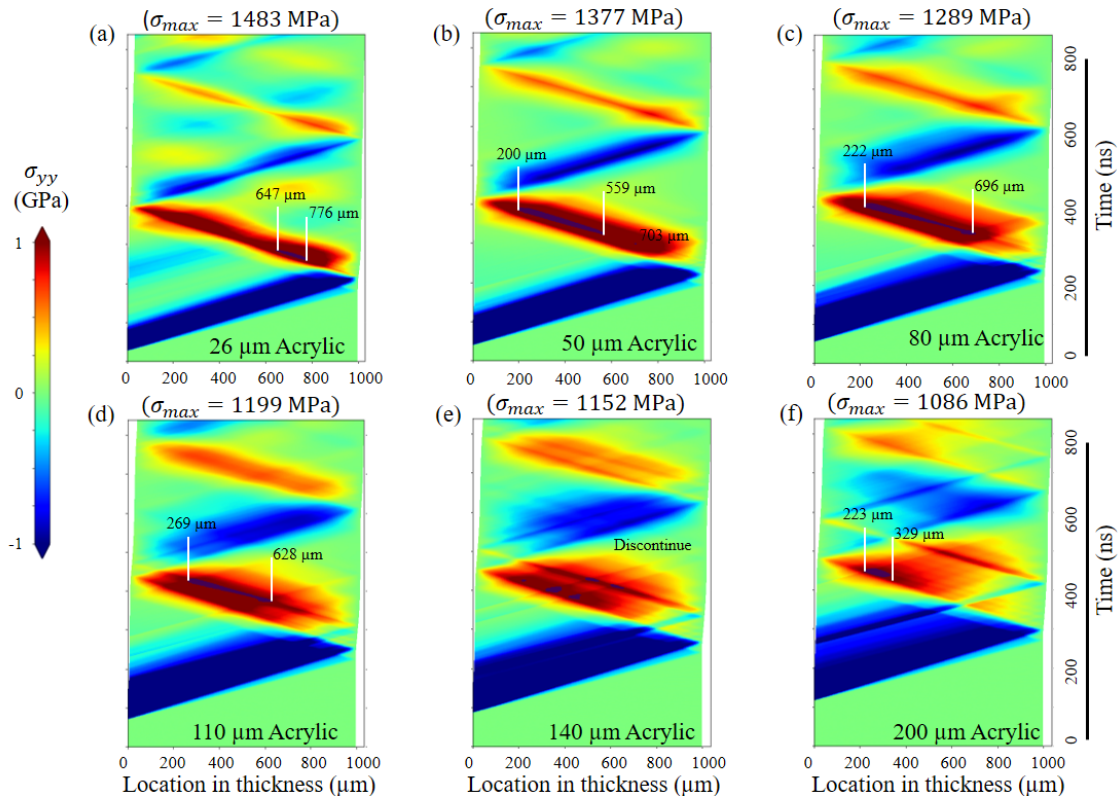

Figure 3.19: Axial compression and tension stress level σ_{yy} (blue and red colors respectively) during the wave propagation through pure aluminum + adhesive tape (horizontal axis) with an applied laser shock loading of 1.8 GW/cm^2 for different glue thickness (26 µm, 50 µm, 80 µm, 110 µm, 140 µm and 200 µm) represented as a, b, c, d, e, and f accordingly.

Figure 3.19 depicts the stress propagation through pure aluminum + adhesive tape with different glue thicknesses of 26 µm, 50 µm, 80 µm, 110 µm, 140 µm and 200 µm which are given as a, b, c, d, e, and f. The blue and red colors represent the compression and traction waves, respectively. We also noted the maximum tensile stress levels (GPa) which are colored in black. As one can see, the tensile zone is approaching to the targets' front face and becoming more localized with the increase of the glue thickness. However, at the same time, the maximum tensile stress level becomes lower (from 1483 MPa to 1086 MPa).

The maximum tensile zone is identified within the 1 mm pure aluminum taped target under the laser shock application. The increase of the glue thickness in the aluminum tape part leads to decrease in the maximum tensile stress but giving more localized stress which is close to the front face. Therefore, the glue thickness could be adjusted to optimize the localization of the maximum tensile zone, and the drop in the stress values due to the attenuation could be compensated by the increase of the energy. With this optimization, laser applications from the paint side might be modified for the industrial usage.

3.3 Behavior of Epoxy and Polyurethane Coatings under laser shock loading

Since the main focus of the thesis is the AA 2024 - T3 based substrates, principal results are around the coated layers on this substrate. In order to reduce the ablative effects which are created by the laser, aluminum tape is used on paint parts of the specimens that will be explained schematically in detail for each sample. In addition, gold coating is used on paint side of specimens for the laser applications from the substrate side.

In figure 3.20, optical microscope images of two investigated main configurations are shown. First one is AA 2024 + epoxy primer. The worked epoxy thickness range of 24-30 μm and the substrate thicknesses is 970 μm - 1 mm. The second type of specimen is with an epoxy primer (30 μm) and a polyurethane top coat (49 μm) on top of the AA 2024-T3 target (970 μm - 1 mm).

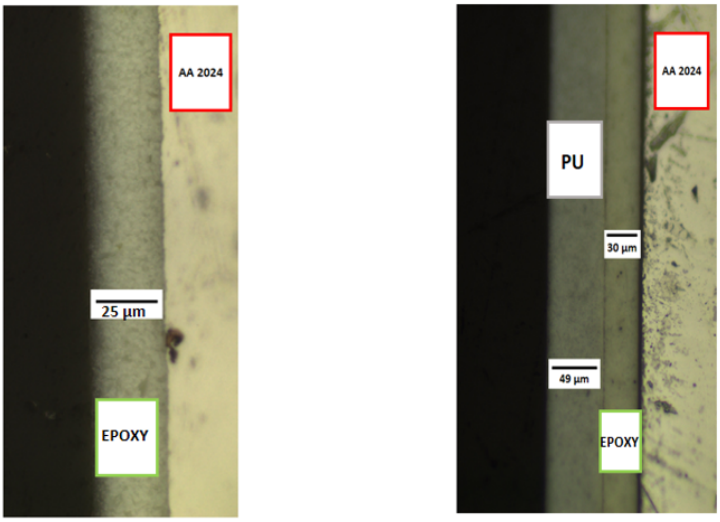

(a) AA 2024 + Epoxy Primer

(b) AA 2024 + Epoxy Primer + Polyurethane Top Coat

Figure 3.20: Specimen configurations with different layer architectures.

In this section, different specimens are investigated with VISAR diagnostic and numerical analysis is done for further process optimization.

3.3.1 AA 2024 + Epoxy Primer

In this part, the specimens consist of AA 2024-T3 base materials with epoxy primer coatings as demonstrated in figure 3.21. Samples are named as: RES1, HAI1 and RES2. RES1 is composed of 970 μm of AA 2024-T3 base with a surface treatment of chemical etching (CE) + epoxy primer of 28 μm. HAI1 has 800 μm of AA 2024 - T3 base with a surface treatment of chromic acid anodization (CAA) + epoxy primer primer of 24 μm. RES2 target has AA 2024-T3 with a thickness of 970 μm, surface treatment of chemical etching (CE) and epoxy primer of 25 μm. HAI1 and RES1 samples are subjected to paint sided applications with the usage of adhesive tape. On the other hand, for RES2 target, laser impacts are applied from the substrate side with a gold coating on the epoxy side.

Figure 3.21 gathers the samples with aluminum tape configuration in which the laser impacts are applied for each different specimen.

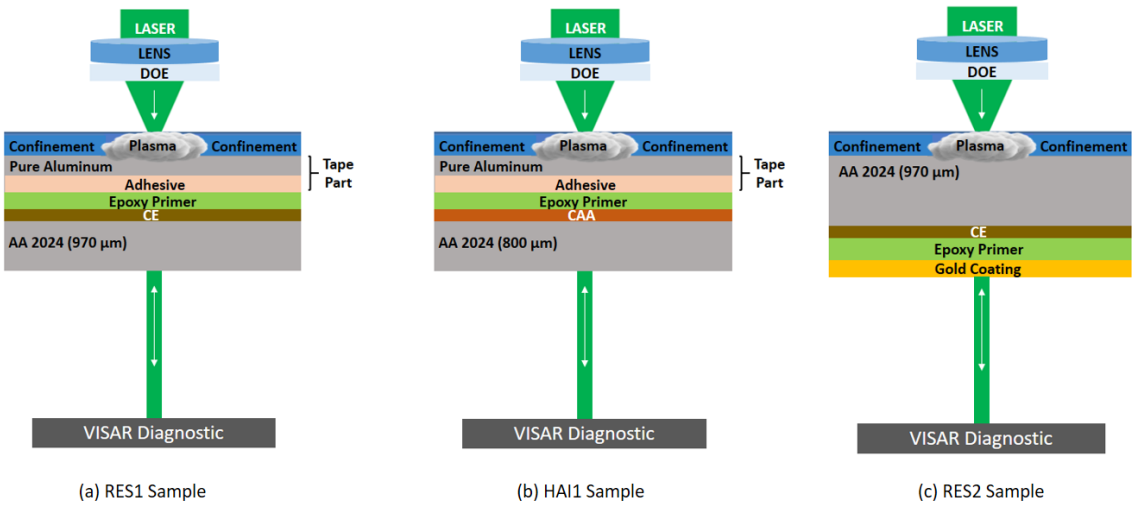

Figure 3.21: Specimen configurations with the applied laser impact.

3.3.1.1 Characterization via VISAR

This subsection is divided into two parts according to the applied laser impact side of the substrate. First, the obtained results will be given for RES1 and HAI1 samples (laser from the epoxy side) and secondly for the RES2 (laser from the substrate side).

RES1 Specimen

For this sample, laser impacts are applied from the applied tape side as previously demonstrated in figure 3.21a. Table 3.10 gathers the worked power density for RES1 specimen which is in the range of 0.4 to 2 GW/cm^2 with an applied mono impact.

Sample	Focal (mm)	Impact Type	Power Density (GW/cm^2)
RES11	4	Mono	0.4
RES12	4	Mono	0.4
RES13	4	Mono	1
RES14	4	Mono	1
RES15	4	Mono	2
RES16	4	Mono	2

Table 3.10: Summary of used focal spot, applied impact type and power densities on sample RES1.

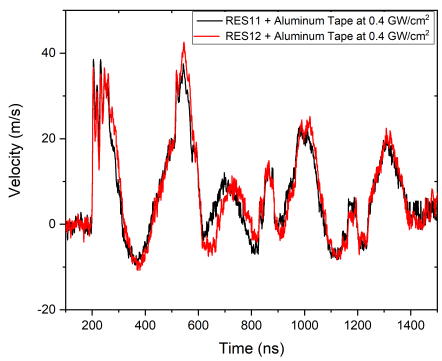

(a) 0.4 GW/cm^2 laser impact

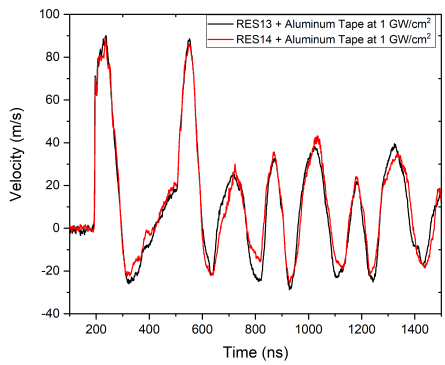

(b) 1 GW/cm^2 laser impact

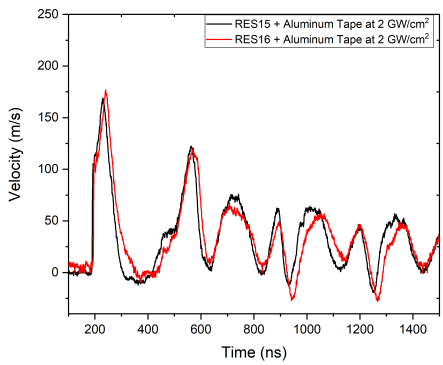

(c) 2 GW/cm^2 laser impact

Figure 3.22: Experimentally obtained back face velocity curves at different power densities for RES1 + aluminum tape.

Figure 3.22 demonstrates that even with a complex multi-layer system, VISAR diagnostic was precise enough to give us reproducible results.

HAI1 Specimen

The same procedure is followed for HAI1 specimen within the same applied power density range of 0.4 to 3 GW/cm^2 as shown in table 3.11. Mono laser impact is applied through 4 mm of focal spot.

Sample	Focal (mm)	Impact Type	Power Density (GW/cm^2)
HAI11	4	Mono	0.4
HAI12	4	Mono	0.4
HAI13	4	Mono	0.8
HAI14	4	Mono	0.8
HAI15	4	Mono	2
HAI16	4	Mono	2
HAI17	4	Mono	3
HAI18	4	Mono	3

Table 3.11: Summary of used focal spot, applied impact type and power densities on sample HAI1.

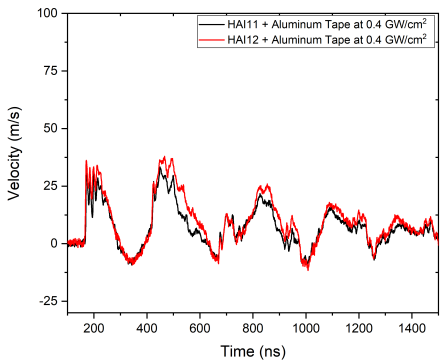

(a) 0.4 GW/cm^2 laser impact

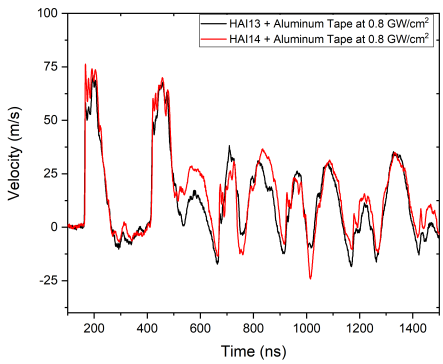

(b) 0.8 GW/cm^2 laser impact

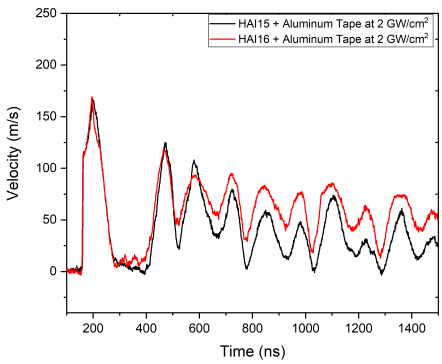

(c) 2 GW/cm^2 laser impact

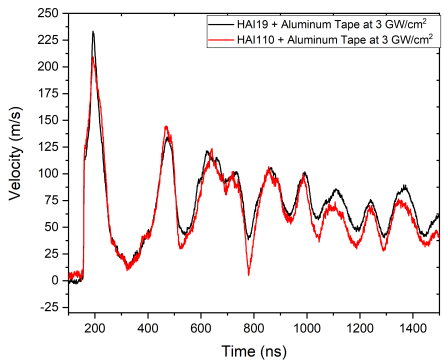

(d) 3 GW/cm^2 laser impact

Figure 3.23: Experimentally obtained back face velocity curves at different power densities for HAI1 + aluminum tape.

Figure 3.23 gathers the repeated VISAR signals for each power density. Even though they seem reproducible, there are relatively small differences especially at 2 GW/cm^2. For this type of specimen paint stripping is not obtained within the worked power density range. The extracted signals are demonstrating the capacity of the VISAR diagnostic to detect signals regardless of the complexity of the material.

RES2 Specimen

For this specimen, generating reproducible signals via VISAR diagnostic was challenging. Since the applied gold coat has a nanometric thickness range, arrangement of VISAR's probe laser was a challenge without damaging the gold and/or primer coat. Even though several shots are generated, only the ones at 2.3 GW/cm^2 were reproducible which are further used for the analysis of laser adhesion tests approach that will be explained in section 4.1.1 afterwards. The applied laser impacts are from the substrate side of the specimens with the same used principle for samples RES1 and RES2. The used spot size is 4 mm with the mono impact laser configuration. 3 signals are given in which one is at 2 GW/cm^2 and two of them at 2.3 GW/cm^2 as shown in table 3.12.

Sample	Focal (mm)	Impact Type	Power Density (GW/cm^2)
RES21	4	Mono	2
RES22	4	Mono	2.3
RES23	4	Mono	2.3

Table 3.12: Summary of used focal spot, applied impact type and power densities on sample RES2.

In figure 3.24 both the reproducible signal at 2.3 GW/cm^2 and the one at 2 GW/cm^2 are given.

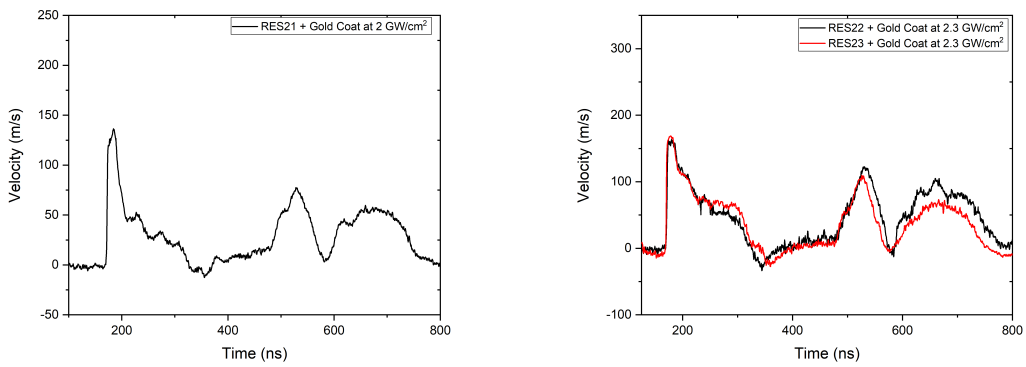

(a) 2 GW/cm^2 laser impact

(b) 2.3 GW/cm^2 laser impact

Figure 3.24: Experimentally obtained back face velocity curves at different power densities for RES2 + gold coat.

Even though the reproducible signal is obtained for one set of power density, for the

next chapters it helped us to optimize the parameters for both paint stripping and paint adhesion tests.

3.3.1.2 Comparison of VISAR and Numerical Simulations

In this section, RES1 and RES2 specimens are investigated, numerically. Figure 3.25 demonstrates the RES2 and RES1 samples, respectively. First, RES2 sample is studied to validate the numerical model. After, RES1 sample is investigated in the following subsection. For RES2 specimen, laser is applied from the substrate side (aluminum in this case) with a gold coating on the other side of the samples for reflective purposes via VISAR. As previously explained for RES1 sample, aluminum tape is used and laser impacts are applied from the epoxy side of specimens.

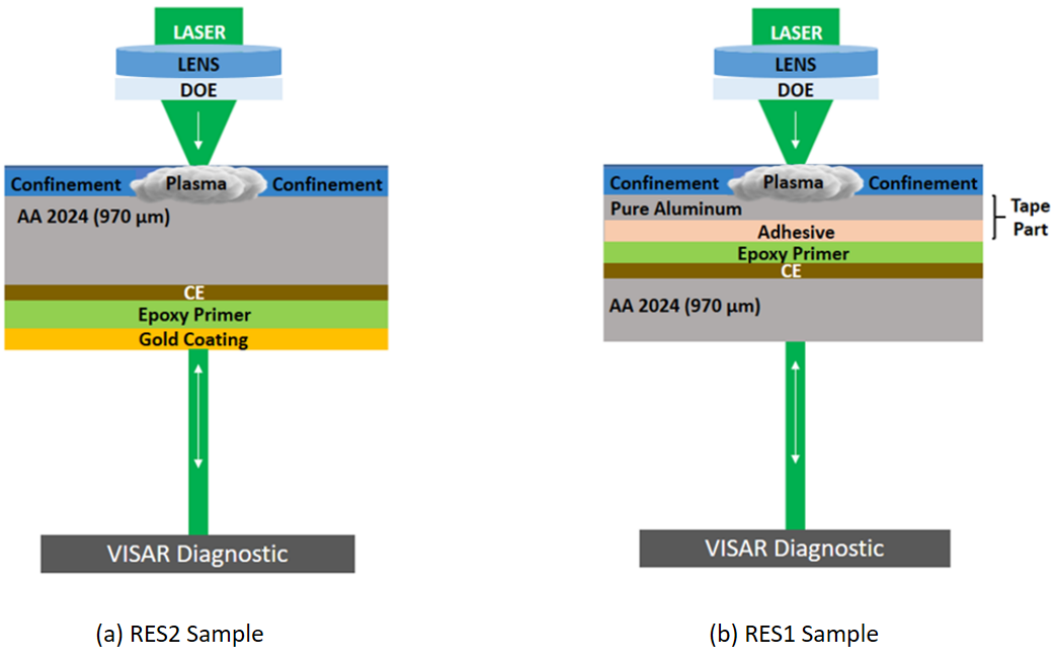

Figure 3.25: RES2 and RES1 specimen configurations with the applied laser impact.

RES2 Specimen

Since the only reproducible signal is at 2.3 GW/cm^2, the model validation is done at this power density as given in 3.13. As already mentioned, hence the gold coat is in nanometric range, it is not included in the numerical model as an additional layer.

Sample	Focal (mm)	Impact Type	Power Density (GW/cm^2)
RES22	4	Mono	2.3

Table 3.13: Summary of used focal spot, applied impact type and the power density on sample RES2.

Figure 3.26 compares the predicted and experimental back face velocity profiles for 2.3 GW/cm^2. As can be seen, there is a good agreement between the model and the

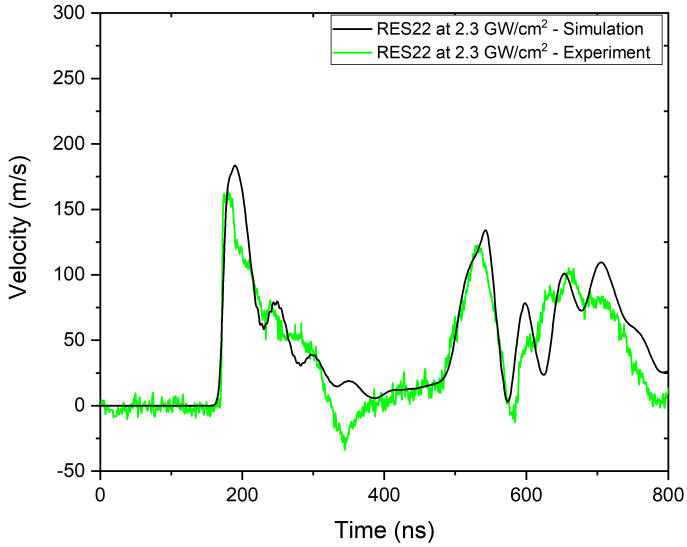

Figure 3.26: Experimental and numerical comparison at 2.3 GW/cm^2.

experiment in the sense that the numerical curve follows the experimental curve. However, there is a slight difference between the curves. This difference occurs due to lack of the exact mechanical properties of the epoxy primer and the interface between aluminum/epoxy. Overall, it can be concluded that the model is capable of simulating the shock wave propagation inside the aluminum/epoxy specimen [146].

RES1 Specimen

For this specimen, the same power densities are used which are studied experimentally. As a reminder, they are given once more in table 3.14.

Sample	Focal (mm)	Impact Type	Power Density (GW/cm^2)
RES11	4	Mono	0.4
RES12	4	Mono	0.4
RES13	4	Mono	1
RES14	4	Mono	1
RES15	4	Mono	2
RES16	4	Mono	2

Table 3.14: Summary of used focal spot, applied impact type and power densities on sample RES1.

All power densities are investigated but for the simplicity, BFV comparison of 0.4 GW/cm^2 and 2 GW/cm^2 are given in figure 3.27. As one can see, good correlation is obtained for both power densities with a slight difference of the period and maximum velocity of the signals. After the validation of BFV curves, maximum axial stress levels at different interfaces are studied which will be explained in the following pages.

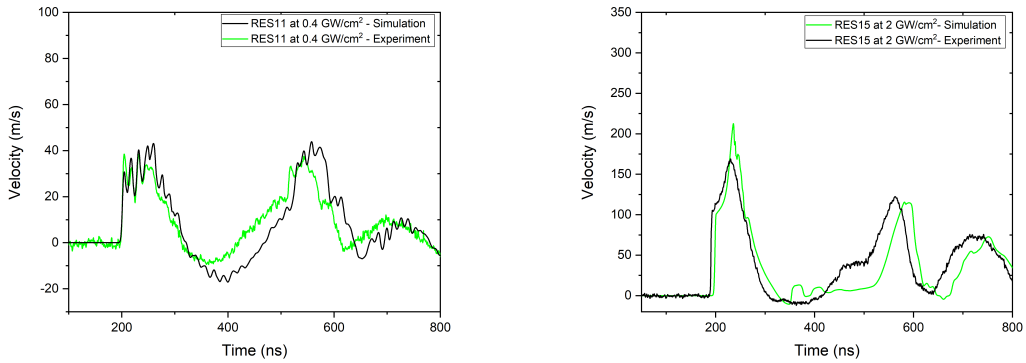

(a) 0.4 GW/cm^2 laser impact and simulation (b) 2 GW/cm^2 laser impact and simulation

Figure 3.27: Experimentally obtained back face velocity curves at different power densities for RES1 + aluminum coat.

In order to quantify the stresses, epoxy-aluminum substrate interface and glue - epoxy interface are studied separately via numerical work. Hence the glue delamination limit is already defined in the subsection 3.2.2 as $\sigma_{yy,threshold}$ = 165MPa, the value for the glue delamination is already known. In addition, epoxy-aluminum substrate is investigated. Table 3.15 gathers the $\sigma_{yy,threshold}$ values for both at the epoxy-aluminum substrate interface ($\sigma_{yy,epoxy}$) and glue - epoxy interface ($\sigma_{yy,glue}$) which are extracted via numerical work.

Sample	Power Density (GW/cm^2)	$\sigma_{yy,glue}$ (MPa)	$\sigma_{yy,epoxy}$ (MPa)
RES11	0.4	135	160
RES13	1	>165	244
RES15	2	>165	188

Table 3.15: Summary of the used power densities, $\sigma_{yy,epoxy}$ and $\sigma_{yy,glue}$ for sample RES1.

At 0.4 GW/cm^2, there is no observed glue delamination and stripping (as known experimentally). At 1 GW/cm^2, there is a glue delamination with a value of >165 MPa, numerically. For the shots at 2 GW/cm^2, the same results have been obtained (>165 MPa). In fact, when the debonding occurs at the glue interface, the stress within it drops to zero and due to the small thickness of epoxy, the $\sigma_{yy,epoxy}$ also drops to zero which acts as a stopping mechanism for the stripping.

As shown previously in figure 3.27, the dynamical response of sample RES1 has been validated experimentally and numerically until 2 GW/cm^2. Using this validated model, the maximum axial tensile stress as function of applied power density for epoxy and glue interfaces are extracted, respectively as shown in Figure 3.28. Since no stripping is obtained until 2 GW/cm^2, the stress analysis is extended numerically to 3 GW/cm^2. As one can see, at 3 GW/cm^2, $\sigma_{yy,glue}$ is decreasing while $\sigma_{yy,epoxy}$ is increasing. Therefore, there might be a chance of stripping of epoxy primer without glue debonding according

to the numerically obtained results (see section 5.2 for validation tests).

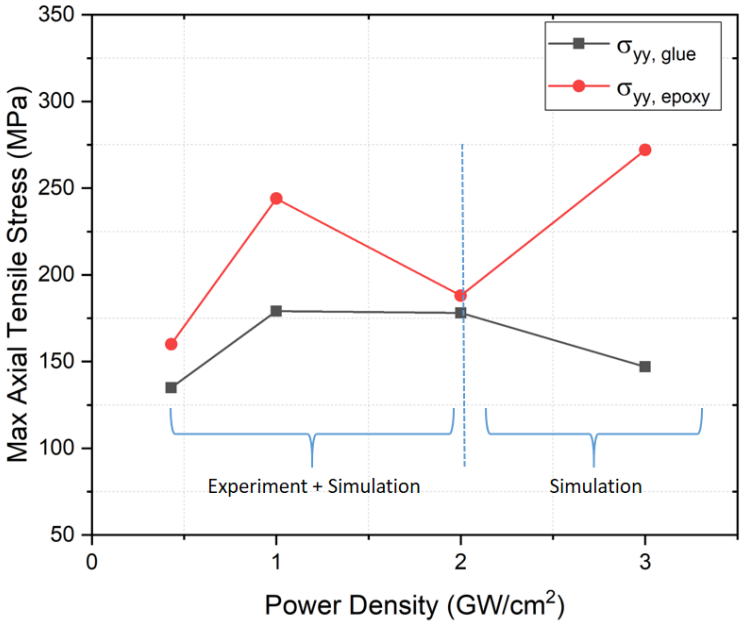

Figure 3.28: Maximum axial tensile stress for epoxy and glue interfaces as function of applied power densities.

In order to have a better understanding, space-time diagrams are constructed for 0.43 GW/cm^2 and 3 GW/cm^2.

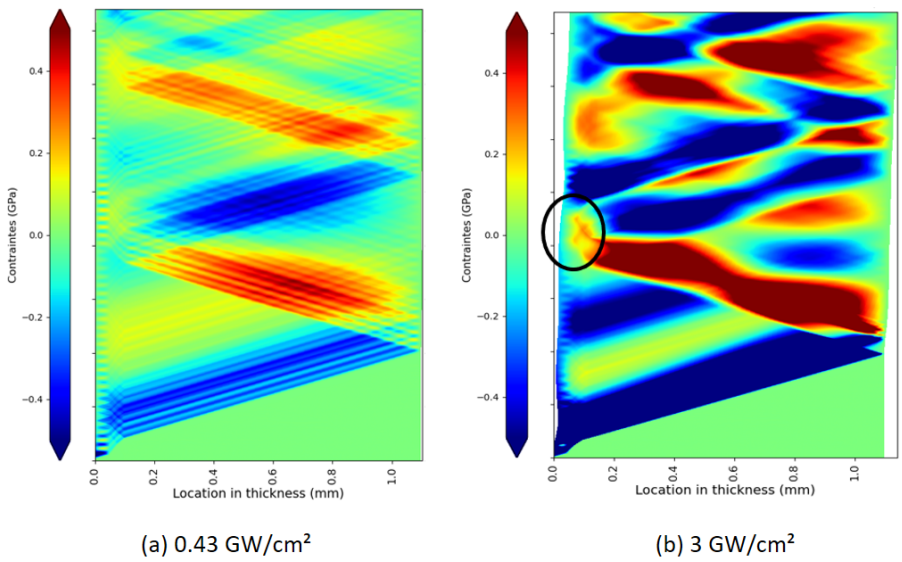

Figure 3.29: Space-time diagrams at 0.43 GW/cm^2 and 3 GW/cm^2.

The provided space-time diagrams show the higher tensile stress occurance at the epoxy-aluminum substrate interface at 3 GW/cm^2 (see figure 3.29b). As one can see, the crossing of a reflection of the compression and the tensile wave coming from the reflection within the tape and the epoxy is the reason for the created stripping at this

power density. At 3 GW/cm^2 , one can see that the blue color (compression) is dominated at the glue interface. On the other hand, the red color is at the substrate-epoxy interface as we marked in black circle. This behavior is not observed for the 0.43 GW/cm^2 (see figure 3.29a).

3.3.2 AA 2024 + Epoxy Primer + Top Coat

In figure 3.30, the sample configuration is given. On top of AA 2024 - T3 (970 μm) target there is a surface treatment of chromic acid anodization (CAA), 25-30 μm of an epoxy primer, polyurethane base coat as a top coat within the range of 50 μm and an aluminum tape of 80 μm including the glue. For the simplicity, the worked sample is named as RES3.

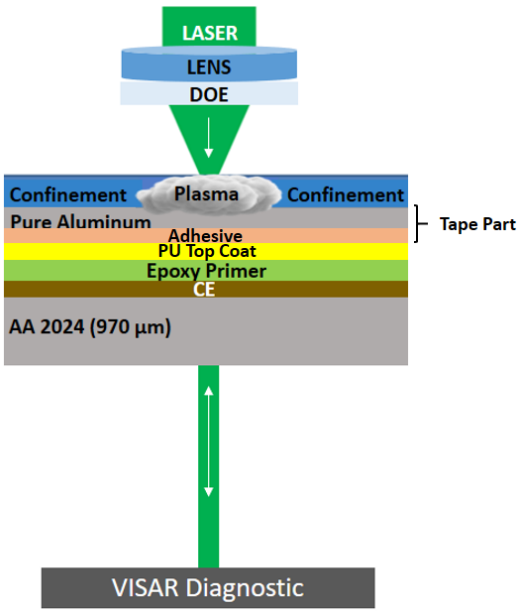

Figure 3.30: RES3 specimen with the applied laser and VISAR configuration.

3.3.2.1 Characterization via VISAR

As shown in table 3.16, the worked power density for is in the range of 0.4 to 3 GW/cm^2 from the aluminum tape side which is applied on top of polyurethane based top coat of the targets.

Sample	Focal (mm)	Impact Type	Power Density (GW/cm^2)
RES31	4	Mono	0.4
RES32	4	Mono	0.4
RES33	4	Mono	1
RES34	4	Mono	1
RES35	4	Mono	2
RES36	4	Mono	2
RES37	4	Mono	3
RES38	4	Mono	3

Table 3.16: Summary of used focal spot, applied impact type and power densities on sample RES3.

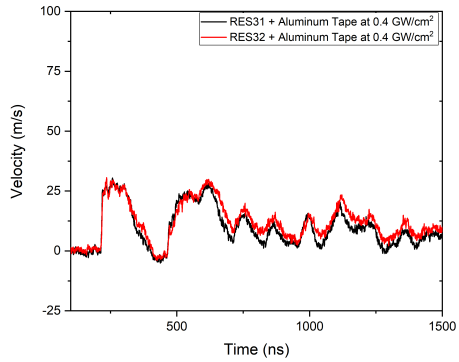

(a) 0.4 GW/cm^2 laser impact

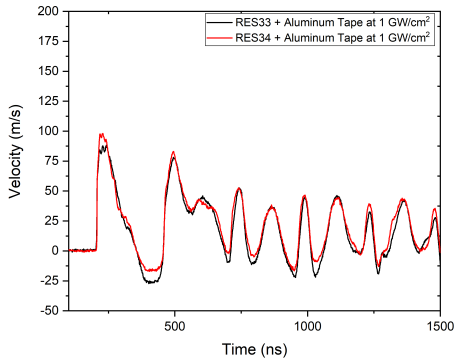

(b) 1 GW/cm^2 laser impact

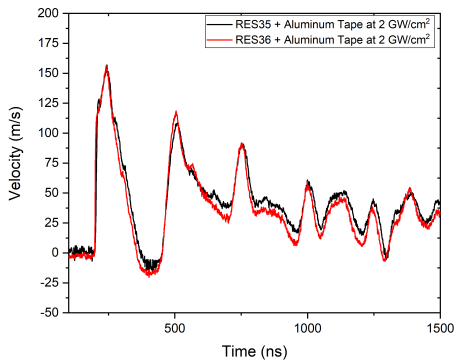

(c) 2 GW/cm^2 laser impact

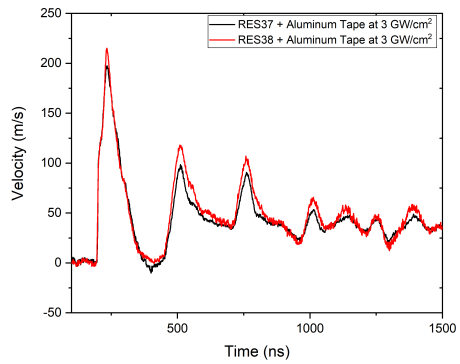

(d) 3 GW/cm^2 laser impact

Figure 3.31: Experimentally obtained back face velocity curves at different power densities for RES3 + aluminum tape.

Figure 3.31 gives consistent results for each applied power densities. After 0.4 GW/cm^2, the reflections which are visible in the first peak of the signals disappeared. Since modelling the targets with just an epoxy primer layer is a complicated phenomena due to the lack of mechanical properties, no further analysis is done for these multi layer targets.

3.4 High strain rate response of CFRP under laser shock loading

Hence the composite structure itself is a deep phenomena, here the presented results just cover the CFRP results as a base material without any coating on top of them. First sample properties are explained briefly and after the results obtained via VISAR diagnostic for characterization of specimens.

3.4.1 Sample Properties

Epoxy matrix is a HexPly M21 type which is a tough matrix preferred for aeronautical applications. The matrix is a mix of a thermoset epoxy resin and thermoplastic nodules whose make the whole sample tough. As mentioned previously, the thicknesss of the sample is around 2.3-2.4 mm.

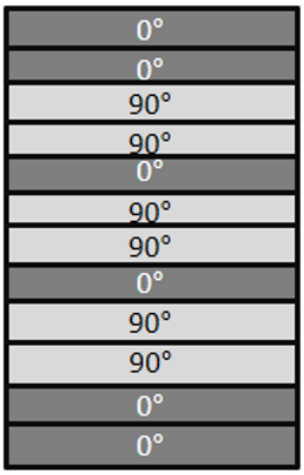

Figure 3.32: Ply directions for used CFRP type.

3.4.2 Characterization via VISAR

The dynamic responses of composites are monitored. The used spot size is 4 mm via mono impact at power densities of 0.24 GW/cm^2 and 0.52 GW/cm^2. The characterization covers the shock back and forth from the obtained signals. These periods allow us to calculate the initial sound speed (within the elastic regime). Also, from these periods, ply thicknesses and the whole sample's thickness can be obtained. As shown in figure 3.33, the period between two peaks is around 1493 ns. If one wants to calculate the speed of sound, it becomes:

$$C_0 = \frac{2 \times thickness}{\Delta T} = \frac{2 \times 2.35mm}{1493ns} = 3148m/s \tag{3.3}$$

The found speed of sound is around 3148 which is in a good agreement with the literature [44].

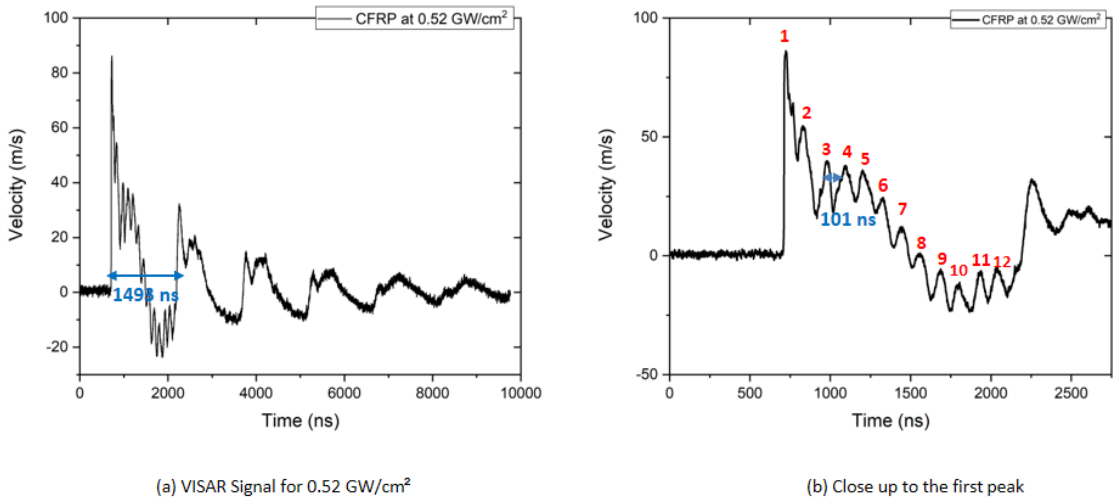

(a) VISAR Signal for 0.52 GW/cm²

(b) Close up to the first peak

Figure 3.33: Obtained signals via VISAR at 0.52 GW/cm^2.

By zooming in to the first peak of the signal as in figure 3.33b, we can clearly track the number of plies which are 12. Since it's known that the ply thickness is around 180-190 μm, by using the very same equation 3.3, the time of travel within the one ply is calculated as 101 ns, approximately.

In order to be sure about the reproducibility of the signals, each shot was repeated at least 2 times. As an example for the reproducibility of the signals and the accuracy of the measurements, repeated signals at 0.24 GW/cm^2 are demonstrated in figure 3.34.

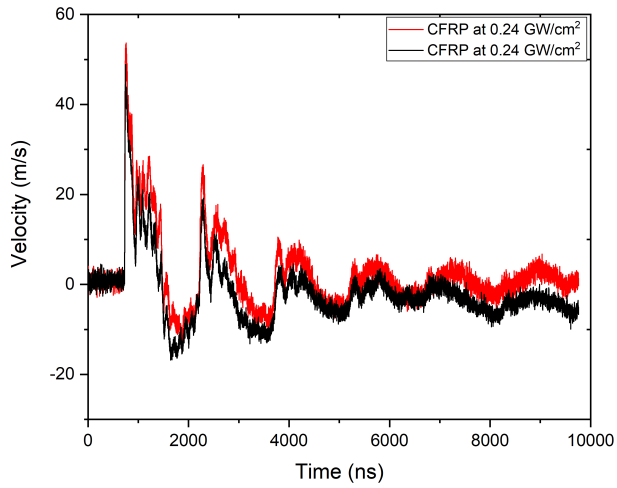

Figure 3.34: Obtained signals via VISAR at 0.24 GW/cm^2.

The obtained signals via VISAR analysis for the composite specimens are just to show the capability of the diagnostic. As already mentioned, no further deeper analysis is performed for this kind of target.

Summary and Discussion

The comparison of P_{HEL} values for pure aluminum, AA 2024-T3 and AL-Li 2060 is given in table 3.17 for comparison. From the results, it can be observed that different aluminum alloys exhibit different behavior. AL-Li has higher P_{HEL} that makes this base material more suitable for industrial applications.

Pure Aluminum	AA 2024	AL-Li 2060
0.3 GPa	0.85 GPa	1.4 GPa

Table 3.17: Summary of calculated P_{HEL} values for different types of aluminum specimens.

In order to have a general overview of the procedure, table 3.18 is generated. The findings prove the capacity of the VISAR diagnostic and creates a promising base for process optimization by coupling with the numerical work for laser stripping and laser paint adhesion test applications.

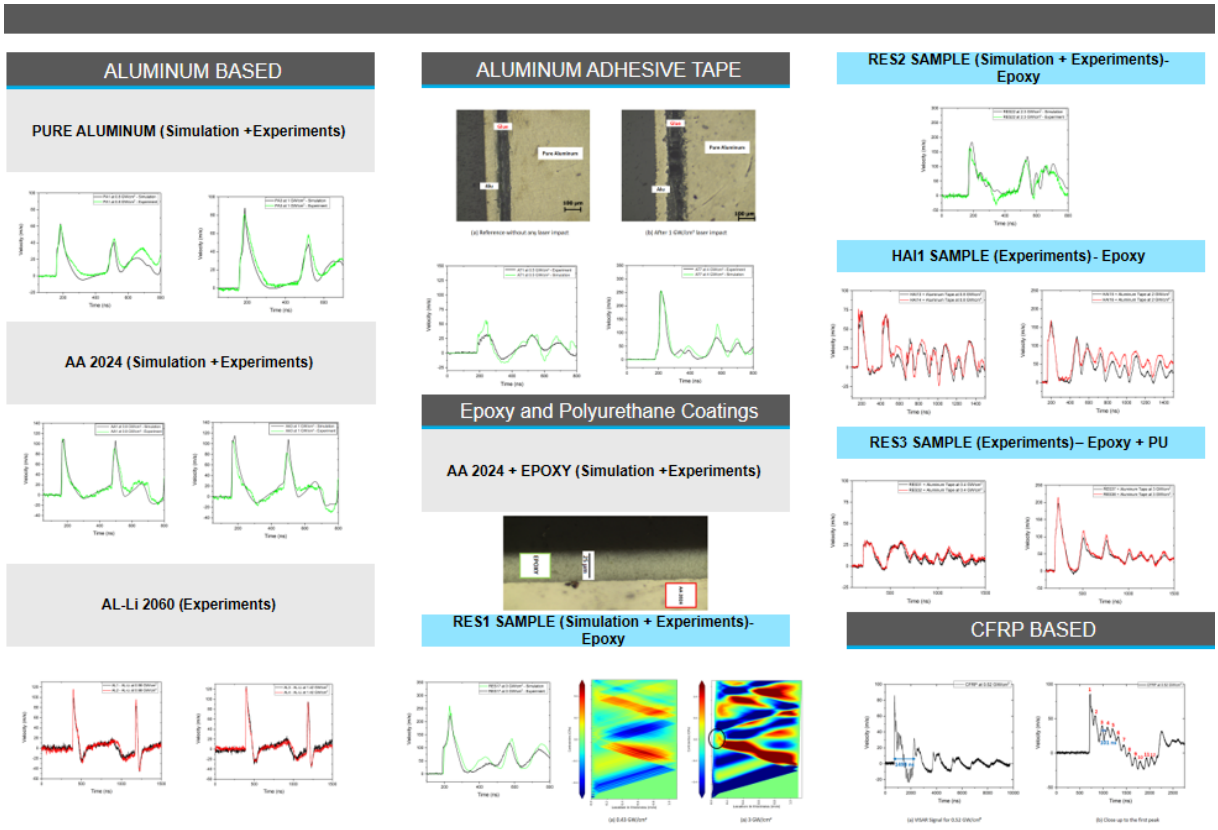

Table 3.18: Summary of obtained results.

Conclusion

This chapter has covered the investigation of pure aluminum, AA 2024-T3, AL-Li 2060-T8 E30 and CFRP based specimens. Pure aluminum, AA 2024-T3 and AA 2024-T3 + Epoxy Primer specimens are analysed both experimentally and numerically. AA 2024-T3 + Epoxy Primer + Top Coat, AL-Li 2060- T8 E30 and CFRP based specimens are just investigated via experimental work. For aluminum based materials, experimental validation is done via VISAR diagnostic at different applied power densities. Afterwards, P_{HEL} values for each sample are compared which is calculated thanks to the experimental BFV curves. For pure aluminum, the found P_{HEL} is around 0.33 GPa, for AA 2024 it is 0.85 GPa and for AL-Li 2060 it is 1.4 GPa. Since the P_{HEL} values for different materials vary, it may be difficult to develop a process window that is common to all industrial applications regardless of the material type.

Before moving to the second part of the chapter which is the behavior of aluminum tape under laser shock loading, numerical validations are done for pure aluminum and AA 2024. The results show that, experimental and numerical work have a good correlation within the worked power density range. These validations are an important step before moving forward to several paint layer configurations.

For the second part, aluminum tape is investigated with the same followed approach as previously. It is proven that by using a thick glue layer in the aluminum tape, maximum tensile zone can be modified for pure aluminum substrates. We proved that the validated methodology could be used to model polymers under high strain rate of deformation and the validated models can also serve as a potential candidate for optimizing laser paint stripping process.

In the third section, behaviour of epoxy and polyurethane coatings under laser shock loading is investigated. This section is divided into two parts as : AA 2024 + Epoxy and AA 2024 + Epoxy + Polyurethane. For the AA 2024 + Epoxy, laser impacts are applied both from the epoxy and the substrate sides of the specimens. Numerical work is conducted for RES1 specimen. σ_{yy} values and space-time diagrams are extracted both for the epoxy and the tape interface. The findings suggest that the crossing of a reflection of the compression and the tensile wave coming from the reflection within the tape and the epoxy might be a reason for a possible stripping at 3 GW/cm^2. In addition to this sample, for RES2 sample, numerical and experimental work is coupled. A good agreement is found between the model and the experiment with a slight difference. This difference occurs due to lack of the exact mechanical properties of the epoxy primer and the interface between aluminum/epoxy. Overall, it can be concluded that the model is capable of simulating the shock wave propagation inside the aluminum/epoxy specimen. Very

same methodology is followed for the specimens of AA 2024 + Epoxy + Top Coat, experimentally.

In the last part, CFRP base materials are investigated. Their characterization is done via VISAR. Number of plies are tracked, time of travel within a ply is calculated and also the time of travel within the composite is extracted thanks to the VISAR signals. No further numerical model is developed for this specimen type.

Conclusion FR

Ce chapitre comprend l'étude de spécimens en aluminium pur, AA 2024-T3, AL-Li 2060-T8 E30 et à base de CFRP. Les spécimens en aluminium pur, AA 2024-T3 et AA 2024-T3 + Apprêt Epoxy sont analysés à la fois expérimentalement et numériquement. Les spécimens en AA 2024-T3 + Epoxy Primer + Top Coat, AL-Li 2060- T8 E30 et CFRP sont étudiés par un travail expérimental. Pour les matériaux à base d'aluminium, la validation expérimentale est effectuée via le diagnostic VISAR à différentes densités de puissance appliquées. Ensuite, les valeurs de P_{HEL} pour chaque échantillon sont comparées et sont calculées grâce aux courbes BFV expérimentales. Pour l'aluminium pur, la valeur P_{HEL} trouvée est d'environ 0,33 GPa, pour AA 2024 elle est de 0,85 GPa et pour AL-Li 2060 elle est de 1,4 GPa. Par conséquent, l'AL-Li 2060 apparaît comme celle qui a le P_{HEL} le plus élevé, ce qui rend ce matériau de base prioritaire pour l'utilisation industrielle. Étant donné que différents matériaux de base ont des valeurs P_{HEL} différentes, il pourrait être difficile de définir une fenêtre de processus commune pour les applications industrielles, quel que soit le type de matériau de base.

Avant de passer à la deuxième partie du chapitre, qui concerne le comportement du ruban d'aluminium soumis à un choc laser, des validations numériques sont effectuées pour l'aluminium pur et l'AA 2024. Les résultats montrent que les travaux expérimentaux et numériques ont une bonne corrélation dans la gamme de densité de puissance travaillée. Ces validations sont une étape importante avant de passer à plusieurs configurations de couches de peinture.

Pour la deuxième partie, le ruban d'aluminium est étudié avec la même approche suivie que précédemment. Il est prouvé qu'en utilisant une couche de colle épaisse dans le ruban d'aluminium, la zone de traction maximale peut être modifiée pour les substrats en aluminium pur. Nous avons prouvé que la méthodologie validée pouvait être utilisée pour modéliser des polymères soumis à des taux de déformation élevés et les modèles validés peuvent également servir de candidat potentiel pour optimiser le processus de décapage de la peinture au laser.

Dans la troisième section, le comportement des revêtements époxy et polyuréthane sous une charge de choc laser est étudié. Cette section est divisée en deux parties l'AA 2024 + Epoxy et AA 2024 + Epoxy + Polyuréthane. Pour le AA 2024 + Epoxy, les impacts laser sont appliqués à la fois du côté de l'époxy et du côté du substrat des spécimens. Les travaux numériques sont menés pour l'éprouvette RES1. Les valeurs de σ_{yy} et les diagrammes espace-temps sont extraits à la fois pour l'interface époxy et l'interface ruban. Les résultats suggèrent que le croisement d'une réflexion de l'onde de compression et de l'onde de traction provenant de la réflexion à l'intérieur du ruban et de l'époxy pourrait être la raison d'un possible décapage à 3 GW/cm^2. En plus de cet échantillon, pour

l'échantillon RES2, les travaux numériques et expérimentaux sont couplés. Un bon accord est trouvé entre le modèle et l'expérience avec une primaire. Cette différence est due à l'absence de propriétés mécaniques exactes du primaire époxy et de l'interface entre l'aluminium et l'époxy. Globalement, on peut conclure que le modèle est capable de simuler la propagation de l'onde de choc à l'intérieur de l'éprouvette en aluminium/époxy. La même méthodologie est suivie pour les spécimens de AA 2024 + Epoxy + Top Coat, expérimentalement.

Dans la dernière partie, les matériaux de base en CFRP sont étudiés. Leur caractérisation est effectuée via VISAR. Le nombre de plis est suivi, le temps de parcours dans un pli est calculé et le temps de parcours dans le composite est également extrait grâce aux signaux VISAR. Aucun autre modèle numérique n'est développé pour ce type de spécimen.

4

Laser Paint Adhesion Tests

Introduction

This chapter focuses on the laser paint adhesion tests analysis on specimens. Several sets of samples are tested to evaluate the capability of the process. The main goal of the experiments are to study the sensitivity of the process according to:

- Layer Thickness
- Substrate Thickness
- Surface Treatment
- Type of Coated Layer
- Substrate Type
- Effect of Thermal Ageing

to distunguish the effects of mentioned parameters and to define a common process window for laser paint stripping applications within the industrial framework.

This study is based on testing of material manufacturing to control specific properties. To help in the overall comprehension of the physics behind the laser paint adhesion tests, numerical simulations are performed using LS-Dyna to discriminate the effect of layer thickness and influence of the thermal ageing configuration on chemical and mechanical properties.

Introduction FR

Ce chapitre se concentre sur l'analyse des tests d'adhésion de peinture au laser sur des échantillons. Dans cette section, plusieurs séries d'échantillons sont testées pour évaluer la capacité du procédé. L'objectif principal des expériences est d'étudier la sensibilité du procédé en fonction de :

- Epaisseur de la couche
- Epaisseur du substrat
- Traitement de surface
- Type de couche revêtue
- Substrate Type
- Effet du vieillissement thermique

Distinguer les effets des paramètres mentionnés et définir une fenêtre de processus commune pour les applications de décapage laser dans le cadre industriel.

Cette étude est basée sur des essais de fabrication de matériaux pour contrôler des propriétés spécifiques. Pour aider à la compréhension globale de la physique les tests d'adhésion de la peinture au laser, des simulations numériques sont réalisées à l'aide de LS-Dyna pour discriminer l'effet de l'épaisseur de la couche et l'influence de la configuration du vieillissement thermique sur les propriétés chimiques et mécaniques.

4.1 Effect of Layer Thickness

Epoxy primer layer is applied on top of the base materials. It has a thickness range of 20-30 μm for typical aeronautical applications [147]. Moreover, the polyurethane top-coats which are applied on epoxy primers are in the thickness range of 50-100 μm [147]. In this work, both layer configurations are applied at various thicknesses to simulate the thickness deviation due to manual spraying operations. Since there are variations on the thickness because of the spraying conditions, adhesion levels might be different from one sample to another. In order to test the adhesion levels, laser impacts are applied (mono impact) from the aluminium side of samples which are AA 2024-T3 + Epoxy Primer and AA 2024-T3 + Epoxy + Top Coat as seen in figure 4.1. After, adhesion levels are linked with the applied power density.

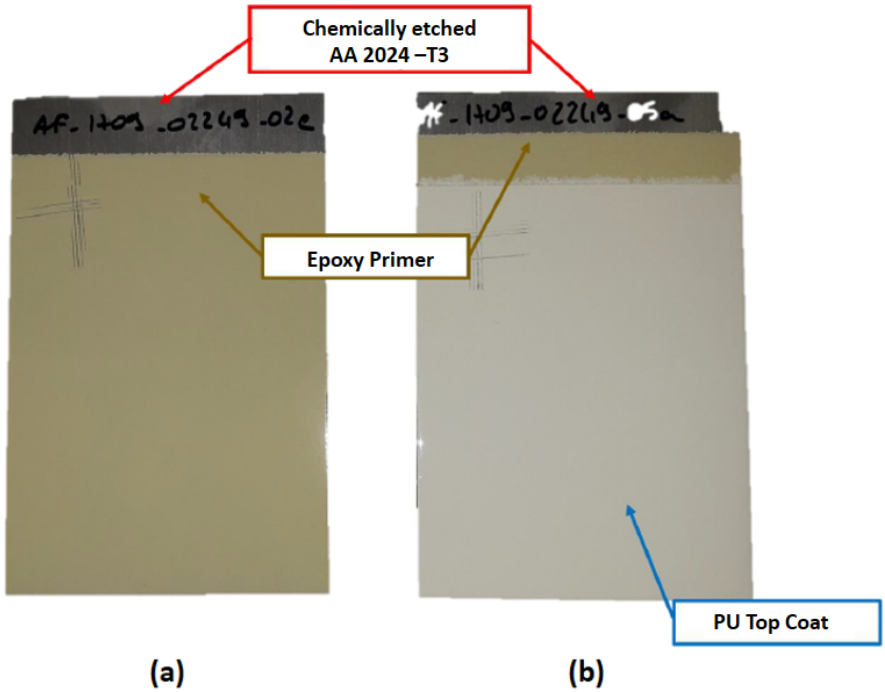

Figure 4.1: Painting Architecture provided by RESCOLL: (**a**) Chemically etched AA 2024 T3 substrate with Epoxy Primer (CA 7049), (**b**) Chemically etched AA 2024 T3 substrate with Epoxy Primer (CA 7049) & Polyurethane Top Coat (CA 8800).

Figure 4.2 represents a general view for the studied specimens in this section. The section is divided into two parts with a first part of AA 2024-T3 + Epoxy (figure 4.2a) and a second part for AA 2024-T3 + Epoxy + Top coat (figure 4.2b) materials. AA 2024-T3 + Epoxy samples include a zone without coating and with only epoxy primer. For the AA 2024-T3 + Epoxy + Top coat specimens, there are zones without coating, with only primer and primer + top coat.

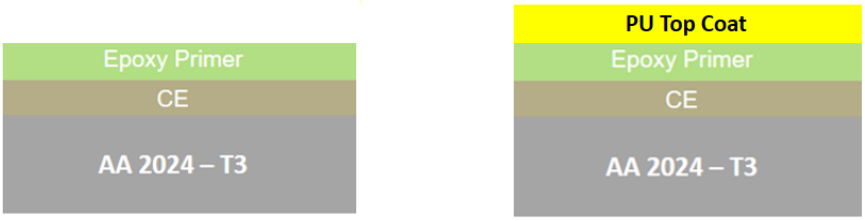

(a) AA 2024 - T3 + Epoxy Primer (b) AA 2024 - T3 + Epoxy Primer + PU Top Coat

Figure 4.2: Schematic representation of specimens.

4.1.1 AA 2024-T3 + Epoxy

To see the effect of epoxy thickness on paint adhesion levels, experiments are conducted with three different thicknesses which are 25±2.5, 43±3.2 and 56±3 μm. All samples in this section are AA 2024-T3 (970μm - 1 mm) based with a chemical etching surface treatment manufactured by RESCOLL. For the simplicity, samples are named as A, B and C (see Table 4.1).

Substrate	Surface Treatment	Epoxy Thickness	Label
AA 2024-T3 (970μm - 1 mm)	Chemical Etching	Epoxy Primer (25±2.5 μm)	A
AA 2024-T3 (970μm - 1 mm)	Chemical Etching	Epoxy Primer (43±3.2 μm)	B
AA 2024-T3 (970μm - 1 mm)	Chemical Etching	Epoxy Primer (56±3 μm)	C

Table 4.1: Categorization of each sample with their respective base material, surface treatment and thickness.

Thickness characterization is performed for each sample with a cross-section cut and optical microscope as shown in figure 4.3 with their respective thickness values.

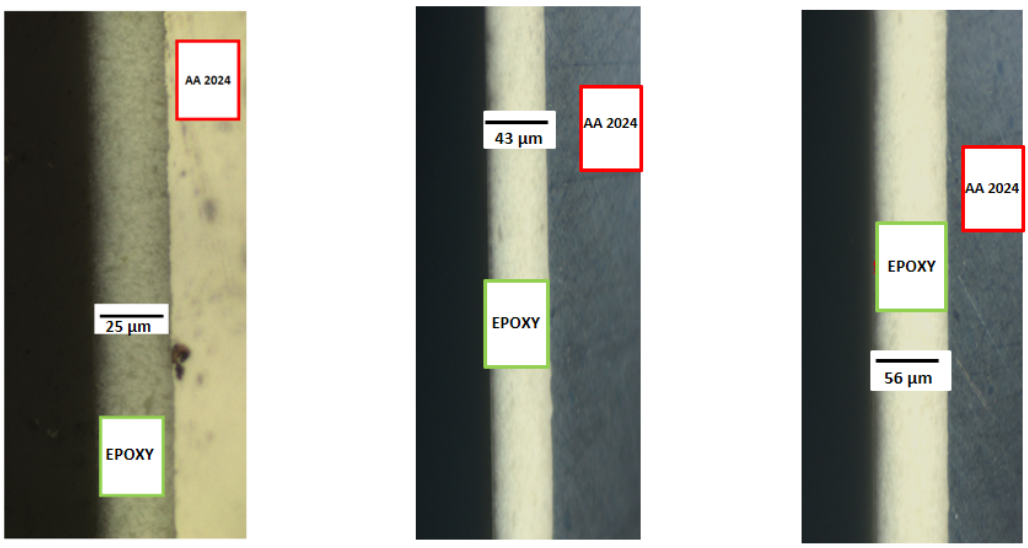

(a) (b) (c)

Figure 4.3: Representation of thickness measurements on sample A, B and C.

Figure 4.4 represents the process where mono impacts are applied from the aluminum side of specimens with water confinement regime. Paint stripping thresholds can be extracted as the smallest power density from which the first flight off of the coating is detected with the primary goal of relating the power density with the adhesion behavior of coated specimens. While calculating the power densities, the laser's pulse duration, laser's energy and focal spot (4 mm) are the main parameters. As explained in part 2.3, the energy is calibrated shot by shot and the laser pulse duration was kept constant as 7 ns for these measurements at Hephaistos facility. In addition, VISAR diagnostic is used during the experiments to monitor the wave behavior within the targets.

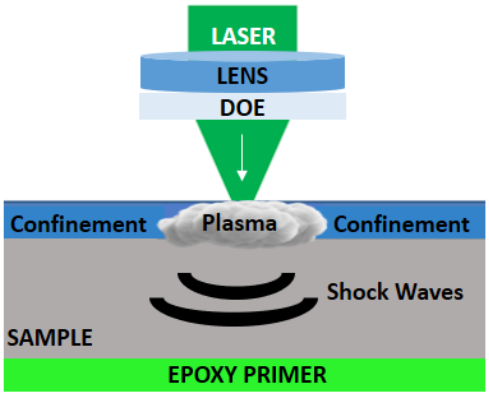

Figure 4.4: Applied impact and sample configuration.

The used power density range for all samples is in between 0.3 GW/cm^2-2.3 GW/cm^2. These values are chosen according to layer stripping threshold which is the value of obtained complete epoxy stripping, visually, during the laser experiments. Each power density has been applied at least 3 times in different locations of the 80 mm x 125 mm sized samples, to be sure about the reproducibility of the behavior.

After having applied laser impacts, each spot is correlated with their respective optical microscope image to follow their adhesion behavior and stripping pattern. As shown in figure 4.5, the four different zones can be defined as function of adhesion pattern: the zone with complete stripping, the zone with damage ring, the zone where the paint debonding/breakaway starts (the range in between no stripping and complete stripping) and the zone without any stripping. Obtained stripping patterns highlight the importance of paint adhesion tests within the same samples as function of epoxy primer thicknesses. Paint debonding starts at 0.3 GW/cm^2 for sample A and around 0.5 GW/cm^2 for sample B and C. However, complete and reproducible stripping values are defined as the stripping threshold points that are 0.5 GW/cm^2 for Sample A, 0.7 GW/cm^2 for Sample B and 0.9 GW/cm^2 for Sample C (see figure 4.6). Moreover, for sample A, damage ring occured in the range of 0.9-2.3 GW/cm^2 which is explained in the following pages via numerical work.

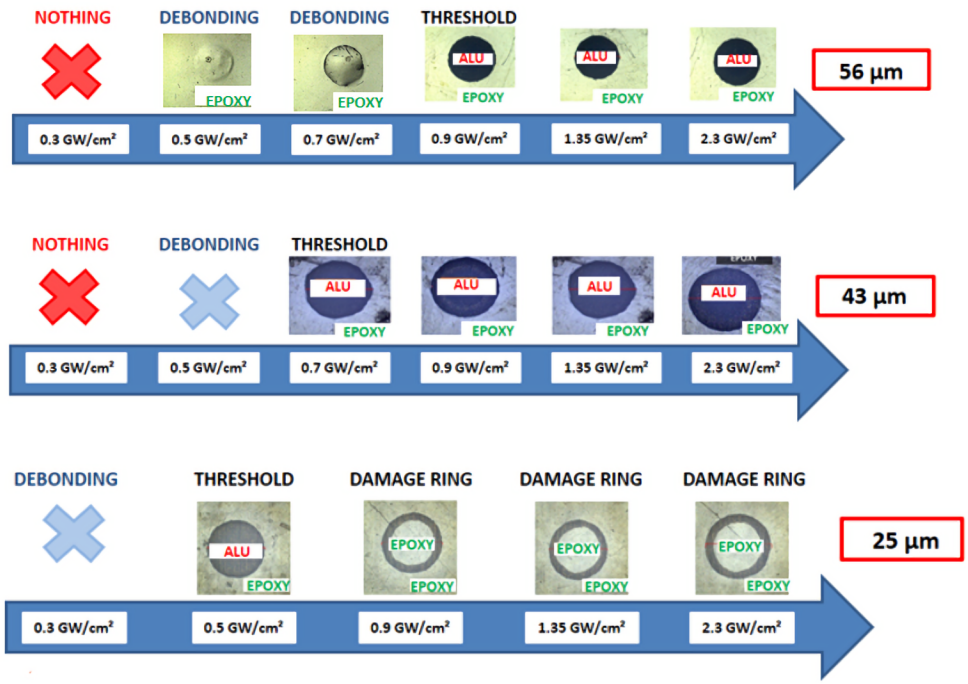

Figure 4.5: Sample A, B and C, respectively with after applied laser impacts and corresponding microscope images.

In order to visualize a process parameter window, figure 4.6 is generated as function of applied power density versus sample in which pink range represents no stripping zone, green part is where the debonding starts, the yellow part is for the damage ring and the purple one is for the stripping range.

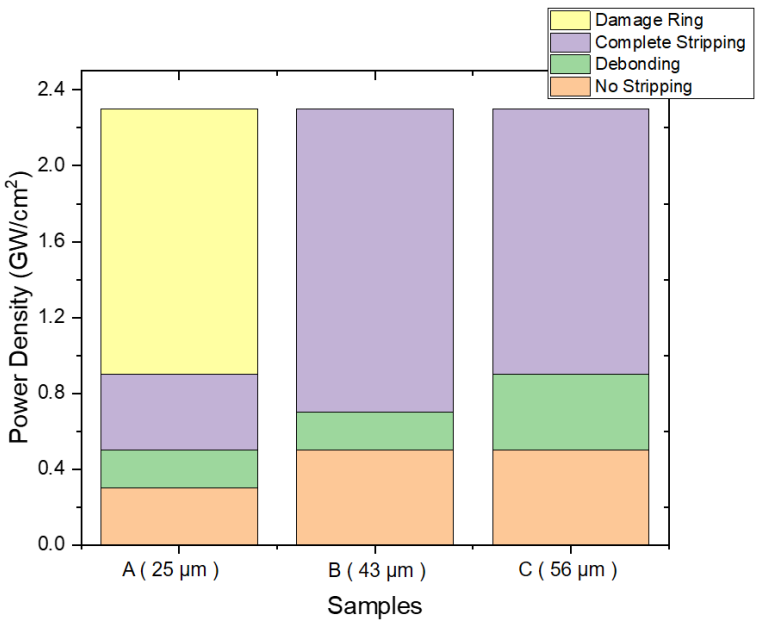

Figure 4.6: Sample A, B and C, respectively within stripping, partial stripping, debonding and no-stripping ranges.

The obtained results show that, having a common process window regardless of the epoxy thickness is challenging due to the sensitivity of the process for these specimens. However, thanks to the sensitivity of the process, laser based paint adhesion test can be an innovative tool for paint adhesion investigations.

Before moving to the origin of damage ring phenomena, first, the numerical model for AA 2024 + Epoxy is validated. VISAR signal is obtained by having a gold coating, as explained in section 2.1.4, on top of epoxy primer to have a good reflectivity as shown in figure 4.7.

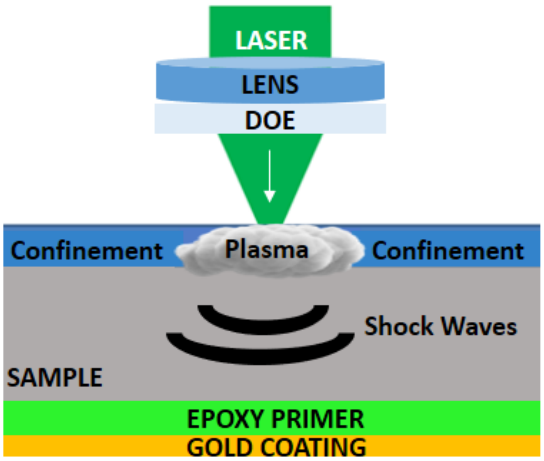

Figure 4.7: Specimen architecture with aluminum base material, epoxy and gold coating.

In figure 4.8, shown signal is at 2.3 GW/cm^2 power density for the sample A in which there is a damage ring phenomena occurs. Since the VISAR measurement is from the center of the focal spot, where there is still paint at this power density at the center (damage ring), extracted signal represents the full wave propagation without including any stripping pattern to track as presented in figure 4.8. As one can see, velocity-time signal is extracted via VISAR diagnostic within the target which is the green signal. The experimental work is also coupled with numerical analysis as described in section 3.3. The found numerical curve is shown as black in figure 4.8 which has a relatively good agreement with the experimental curve.

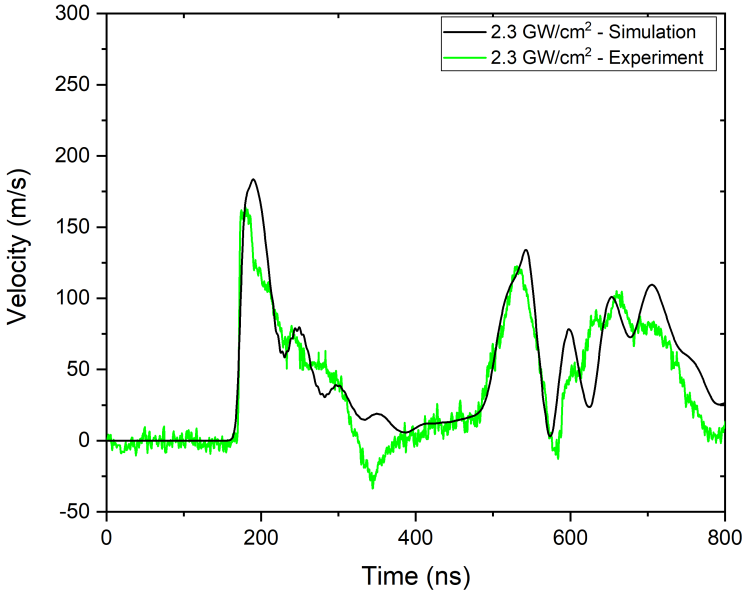

Figure 4.8: Back face velocity comparison of VISAR and simulation at 2.3 GW/cm^2 for AA 2024 -T3 + Epoxy (25 μm).

After the model validation, maximum axial tensile stresses were extracted via numerical work both at the center and at the edges of the focal spot for damage ring and complete stripping patterns of each specimen. The worked power density range covers 0.3 GW/cm^2 to 2.3 GW/cm^2. Obtained optical microscope images are given in figure 4.9 which also includes "C" and "E" points to represent center and edge, respectively.

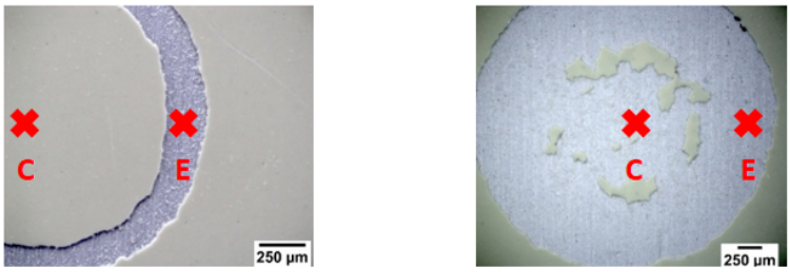

(a) Partial Stripping within the range of 0.9 – 2.3 GW/cm²

(a) Complete Stripping within the range of 0.5 – 0.9 GW/cm²

Figure 4.9: Representative damage ring and complete stripping patterns for Sample A.

Figure 4.10 demonstrates the maximum axial tensile stresses at aluminum-epoxy interface as function of applied power densities for each specimen. Extracted results are divided into two main groups as edge and center which are previously shown in figure 4.9.

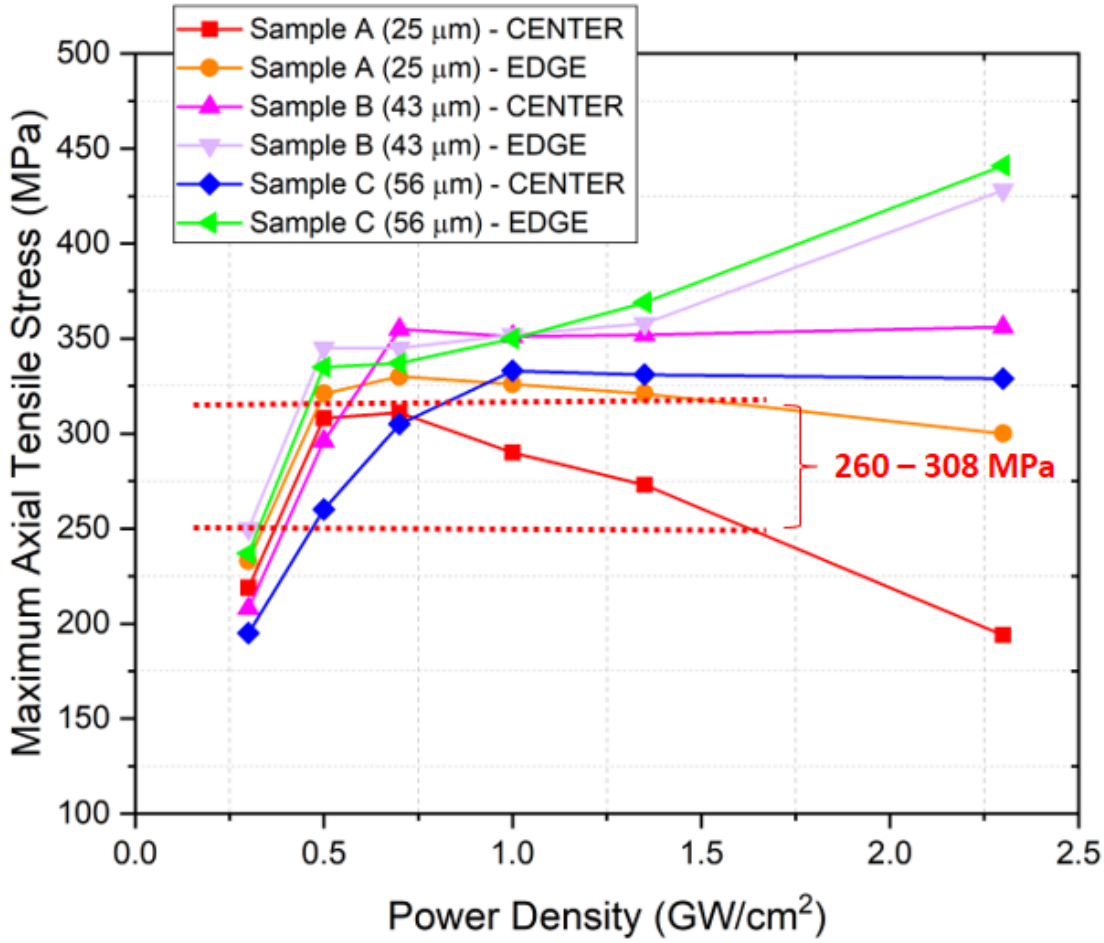

Figure 4.10: Obtained maximum axial stress at the center and at the edge of the focal spot as function of applied power density by numerical work.

The common threshold/debonding range as function of maximum axial tensile stress can be defined as 260-308 MPa. The graph can be divided in five parts for the range of 0.3-2.3 GW/cm^2. The first zone is for the power density of 0.3 GW/cm^2 where the debonding is observed for the sample A. One can see that the sample A has the highest maximum tensile stress (at center), 219 MPa, in comparison with other samples at this power density.

The second zone demonstrates the data point of 0.5 GW/cm^2 in which the paint stripping occurs for sample A (threshold), experimentally. As shown in figure 4.10, the maximum tensile stress is at its highest (308 MPa) for sample A at the center in comparison with sample B (289 MPa) and C (260 MPa), numerically. However, for the same power density value, for these specimens, at the edge of the spot, the found tensile stresses are higher than the threshold stress value. Since there is already a debonding creation at this power density for sample B and C, which might be an explanation of these findings.

The third zone covers the maximum tensile stresses at 0.7 GW/cm^2 where the paint stripping occurs for sample B. For sample B, it's above the tensile threshold level as expected hence there is a complete stripping at this power density for that specimen. For sample C, the maximum tensile stress at the center is below the threshold at this value.

In the fourth zone which is at 0.9 - 1 GW/cm^2, for sample C, threshold is obtained, experimentally. Numerically, obtained maximum tensile stresses for both at the edge and at the center are higher than the threshold level. As one can see that the tensile stress (center) is lowest for sample A in this region since the damage creation is present for sample A at that power density.

For the fifth zone, power density range of 1-2.3 GW/cm^2 is studied. For sample A, both for the edge and the center, there is a decrease of the tensile stress. For sample B and C, at the center, the curves started to have a constant behavior. On the other hand, at the edge, increasing pattern is observed for those samples.

For sample B and C, the extracted stress values for both at the edge and at the center for each power density after reaching their threshold values, are always found higher than the threshold stress which is a proof of continuous complete stripping with the increase of the power density. On the other hand, for sample A, where the damage ring phenomena is observed, both at the edge and at the center, maximum tensile stress levels continue to decrease with the increase of the power densities.

In order to understand the failure process of the aluminum/epoxy interface, a detailed stress analysis was performed for both epoxy thicknesses. The analysis was focused on the σ_y. Figure 4.11 plots the σ_y stresses developed at the interface of the aluminum/epoxy at various stages of the wave propagation for sample A at 1 GW/cm^2. The figure 4.11c at 200 ns and figure 4.11d at 234 ns show a clear propagation for the tensile stress distribution which are immersed to each other since they occur within a close time range.

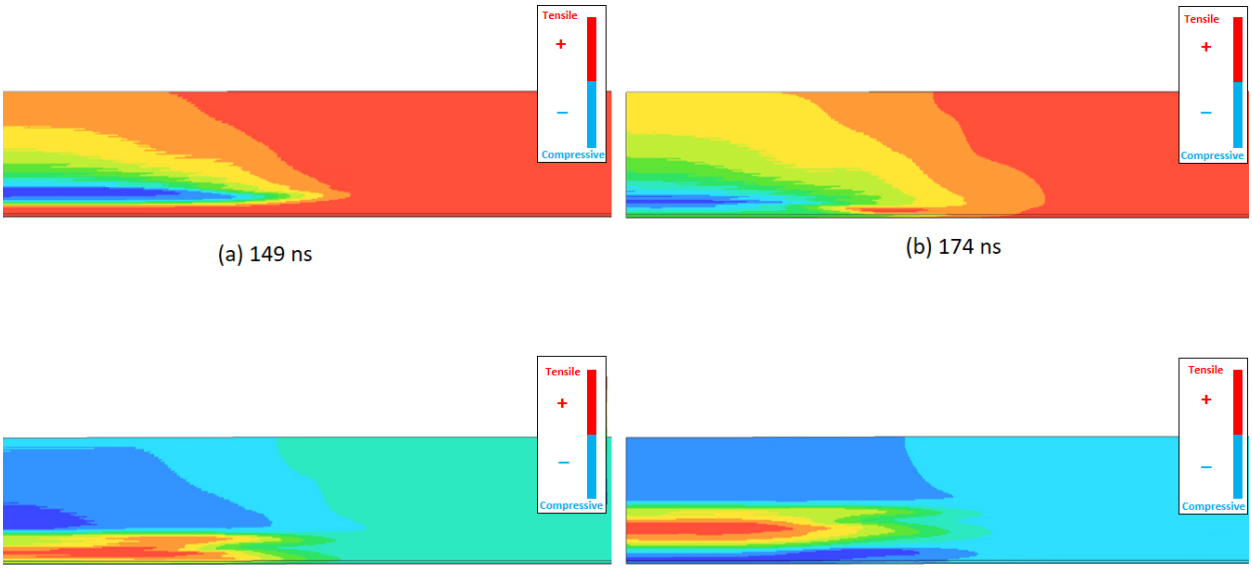

(a) 149 ns (b) 174 ns

(c) 200 ns (d) 234 ns

Figure 4.11: Numerically obtained various stages of shock wave propagation for sample A at 1 GW/cm^2.

For the failure process of the aluminum/epoxy interface, stress is performed for σ_y at 1 GW/cm^2 for sample C to evaluate the comparison of different thicknesses and complete/partial stripping patterns (see figure 4.12).

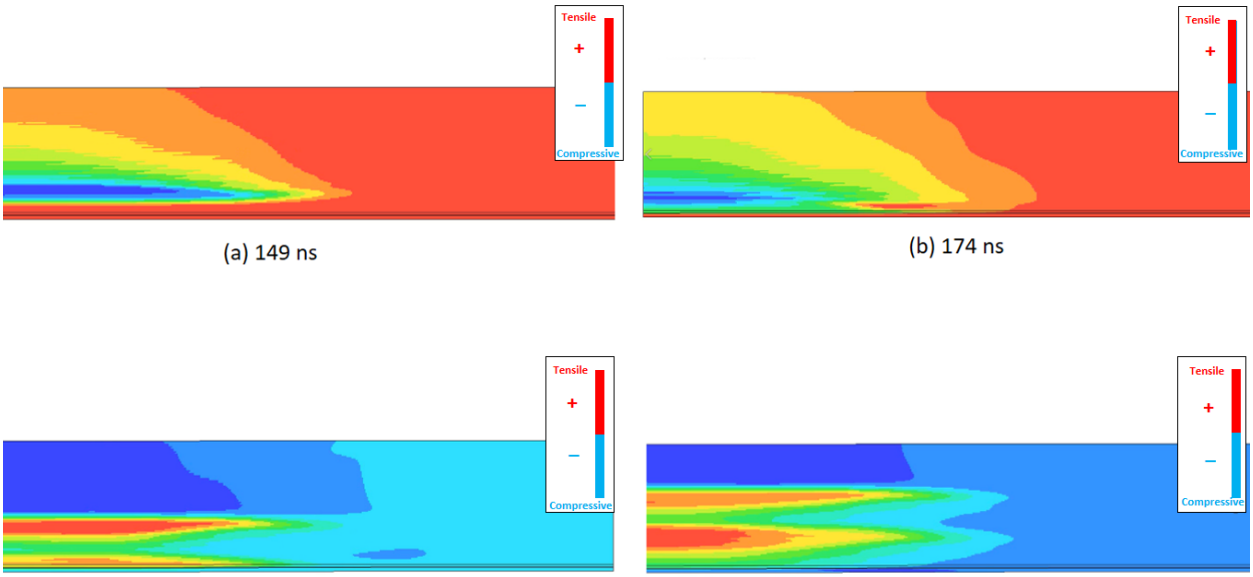

(a) 149 ns (b) 174 ns

(c) 229 ns (d) 269 ns

Figure 4.12: Various stages of shock wave propagation for sample C.

As one can see from the figure 4.12, tensile stress propagation can be tracked clearer and separated from each other as shown in figure 4.12c at 229 ns and 4.12d at 269 ns.

The numerical study allowed us to analyze the elasto-plastic interaction for different epoxy thicknesses. Since the occurrence of elastic and plastic waves interfere (elasto-plastic regime), for sample A, the decrease of the maximum axial stress at the interface with the increase of the power density can be explained by that. The damage ring occurance observed within the elasto-plastic regime according to the σ_{yy} calculations via numerical work at the epoxy-aluminum interface of sample A. Figure 4.13 demonstrates the σ_{yy} is plotted as function of pressure. The used relation between power density and the pressure is as previously explained in equation 1.8.

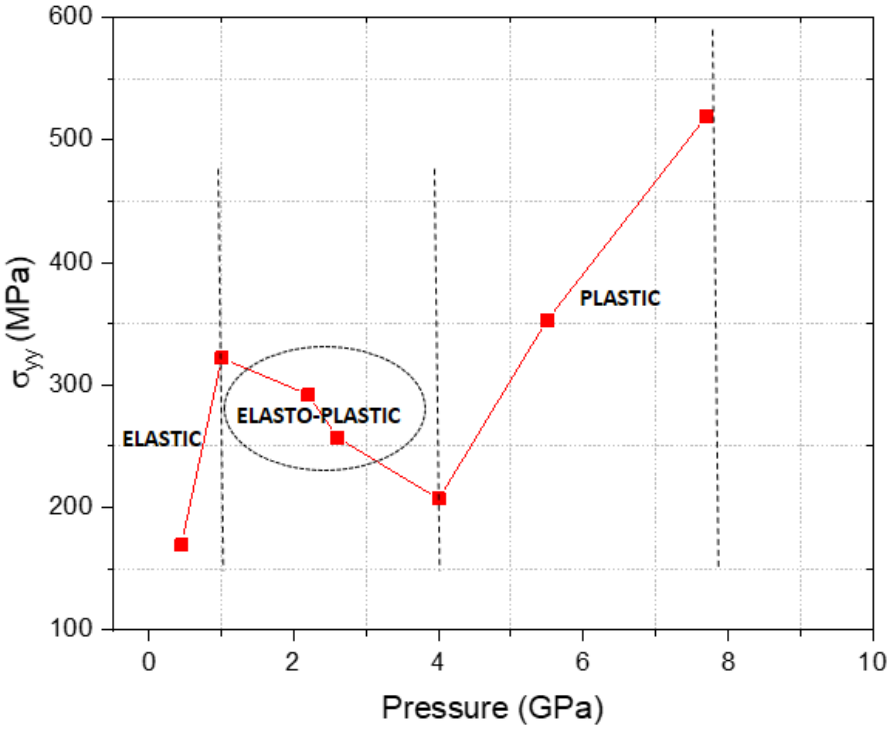

Figure 4.13: σ_{yy} as function of applied pressure for sample A.

The elasto-plastic regime for sample A is within the range of damage ring pattern creation. If the elastic precursor occurs at higher velocities than the one for AA 2024-T3, the damage ring phenomena can be eliminated for thinner epoxy specimens within the same power density range. As previously discussed in subsection 3.1.1.3, AL-Li has a higher elastic limit that makes the material to have a larger elastic zone regimes. According to these findings, it can be said that the process optimization can be done as function of used base material.

In conclusion, the damage ring phenomena appears to be caused by mixed effects. Apart from the elasto-plastic regime, the reflections of waves have different behaviors for different epoxy thicknesses as shown in figure 4.11 and figure 4.12. In addition, edge effects (as explained in subsection 1.3.2.4) are compensating the elasto-plastic behavior and eventually contributes to the stripping at the edges of the applied focal spot.

4.1.2 AA 2024-T3 + Epoxy + Top Coat

Figure 4.14 shows the used mono impact configuration for this type of specimen with an epoxy primer and polyurethane top-coat on top of aluminum base target.

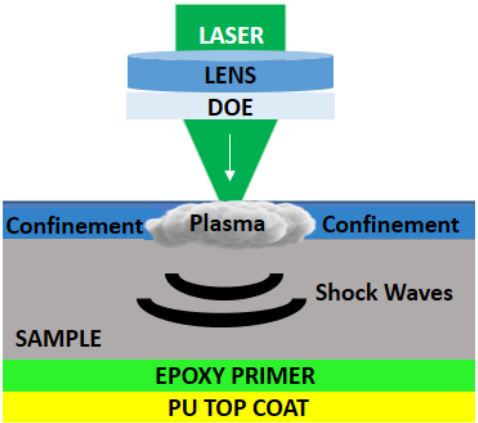

Figure 4.14: Sample configuration of epoxy primer and polyurethane top-coat (PU).

Layer characteristics are determined on specimens in terms of thickness range both before and after laser stripping in order to validate the substrate material health and coating properties. The influence of polyurethane top-coat thickness is studied in order to verify the laser stripping process window for industrial aircraft applications.

Sample No	Coating Type	Thickness (μm)
	Epoxy Primer Specification	20 to 30
	Polyurethane Top-Coat specification	50 to 75
1	Epoxy Primer	24 ± 1.9
1	Polyurethane Top-Coat	26.8 ± 1.9
2	Epoxy Primer	27.9± 1.7
2	Polyurethane Top-Coat	18.9± 3.5
3	Epoxy Primer	22.7± 6
3	Polyurethane Top-Coat	122.6± 7.8
0	Epoxy Primer	18

Table 4.2: Thickness specification of each sample before laser operations.

Structural anticorrosion epoxy primer (CA 7049) and polyurethane top coat (CA 8800 provided) are manufactured on AA 2024-T3 specimens with a thickness of 970 μm- 1 mm. Coated samples have been labeled as 0, 1, 2 and 3 (see table 4.2). Epoxy primer is applied on top of aluminum to achieve the typical range for aeronautics applications (20 to 30 µm) [147]; while the polyurethane top-coats are applied at various thicknesses to simulate the thickness deviation due to manual spraying operations. The laser stripping process is applied on a zone which includes both epoxy primer and top coat for all 3 specimens. The sample labeled as 0 just coated with an epoxy primer and kept as a reference plate (no stripping application) see Table 4.2. For the all mentioned specimens in table 4.2,

thickness measurements were operated at RESCOLL company. However, a sample which has a typical range of epoxy primer (20 to 30 μm) and polyurethane top coat (50 to 100 μm) for aeronautics applications is included below which was characterized at PIMM (see figure 4.15).

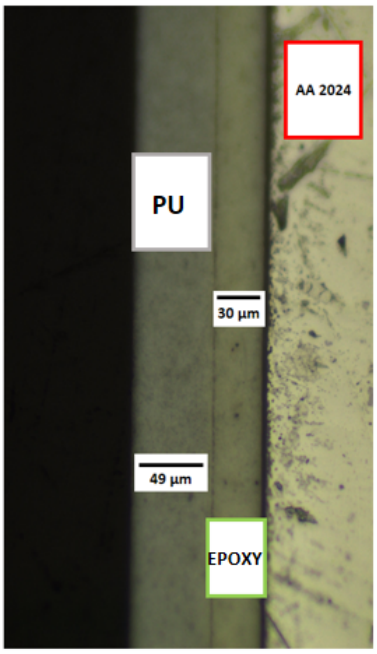

Figure 4.15: Sample with a typical range of thicknesses for epoxy primer and polyurethane top-coat (PU).

In figure 4.16, applied epoxy primer, polyurethane top-coat and the shot for stripping threshold determination are presented.

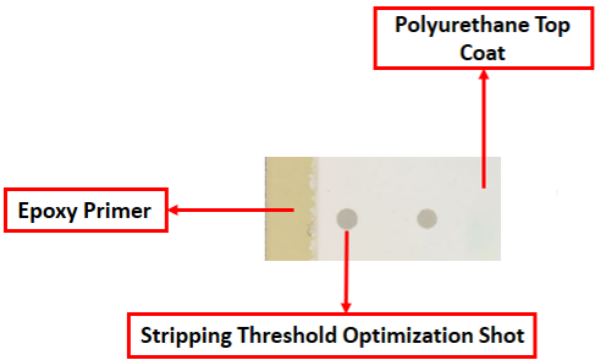

Figure 4.16: Zone Definition on sample 1 as a representative.

As one can see from figure 4.17, the remaining thickness of coatings (in blue) after laser impacts are evaluated as function of applied power density (where the stripping threshold occurs). The stripping threshold is calculated from the first flight off of the coating for each sample, as previously discussed. For the sample 2, its found as 0.7 GW/cm^2, for sample 1 as 0.9 GW/cm^2 and for the sample 3 its 2.7 GW/cm^2 which are

marked in white on the pink curve for each specimen in figure 4.17. With the increased top coat thickness, stripping threshold as function of power density is increased as well.

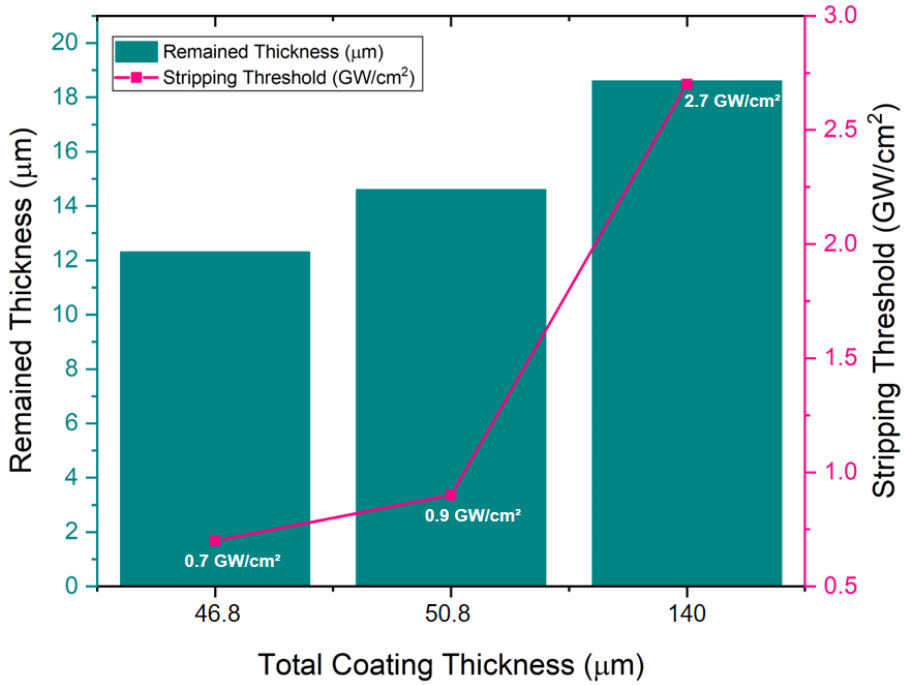

Figure 4.17: The representation of remained thickness versus the total thickness as function of stripping threshold.

It can be said that, increasing power density enables us to strip higher thicknesses. In addition, for all sample types, after laser stripping operations, there is a remaining epoxy primer coating which ensures the front face substrate health after laser stripping operations (see Table 4.3). Since the remained thicknesses are always found within the range of epoxy layer or smaller, no further physico-chemical characterization is performed. It is concluded that the paint removal takes place within the epoxy primer not at the epoxy primer interface.

For all specimens, the ratio of remained thickness to total thickness is in between 13-28 %. There is no followed specific trend for remained thickness as function of total thickness and/or applied power density. However, with the increased total thickness, the remained thickness is increased on the targets.

Total Thickness (μm)	**Remained Thickness (μm)**	$\frac{\textbf{Remained Thickness}}{\textbf{Total Thickness}}$ **(%)**
46.8	12.3	26
50.8	14.6	28
140	18.6	13

Table 4.3: Remaining thickness as function of total thickness of specimens after laser stripping operations.

4.2 Effect of Specimen Thickness, Surface Treatment and Layer Type

4.2.1 AA 2024-T3 + Epoxy

Two kind of samples are investigated which are both AA 2024-T3 with an epoxy primer layer. They were painted and prepared by manufacturers (RESCOLL, AkzoNobel & HAI). There are two different surface treatments for all sample types: Chromic acid anodization (CAA) and chemical etching (CE). Sample AA 2024-T3 CAA + Epoxy 37035A is labeled as Sample D and AA 2024-T3 CE + Epoxy CA 7049 is labeled as Sample E as explained in Table 4.4. Same laser impact configuration is applied on these samples as in figure 4.4.

Base Material	AA 2024-T3 CAA (800 μm) - D	AA 2024-T3 CE (970 μm) - E
Structural Primer	Epoxy 37035A (28.5 ±1.2 μm)	Epoxy CA 7049 (28.1±1.8 μm)

Table 4.4: Categorization of each sample with the thickness of each layer, respectively. CAA refers to Chromic Acid Anodization & CE is for Chemical Etching.

The thickness of the AA 2024-T3 is 800 and 970 μm for all configurations. For the Sample D, the thickness of the epoxy layer is as 28.5±1.2 μm and substrate surface has a chromic acid anodization surface treatment. For Sample E, the epoxy thickness is 28.1 ±1.8 μm with a surface treatment of chemical etching (all the stack sizing and descriptions are gathered in Table 4.4).

For Sample D and Sample E, damage ring and complete stripping phenomenas are studied. With the increase of the power density, paint adhesion level status is observed on specimens. For Sample D, complete stripping is observed at 1.75 GW/cm^2 whereas for Sample E, the damage ring is occured at the same applied power density. Also, one can see that for Sample E at 2.28 GW/cm^2, damage ring formation is seen and for Sample D at 2.28 GW/cm^2 also damage ring formation is observed in a different size. In order to deeper investigate this phenomena, additional numerical work was followed for the cases of damage ring and complete stripping as explained in the previous section (section 4.1.1).

Figure 4.18 shows the profilometer results for the stripped epoxy depth along the focal spot with corresponding microscope images for spots. Comparing the obtained depth vs scanning distance curves, we can have an idea about the surface health after the laser stripping process (since the thickness of an epoxy layer is known before any laser impact). In addition, for partial stripped impacts, almost perfect top-hat shape is observed in the middle of the spots. As one can see from figure 4.18, in this power density range (for 1.75 & 2.28 GW/cm^2), the stripped/affected diameter becomes smaller with the increase of the power density. Whereas it is 4080 μm for Sample D at 1.75 GW/cm^2, then it decreases to 3452 μm at 2.28 GW/cm^2. And for Sample E, the stripped/affected diameter is 3632

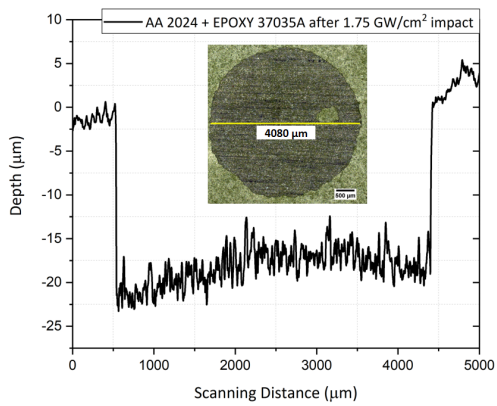

(a) AA 2024 + Epoxy (Sample D) 37035A after 1.75 GW/cm^2 impact.

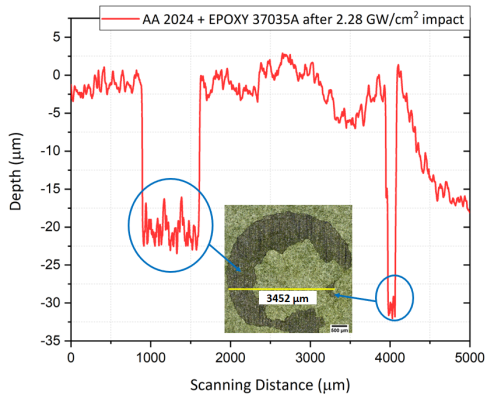

(b) AA 2024 + Epoxy 37035A (Sample D) after 2.28 GW/cm^2 impact.

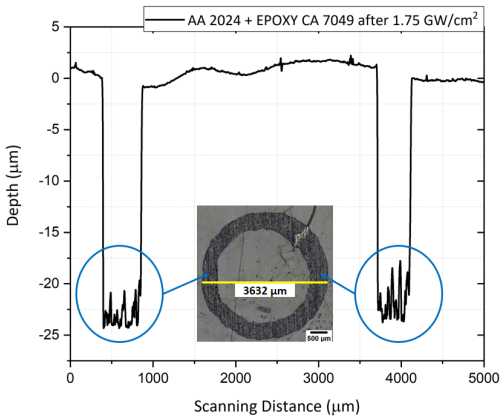

(c) AA 2024 + Epoxy CA 7049 (Sample E) after 1.75 GW/cm^2 impact.

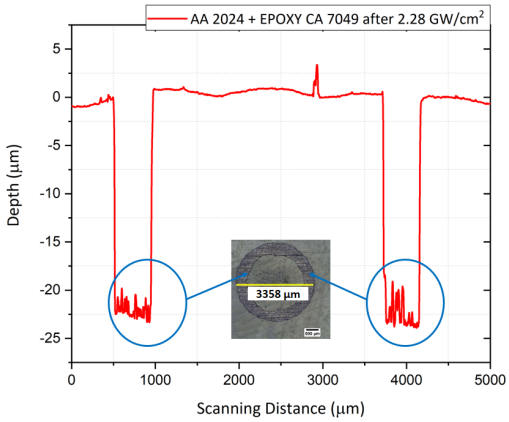

(d) AA 2024 + Epoxy CA 7049 (Sample E) after 2.28 GW/cm^2 impact.

Figure 4.18: Obtained depth profiles for different power density values and different type of epoxies.

μm at 1.75 GW/cm^2 and it then also decreases to 3588 μm.

Hence the epoxy thickness is 28.1-28.5 μm as a result of the depth observations, the substrate is not damaged by the laser impacts except at the 2.28 GW/cm^2 for Sample D hence at this power density, the maximum depth reached more than 30 μm (see figure 4.18b). In addition, the results show that the adhesion is sensitive to the surface preparation, type of the epoxy primer and substrate thickness. However, since there is not one specific controlled parameter, it can not be concluded with the precise effect of each parameter for this set of study.

4.2.2 AL-Li 2060 T8 E30 + External Aircraft Coatings

Since no paint removal is obtained for AL-Li 2060 T8 E30 + Epoxy primer specimens for different surface treatment configurations, this section is focused on AL-Li 2060 T8 E30

(2.5 mm thick) + External Aircraft Coatings with a thin film sulphuric acid anodization and sol gel surface treatments which is illustrated in figure 4.19. The investigated samples consist of previously mentioned two different surface treatments with an applied same type of primer (14-15 μm) and top coat (21-22.5 μm) finish. The effect of different surface treatments on adhesion level are investigated.

(a) Sol-Gel Surface Treatment (b) TFSAA Surface Treatment

Figure 4.19: Samples' configuration with their respective surface treatments.

As shown in figure 4.20, for the simplicity, the sample with a sol gel surface treatment named as "S" and the one with thin film sulphuric acid anodized is as "M". In the graph, the pink part represents the range without stripping, green is where the paint debonding starts and the purple part where the complete paint removal occurs.

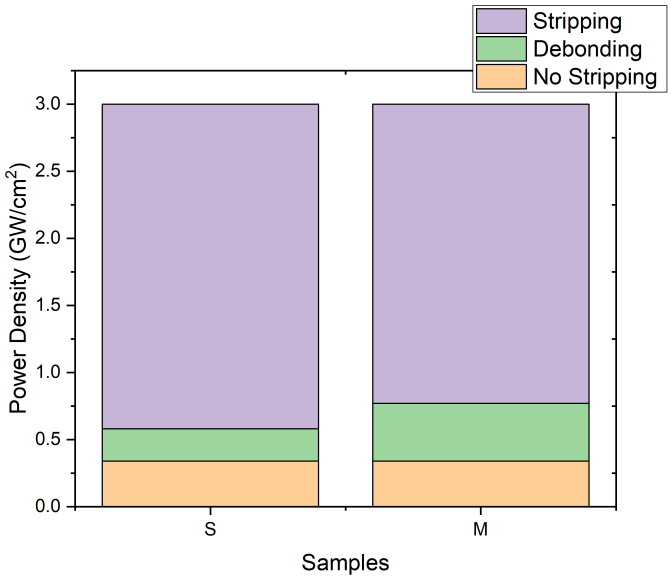

Figure 4.20: Sample S and M, respectively within stripping, debonding and no-stripping ranges.

These samples helped us to monitor the effect of different surface treatments for laser paint adhesion tests. Since the specimens have same layer configurations with relatively similar thicknesses, it allowed us to observe sol-gel and sulphuric acid anodizing surface treatments' impact. The paint stripping thresholds are obtained as 0.6 and 0.8 GW/cm^2, respectively for sol-gel and thin film sulphuric acid anodized ones. Even though there is a small difference for the stripping threshold, the test permitted us to detect it.

4.3 Effect of Substrate Type

As shown in figure 4.21, in this section, detailed analysis of AA 2024-T3 + all the external aircraft coatings (EAC) and CFRP + all the external aircraft coatings (EAC) are studied. Although the thickness of base materials are not the same, paint adhesion and laser stripping properties are investigated to compare the capabilities on metal and composite based substrates.

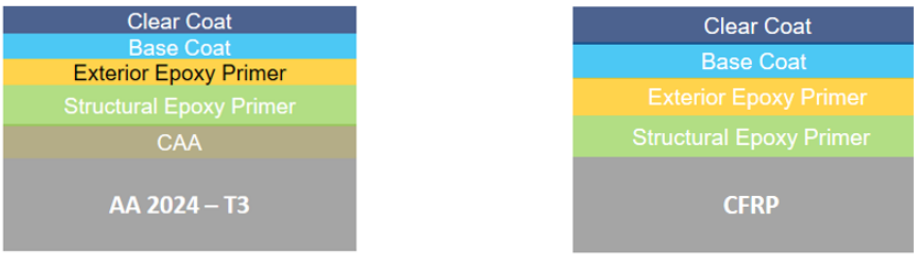

(a) AA 2024 – T3 + External Coatings (b) CFRP + External Coatings

Figure 4.21: Configuration for AA 2024-T3 and CFRP based specimens, respectively.

4.3.1 AA 2024-T3 + External Aircraft Coatings

The investigated specimen was painted and prepared by manufacturers (AkzoNobel & HAI) with a surface treatment of Chromic acid anodization (CAA) which labeled as F. The sample consists of structural primer, exterior primer, base coat and clear coat. In order to determine the thickness of each layer, specimens are cut by a metallographic cut-off machine then observed by an optical microscope (ZEISS Axio Imager 2). Figure 4.22 shows typical view for Sample F.

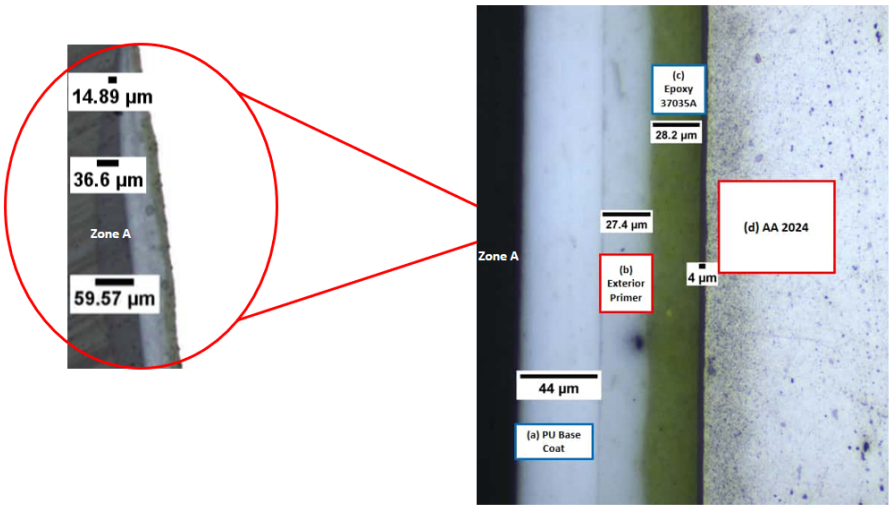

Figure 4.22: Figure on the right is the cross-section cut of AA 2024-T3 CAA + EAC under the optical microscope. The figure left is the zoom-out of the cross section to demonstrate the thickness variation for the clear coat layer.

The base material, AA 2024-T3 sample, has a thickness of 800 μm. Structural primer has a thickness range of 28.2 ± 4 μm and exterior primer is measured as 27.4 ± 2.5 μm for the investigated Sample F. Moreover, the polyurethane made base coat has a thickness of 44 ± 4.5 μm for analyzed samples. In addition, the final layer (clear coat) has a thickness in between 14.9-60 μm as labeled as Zone A (figure 4.22). Since the clear coat is a transparent layer, we can not identify it without zooming out from the cross-section cut.

For this specimen, the obtained paint stripping threshold is found as 2.77 GW/cm^2. Above the stripping threshold, the power density is increased gradually at different locations on the target at 3.2 GW/cm^2, 5.8 GW/cm^2 and 8.8 GW/cm^2 through 4 mm focal spot size. Then, samples are investigated by optical microscopy to observe the stripped surface status and layer characteristics, qualitatively. Figure 4.23 presents the optical microscope analysis of Sample F specimen's surfaces after laser impacts where green layer is the structural epoxy primer (Epoxy 37035A layer). As the surface visually appears more or less green (the structural primer color), these results show that, both at low and high applied power densities, structural primer stays present on the substrate. Therefore, the exterior primer coating + subcoating assembly are stripped for the Sample F type. However, with the increase of the power density, the structural primer presence is reduced on the bare surface. Although, optical microscope analysis gives us a qualitative information about the layer status after laser impact, since there are thickness variations mostly due to clear coat thickness as explained previously, we can not expect them to have homogenously distributed thickness all around the sample. That is why instead of profilometer analysis, physico-chemical characterization is done for this sample type to obtain more quantitative data.

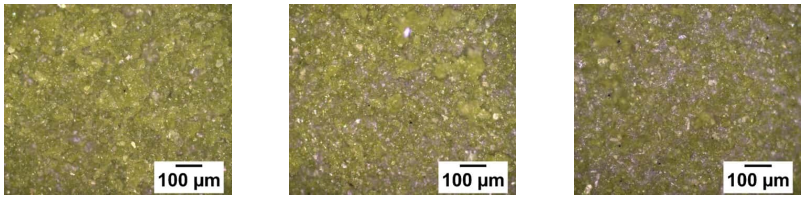

(a) 3.2 GW/cm^2 laser impact (b) 5.8 GW/cm^2 laser impact (c) 8.8 GW/cm^2 laser impact

Figure 4.23: Close-Up Optical Microscope Analysis of surfaces after laser impulsion for Sample F, respective power density values.

In order to better understand the nature of the remaining organic content structure, FTIR is utilized [148, 149]. It is challenging to identify epoxy resins by FTIR since this family of thermoset contains a great amount of prepolymer-hardeners. However, in most cases, they can be tracked back by the presence of some specific groups such as phenyls (1610 cm^{-1}) [150, 151], secondary alcohols (2 hydroxypropylether) at (3400-3420 cm^{-1}), isopropyl groups (2966 cm^{-1}) [152], ethers (Ar-O-CH_2) and alcohol (CH-OH) groups respectively at 1039 cm^{-1} and 1109 cm^{-1} [152] as shown in figure 4.24.

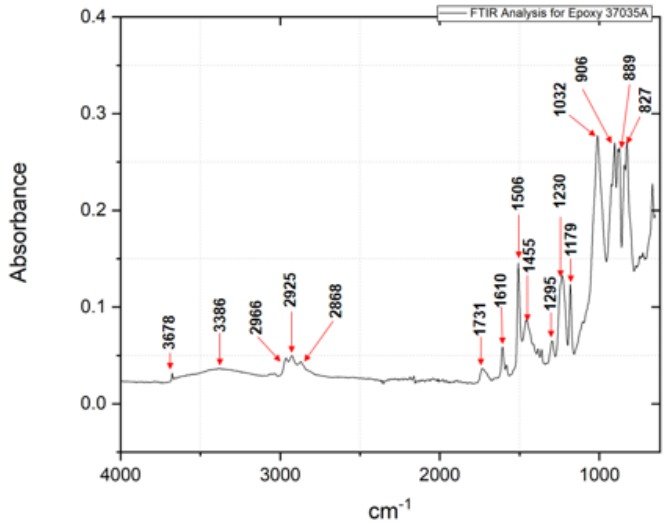

Figure 4.24: FTIR spectra for the epoxy 37035A.

Since the Epoxy 37035A layer remained after 3.2 GW/cm^2 and 5.8 GW/cm^2 for Sample F according to the optical microscope observations, it is also verified by FTIR spectras (see figure 4.25). Although we can not conclude the result as complete selective stripping, the comparison of these two different power densities underlined the more similar characteristic behavior for the impact of 3.2 GW/cm^2 with the single epoxy layer by taking into account the obtained peaks at (3666, 3384, 2974 and 2901 cm^{-1}) see figure 4.25a. Hence corresponding peaks do not have a correlation for Sample F after 5.8 GW/cm^2 and Epoxy 37035A (see figure 4.25b).

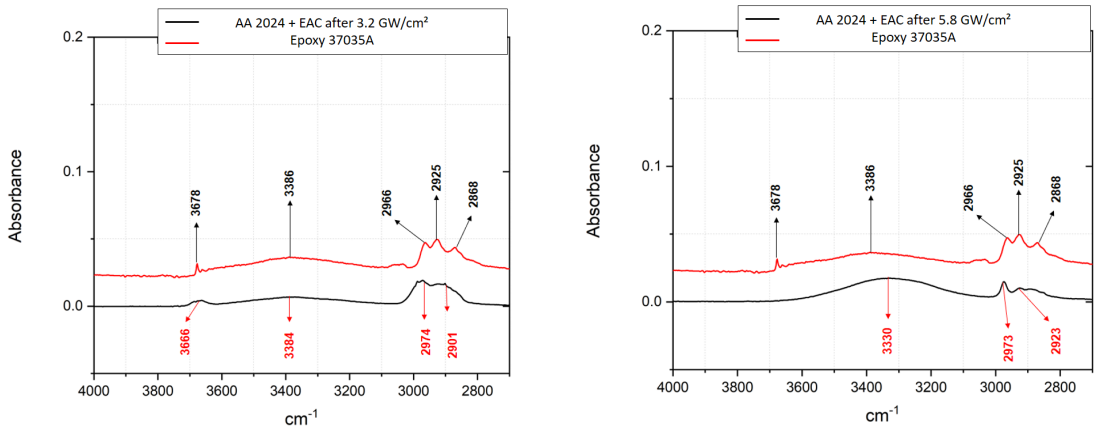

(a) FTIR Spectra for Epoxy and AA 2024-T3 CAA + EAC after 3.2 GW/cm^2 laser impact.

(b) FTIR Spectra for Epoxy and AA 2024-T3 CAA+EAC after 5.8 GW/cm^2 laser impact.

Figure 4.25: Comparison of FTIR Spectras.

4.3.2 CFRP + External Aircraft Coatings

The figure 4.26 represents the layer configurations and thicknesses with respect to each layer. For composite samples, laser impacts are applied from the composite side of specimens to evaluate laser adhesion levels. The used specimen consists of a composite base, structural epoxy primer (40 μm), external epoxy primer (25 μm) with base (56 μm) and clear coat (44 μm).

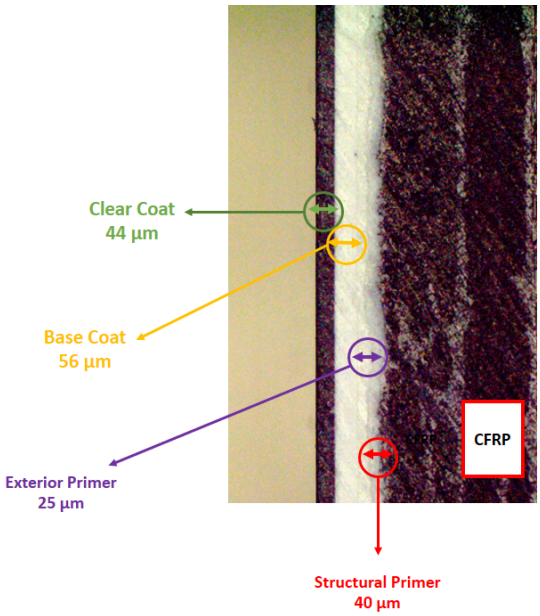

Figure 4.26: CFRP + external aircraft coatings with their respective thickness.

After applied laser impacts, stripping threshold is found as 1.5 GW/cm^2 for 2.35 mm thick of CFRP material. After obtained threshold value, power density is increased to see the adhesion levels of external aircraft coatings with respect to applied power density values which are 1.11 GW/cm^2, 3.23 GW/cm^2 and 6.71 GW/cm^2 (see figure 4.27).

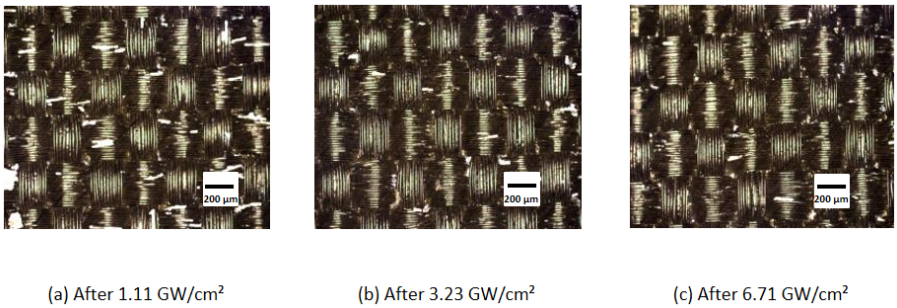

Figure 4.27: CFRP based sample after applied laser impacts at 1.11 GW/cm^2, 3.23 GW/cm^2 and 6.71 GW/cm^2 with their corresponding microscope images, respectively.

With the increased power density, paint removal is increased as one can see qualitatively from figure 4.27 by tracking the white spots. Since the main focus was aluminum

based substrates, no further deeper analysis have been performed on these specimens.

4.4 Effect of Thermal Ageing

During the time spent in the air, the external parts of the aircraft suffer damage. With temperatures ranging from -55 to 120°C in the air, thermal ageing phenomena leads to a failure [10].

The stripping process was already studied for virgin (unaged) coatings but the effect of ageing on the stripping process is a grey zone due to the mechanical and/or chemical changes with the induced thermal ageing. Aluminum plates (AA 2024 - T3) coated with cross-linked epoxy have been investigated as shown in figure 4.4, previously. The chemical and physical characteristics of the epoxy network are analyzed by Fourier Transform InfraRed (FTIR) spectroscopy. The work was conducted at high temperature, 120 °C, to further examine the behavior of the material under extreme conditions. This temperature has been used to obtain fast ageing conditions as it is conducted above the glass transition temperature of the network. After the samples have been aged for 3 weeks at 120 °C, the laser shock impacts have been applied on them. These experiments were carried out on the aluminum side to avoid creating epoxy ablation. Same approach is used as before with the variation of the applied power density to determine the epoxy removal threshold within the material if it occurs and adhesion levels. Eventually, laser adhesion tests coupled with physico-chemical analysis.

4.4.1 Physico-Chemical Analysis

During the ageing stages, several absorption spectras are obtained. These will be analyzed in detail and will allow us to determine the structural changes in the epoxy network that take place. When epoxy resin networks undergo a temperature increase, the major changes observed are the formation of carbonyl and amide products.

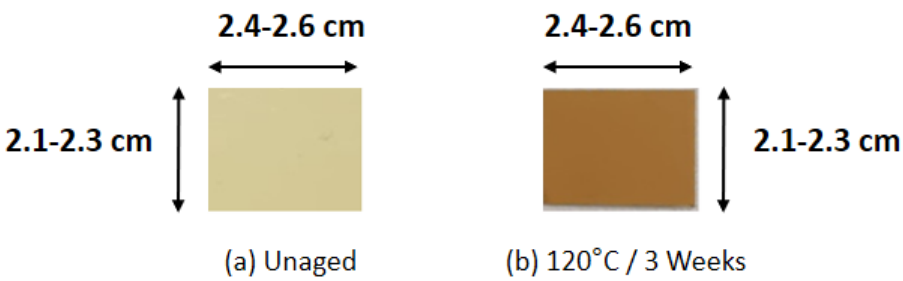

Figure 4.28: Aged and non-aged samples with a change in color observed with ageing.

The FTIR analyses therefore start at t=0, they will serve as a reference for detecting possible changes and are continued until oxidation has taken place on the plates and

films. This phenomenon can also be observed by the naked eye with the change in colour as the epoxy turns increasingly brown as can be seen in figure 4.28 (for simplicity, the samples named as Unag (for the unaged ones) and Ag(for the aged specimens)). These samples are prepared using the cut-off machine (size of 2.1 to 2.6 cm). After analysis of the spectra, the significant changes observed are those around the bands at 1720 cm^{-1} and 1650 cm^{-1}. These are the characteristic of carbonyl and amide functions respectively. The consumption of OH (around 3000-3600 cm^{-1}) is an evidence of the destruction of the hydroxypropylether group and the appearance of various species (carbonyls, amides) in the 1600-1800 cm^{-1} region (see figure 4.29) [153].

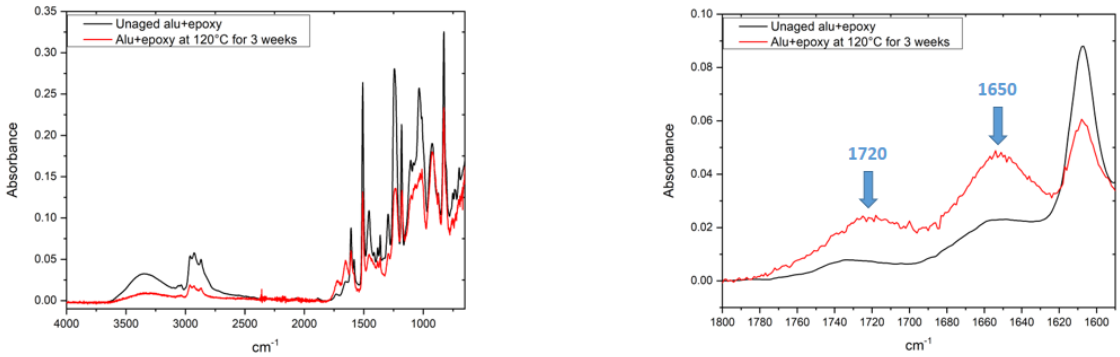

(a) FTIR Analysis for AA 2024 + Epoxy

(b) Close up to FTIR Analysis for AA 2024 + Epoxy

Figure 4.29: FTIR Analysis for AA 2024-T3+Epoxy.

In addition to FTIR measurements, DSC analysis has been performed as well. The aim was to observe the evolution of the Tg (glass transition temperature) during ageing as it is related to its node number indirectly. The DiMarzio relation (equation 4.1) considers the parameter n which depends on this number. From this principle, it is possible to know the behaviour of the polymer chain without knowing its exact composition. Indeed, there are different factors of structural modifications caused by ageing, such as the modification of the chain rigidity, the chain cuts and the cross-linkings.

$$T_g = \frac{T_{gl}}{1 - k \times F \times n} \tag{4.1}$$

where T_{gl} is the glass transition of the corresponding « virtual » linear polymer , k is a universal constant, F is flexibility factor (g mol^{-1}), n is cross-linking density (g mol^{-1}) [154]. By measuring the Tg via DSC, it is possible to determine whether the number of cross-links increases or decreases with ageing. The values are given in figure 4.30 for non-aged plates and aged at 120°C for 3 weeks. It is thus found that the longer the plates are kept in the oven, Tg decreases more. It can be concluded that the number of cross-links decreases within the epoxy network with the ageing.

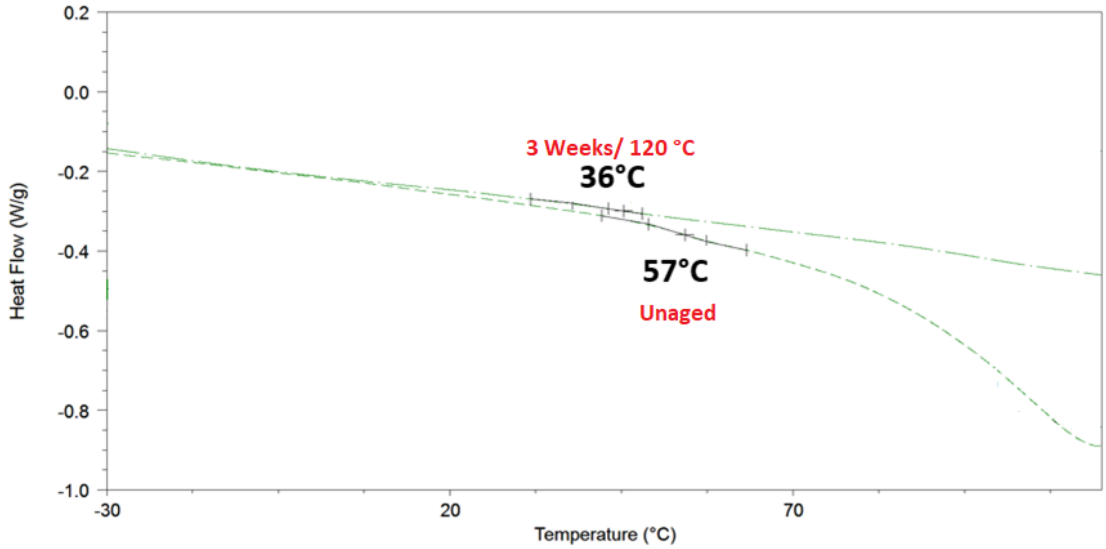

Figure 4.30: DSC results for AA 2024-T3+Epoxy Primer sample.

Samples are also analyzed by TGA to check the remaining quantity of the epoxy which is deposited on the aluminum substrate. The results represented in figure 4.31 show that with thermal ageing, epoxy on the aluminium substrate decreases (from 1.336% to 0.688% at 120°C). Hence the longer the ageing lasts, less epoxy material remains on the plate. This could be due to oxidation and evaporation of degraded parts. Hence the mass of aluminum itself remains constant and the mass of the light thin layer of epoxy is decreased, very low mass loss is observed

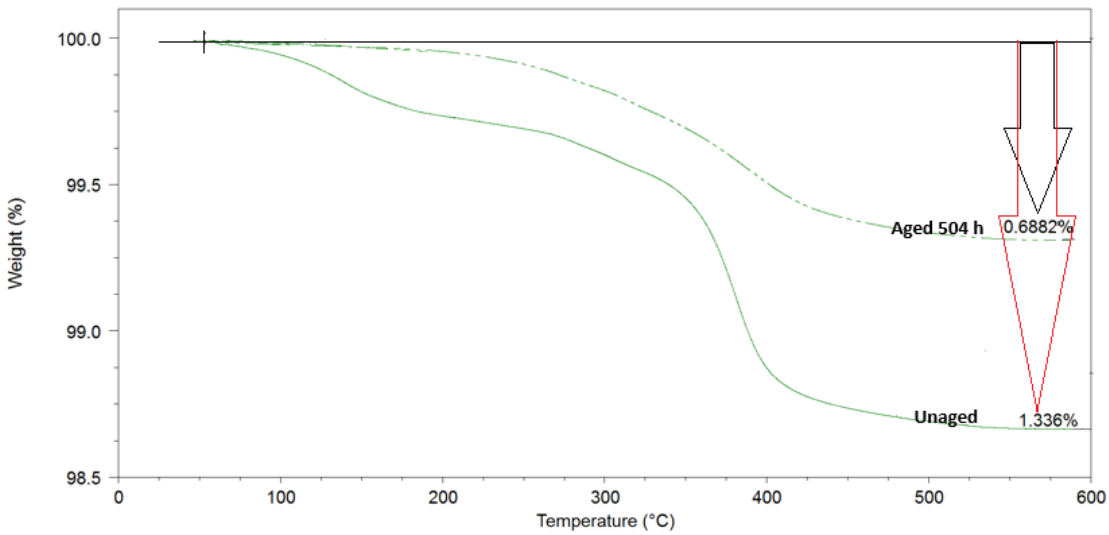

Figure 4.31: TGA results for AA 2024-T3 + Epoxy Primer sample.

4.4.2 Laser Adhesion Tests and Post-Mortem Analysis

After removal from the oven, the AA 2024+Epoxy samples were used for laser shooting. The unaged plate was the first to be tested as a reference. In order to have as few factors as possible influencing the level of stripping and adhesion, all samples had a 43 μm thick epoxy layer, sample B, (as explained in subsection 4.1.1) for the thermal ageing experiments.

All samples were tested to see the effect of thermal ageing and adhesion level changes. In the beginning, threshold determination (the lowest value that complete epoxy stripping occurred) was made for each type of sample as function of power density. Figure 4.32 shows the different responses of the plates as a function of the applied power density. Images of each shots were analyzed using an optical microscope to have a more clear view and also to calculate the diameter of the stripped spot created by the shot. For the case of the non-aged plate, the exfoliation condition was not present and there was a direct threshold followed by a complete stripping afterwards. On the contrary, for the aged plate, an exfoliation state was present before the threshold. By increasing the power density, a complete stripping followed.

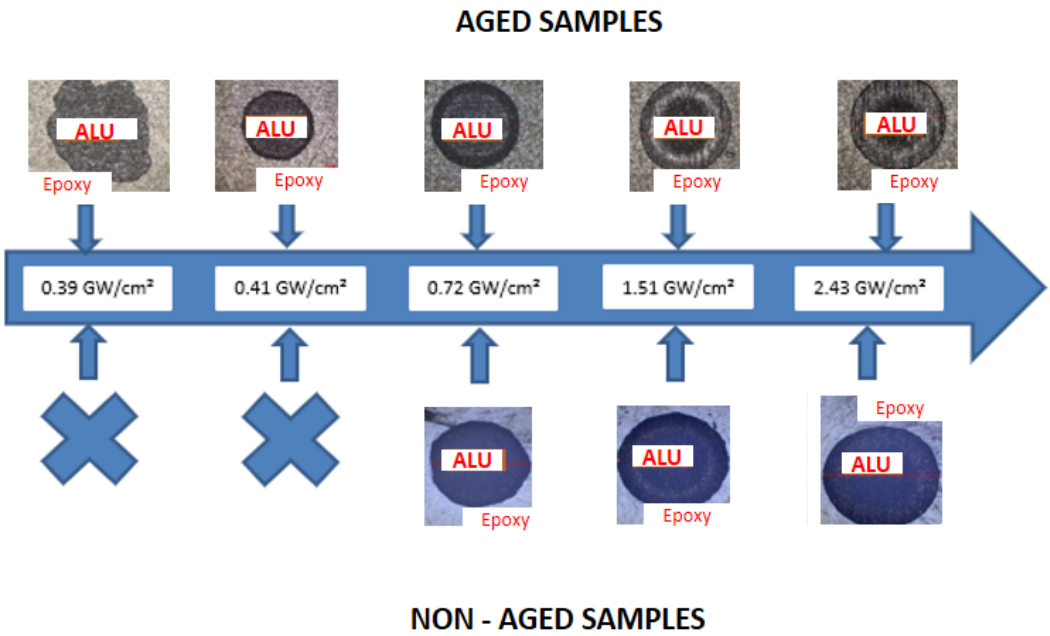

Figure 4.32: Comparison of applied laser impacts on Aged (120°C for 3 weeks) and Non aged Samples.

Chemical changes were observed due to the thermal oxidation of the epoxy network constituting the coating. This chemical degradation results in chain scissions, disappearance of hydroxyl isopropyl ether groups and mass loss [10]. Therefore, different thresholds were obtained with the laser shots, the higher the ageing the easier it was to strip the paint. This provides a basis for further experiments and understanding what

happens at the layer level.

4.4.3 Numerical Analysis and Validation

In literature, limited work has covered the elastic modulus of thermally aged epoxys. These works used static tensile testing, compresion testing and 3-point bending methods for determining Young's modulus of epoxy. Even though it is not possible to have a conclusive results on the effect of ageing on epoxys, it is clear that there is an induced effect due to thermal ageing on the elastic and/or shear modulus of the epoxys from these studies. In addition, different changes can be obtained at several ageing conditions in comparison with the literature [155].

In order to better understand the mechanical changes due to induced thermal ageing, experimental set up (VISAR) is used to compare velocity-time signals for non-aged samples at the applied power density of 0.43 GW/cm^2 at Monarque facility. The applied laser impacts for these specimens were from the epoxy sides of the targets. Aluminum of 5-8 μm is coated from epoxy side of specimens to reduce the ablation affects on epoxy. Simulation is done by neglecting this aluminum layer, just by taking into consideration of epoxy and aluminum substrate as shown in figure 4.33.

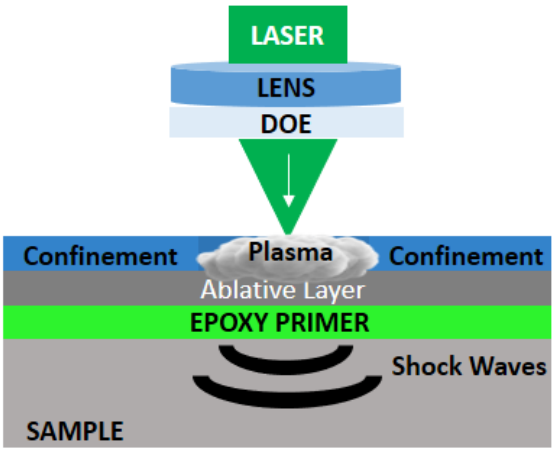

Figure 4.33: Impact configuration for validation tests.

After obtaining velocity-time curves (see figure 4.36), stress extraction at the epoxy-aluminum interface has been done. Material models for AA 2024 -T3 and epoxy have been used as explained previously in the section 2.5.2. In order to fit the experimental and simulation curves, shear modulus parameter has been optimized, numerically which is related with the elastic modulus obtained by intendation curves.

The results of the micro-indentation represented by the figure 4.34. The figure shows that the longer the plates are kept in the oven, more the Young's modulus increases.

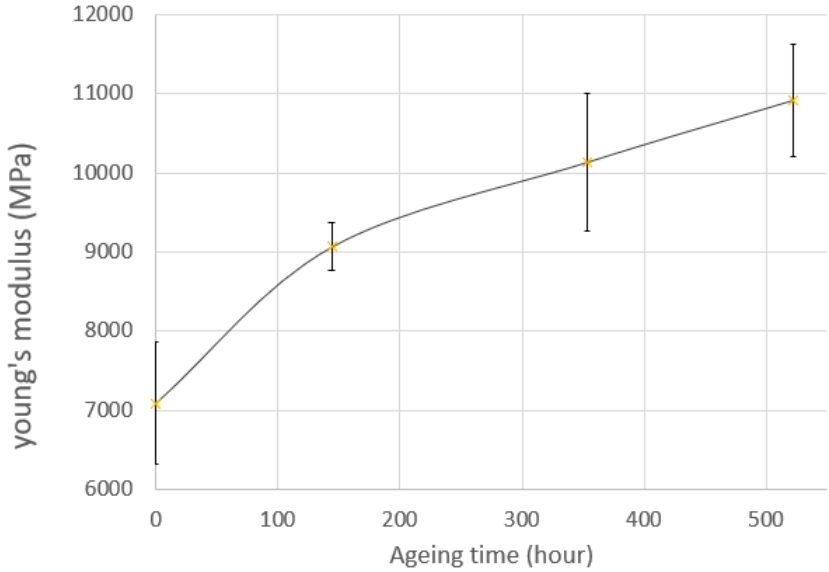

Figure 4.34: Evolution of Young's modulus as function of ageing time.

Also, we noticed that the Young's modulus curve as function of ageing time increases linearly with the change in the slope at 150 hours. For the first part of the linearity on the curve, the increase in Young's modulus could be due to the evaporation of the unreacted molecules that are trapped in the material, which can serve as a plasticizer in the system. The second linear line could be explained by the decrease of the sub-glassy relaxation β. Indeed, these relaxations are related to the local molecular motions [156] that characterize all epoxy–amine networks, mainly observed in motions of the hydroxylpropylether units [157]. After oxidation in the air, with the increase of the oxidation time, the amplitude of the β relaxation decreases due to the oxidation of the alcohol group, which plays a key role through hydrogen bonding. Hence the Young's modulus of epoxy increase. This phenomena of increase in the the Young's modulus can be called as internal antiplasticization [158] as it is presented in the Figure 4.35 which is found in the literature with $T_1 = T_\beta$ and $T_2 = T_g$.

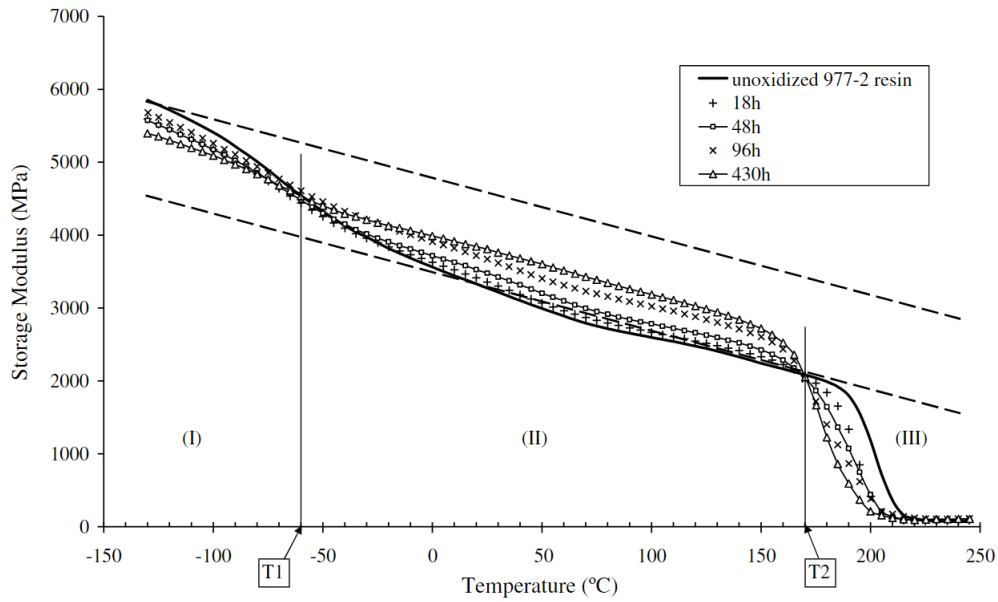

Figure 4.35: Flexural storage modulus (1Hz) against temperature for the unoxidized and aged samples [158].

To conclude, the main change due to ageing was the appearance of oxidation products, the evaporation of the unreacted molecules (in particular diluent) and the chain scisson of polymer with the evaporation of degraded parts and finally the increase of Young's modulus.

As known, the relation between the elastic modulus and the shear modulus is as follows [159]:

$$G = \frac{E}{2(1+\nu)} \tag{4.2}$$

where G is the shear modulus, E is the elastic modulus (obtained experimentally), ν is the Poisson ratio which is taken as 0.4 for the epoxy.

For non-aged specimen, the elastic modulus is found as 7 GPa and shear modulus is calculated as 2.5 GPa from the equation 4.2.

Feeding the numerical model with the calculated shear modulus, figure 4.36 is obtained. By coupling experiments and numerical work, good correlations have been observed for the first peak and the period of the signals.

In addition to theoretical relation between the glass temperature and the elastic modulus, conducted measurements via nano-intendation tool give a higher elastic modulus for the aged specimen in comparison with the non-aged one as shown in figure 4.34. Elastic modulus found approximately as 10 GPa for the aged specimen and shear modulus is calculated as 3.57 GPa.

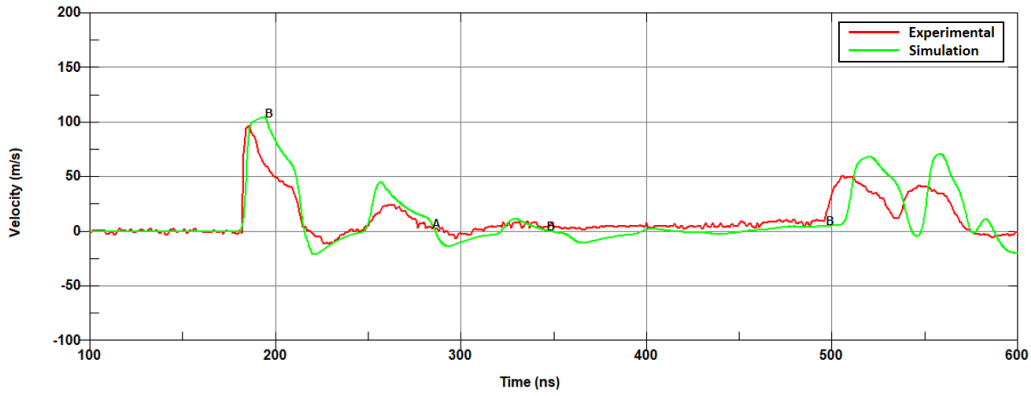

Figure 4.36: VISAR signals and numerical comparison of back face velocities for non-aged samples.

By using the the calculated shear modulus, axial tensile stresses at the epoxy-aluminum interface have been extracted. From the calculated stresses, no significant difference is obtained between aged and non aged specimens (see figure 4.37). As a conclusion of this set of study, it can be said that the created adhesion level differences observed by laser adhesion tests for these specimens are due to chemical changes created by thermal ageing within the aluminum-epoxy interface which might be caused by intermolecular and inter-atomic interactions that take place.

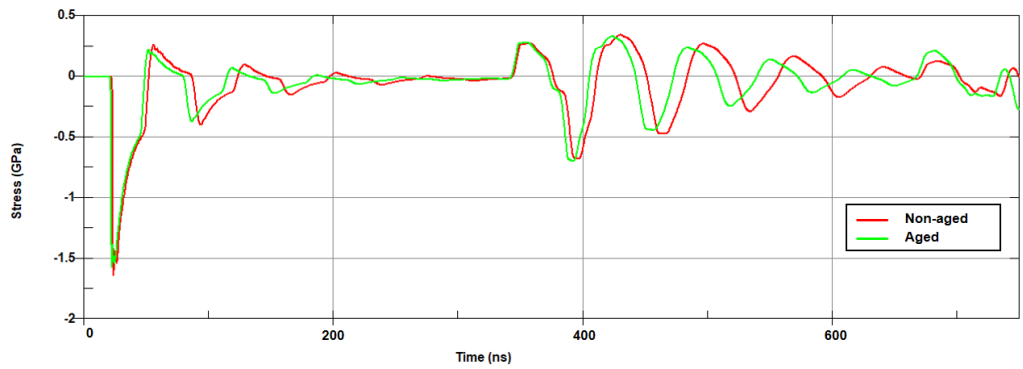

Figure 4.37: Stress distribution along the epoxy-aluminum interface.

In order to deeper investigate that phenomena, as Bouchet *et al.* explained, 3-layer approach can be useful which includes a real interphase between the organic coating and the substrate [160]. The detailed study might be conducted to analyze both mechanical and chemical properties of aluminum/created interface and epoxy/created interface to have a clearer picture for the procedure. In addition, the effect of thermal ageing should be analysed not just on epoxy but also on aluminum to have a conclusive approach.

Conclusion

Adhesion relations are examined to investigate the sensitivity of the laser paint adhesion tests according to layer thickness, substrate thickness, surface treatment, type of coated layer, substrate type and effect of thermal ageing.

AA 2024 - T3 + Epoxy configuration is studied for different epoxy thicknesses. For 25 μm thick epoxy (sample A), the damage ring phenomena is observed. In order to understand the physical phenomena behind the damage ring for AA 2024 - T3 + Epoxy configuration, experimental and numerical work is coupled. Numerical model is verified via VISAR signal and then maximum axial tensile stresses are extracted both at the edge and at the center of the specimens. For sample A, the maximum axial stress is inversely proportional with the applied power density which is in a good correlation with the observed stripping patterns, experimentally. Debonding ranges as function of tensile stress are: for sample A it's in between 219-308 MPa, for sample B it's around 296-355 and for sample C it's about 260-333 MPa. The common debonding/threshold window can be defined as 260-309 MPa for the all three specimens.

For the AA 2024 - T3 + Epoxy + Top Coat configuration, increasing power density enables us to strip higher thicknesses. In addition, for all sample types, after laser stripping operations, there is a remaining coating which ensures the front face substrate health after laser stripping operations.

For AL-Li 2060 T8 E30 + External coatings, the effect of different surface treatments are investigated. It can be concluded that, created adhesion levels with the sol-gel surface treatment is weaker than the thin film sulphuric acid anodized ones according to obtained stripping threshold values. This finding is in a good agreement with the literature. The results suggest that the target with a sol-gel treatment has a poorer adhesion level than the one with a thin film sulphuric acid anodized. Many studies in the literature show that sol-gel technique leads to a somewhat lower evaluation due to the incompatibility between the treatment and the primer layer bonding, and this could contribute to lower durability [161].

For AA 2024 - T3 + External Aircraft Coatings, selective paint removal and adhesion relations in between different layers are investigated both via laser and physico-chemical characterization at applied different power densities. Same approach is applied for CFRP + External aircraft coatings. However, for this type of specimens, paint removal and adhesion levels observed qualitatively since the main focus is the aluminum based substrates.

Finally, the thermal ageing phenomena is investigated via numerical simulation of shock wave propagation into an aluminum/epoxy specimen. For thermal ageing simulations, the axial stress values at the epoxy/aluminum interfaces are found almost the same for both aged and non-aged specimens. It is concluded that the created different adhesion levels for aged and non-aged specimens are due to the chemical reactions. To deeper investigate this phenomena, created interface can be taken as a third layer in between aluminum and epoxy. Another proposition as a future work is also the observation/analysis of thermal ageing on aluminum substrate itself to distinguish the caused effects by epoxy layer.

By coupling experimental and numerical work, laser adhesion and paint stripping technology can be optimized. Especially, when the numerical work fed with the actual material properties, it is a promising contribution for future work that seeks to optimize the laser paint adhesion test and to conduct virtual testing.

Conclusion FR

Les relations d'adhésion sont examinées pour étudier la sensibilité des essais d'adhésion de la peinture au laser en fonction de l'épaisseur de la couche, de l'épaisseur du substrat, du traitement de surface, du type de couche appliquée, du type de substrat et de l'effet du vieillissement thermique.

La configuration AA 2024 - T3 + Epoxy est étudiée pour différentes épaisseurs d'époxy. Pour une épaisseur d'époxy de 25 µm (échantillon A), le phénomène d'anneau d'endommagement est observé. Afin de comprendre les phénomènes physiques à l'origine de l'anneau d'endommagement pour la configuration AA 2024 - T3 + Epoxy, des travaux expérimentaux et numériques sont couplés. Le modèle numérique est vérifié par le signal VISAR, puis les contraintes de traction axiale maximales sont extraites à la fois au bord et au centre des échantillons. Pour l'échantillon A, la contrainte axiale maximale est inversement proportionnelle à la densité de puissance appliquée. A partir des valeurs seuils de decapage obtenues en fonction de la contrainte de traction sont les suivantes : pour l'échantillon A, elles se situent entre 219 et 308 MPa, pour l'échantillon B, entre 296 et 355 et pour l'échantillon C, entre 260 et 333 MPa. La fenêtre commune de décollement/seuil peut être définie comme 260-309 MPa pour les trois échantillons.

Pour la configuration AA 2024 - T3 + Epoxy + Top Coat, l'augmentation de la densité de puissance nous permet de décaper des épaisseurs plus importantes. En outre, pour tous les types d'échantillons, après les opérations de décapage au laser, il reste un revêtement qui garantit la santé du substrat de la face avant après le décapage.

Pour AL-Li 2060 T8 E30 + revêtements externes, l'effet de différents traitements de surface a été étudié. Il peut être conclu que les niveaux d'adhésion créés avec le traitement de surface sol-gel sont plus faibles que les couches minces anodisées à l'acide sulfurique selon les valeurs de seuil de décapage obtenues. Ce résultat est en bon accord avec la littérature. Les résultats suggèrent que la cible avec un traitement sol-gel a un niveau d'adhésion plus faible que celle avec un film mince anodisé à l'acide sulfurique. De nombreuses études dans la littérature montrent que la technique sol-gel conduit à une évaluation un peu plus faible en raison de l'incompatibilité entre le traitement et l'adhérence de la couche d'apprêt, ce qui pourrait contribuer à une durabilité plus faible [161].

Pour le AA 2024 - T3 + revêtements extérieurs d'aéronefs, l'enlèvement sélectif de la peinture et les relations d'adhésion entre les différentes couches sont étudiés à la fois par laser et par caractérisation physico-chimique à différentes densités de puissance appliquées. La même approche est appliquée pour le CFRP + revêtements externes d'avion. Cependant, pour ce type de spécimens, l'enlèvement de la peinture et les niveaux

d'adhésion sont observés de manière qualitative puisque l'accent est mis sur les substrats à base d'aluminium.

Enfin, le phénomène de vieillissement thermique est étudié via la simulation numérique de la propagation d'une onde de choc dans une éprouvette en aluminium/époxy. Pour les simulations de vieillissement thermique, les valeurs de contrainte axiale aux interfaces époxy/aluminium sont presque les mêmes pour les spécimens vieillis et non vieillis. Il est conclu que les différents niveaux d'adhésion créés pour les spécimens vieillis et non vieillis sont dus aux réactions chimiques. Pour approfondir ce phénomène, l'interface créée peut être considérée comme une troisième couche entre l'aluminium et l'époxy. Une autre proposition de travail futur est également l'observation/analyse du vieillissement thermique sur le substrat d'aluminium lui-même pour distinguer les effets causés par la couche d'époxy.

En couplant le travail expérimental et numérique, la technologie d'adhésion et de décapage au laser peut être optimisée. En particulier, lorsque le travail numérique est alimenté par les propriétés réelles des matériaux, il s'agit d'une contribution prometteuse pour les travaux futurs qui visent à optimiser le test d'adhésion de la peinture au laser et à effectuer des tests virtuels.

5

Development of Laser Paint Stripping

Introduction

This chapter begins by recapping the stripping capabilities from the substrate side as explained by the end of the previous chapter. Then, laser paint stripping rates for different laser technologies from the substrate side of specimens via mono impact is investigated and evaluated as function of different base materials (AA 2024 and CFRP). The second section consists of validation and development of laser paint stripping optimization from the paint side of the specimens via mono impact. The subject parameter for the optimization is the glue thickness within the tape where the effect is investigated in order to create the stripping pattern by having a lower applied power density. Finally, the third part reports results on the large stripped zones and post-mortem analysis with a natural salt spray test on the same specimens.

Introduction FR

Ce chapitre commence par un rappel des capacités de décapage du côté du substrat, comme expliqué à la fin du chapitre précédent. Ensuite, les taux de décapage de la peinture au laser pour différentes technologies laser du côté du substrat des spécimens par mono impact sont étudiés et évalués en fonction de différents matériaux de base (AA 2024 et CFRP). La deuxième section consiste en un développement de l'optimisation du décapage laser du côté de la peinture des spécimens par un impact unique. Le paramètre sujet à l'optimisation est l'épaisseur de l'adhésif dans le ruban où l'effet est étudié afin de créer le motif de décapage en ayant une densité de puissance appliquée plus faible. Enfin, la troisième partie présente des résultats sur les grandes zones décapées et une analyse post-mortem avec un essai au brouillard salin naturel sur les mêmes spécimens.

Discussion for the Parameter Window

All the samples explained are categorized as different layer configurations, the specimens' thickness/ surface treatment, substrate type and thermal ageing. The parameters for complete stripping are defined as function of power density range as seen in table 5.1 and previously found in Chapter 4. As explained, all the laser impacts were applied from the substrate side for these configurations.

CONFIGURATION	SPECIMEN & THICKNESSES	POWER DENSITY RANGE (GW/cm²) for STRIPPING
LAYER THICKNESS AA 2024: 970 µm CE: Chemical Etching (≈ 5 µm)	Epoxy Primer Chemical Etching AA 2024-T3 AA 2024 + Primer Top Coat Epoxy Primer Chemical Etching AA 2024-T3 AA 2024 + Primer + Top Coat	AA 2024 + Primer • Sample A (25 µm) - 0.5 GW/cm² • Sample B (43 µm) - 0.7 GW/cm² • Sample C (56 µm) - 0.9 GW/cm² AA 2024 + Primer + Top Coat • Sample 1 (Primer: 25 µm, Top Coat: 26.8 µm) 0.9 GW/cm² • Sample 2 (Primer: 28 µm, Top Coat: 19 µm) 0.7 GW/cm² • Sample 3 (Primer: 23 µm, Top Coat: 122.6 µm) 2.7 GW/cm²
SPECIMEN THICKNESS & SURFACE TREATMENT AA 2024: 970 µm AA 2024: 800 µm AL-Li: 2.5 mm TFSAA: Thin Film Sulphuric Acid Anodization	Epoxy Primer Surface Treatment AA 2024-T3 AA 2024 + Primer Top Coat Epoxy Primer Sol Gel AA 2024-T3 AL-Li –Sol Gel Top Coat Epoxy Primer TFSAA AA 2024-T3 AL-Li –TFSAA	AA 2024 + Primer • Sample D (AA 2024: 800 µm, Primer: 28 µm) - 1.75 GW/cm² - Surface Treatment: Chromic Acid Anodization • Sample E (AA 2024: 970 µm, Primer: 28 µm) - 0.6 GW/cm² - Surface Treatment: Chemical Etching AL-Li + Primer + Top Coat • Sample S (Sol-Gel) 0.6 GW/cm² • Sample M (TFSAA) 0.8 GW/cm²
SUBSTRATE TYPE AA 2024: 970 µm CFRP: 2.5 mm CAA: Chromic Acid Anodization	Clear Coat Base Coat Epoxy Primer 2 Epoxy Primer 1 CAA AA 2024-T3 AA 2024 + EAC Clear Coat Base Coat Epoxy Primer 2 Epoxy Primer 1 CFRP CFRP + EAC	AA 2024 + External Aircraft Coatings (EAC): 2.77 GW/cm² CFRP+ External Aircraft Coatings (EAC): 1.5 GW/cm²
THERMAL AGEING AA 2024: 970 µm CE: Chemical Etching (≈ 5 µm)	Epoxy Primer Chemical Etching AA 2024-T3 AA 2024 + Primer	AA 2024 + Primer (43 µm) Non-aged: 0.72 GW/cm² Aged: 0.4 GW/cm²

Table 5.1: Summary of paint stripping parameters as function of different configurations.

For sample A, B and C different epoxy thicknesses are studied for the same base material (AA 2024). The found complete stripping values are 0.5, 0.7 and 0.9 GW/cm^2, respectively. After, the effect of top coat thickness is investigated for AA 2024 + Epoxy Primer + Polyurethane Top Coat configuration. With the increase of the top coat thickness, stripping threshold becomes higher.

The effect of specimen thickness and the surface treatment on AA 2024 + Epoxy specimens are observed. The sample of an AA 2024 (800 μm) base with a chromic acid anodization surface treatment has a higher stripping threshold (1.75 GW/cm^2) than the one of an AA 2024 (970 μm) with a chemical etching surface treatment. In addition, AL-Li specimens are investigated with different surface treatments but with the same primer + top coat configuration. Specimens have two different surface treatments: sol gel and thin film sulphuric acid anodization. The one with the sol-gel surface treatment has lower stripping threshold (0.6 GW/cm^2) than the one with the thin film sulphuric acid anodization (0.8 GW/cm^2).

AA 2024 and CFRP based specimens are compared as well to have a general view of the procedure. The results show that the stripping threshold for AA 2024 + EAC is around 2.77 GW/cm^2 and for CFRP + EAC is around 1.5 GW/cm^2.

Finally, thermal ageing effect is studied on AA 2024 (970 μm) + Epoxy primer specimens with a chemical etching surface treatments. The stripping values are found as 0.72 GW/cm^2 for the non-aged one and 0.4 GW/cm^2 for the aged one at 120 °C for 3 weeks.

Figure 5.1 is a collection of the data represented previously in table 5.1. It can be seen that obtaining a common process range/window for the stripping as function of all different parameters is challenging. However, as seen, by re-grouping some specimens, common process ranges might be created. For example, for the samples which are named as A, B, 1, E, S, Ag (aged AA 2024+epoxy as explained in section 4.4), Unag (unaged as in section 4.4) and M, the common stripping window is in between 0.8-0.9 GW/cm^2. On the other hand, for A, B, 1, E, S, Ag, Unag, M, C, 2 and CFRP+EAC, this value is in between 1.5-1.75 GW/cm^2. For the targets of B, 1, S, Ag, Unag, M, C, 2, CFRP+EAC and D the common stripping range becomes broader as 1.75-2.28 GW/cm^2. Finally, for B, 1, S, Ag, Unag, M, C, 2, CFRP+EAC, AA+EAC and 3 the window is found within the range of 2.77-3 GW/cm^2.

Even though it is hard to obtain a common process window for all types of specimens, by re-grouping them, small windows are created. As previously noted, due to the high sensitivity of the process, this is a particular way for paint adhesion testing using laser impacts in addition to stripping applications.

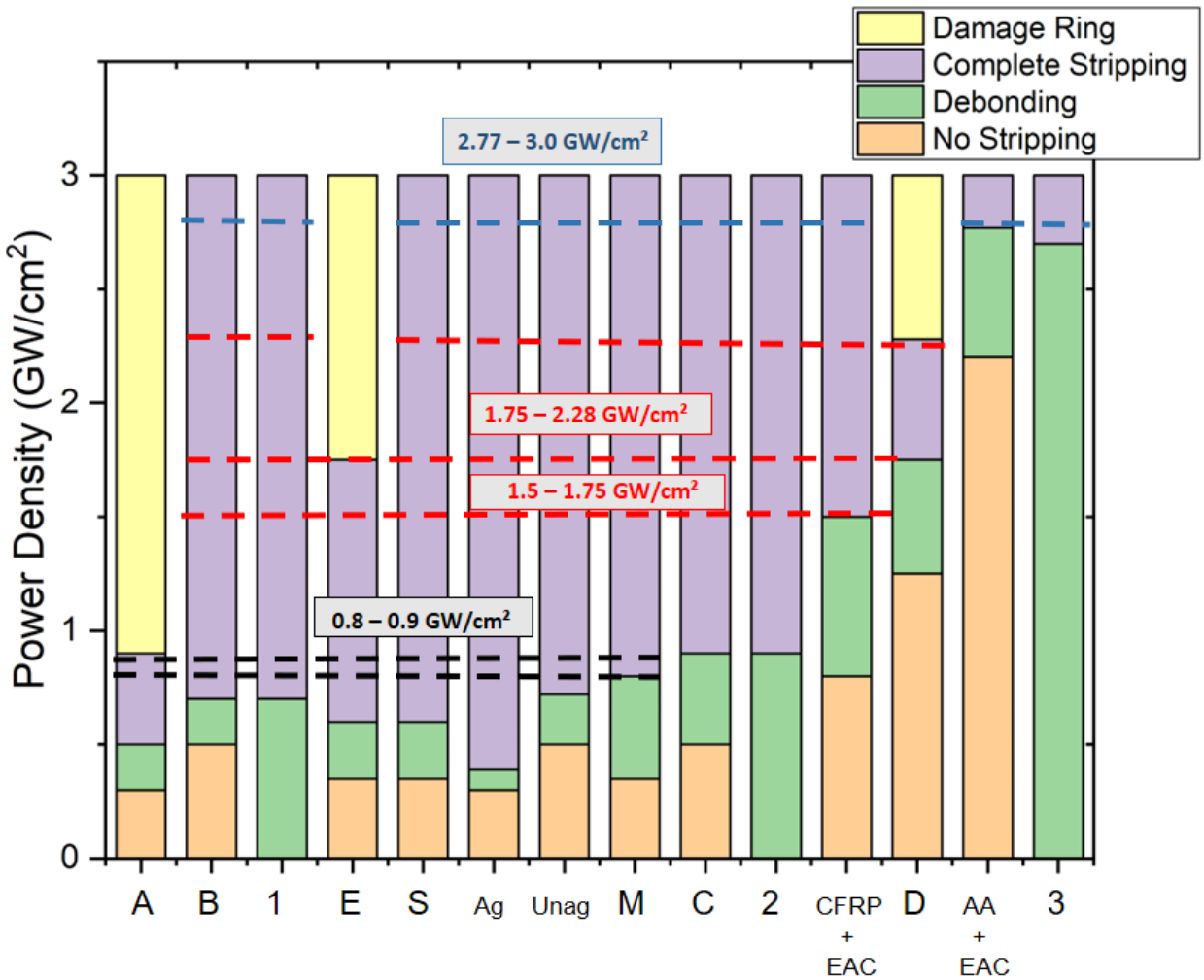

Figure 5.1: Overview of the process within different specimens.

5.1 Development of Laser Paint Stripping from the Substrate Side of Specimens via mono impact

After observing the threshold values which are where removal of the paint is absolute, stripping rate is calculated according to the following formula:

$$SR = A \times f \tag{5.1}$$

in which SR represents the stripping rate, A is the surface area which is related/extracted from the stripping threshold power density values and f is the repetition rate of the laser. All the experiments are conducted at Hephaistos facility. However, for an estimated stripping rate status at Monarque facility, same threshold power density values are used for stripping rate versus laser technology comparison.

Since there are many different specimens, the recap table is created as function of stripping rate for them all as given in table 5.2. S.R represents the stripping rate for

Hephaistos and Monarque, respectively. The used sample acronyms are the same ones as previously given in table 5.1.

Sample	S.R- Hephaistos (m^2/h)	S.R-Monarque (m^2/h)
A	2.88	7.2
B	2.05	5.14
C	1.6	4
1	1.6	4
2	2.05	5.14
3	0.53	1.33
D	0.82	2.05
E	2.4	6
S	2.4	6
M	1.8	4.5
AA + EAC	0.51	1.29
CFRP + EAC	0.95	2.39
Unag	2	5
Ag	3.6	9

Table 5.2: Stripping Rates for different laser technologies and for different specimens.

Since the AA + EAC and CFRP + EAC samples' configurations are the main target for the project, stripping rate calculation graphs are just given for them.

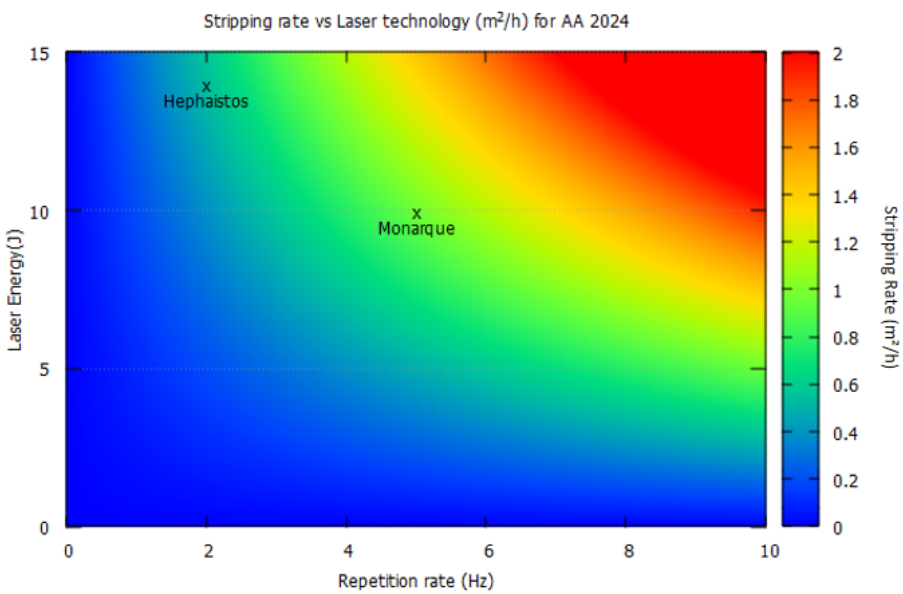

Figure 5.2: Stripping rate for AA 2024 + EAC for different laser technologies.

By using equation 5.1, stripping rate is found as 0.51 m^2/h at Hephaistos facility and estimated as 1.29 m^2/h at Monarque facility for AA 2024 + EAC specimen.

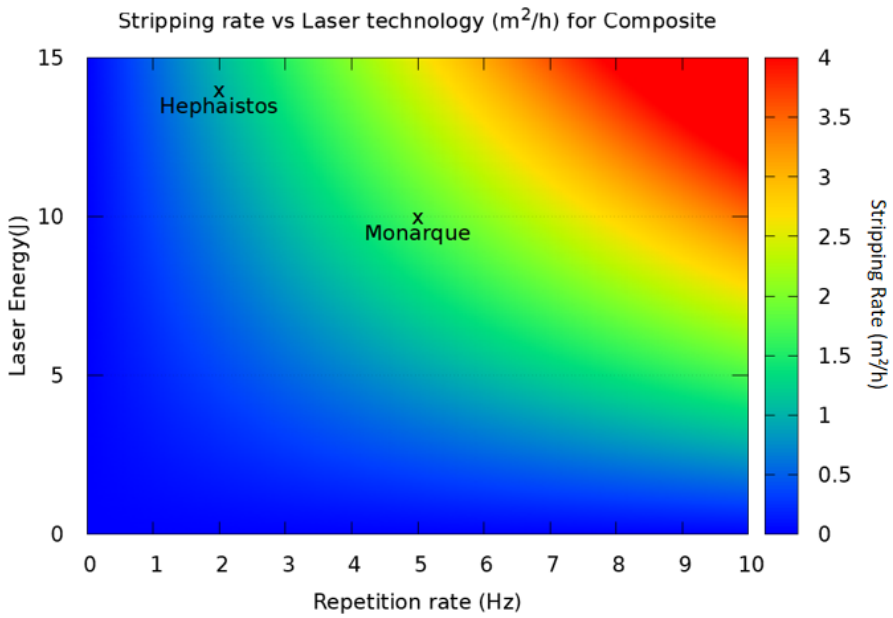

Figure 5.3: Stripping rate for CFRP + EAC for different laser technologies.

For CFRP + EAC specimen, stripping rate is calculated as 0.95 m^2/h for Hephaistos and estimated as 2.39 m^2/h for Monarque facility.

Hence the expected stripping rate is in between 0.4-1 m^2/h according to the VULCAN project's framework, obtained results are within the range at Hephaistos facility for the specimens of AA 2024 + EAC and CFRP + EAC. It can not be fully concluded for Monarque facility, since all the calculations are based on the estimated values.

5.2 Validation of Laser Paint Stripping from the Painted Side of Specimens

As discussed in chapter 3, at 3 GW/cm^2, the epoxy primer stripping is achieved as predicted by the numerical work (see figure 5.4a) for RES1 specimen. The extracted VISAR signal is coupled with the numerically obtained curve as seen in figure 5.4b. The curves are in good agreement with each other. Therefore, the stress values at different interfaces are extracted to complete the validation.

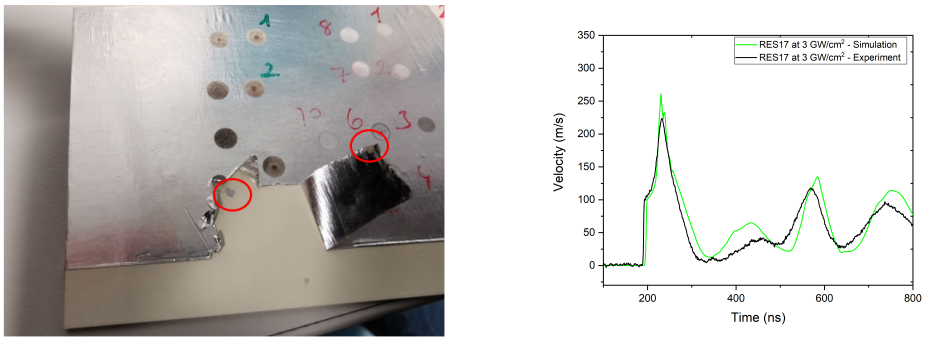

(a) Stripped Specimen

(b) Validate signal at 3 GW/cm^2.

Figure 5.4: Stripped target and validated experimental and numerical signals at 3 GW/cm^2.

According to the numerical work, $\sigma_{yy,glue}$ (MPa) and $\sigma_{yy,epoxy}$ are extracted. $\sigma_{yy,glue}$ is found as 147 MPa (< 165) which is lower than the glue delamination. Moreover, $\sigma_{yy,epoxy}$ is found as 280 MPa which can be defined as the stripping threshold for this target. Figure 5.5 represents the stress values at different interfaces with a higher value of stress at the epoxy interface than the glue one.

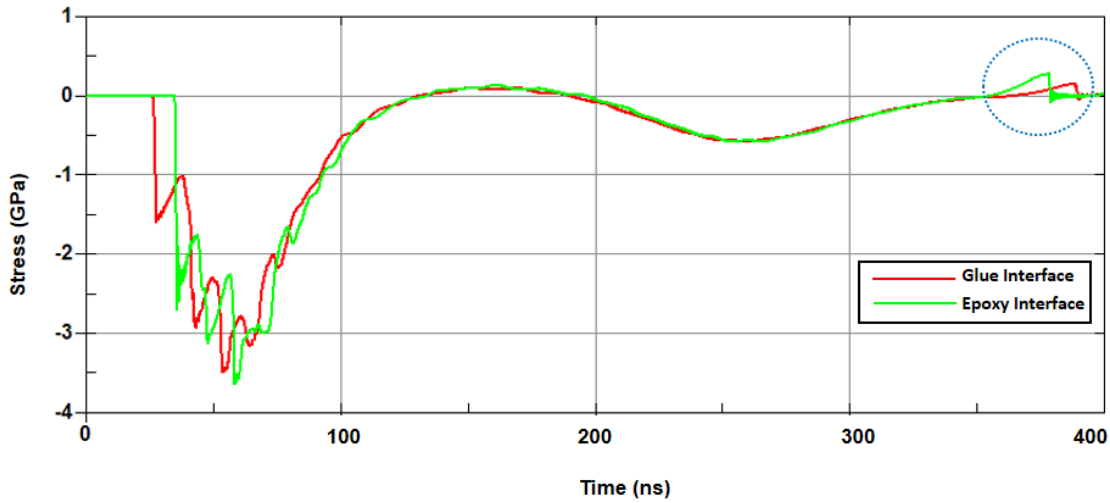

Figure 5.5: σ_{yy} values as function of time for glue and epoxy interfaces, respectively.

Since the stripped epoxy layer was attached to the glue part of the adhesive after the operation as seen in figure 5.4a, it might be an explanation for not having an glue delamination at this power density. In addition, these findings are promising approach of re-use and recycling purposes of the paint for industrial applications. In addition, these results show the capability of the numerical work for both the development and the optimization processes for the laser paint stripping applications.

5.3 Optimization of Laser Paint Stripping from the Painted Side of Specimens

For the optimization of the process, different glue thicknesses within the aluminum tape are investigated. The purpose of the study was to change the glue thickness and manage to have same stress levels required for the paint stripping at the aluminum-epoxy interface. Since thicker glue provides an attenuation of the wave, it requires the usage of higher power density. By reducing the glue thickness, this attenuation can be modified and stripping can be achieved with a lower power density. The commercial glue has a thickness of 26-30 μm. For this study, the thickness is modified, numerically, as 15 μm to optimize the procedure.

The goal was to obtain the epoxy primer stripping first and prevent to have a tape debonding from the substrate before the stripping. As previously discussed in subsection 3.2.2, the threshold of the interface bonding between the tape and the substrate is calibrated according to the numerous experiments. This threshold value is found as $\sigma_{yy_{threshold}}$ = 165 MPa.

Table 5.3 gathers the required power density for paint stripping. σ_{yy} values are extracted, numerically, for both the epoxy-aluminum substrate interface ($\sigma_{yy,epoxy}$) and glue - epoxy interface ($\sigma_{yy,glue}$) for different glue thicknesses.

Glue Thickness (μm)	Power Density (GW/cm^2)	$\sigma_{yy,glue}$ (MPa)	$\sigma_{yy,epoxy}$ (MPa)
26	3	147	280
15	1.45	166	275

Table 5.3: Required power density for paint stripping, $\sigma_{yy,epoxy}$ and $\sigma_{yy,glue}$ for sample different glue thicknesses.

At 3 GW/cm^2 for 26 μm thick glue, there is no glue delamination as demonstrated previously. The found maximum stress value at the glue-epoxy interface is 147 MPa which is lower than the threshold (165 MPa) as explained in the previous subsection. For 15 μm thick glue, at 1.45 GW/cm^2, the stress value at the epoxy interface is found as 275 MPa which is taken as stripping since it is within the range of threshold. The value for the glue-epoxy interface is found as 166 MPa that is higher than the threshold. However, the stress at the glue-epoxy interface reaches this value after epoxy stripping occurs (see figure 5.6).

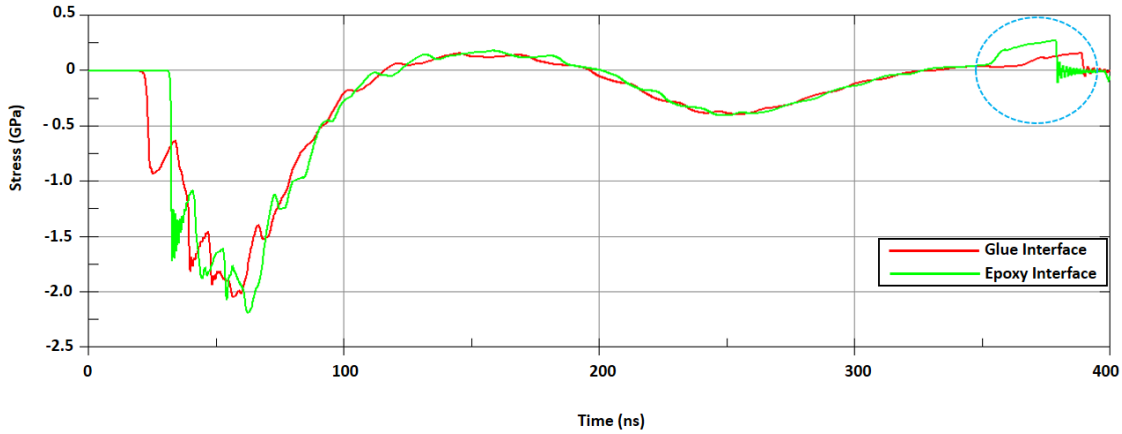

Figure 5.6: σ_{yy} values as function of time for glue and epoxy interfaces, respectively.

The findings support the possibility of the process optimization. By using thinner glue within the tape, paint stripping can be achieved with the lower power density for this specific specimen. Apart from the glue thickness, other parameters like pulse duration can be modified for the future studies hence the validated model exists.

5.4 Large Stripped Zones

Laser stripping was applied on samples with a thickness deviation of ± 10-20%. First, the stripping threshold is determined as function of power density which is the first flight off of the top coats as explained previously in 4.1.2. After obtained threshold values, same power densities were applied on specimens to create large stripping zones with a spot overlap of 20-30%.

Mono pulse laser beam was applied from the AA 2024 T3 part of the specimens with a configuration of AA 2024 T3 + Epoxy Primer + Polyurethane with a solid confinement (see Figure 5.7). Solid confinement is a double face transparent adhesive which is acrylate. Le Bras et. al. explained that it induces approximately the same pressure values as water confinement in the range of worked power densities [162].

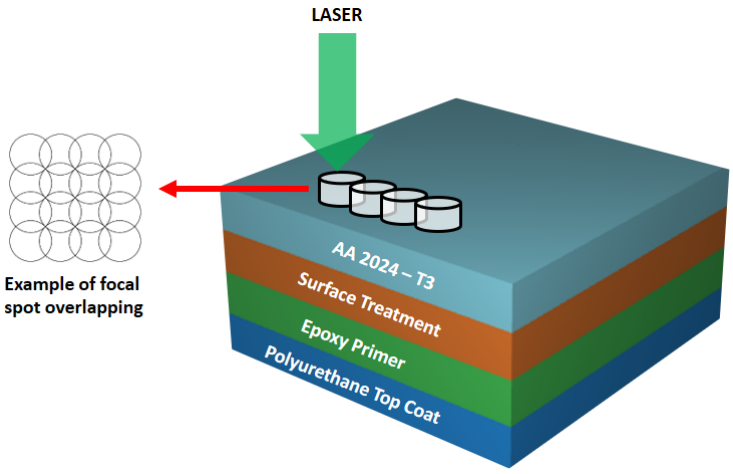

Figure 5.7: Specimen's Architecture.

In Figure 5.8, applied epoxy primer, polyurethane top-coat, the shot for stripping threshold determination and stripped zone after laser impacts are presented. The total stripped area was in the range of 5 cm x 5 cm for further additional analysis (neutral salt spray test).

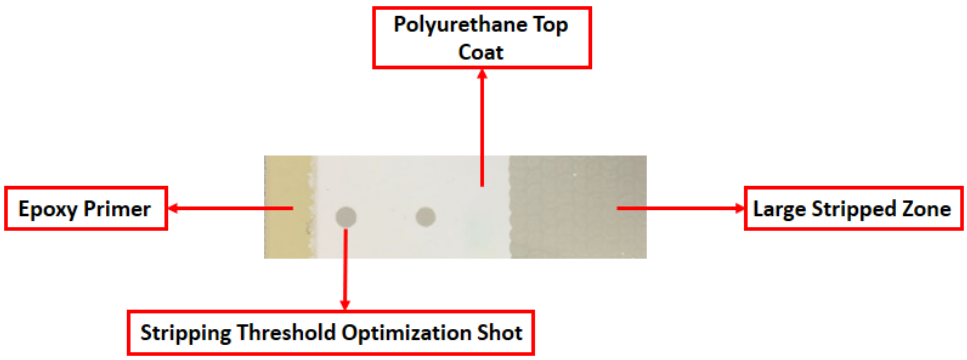

Figure 5.8: Zone Definition on sample labeled as 1 as a representative.

There is a lack of information on the epoxy primer health after applied laser impacts. In order to have an evaluation about the epoxy primer status for the corrosion resistance, neutral salt spray test has been applied. The coating properties were investigated as function of adhesion levels and anticorrosion properties. These tests are carried out by RESCOLL, Pessac, France. The tests are based on the immersing samples in deionized water (50g/L NaCl) for 14 days at the ambient temperature. The main idea was to test the resistance of the coating to the water immersion.

Aluminum and its alloys are widely used in the aeronautics industry. However, they end up having pitting corrosion easily in some solutions such as NaCI like in our case. In order to have an anti-corrosion properties, for aircraft applications, epoxy has been used for many years [163]. Apart from investigating corrosion properties of AA 2024-T3, this test might also give information about adhesion levels between anti-corrosive primer and

aluminium, qualitatively.

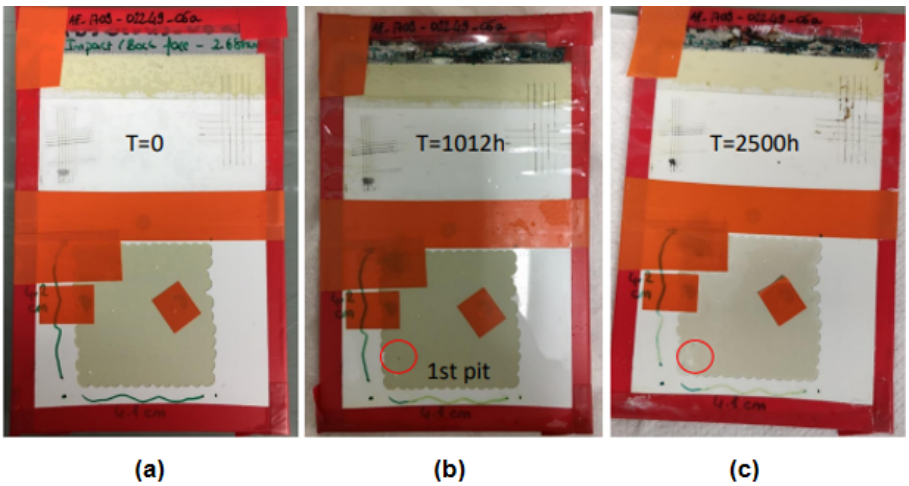

Figure 5.9: Neutral Salt Spray Test: (a) T = 0 (the specimen before any operation), (b) T = 1012h (the sample after 1012 hours of neutral spray application), (c) T = 2500h (the sample after 2500 hours of neutral spray application).

These tests only cover the sample labeled as 3 (as given in 4.2) since it has the highest top-coat thickness before any laser application and one of the lowest remained epoxy thickness after applied laser impacts. Figure 5.9 demonstrates the different stages of the test where T=0 represents the specimen before any neutral salt spray, T=1012h is the sample after 1012 hours of neutral salt spray application and T=2500h is the target after 2500 hours. Although a small pit creation occurs at 1012h, obtained results might be concluded as there is no significant defect created with the neutral salt spray tests (see Figure 5.9). In addition, according to this test it can be said that the primer performance is not affected by the laser shock application. For further applications, such as re-painting of aeronautical parts after laser stripping, it can be a good compromise to have a healthy primer on top of aluminum substrates with a sufficient adhesion between two.

Conclusion

This chapter has covered stripping capabilities from the substrate side, analysis of laser paint stripping rates for different laser technologies from the substrate side as well as the development of laser paint stripping optimization from the paint side of specimen and the large stripped zones.

For the stripping capabilities from the substrate side what can be concluded is that it is challenging to obtain a common process window for all type of specimens. However, by re-grouping them, small windows are created.

Stripping rates are calculated for all studied samples from the substrate side to compare the stripping rates with the laser technology. Since the AA + EAC and CFRP + EAC samples' configurations are the main target for the project, stripping rate calculation graphs are just given for them. It is concluded that the stripping rates are in the project's framework (0.4-1 m^2/h) with the laser at Hephaistos facility for the target specimens.

The validation and development of laser paint stripping from the painted side of specimens are investigated. After completing the validation, the optimization is done by lowering the glue thickness within the tape. The findings support the possibility of the process optimization. By using thinner glue within the adhesive tape, paint stripping can be achieved with the lower power density. Apart from the glue thickness, other parameters like pulse duration or pulse impact configuration can be modified for the future studies since the validated model exists.

Laser stripping was applied on samples with specified thickness and a deviation of ± 10-20%. First, the stripping threshold is determined as function of power density which is the first flight off of the top coats as explained previously in 4.1.2. After obtained threshold values, same power densities were applied on specimens to create large stripping zones with a spot overlap of 20-30%. Then, in order to gather information about the epoxy primer health for the corrosion resistance after stripping, neutral salt spray test has been applied at RESCOLL, Pessac, France. These tests just cover the sample labeled as 3 since it has the highest top-coat thickness before any laser application and one of the lowest remained epoxy thickness after applied laser impacts. Obtained results might be concluded as there is no significant created defect with the neutral salt spray tests.

Conclusion FR

Dans ce chapitre, les capacités de décapage du côté du substrat, l'analyse des taux de décapage laser pour différentes technologies laser du côté du substrat, le développement de l'optimisation du décapage laser du côté de la peinture du spécimen et les grandes zones décapées sont étudiés.

Pour les capacités de décapage du côté du substrat, on peut conclure qu'il est difficile d'obtenir une fenêtre de processus commune pour tous les types de spécimens. Cependant, en les regroupant, de petites fenêtres sont créées. Le procédé est également une approche innovante pour les tests d'adhésion de peinture via l'utilisation de laser de choc grâce à la sensibilité de la procédure.

Les taux de décapage sont calculés pour tous les échantillons étudiés du côté du substrat afin de comparer les taux de décapage avec la technologie laser. Les configurations des échantillons AA + EAC et CFRP + EAC étant la cible principale du projet, les graphiques de calcul du taux de décapage sont présentés dans le tableau ci-dessous. On peut conclure que les taux de décapage répondent aux spécifications du projet (0.4-1 m^2/h) avec le laser de l'installation Hephaistos pour les spécimens cibles.

Ensuite, le développement du décapage laser de la face peinte des spécimens est étudié. Ici, l'optimisation est réalisée en diminuant l'épaisseur de la colle dans le ruban adhésif. Les résultats obtenus confirment la possibilité d'optimiser le procédé. En utilisant une colle plus fine dans le ruban adhésif, le décapage de la peinture peut être réalisé avec une densité de puissance plus faible. Outre l'épaisseur de la colle, d'autres paramètres comme la durée d'impulsion peuvent être modifiés pour les études futures puisqu'un modèlé validé existe.

Le décapage laser a été appliqué sur des échantillons d'épaisseur spécifiée avec une déviation d'épaisseur de ± 10-20%. Tout d'abord, le seuil de décapage est déterminé en fonction de la densité de puissance qui correspond au premier décollement des couches de finition comme expliqué précédemment dans 4.1.2. Après avoir obtenu les valeurs de seuil, les mêmes densités de puissance sont appliquées sur les échantillons afin de générer de grandes zones de décapage avec un recouvrement des spots de 20-30%. Ensuite, afin d'avoir une information sur la santé du primaire époxy pour la résistance à la corrosion après décapage, un test de brouillard salin neutre a été réalisé par RESCOLL, Pessac, France. Les tests portent uniquement sur l'échantillon marqué 3, car il présente l'épaisseur de couche supérieure la plus élevée avant l'application du laser, et l'une des plus faibles épaisseurs d'époxy restantes après les impacts de laser. Les résultats commeobtenus permettent de conclure qu'il n'y a pas de défaut significatif causé par le brouillard salin.

Conclusion

This thesis has presented a new stripping process which is based on spallation phenomena produced by shock wave propagation via laser-plasma interaction both from the substrate and the coating side of specimens. This technique can be used for thin coatings via pure mechanical effects applied on a stack of AA 2024-T3, AL-Li 2060 and CFRP specimens. Much appreciated to the precision of the laser stripping method, it opened us up to an unconventional perspective of laser paint adhesion test with the same technique. The work is based on the European Project of Clean Sky 2, VULCAN (deVelopment of a Universal seLeCtive stripping solution for Aircraft coatiNgs). The project aims at developing an industrial laser stripping process which is able to selectively remove layer by layer the top coat of a an aircraft paint system, with an accuracy of 1 μm.

The main objective of the work was to distinguish the mechanical, chemical and adhesive/interface based effects on paint adhesion levels. As an application of this approach, laser paint stripping with different configurations was developed. The common process window was defined as function of power density for laser paint stripping applications by sub-grouping targets.

The first chapter presented a background and specifications for paint usage in the industry, methods for paint adhesion tests and existing laser paint stripping methods in the literature. After, physical phenomena behind the laser adhesion test was detailed including plasma creation and different laser impact configurations. Eventually, objectives of the thesis were explained.

The second chapter demonstrated the different samples, tools and methods used. First the specimens were explained and then material characterization and physicochemical tools were given. Optical microscopy was used both before and after laser impacts for the coating characterization. Profilometer was used to see the stripped depth after applied laser impacts. FTIR, TGA and DSC were used to characterize the nature of the coatings. Finally, micro indentation tester was utilized to extract the Young's Modulus

of aged and unaged specimens. Afterwards, used lasers and laser characterizations were presented followed by a demonstration of VISAR diagnostics. Finally, material models and equation of states were explained with the proper parameter choices.

The third chapter investigated materials under shock. First, substrate characterization was done. Then, single and several layers of paint configurations were analyzed and in parallel, a process simulation for validation purposes was conducted. Finally, applications to adhesive tape under laser shock was done. The work covered experimental and numerical work on pure aluminum (99 %), AA 2024 -T3 and AA 2024 -T3 + Epoxy Primer. AA 2024 -T3 + Epoxy Primer + Top Coat, AL-Li 2060- T8 E30 and CFRP based specimens were just investigated via experimental work. In addition to base materials (pure aluminum, AA 2024 - T3, AL-Li 2060- T8 E30 and CFRP) polymer based materials (epoxy, polyurethane, and acrylic) are investigated as well. It was crucial to understand the behavior of the polymers in order to produce conclusive results, since this particular topic is not widely studied in the literature. The monitored results were combined with numerical work, and the parameters for laser stripping applications were optimized.

In the fourth chapter, adhesion relations are examined for different specimens' configurations as function of thickness, coating type and thermal ageing. The findings imply that, due to the sensitivity of the procedure, it is not feasible to delineate a common process window (for all sort of samples studied) for laser paint stripping regardless of the target. Nonetheless, due to the procedure's sensitivity, it has the implication to be a fresh tool for laser paint adhesion tests. In addition, the damage ring phenomena was delved both numerically and experimentally. It can be concluded that the circumstance of the elasto-plastic interaction might be a main cause of it. Moreover, edge effects and reflections within the thin epoxy layer can be complimentary reasons. By coupling experimental and numerical work, laser adhesion and paint stripping technology can be optimized. Future research that aims to ameliorate the laser paint adhesion test and address virtual testing is likely to profit from the numerical work, particularly when it's fed with the real material properties.

In the fifth chapter, laser paint stripping validation and development are explained from the paint side. Afterwards, created large stripping zones were presented a spot overlap of 20-30%. Then, in order to gather information about the epoxy primer health for the corrosion resistance after stripping, neutral salt spray test was applied at RESCOLL, Pessac, France. The results obtained can be inferred as a neutral salt spray test did not reveal any significant defects.

Conclusion FR

Ce travail a présenté un nouveau procédé de décapage, basé sur des phénomènes de spallation par la propagation d'ondes de choc via l'interaction laser-plasma à la fois du côté du substrat et du côté du revêtement des échantillons. Cette technique peut être utilisée pour les revêtements minces via des effets mécaniques purs. Elle a été appliquée sur un empilement d'éprouvettes en AA 2024-T3, AL-Li 2060 et CFRP. La sensibilité de la procédure de décapage laser, nous a ouvert une nouvelle perspective : le test d'adhésion de peinture basé sur la même méthodologie de choc laser. Ce travail de thèse s'intègre dans le projet européen Clean Sky 2, VULCAN (deVelopment of a Universal seLeCtive stripping solution for Aircraft coatiNgs). Le projet vise à développer un procédé industriel de décapage au laser capable d'éliminer sélectivement, couche par couche, la couche supérieure d'un revêtement d'avion avec une précision de 1 µm.

L'objectif principal de ce travail était de distinguer les effets mécaniques, chimiques et de l'adhésion de l'interface sur les niveaux d'adhésion de la peinture. Comme application de cette approche, le décapage de peinture au laser avec différentes configurations a été développé. La fenêtre commune du processus a été définie en fonction de la densité de puissance pour les applications de décapage laser en sous-groupes de cibles.

Le premier chapitre présente le contexte et les spécifications de l'utilisation de la peinture dans l'industrie, les méthodes de test d'adhésion de la peinture et les méthodes de décapage laser existantes dans la littérature. Ensuite, les phénomènes physiques derrière le test d'adhésion au laser ont été détaillés, y compris la création de plasma et les différentes configurations d'impact du laser. Enfin, les objectifs de la thèse ont été expliqués.

Le deuxième chapitre a détaillé les différents échantillons et les méthodes utilisées. Les échantillons ont d'abord été décrits, puis la caractérisation des matériaux et les outils physico-chimiques ont été présentés. La microscopie optique a été utilisée avant et après les impacts laser pour la caractérisation du revêtement. Le profilomètre a été utilisé pour

voir la profondeur de décapage après les impacts laser appliqués. Le FTIR, le TGA et le DSC ont été utilisés pour caractériser la nature des revêtements. Enfin, le testeur de micro indentation a été utilisé pour extraire le module d'Young des spécimens vieillis et non vieillis. Ensuite, les lasers utilisés et leurs caractérisations ont été présentés. Le diagnostic VISAR a été détaillé. Enfin, les modèles de matériaux et l'équation d'état ont été expliqués avec les choix de paramètres appropriés.

Le troisième chapitre est consacré à l'étude des matériaux sous choc. Tout d'abord, la caractérisation du substrat a été effectuée. Ensuite, des configurations à une et plusieurs couches de peinture ont été analysées. En parallèle, une simulation du processus à des fins de validation a été réalisée. Enfin, l'utilisation de ruban adhésif sur les échantillons d'aluminium et epoxy sous choc laser ont été réalisées. Le travail a couvert un travail expérimental et numérique sur l'aluminium pur (99 %), AA2024 -T3 et AA 2024 -T3 + Epoxy Primer. AA 2024 -T3 + Epoxy Primer + Top Coat,AL-Li 2060- T8 E30 et des échantillons à base de CFRP ont été étudiés dans un travail expérimental. En plus des matériaux de base (aluminium pur, AA 2024 - T3, AL-Li2060- T8 E30 et CFRP), la compréhension du comportement des polymères (époxy, polyuréthane et acrylique dans notre cas) a été étudiée. Cela a été un élément clé pour obtenir des résultats concluants. Les résultats expériementaux ont été couplés avec un travail numérique puis utilisés pour optimiser les paramètres pour les applications de décapage laser.

Dans le quatrième chapitre, les relations d'adhésion sont examinées pour différentes configurations d'éprouvettes en fonction de de l'épaisseur, du type de revêtement et du vieillissement thermique. Les résultats suggèrent que, en raison de la sensibilité du processus, il n'est pas possible de définir une fenêtre de processus commune (pour tous les types de spécimens étudiés) pour les paramètres de décapage de la peinture au laser, quelle que soit la cible. Cependant, la sensibilité du procédé le place comme un outil innovant pour les tests d'adhésion de la peinture au laser. Le phénomène d'anneau de dommage a été étudié numériquement et expérimentalement. On peut conclure que l'apparition de l'interaction élasto-plastique pourrait en être la cause principale. En outre, les effets de bord et les réflexions à l'intérieur de la cible peuvent être des raisons complémentaires. En couplant le travail expérimental et numérique, l'adhésion laser et la technologie de décapage de la peinture peuvent être optimisées. En particulier, lorsque le travail numérique est alimenté par les propriétés réelles des matériaux, il s'agit d'une contribution prometteuse pour les travaux futurs qui cherchent à optimiser l'essai d'adhésion de la peinture au laser et à réaliser des essais numériques.

Dans le cinquième chapitre, de grandes zones de décapage ont été créées avec un chevauchement de 20-30%. Ensuite, afin d'avoir une information sur la santé du primaire époxy pour la résistance à la corrosion après décapage, un test de brouillard salin neutre a été appliqué à RESCOLL, Pessac, France. Les résultats obtenus montrent qu'il n'y a pas

de défaut significatif créé par les tests au brouillard salin neutre.

Perspectives

This work presented the capability of selective laser paint stripping and laser paint adhesion tests for a single and multiple stack of layers. This opens up future opportunities to further optimize and understand the nature of the process by conducting additional experimental and numerical work:

- As explained previously, there is not much work done including laser shock waves within the polymers in the literature. Hence, it is challenging to find data for the process. In addition, since the polymer families have a broad data set, it is not easy to sort out the material parameters to use for the numerical works. In order to feed the numerical models, exact material parameters are needed. Therefore, additional mechanical tests should be performed for both different types of epoxies and polyurethane based coatings.
- After obtained exact material parameters, simulations could be conducted on different base materials including AL-Li and CFRP. In addition, for the process optimization, different pulse durations can be used to see the effect on paint stripping and adhesion tests. Moreover, double and symmetrical impact configurations might be developed as well.
- Thermal ageing can be investigated deeper. To better understand the produced effects, the interface between coating and substrate can be taken as a third layer in between aluminum and epoxy. Another proposition as future work is also to observe thermal ageing on the aluminum substrate itself to distinguish the caused effects by the epoxy layer. Apart from that, ageing conditions might be studied on multi stack layer configurations. Furthermore, UV ageing might be used to present the real life conditions followed by laser impacts to compare the ageing effects.
- Re-painting capability can be studied using different configurations. For example, it can be done on a primer + top coat by applying just top coat after stripping. Also, the same sample can be painted on both primer and a top coat after laser impact. Then the re-application of laser impacts can be conducted to compare the adhesion and stripping levels/pattern with the initial conditions.

Perspectives FR

Ce travail a présenté du capacité de décapage sélectif de la peinture par laser et les tests d'adhésion de la peinture par laser pour un empilement simple et multiple de couches. Cependant, afin d'optimiser et de comprendre la nature du processus, des travaux expérimentaux et numériques supplémentaires sont nécessaires :

- Comme expliqué précédemment, il n'y a pas beaucoup de travaux incluant les ondes de choc laser dans les polymères dans la littérature. Il est donc difficile de trouver des données sur ce processus. De plus, comme les familles de polymères disposent d'un large ensemble de données, il n'est pas facile de trier les paramètres matériaux à utiliser pour les travaux numériques. Afin d'alimenter les modèles numériques, les paramètres exacts des matériaux sont nécessaires. Par conséquent, des tests mécaniques supplémentaires doivent être réalisés pour les différents types d'époxies et de revêtements à base de polyuréthane.

- Après avoir obtenu les paramètres exacts des matériaux, des simulations pourraient être menées sur différents matériaux de base, notamment AL-Li et CFRP. En outre, pour l'optimisation du processus, différentes durées d'impulsion peuvent être utilisées pour voir l'effet sur le décapage de la peinture et les tests d'adhésion. Enfin, des configurations d'impact doubles et symétriques pourraient également être développées.

- Le vieillissement thermique peut être étudié de manière plus approfondie. Pour mieux comprendre les effets produits, l'interface entre le revêtement et le substrat peut être considérée comme une troisième couche entre l'aluminium et l'époxy. Une autre proposition de travail futur consiste également à observer le vieillissement thermique sur le substrat d'aluminium lui-même pour distinguer les effets causés par la couche d'époxy. En dehors de cela, les conditions de vieillissement pourraient être étudiées sur configurations à couches multiples. En outre, le vieillissement UV pourrait être utilisé pour présenter les conditions réelles suivies par les impacts laser pour comparer les effets du vieillissement.

- La capacité de remise en peinture peut être vérifiée en utilisant différentes configurations. Par exemple, elle peut être effectuée sur un apprêt + couche de finition en appliquant uniquement la couche de finition après décapage. De même, le même échantillon peut être peint avec un primaire et une couche de finition après un impact laser. Ensuite, la réapplication des impacts laser peut être effectuée pour comparer l'adhérence et les niveaux de décapage avec les conditions initiales.

Articles & Conferences

ARTICLES

- High strain rate modeling of pure aluminium ablative layer under laser shock, **Co-author**
  Under preparation

- Laser Paint Adhesion and Laser Paint Stripping Properties of External Aircraft Coatings, **First author**
  Under preparation

- Structural and Coating Laser Shock Adhesion Tests : Review, New Trends and Perspectives, **First author**
  Under preparation

- Evaluation of Adhesion and Laser Stripping Properties of External Aircraft Coatings on Aluminum and Composite Based Substrate, Conference paper, EASN-Barcelona, 2022, **First author**

- Laser Stripping of Thermally Aged Epoxy Coatings For Aeronautical Applications, Conference paper, ECCM-Lausanne, 2022, **First author**

- Towards the Development of a Laser Shock-based Disassembly Process For Adhesively Bonded Ti/CFRP Structural Parts: Experiments and Numerical Simulation, Conference paper, ECCM-Lausanne, 2022, **Co-author**

- Selective Interlaminar Delamination Process in CFRP by Laser Shock, ECCM-Lausanne, 2022, **Co-author**

- New methodology of dynamical material response of dissimilar FSWed Al alloy joint under high strain rate laser shock loading, Materials & Design, 2022 - Elsevier, **Co-author**
  https://doi.org/10.1016/j.matdes.2022.111080

- Modeling of multi-edge effects in the case of laser shock loadings applied on thin foils: Application for material characterization of aluminum alloys, Journal of Applied Physics, 2022, **Co-author**
  https://doi.org/10.1063/5.0080326

- Towards selective laser paint stripping using shock waves produced by laser-plasma interaction for aeronautical applications on AA 2024 based substrates, Optics & Laser Technology, 2021, **First author**
  https://doi.org/10.1016/j.optlastec.2021.107095

- Beam size dependency of a laser-induced plasma in confined regime: Shortening of the plasma release. Influence on pressure and thermal loading, Optics & Laser Technology, 2021, **Co-author**
  https://doi.org/10.1016/j.optlastec.2020.106689

- Development of a Numerical Model to Simulate Laser-Shock Paint Stripping on Aluminum Substrates, MDPI-Aerospace, 2021, **Co-author**

CONFERENCES

- 12th EASN International Conference on "Innovation in Aviation & Space for opening New Horizons", Barcelona, 18-21 October 2022 - **Oral Presentation**

- 7èmes journées VH Vélocimétrie Hétérodyne - Expérimentations Matériaux sous Choc, Gramat, France, 5-7 October 2022 - **Oral & Poster Presentation**

- ECCM Conference, Composites Meet Sustainability, Lausanne, 26-30 June 2022 - **Oral Presentation**

- Visiting Researcher to University of Patras, Erasmus+, Greece, 1-30 May 2022 - **Visiting Researcher**

- Seconde école du GDR ACO-CHOCOLAS Matériaux sous Hautes Vitesses de Déformation, Ile d'Oleron, France, 10-15 October 2021 - **Oral Presentation**

- Forum Interaction Laser-Plasma, Corsica, 25-30 September 2021 - **Poster Presentation**

- COST-Certbond Training School, Trieste, Italy, 20-22 September 2021 - **Oral Presentation**

- Forum Interaction Laser-Plasma, Fréjus, France, October 2019 - **Poster Presentation**

References

[1]N. Fusetani. "Antifouling compounds." In: *Clare AS* 2307.020038 (2006).

[2]O.S.I Fayomi, O. Agboola, I.G. Akande, and A.O. Emmanuel. "Challenges of coatings in aerospace, automobile and marine industries." In: *Technologies and Materials for Renewable Energy, Environment and Sustainability* (2020). DOI: https://doi.org/10.1063/5.0033579.

[3]O. Guseva, S. Brunner, and P. Richner. "Analysis of the Environmental Parameters for Aircraft Coatings." In: *Macromol. Symp* 187.883–893 (2002).

[4]G. Bierwagen. "Next Generation of Aircraft Coating Systems." In: *Journal of Coatings Technology* 73 (2001), pp. 45–52. DOI: https://doi.org/10.1007/BF02730030.

[5]J.E.C. Smith. "Advances in protective coatings and processes for aerospace applications." In: *Aircraft Engineering and Aerospace Technology* 67.5 (1995), pp. 13–16.

[6]N.N. Voevodin, V.N. Balbyshev, and M.S. Donley. "Investigation of corrosion protection performance of sol–gel coatings on AA2024-T3." In: *Progress in Organic Coatings* 52 (2005), pp. 28–33. DOI: https://doi.org/10.1016/j.porgcoat.2004.05.006.

[7]L. Jinsong and L. Kin-tak. *Multifunctional Polymer Nanocomposites*. 6000 Broken Sound Parkway NW, Suite 300 Boca Raton: CRC Press, 2010.

[8]R.J. Rioja and J. Liu. "The evolution of Al-Li base products for aerospace and space applications." In: *Metallurgical and Materials Transactions* 43A.3325-3337 (2012).

[9]C. Negoita, N. Cristache, and M. Bodor. "The epoxy resin-history and perspectives." In: *MATERIALE PLASTICE* 53.3 (2016), p. 564.

[10]E. Ernault. "Thermo-oxydation de résines époxy/amine. Mécanique des structures." PhD thesis. ENSAM, Paris Tech, 2016.

[11]M. Pawlik, Y. Lu, and H. Le. "Effects of surface modification and graphene nanoplatelet reinforcement on adhesive joint of aluminium alloys." In: *International Journal of Adhesion and Adhesives*, (2020).

[12]E. Ernault, E. Richaud, and B. Fayolle. "Origin of epoxies embrittlement during oxidative ageing." In: *Polymer Testing* 63 (2017). DOI: https://doi.org/10.1016/j.polymertesting.2017.09.004.

[13]R.O. Allen and P. Sanderson. "Characterization of Epoxy Glues with FTIR." In: *Applied Spectroscopy Reviews* (1998). DOI: http://dx.doi.org/10.1080/05704928808060457.

[14]B. Passilly and R. Delannoy. "Characterization of the ageing of an epoxy resin using high temperature nanoindentation." In: *Matériaux Techniques* (2019). DOI: 10.1051/mattech/2019004.

[15]M. Minervino. "Effets de la thermo oxydation sur le comportement mécanique de composites pour applications aéronautiques." ISAE-ENSMA École Nationale Supérieure de Mécanique et d'Aérotechnique, Poitiers. PhD thesis. 2014.

[16]M.R. Islam, M.D.H. Beg, and S.S. Jamari. "Development of vegetable-oil-based polymers." In: *Journal of Applied Polymer Science* (2014).

[17]E. Delebecq, J.P. Pascault, B. Boutevin, and F. Ganachaud. "On the Versatility of Urethane/Urea Bonds: Reversibility, Blocked Isocyanate, and Non-isocyanate Polyurethane." In: *Chemical Reviews* (2013).

[18]C. Fang, X. Zhou, Q. Yu, S. Liu, D. Guo, R. Yu, and J. Hu. "Synthesis and characterization of low crystalline waterborne polyurethane for potential application in water-based ink binder." In: *Progress in Organic Coatings* (2013), pp. 61–71. DOI: https://doi.org/10.1016/j.porgcoat.2013.08.004.

[19]T.C. Grace, S. C. Neto, and F. Vecchia. "Rigid foam polyurethane (PU) derived from castor oil (Ricinus communis) for thermal insulation in roof systems." In: *Frontiers of Architectural Research* (2012), pp. 348–356. DOI: https://doi.org/10.1016/j.foar.2012.09.005.

[20]D. K. Chattopadhyay and R. V. Kothapalli. "Structural engineering of polyurethane coatings for high performance applications." In: *Progress in Polymer Science* 32.3 (2007), pp. 352–418. DOI: 10.1016/j.progpolymsci.2006.05.003.

[21]E.A. Starke and J.T. Staley. "Application of modern aluminum alloys to aircraft." In: *Prog. Aerosp Sci* 32.131-172 (1996).

[22]S. Kumar and P. N. Padture. "Metallurgical Design and Industry." In: 271-346 (2018).

[23]https://www.safran-aircraft-engines.com/fr/moteurs-civils/avions-court-et-moyen-courriers/leap/leap-1a. "Leap-1a: moteur de l'airbus a320neo". In: (accessed:02/22).

[24]J.C. Williams and E.A. Starke. "Progress in structural materials for aerospace systems." In: *Acta Mater* 51.5775-5779 (2003).

[25]S. Rana and R. Fanguerio. "Advanced composites in aerospace engineering: processing, properties, and applications." In: (2016).

[26]J. S. Foley and P. Barone. "AUTOMATED LASER PAINT STRIPPING." In: *Metal Finishing* 90 (1992), pp. 48–50.

[27]J. Kozol. "An Environmentally Safe and Effective Paint Removal Process for Aircraft." In: *JOM* (2001), pp. 20–21. DOI: https://doi.org/10.1007/s11837-001-0172-y.

[28]M.J. Then. *THE FUTURE OF AIRCRAFT PAINT REMOVAL METHODS.* 1989.

[29]S. Pantelakis, T. Kermanidis, and G.N. Haidemenopoulos. "Mechanical behavior of 2024 A1 alloy specimen subjected to paint stripping by laser radiation and plasma etching." In: *Theoretical and Applied Fracture Mechanics* 25 (1996), pp. 139–146.

[30]R.A. Dickie. "Paint adhesion, corrosion protection and interfacial chemistry." In: *Progress in Organic Coatings* 25 (1994), pp. 3–22.

[31]K.L. Mittal. "ADHESION MEASUREMENT OF THIN FILMS." In: *Electrocomponent Science and Technology* 3 (1976), pp. 21–42.

[32]D.S. Rickerby. "A review of the methods for the measurement of coating-substrate adhesion." In: *Surface and Coatings Technology* 36 (1988), pp. 541–557.

[33]J. Strong. "Evaporated aluminum films for astronomical mirrors." In: *Publ. A.S.P.* 46.18 (1934).

[34]O.S. Heavens and L.E. Collins. "L'epitaxie dans les lames polycrystallines." In: *J. Phys. Radium* 13 (1954), pp. 658–660.

[35]C. Bolis, L. Berthe, M. Boustie, M. Arrigoni, S. Barradas, and M. Jeandin. "Physical approach of adhesion test using laser driven shock wave." In: *Journal of Applied Physics* 40.10 (2007).

[36]T. Maiman. "Stimulated Optical Radiation in Ruby." In: *Nature* 187 (1960), pp. 493–494. DOI: https://doi.org/10.1038/187493a0.

[37]J. Hecht. "Short History of Laser Development." In: *Optical Society of America, Applied Optics* 49 (2010). DOI: https://doi.org/10.1364/AO.49.000F99.

[38]J. Miller. "A Brief History of Laser Ablation." In: *American Institute of Physics* 288 (1994). DOI: https://doi.org/10.1063/1.44865.

[39]J.L. Vossen. "Measurement of Film-Substrate Bond Strength by Laser Spallation, Adhesion Measurement of Thin Films, Thick Films and Bulk Coatings." In: *American Society for Testing and Materials* (1978), pp. 122–133.

[40]J. Yuan and V. Gupta. "System and method for measuring the interface tensile strength of planar interfaces." In: *Journal of Applied Physics* (1995, US PATENT No. 5 438 402).

[41]J. Yuan and V. Gupta. "Measurement of Interface Strength by the Modified Laser Spallation Technique." In: *Journal of Applied Physics* 74 (1993), pp. 2388–2410.

[42]S. Barradas, R. Molins, M. C. Jeandin, M. Arrigoni, M. Boustie, C. Bolis, L. Berthe, and M. Ducos. "Application of laser shock adhesion testing to the study of the inter-lameller strength and coating-substrate adhesion in cold-sprayed copper coating of aluminum." In: *Surface and coating technology* 197 (2005).

[43]E. Gay. "Comportement de composites sous choc induit par laser: Développement de l'essai d'adhérence par choc des assemblages de composites collés." PhD thesis. ENSAM, Paris Tech, 2011.

[44]R. Ecault. "Etude expérimentale et numérique du comportement dynamique de composites aéronautiques sous choc laser. Optimisation du test d'adhérence par ondes de choc sur les assemblages composites collés." PhD thesis. Ecole Nationale Supérieure de Mécanique et d'Aérotechique, 2013. URL: https://tel.archives-ouvertes.fr/tel-01242721.

[45]D. Courapied. "Etude de l'interaction laser matière en régime de confinement par eau avec deux impulsions laser. Application au test d'adhérence par choc laser." 2016ENAM0073. PhD thesis. 2016. URL: https://pastel.archives-ouvertes.fr/tel-01495241.

[46]S. Bardy. "Controle et optimisation de test d'adhérence par choc laser sur assemblages collés." PhD thesis. ENSAM, Paris Tech, 2017.

[47]M. Sagnard. "Detection of weak bonds in bonded cfrp assemblies using symmetrical laser shock adhesion test (s-lasat.)" PhD thesis. ENSAM, Paris Tech, 2019.

[48]M. Scius-Bertrand, L. Videau, A. Rondepierre, E. Lescoute, Y. Rouchausse, J. Kaufman, D. Rostohar, J. Brajer, and L. Berthe. "Laser induced plasma characterization in direct and water confined regimes: new advances in experimental studies and numerical modelling." In: *Journal of Physics D: Applied Physics* 54.5 (2020). DOI: https://doi.org/10.1088/1361-6463/abc040.

[49]M. Scius-Bertrand. "Endommagements maîtrises par chocs laser symétriques et désassemblages des collages ." ENSAM, Paris Tech. PhD thesis. 2021.

[50]L. Berthe, M. Arrigoni, M. Boustie, J.P. Cuq-Lelandais, C. Broussillou, G. Fabre, M. Jeandin, V. Guipont, and M. Nivard. "State-of-the-art laser adhesion test (LASAT)." In: *Nondestructive Testing and Evaluation* 26.3-4 (2011), pp. 303–317. DOI: https://doi.org/10.1080/10589759.2011.573550.

[51]J. A. Fox. "Effect of water and paint coatings on laser irradiated targets." In: *Applied Physics Letters* 24 (1974), pp. 461–464. DOI: https://doi.org/10.1063/1.1655012.

[52]R. Fabbro, J. Fournier, P. Ballard, D. Devaux, and J. Virmont. "Physical study of laser produced plasma in confined geometry." In: *Journal of Applied Physics* 68.2 (1990), pp. 775–784. DOI: https://doi.org/10.1063/1.346783.

[53]N. C. Anderholm. "Laser-generated stress waves." In: *Applied Physics Letters* 16.3 (1970), pp. 113–115. DOI: https://doi.org/10.1063/1.1653116.

[54]M.P. Bellan. *Fundamentals of Plasma Physics.* 1st ed. Cambridge University Press, 2008, p. 628. ISBN: 9780521528009.

[55]P. Mora. "Theoretical model of absorption of laser light by a plasma." In: *Physics of Fluids* 25.6 (1982).

[56]B. W. Thompson. *An Introduction to Plasma Physics.* 2nd ed. Pergamon, 1962, p. 282. ISBN: 9781483164779.

[57]A. Rondepierre, A. Sollier, L. Videau, and L. Berthe. "Review on Laser Interaction in Confined Regime: Discussion about the Plasma Source Term for Laser Shock Applications and Simulations." In: *MDPI, Metals* 11.2032 (2021). DOI: https://doi.org/10.3390/met11122032.

[58]T. Sakka, K. Takatani, Y. Ogata, and M. Mabuchi. "Laser ablation at the solid-liquid interface: Transient absorption of continous spectral emission by ablated aluminium atoms." In: *Journal of Applied Physics D* 35 (2001).

[59]A. Kanitz, M.R. Kalus, E. Gurevich, A. Ostendorf, S. Barcikowski, and D. Amans. "Review on experimental and theoretical of investigations of the early stage, femtoseconds to microseconds processes during laser ablation in liquid-phase for the synthesis of colloidal nanoparticles." In: *Plasma Sources Science Technology* 28 (2019).

[60]A. Sollier. "Etude des plasmas generes par interaction laser-matiere en regime confine. Application au traitement des materiaux par choc laser." 2011ENAM0033. PhD thesis. 2002. URL: https://tel.archives-ouvertes.fr/tel-00089243.

[61]A. Sollier, L. Berthe, and R. Fabbro. "Numerical modeling of the transmission of breakdown plasma generated in water during laser shock processing." In: *EPJ Applied Physics* 16.2 (2001), pp. 131–139. DOI: https://doi.org/10.1051/epjap:2001202.

[62]L. Berthe, R. Fabbro, P. Peyre, and E. Bartnicki. "Experimental study of the transmission of breakdown plasma generated during laser shock processing." In: *EPJ Applied Physics* 3.2 (1998), pp. 215–218. DOI: https://doi.org/10.1051/epjap:1998222.

[63]L. J. Radziemski and D. A. Cremers. *Laser Induced Plasmas and Applications.* Marcel Dekker, INC., 1989, p. 445. ISBN: 0-8247-8078-7.

[64]C. Le Bras, A. Rondepierre, R. Seddik, M. Scius-Bertrand, Y. Rouchausse, L. Videau, B. Fayolle, M. Gervais, L. Morin, S. Valadon, R. Ecault, D. Furfari, and L. Berthe. "Laser shock peening: toward the the of pliable solid polymers for confinement." In: *Metals* 9.7 (2019). DOI: https://doi.org/10.3390/met9070793.

[65]S. Bardy, B. Aubert, T. Bergara, L. Berthe, P. Combis, D. Hébert, E. Lescoute, Y. Rouchausse, and L. Videau. "Development of a numerical code for laser-induced shock waves applications." In: *Optics and Laser Technology* 124 (2020). DOI: https://doi.org/10.1016/j.optlastec.2019.105983.

[66]G. I. Kanel, S.V. Razorenov, and V.E. Fortov. *Shock-Wave Phenomena and Properties of Condensed Matter.* Springer-Verlag New York, Inc. , 175 Fifth Avenue, New York, NY 10010, USA: Springer, 2004.

[67]L. Berthe, M. Arrigoni, M. Boustie, J.-P. Cuq-Lelandais, C. Broussillou, G. Fabre, M. Jeandin, V. Guipont, and M. Nivard. "New advances for laser adhesion test (LASAT): From thick to thin coatings." In: 2011, pp. 489–495. DOI: https://doi.org/10.2351/1.5062282.

[68]L. Tollier and R. Fabbro. "Study of the laser-driven spallation process by the VISAR interferometry technique. II. Experiment and simulation of the spallation process." In: *Journal of Applied Physics* 83.3 (1998), pp. 1231–1237. ISSN: 00218979. DOI: https://doi.org/10.1063/1.366820.

[69]M. Ghrib, M. Rébillat, N. Mechbal, L. Berthe, and M. Guskov. "Signal-based versus nonlinear model-based damage sensitive features for delamination quantification in CFRP composites." In: vol. 1. 2017, pp. 422–430. DOI: https://doi.org/10.12783/shm2017/13895.

[70]R. Ecault, F. Touchard, L. Berthe, and M. Boustie. "Laser shock adhesion test numerical optimization for composite bonding assessment." In: *Composite Structures* 247 (2020). DOI: https://doi.org/10.1016/j.compstruct.2020.112441.

[71]T. Antoun, L. Seaman, D. Curran, G. Kanel, S. Razonerov, and V.Utkin. "Spall Fracture." In: *Springer Science Business Media* 34.188 (2002).

[72]T. Rességuier and M. Hallouin. "Interaction of two laser shocks inside iron samples." In: *Journal of Applied Physics* 90.9 (2001), pp. 4377–4384. DOI: https://doi.org/10.1063/1.1405816.

[73]M. Boustie, J.P. Cuq-Lelandais, C. Bolis, L. Berthe, S. Barradas, M. Arrigoni, T. Resseguier, and M. Jeandin. "Study of damage phenomena induced by edge effects into materials under laser driven shocks." In: *Journal of Physics D: Applied Physics* 40.22 (2007), pp. 7103–7108. DOI: https://doi.org/10.1088/0022-3727/40/22/036.

[74]J.P. Cuq-Lelandais. "Etude du comportement dynamique de matériaux sous choc laser subpicoseconde." ISAE-ENSMA Ecole Nationale Supérieure de Mécanique et d'Aérotechique-Poitiers. PhD thesis. 2010. URL: https://tel.archives-ouvertes.fr/tel-00564182.

[75]B.H. Hans. "Paint Stripping with Nontoxic Chemicals." In: *METAL FINISHING* (1995). DOI: 10.1016/0026-0576(95)95844-7.

[76]A.W. AlShaer, L. Li, and A. Mistry. "The effects of short pulse laser surface cleaning on porosity formation and reduction in laser welding of aluminium alloy for automotive component manufacture". In: *Optics and Laser Technology* 64 (2014), pp. 162–171. DOI: 10.1016/j.optlastec.2014.05.010.

[77]G. Zhu, Z. Xu, Y. Jin, X. Chen, L. Yang, J. Xu, D. Shan, Y. Chen, and B. Guo. "Mechanism and application of laser cleaning: A review". In: *Optics and Lasers in Engineering* 157 (2022). DOI: doi.org/10.1016/j.optlaseng.2022.107130.

[78]S.M. Bedair and H.P. Jr. Smith. "Atomically clean surfaces by pulsed laser bombardment". In: *Journal of Applied Physics* 40 (1969), pp. 4776–81.

[79]A.L. Schawlow. "Lasers: The intense, monochromatic, coherent light from these new sources shows many unfamiliar properties". In: *Science* 149.3679 (1965).

[80]J.F. Asmus, C.G. Murphy, and W.H. Munk. "Studies on the interaction of laser radiation with art artifacts". In: *Developments in Laser Technology* 41 (1974). DOI: 10.1117/12.953831.

[81]S.J. Lee K. Imen and S.D. Allen. "Laser-assisted micron scale particle removal". In: *Applied Physics Letters* 58 (1991), pp. 203–205.

[82]R. Bordalo, P.J. Morais, H.Gouveia, and C.Young. "Laser Cleaning of Easel Paintings: An Overview". In: *Laser Chemistry* 2006 (2006), p. 9.

[83]G. Schweizer and L. Werner. "Industrial 2-kW TEA CO_2 laser for paint stripping of aircraft". In: *Gas Flow and Chemical Lasers: Tenth International Symposium* (1995).

[84]M. Cooper. *Laser Cleaning in Conservation*. Butterworth-Heinemann, Oxford, UK, 1998.

[85]G. Chita G. Daurelio and M. Cinquepalmi. "Laser surface cleaning, de-rusting, de-painting and de-oxidizing". In: *Applied Physics A: Material Science Process* 69 (1996).

[86]J.M. Lee and K.G. Watkins. "Removal of small particles on silicon wafer by laser-induced airborne plasma shock waves". In: *Journal of Applied Physics* 89 (2001).

[87]A.J. Fernandes D.M. Kane and R.P. Mildren. "Optical microscopy imaging and image-analysis issues in laser cleaning". In: *Applied Physics A: Material Science Process* 77 (2003).

[88]Y. Zhou, L. Zheng, G. Zhao H. Gao, Y. Li, and L. Li. "Cleaning of the first mirrors and diagnostic windows by YAG laser on HL-2A". In: *Phy. Scr.* (2009).

[89]L. Li A.W. AlShaer and A. Mistry. "The effects of short pulse laser surface cleaning on porosity formation and reduction in laser welding of aluminium alloy for automotive component manufacture". In: *Optics and Laser Technology* 64 (2014).

[90]M. Martinez-Calderon, T.A. Haase, N.I. Novikova, F.S. Wells, and G.R. Willmott J. Low. "Turning industrial paints superhydrophobic via femtosecond laser surface hierarchical structuring". In: *Progress in Orgnaic Coatings* 163.2 (2022).

[91]H.A. Jasim, A.G. Demir, B. Previtali, and Z.A. Taha. "Process development and monitoring in stripping of a highly transparent polymeric paint with ns-pulsed fiber laser." In: *Optics and Laser Technology* 93 (2017), pp. 60–66. DOI: https://doi.org/10.1016/j.optlastec.2017.01.031.

[92]"Environmentally safe and effective processes for paint removal." In: *Agard Report LS-201* (1995).

[93]F. Brygo, C. Dutouquet, F.L. Guern, R. Oltra, A. Semerok, and J.M. Weulersse. "Laser fluence, repetition rate and pulse duration effects on paint ablation." In: *Applied Surface Science* 252 (2006), pp. 2131–2138. DOI: https://doi.org/10.1016/j.apsusc.2005.02.143.

[94]J. F. Becker, A. C. Tam, J. B. Gruber, and L. Lam. "Novel Laser Sources and Applications." In: *SPIE Optical Engineering Press* (1995).

[95]P. Peyre, R. Fabbro, P. Merrien, and H.P. Lieurade. "Laser shock processing of aluminium alloys. Application to high cycle fatigue behaviour." In: *Materials Science and Engineering: A* 210.1 (1996), pp. 102–113. ISSN: 0921-5093. DOI: https://doi.org/10.1016/0921-5093(95)10084-9.

[96]P. Peyre and R. Fabbro. "Laser shock processing: a review of the physics and applications." In: *Optical and Quantum Electronics* 27.12 (1995), pp. 1213–1229. ISSN: 1572-817X. DOI: https://doi.org/10.1007/BF00326477.

[97]T. Rostock. "Laser Shock Processing: Aircraft Engine Components." In: 15-17 December 2008, Houston, TX.

[98]T. Iuchi, S. Yamaguchi, T. Ichiyama, M. Nakamura, T. Ishimoto, and K. Kuroki. "Laser processing for reducing core loss of grain oriented silicon steel." In: *J. of Applied Physics* 53 (1982).

[99]Y.Sano. "Development and Applications of Laser Peening System for Field Operation." In: 15-17 December 2008, Houston, TX.

[100]R.J. Raj, P.P. Selvam, and M. Pughalendi. "A Review of Aluminum Alloys in Aircraft and Aerospace Industry". In: *Journal of Huazhong University of Science and Technology* 50 (2021).

[101]R. Rajan, P.Kah, B. Mvola, and J. Martikainen. "Trends in Aluminium Alloy Development and Their Joining Methods". In: *Reviews on Advanced Materials Science* 44.4 (2016), pp. 383–397.

[102]Zuwei Feng. "Formation of Sol-gel Coatings on Aluminium Alloys." PhD thesis. 2011, p. 30.

[103]S. A. Gill, A. Telang, and K. V. Vasudevan. "Characteristics of surface layers formed on inconel 718 by laser shock peening with and without a protective coating." In: *Journal of Materials Processing Technology* 225 (2015). DOI: https://doi.org/10.1016/j.jmatprotec.2015.06.026.

[104]A. Thorvaldsson, H. Stenhamre, P. Gatenholm, and P. Walkenström. "Electrospinning of Highly Porous Scaffolds for Cartilage Regeneration". In: *Indian Journal of Dental Sciences* (2008), p. 155. DOI: https://doi.org/10.1021/bm701225a.

[105]E. Bhambri, J. P. S. Kalra, S. Ahuja, and G. Bhambri. "Evaluation of enamel surfaces following interproximal reduction and polishing with different methods: A scanning electron microscope study." In: *Indian Journal of Dental Sciences* (2017), p. 155. DOI: https://doi.org/10.4103/IJDS.IJDS_12_17.

[106]V. Edon. "Dépôt d'oxydes de grille par pulvérisation cathodique magnétron : corrélation entre les propriétès du plasma et celles des films déposés." Université Paris-Sud. PhD thesis. 2017.

[107]Y. Gui. "Mise au point par pulvérisation cathodique magnétron en condition réactive et caractéri- sations mécaniques et tribologiques de revêtements de phases Magnéli de titane (Ti_nO_{2n-1})". Université de Technologie de Belfort-Montbeliard. PhD thesis. 2014.

[108]A. Billard and F. Perry. "Pulvérisation cathodique magnétron." In: (2005). DOI: https://refractiveindex.info/?shelf=3d&book=liquids&page=water.

[109]A. Amouretti. "Exploration du diagramme de phase de l'hématite Fe_2O_3 par compression dynamique laser ." Sorbonne Université Ecole doctorale 397 : Physique et Chimie des Matériaux. PhD thesis. 2021.

[110]D.H. Lee and N. G. Cho. "Assessment of surface profile data acquired by a stylus profilometer." In: *MEASUREMENT SCIENCE AND TECHNOLOGY* (2012).

[111]P. Griffiths and J.A. Hasseth. *Fourier Transform Infrared Spectroscopy.* Wiley Blackwell, 2007.

[112]J. D. Ferry. *Viscoelastic Properties of Polymer*. New York: John Wiley & Sons, Inc, 1980.

[113]J. W. Dodd and K. H. Tonge. *Thermal Methods: Analytical Chemistry by Open Learning*. Chichester, UK: John Wiley & Sons, Ltd, 1987.

[114]M. E. Brown. *Introduction to Thermal Analysis*. Dordrecht, the Netherlands: Kuwer Academic Publishers, 1998.

[115]E.L. Charsley. "Thermal Analysis-Technique & Applications". In: *The Royal Society of Chemistry* (1992).

[116]A.C. Fischer-Cripps. "Critical review of analysis and interpretation of nanoindentation test data." In: *Elsevier* 13 (2005), pp. 4153–4154. DOI: 10.1016/j.surfcoat.2005.03.018.

[117]Q. Kan, W. Yan, G. Kang, and Q. Sun. "Oliver–Pharr indentation method in determining elastic moduli of shape memory alloys—A phase transformable material". In: *Journal of the Mechanics and Physics of Solids* 61.10 (2013), pp. 2015–2033. ISSN: 0022-5096. DOI: 10.1016/j.jmps.2013.05.007.

[118]S. Ünaldi, K. Papadopoulos, A. Rondepierre, Y. Rouchausse, F. Deliane, K. Tserpes, G. Floros, E. Richaud, and L. Berthe. "Towards selective laser paint stripping using shock waves produced by laser-plasma interaction for aeronautical applications on AA 2024 based substrates". In: *Optics & Laser Technology* 141 (2021). DOI: https://doi.org/10.1016/j.optlastec.2021.107095.

[119]M. Sagnard, L. Berthe, R. Ecault, F. Touchard, and M. Boustie. "Development of the symmetrical laser shock test for weak bond inspection". In: *Optics & Laser Technology* 111 (2019). DOI: https://doi.org/10.1016/j.optlastec.2018.10.052.

[120]W. F. Hemsing. "Velocity sensing interferometer (VISAR) modification." In: *Review of Scientific Instruments* 50.73 (1979). DOI: https://doi.org/10.1063/1.1135672.

[121]Daniel H. Dolan. "Foundations of VISAR analysis." In: (2006).

[122]H. Akel. "VISAR Analysis Theory and Mathematical Formalism." In: (2016).

[123]L.M Barker and R.E Hollenbach. "Laser interferometer for measuring high velocities of any reflecting surface." In: *Journal of applied physics* 43.11 (1972), pp. 4669–4675.

[124]L.M Barker and R.E Hollenbach. "Shock-wave studies of pmma, fused silica,and sapphire." In: *Journal of applied physics* 41.10 (1970), pp. 4208–4226.

[125]G. R. Johnson and V. H. Cook. "A constitutive model and data for metals subjected to large strains, high strain rates and high temperatures." In: *International Ballistics Society* (1983), pp. 541–547.

[126]D. J. Bammann, M. L. Chiesa, G. C. Johnson, T. Tatsumi, T. Kambe, and E. Watanabe. "Modeling Large Deformation and Failure in Manufacturing Processes." In: *International Congress; 19th, Theoretical and Applied Mechanics* (1997), pp. 359–378.

[127]S. Bhamare, G. Ramakrishnan, S. R. Mannava, K. Langer, V. K. Vasudevan, and D. Qian. "Simulation-based optimization of laser shock peening process for improved bending fatigue life of Ti-6Al-2Sn-4Zr-2Mo alloy." In: *Surface Coating Technology.* 232 (2013), pp. 464–474.

[128]B. O'Toole, M. Trabia, R. Hixson, S. K. Roy, M. Pena, S. Becker, E. Daykin, E. Mac Horro, R. Jennings, and M. Matthes. "Modeling plastic deformation of steel plates in hypervelocity impact experiments." In: *Procedia Engineering* 103 (2015), pp. 458–465.

[129]M. Ayad, L. Lapostolle, A. Rondepierre, C. Le Bras, M. Scius-Bertrand, S. Ünaldi, U. Trdan, Y. Rouchausse, J. Grassy, T. Maillot, V. Lapoujade, C. Michel, and L. Berthe. "Modeling of multi-edge effects in the case of laser shock loadings applied on thin foils: Application for material characterization of aluminum alloys." In: *Journal of Applied Physics* (2022). DOI: https://doi.org/10.1063/5.0080326.

[130]M. Sticchi, P. Staron, Y. Sano, M. Meixer, M. Klaus, J. Rebelo-Kornmeier, N. Huber, and N. Kashaev. "A parametric study of laser spot size and coverage on the laser shock peening induced residual stress in thin aluminium samples." In: *Journal of Engineering* (2015), pp. 97–105. DOI: https://doi.org/10.1049/joe.2015.0106.

[131]T.J. Spradlin, R.V. Grandhi, and K. Langer. "Experimental validation of simulated fatigue life estimates in laser-peened aluminum." In: *International Journal of Structural Integrity* (2011). DOI: https://doi/10.1108/17579861111108635.

[132]P. Peyre, L. Berthe, V. Vignal, I. Popa, and T. Baudin. "Analysis of laser shock waves and resulting surface deformations in an Al–Cu–Li aluminum alloy." In: *Journal of Physics D: Applied Physics* 45 (2012). DOI: https://doi.org/10.1088/0022-3727/45/33/335304.

[133]R. Seddik, A. Rondepierre, S. Prabhakaran, L. Morin, V. Favier, T. Palin-Luc, and L. Berthe. "Identification of constitutive equations at very high strain rates using shock wave produced by laser." In: *European Journal of Mechanics - A/Solids* 92 (2021). DOI: https://doi.org/10.1016/j.euromechsol.2021.104432.

[134]D. J. Steinberg, S. G. Cochran, and M. W. Guinan. "A constitutive model for metals applicable at high-strain rate." In: *Journal of Applied Physics* 51.3 (1980), pp. 1498–1504. DOI: 10.1063/1.327799.

[135]*Online materials information resource-MatWeb*. http://www.matweb.com. Accessed 23 March 2021. 2021.

[136]J. López-Puente, A. Arias, R. Zaera, and C. Navarro. "The effect of the thickness of the adhesive layer on the ballistic limit of ceramic/metal armours. An experimental and numerical study". In: *International Journal of Impact Engineering* 32.1 (2005). Fifth International Symposium on Impact Engineering, pp. 321–336. ISSN: 0734-743X. DOI: 10.1016/j.ijimpeng.2005.07.014.

[137]J C Boettger. *SESAME equation of state for epoxy*. Tech. rep. Los Alamos national laboratory, 1994. DOI: 10.2172/10131920.

[138]P. Peyre, I. Chaieb, and C. Braham. "FEM calculation of residual stresses induced by laser shock processing in stainless steels." In: *Modelling and Simulation in Materials Science and Engineering* 15 (2007). DOI: https://doi.org/10.1088/0965-0393/15/3/002.

[139]F. Plassard, J. Mespoulet, and P. Hereil. "Hypervelocity impact of aluminium sphere against aluminium plate: Experiment and LS-DYNA correlation." In: *8th European LS-DYNA Users Conference,Strasbourg* (2011), pp. 1–11.

[140]D. Grady. "The shock wave equation of state." In: *Physics of Shock and Impact, Volume 2*. 2053-2563. IOP Publishing, 2017, 10-1 to 10–107. ISBN: 978-0-7503-1257-8. DOI: 10.1088/978-0-7503-1257-8ch10. URL: https://dx.doi.org/10.1088/978-0-7503-1257-8ch10.

[141]P. Ballard. "Contraintes ŕesiduelles induites par impact rapide. application au choc-laser". École Polytéchnique. PhD thesis. 1991. URL: https://pastel.archives-ouvertes.%20fr/pastel-00001897..

[142]A. Abd El-Aty, Y. Xu, S. Hong Zhang, S. Ha, Y. Ma, and D. Chen. "Impact of high strain rate deformation on the mechanical behavior, fracture mechanisms and anisotropic response of 2060 Al-Cu-Li alloy." In: *Journal of Advanced Research* 18 (2019). DOI: 10.1016/j.jare.2019.01.012.

[143]C.M. Roland, S. Hensel-Bielowka, M. Paluch, and R. Casalini. "Supercooled dynamics of glass-forming liquids and polymers under hydrostatic pressure". In: *Reports on Progress in Physics* 68.6 (2005), p. 1405.

[144]C. Le Bras, C. Fosse, L. Delbreilh, M. Gervais, M. Ayad, A. Soumaila Sounakoye, L. Berthe, S. Valadon, and B. Fayolle. "Transition of elastomers from a rubber to glassy state under laser shock conditions". In: *Soft Matter* (2022), pp. -. DOI: 10.1039/D2SM00056C.

[145]J. E. Mark. *Physical Properties of Polymers Handbook*. Springer New York, NY, 2007.

[146]K. Tserpes, K. Papadopoulos, S. Ünaldi, and L. Berthe. "Development of a Numerical Model to Simulate Laser-Shock Paint Stripping on Aluminum Substrates". In: *Aerospace* (2021), pp. -. DOI: 10.3390/aerospace8090233.

[147]M. G. S. Ferreira, M. L. Zheludkevich, and J. Tedim. "Advanced protective coatings for aeronautical applications." In: *Nanocoatings and Ultra-Thin Films, Technologies and Applications* (2011), pp. 1–11. DOI: 10.1533/9780857094902.2.235.

[148]N.A. Bakar, H. Cui, Abu-Siada A., and S Li. "A review of spectroscopy technology applications in transformer condition monitoring." In: *In Proceedings of the International Conference on Condition Monitoring and Diagnosis (CMD), Xi'an, China* (25–28 September 2016).

[149]H. Cui, A. Abu-Siada, S. Li, and Islam. "Correlation between dissolved gases and oil spectral response." In: *In Proceedings of the 1st International Conference on Electrical Materials and Power Equipment (ICEMPE); Xi'an, China* (14–17 May 2017). DOI: 10.1109/ICEMPE.2017.7982046.

[150]J. Canavate, X. Colom, P. Pages, and F. Carrasco. "Study of the curing process of an epoxy resin by FTIR spectroscopy." In: *Polymer-Plastics Technology and Engineering* 39.5 (2007), pp. 937–943. DOI: 10.1081/PPT-100101414.

[151]O. R. Allen and P. Sanderson. "Characterization of Epoxy Glues with FTIR." In: *Applied Spectroscopy Reviews* 24.3-4 (2006), pp. 175–187. DOI: 10.1080/05704928808060457.

[152]J. Delozanne, N. Desgardin, N. Cuvillier, and E. Richaud. "Thermal oxidation of aromatic epoxy-diamine networks." In: *Polymer Degradation and Stability* 166 (2019), pp. 174–187. DOI: 10.1016/j.polymdegradstab.2019.05.030.

[153]J. Delozanne, L. Desgardin, M. Coulaud, N. Cuvillier, and M. Richaud. "Failure of epoxies bonded assemblies: comparison of thermal and humid ageing." In: *Journal of Adhesion* (2018), pp. 1–11.

[154]T. Devanne. "Vieillissement radiochimique d'un réseau epoxyde." ENSAM, Paris Tech. PhD thesis. 2004.

[155]G. M. Odegard and A. Bandyopadhyay. "Physical aging of epoxy polymers and their composites." In: *Polymer Physics* 49.24 (2011). DOI: 10.1002/polb.22384.

[156]Nadim Ahmed Hazeg. "Contribution à l'étude des phénomènes de relaxation et de vieillissement dans les polymères amorphes." PhD thesis. 2018, p. 41.

[157]S. Cukierman, J.L. Halary, and L. Monnerie. "Dynamic Mechanical Response of Model Epoxy Networks in the Glassy State." In: *Polym. Eng. Sci.* 7 (1991), p. 1478.

[158]N. Rasoldier, X. Colin, J. Verdu, M. Bocquet, L. Olivier, L. Chocinski-Arnault, and M.C. Lafarie-Frenot. "Model systems for thermo-oxidised epoxy composite matrices". In: *Elsevier* 1522–1529.8 (2008), p. 1525.

[159]E. Labašová. "Determination of Modulus of Elasticity and Shear Modulus by the Measurement of Relative Strains." In: *Research Papers Faculty of Materials Science and Technology Slovak University of Technology* 24 (2017).

[160]J. Bouchet, A.A. Roche, and P. Hamelin. "Internal stresses, Young's modulus and practical adhesion of organic coatings applied onto 5754 aluminium alloy." In: *Thin Solid Films* (1997).

[161]S.Y. Park, W.J. Choi, H.S. Choi, H. Kwon, and S.H. Kim. "Recent Trends in Surface Treatment Technologies for Airframe Adhesive Bonding Processing: A Review (1995–2008)". In: *The Journal of Adhesion* 86 (2009).

[162]C. Le Bras. "Etude de matériaux polymères comme confinement solide dans l'application choc laser LSP." Ecole Nationale Supérieure d'Arts et Métiers. PhD thesis. 2022.

[163]S. S. Golru, M. M. Attar, and B. Ramezanzade. ". Effects of surface treatment of aluminium alloy 1050 on the adhesion and anticorrosion properties of the epoxy coating." In: *Applied Surface Science* 345 (2015). DOI: 10.1016/j.apsusc.2015.03.148.

A

Appendix 1

A.1 Background of Surface Treatments

Chemical treatments are usually most efficient with aluminum alloys, especially considering the environmental constraints. Table A.1 is given below which summarizes the main methods of treatments, globally.

Treatments	Nature of treatments
Grit-blast with alumina particle	Mechanical
Cryoblasting	Mechanical
Forest product laboratory (FPL) – including chromic acid etching	Acid etching
Sulfo–ferric etching (P2)	Acid etching
Phosphoric acid anodizing (PAA)	DC-anodizing
Chromic acid anodizing (CAA)	DC-anodizing
Phosphoric-sulphuric acid anodizing (PSA)	DC-anodizing
Boric–sulphuric acid anodizing (BSAA)	DC-anodizing
Sulphuric Acid Anodizing (SAA)	DC-anodizing
AC phosphoric acid anodizing (AC-PAA)	AC-anodizing
AC sulfuric acid anodizing (AC-SAA)	AC-anodizing
Silane	Coupling/ oxidation
Sol-gel	Coupling/ oxidation
Excimer UV laser (Laser)	Mechanical
Plasma-sprayed coating (Plasma)	Ablation/ oxidation
Ion beam enhanced deposition (IBED)	Ablation/ oxidation

Table A.1: Summary of Surface Treatments on Aluminum Alloys.

Since anodizing, etching and sol-gel techniques are used during the work, only these methods are detailed.

A.1.1 Chemical Etching

Mainly 2 types of chemical etching are in use to modify the substrate surface of aluminum alloys: Forest Product Laboratory (FPL) and sulfo-ferric acid (P2) etches. The surfaces treated with acid-etch were reported as incompetent compared to the anodized surfaces so that they are not in use as a stand-alone treatment in primary bonded structures.

Forest product laboratory (FPL): FPL uses dichromate-sulphuric acid etch. It has been reported that the FPL method has a bond durability problem but still in use as a pre-treatment to an anodizing treatment. The FPL surface is passivated generally with a thin oxide layer of about 40 nm in thickness.

Sulfo-ferric etch (P2): P2 uses ferric sulfate which is a non-chromate acid etch process for the replacement of FPL. The P2 method has proven to be as effective as the well known FPL method by having similar characteristics. However, it is proven that it has an unsatisfactory durability performance in wedge tests.

A.1.2 Anodizing

The several electrochemical treatments, i.e., DC- and AC-anodizing, are listed in table A.2.

Treatments [Refs.]	Electrolyte (wt.%)	Voltage (V)	Duration time (min)	Temperature (°C)
DC electrochemical treatments				
CAA [19]	2.5–3.0 CrO_3	$40.0 \pm 1.0/50.0 \pm 1.0$	35–45	40.0 ± 2.0
PAA [19]	10 H_3PO_4	10.0	20	25.0
BSAA [21]	5.0–10.0 H_3BO_3/ 30.0–50.0 H_2SO_4	15.0 ± 1.0	18–22	26.7 ± 2.2
PSA [58]	10.0 H_3PO_4/10.0 H_2SO_4	18 ± 2.0	15	27 ± 2.0
TFSAA [78]	3.0–5.0 H_2SO_4	15	20	25.0–30.0
Treatments [Refs.]	**Electrolyte (wt.%)**	**Voltage (A/dm^2)**	**Duration time (s)**	**Temperature (°C)**
AC electrochemical treatments				
AC-PAA [43]	10 H_3PO_4	4.0	30	50.0
AC-SAA [43]	15 H_2SO_4	10.0	12	80.0

Table A.2: DC- and AC-Electrochemical Surface Treatments Prior to Adhesive Bonding.

Both chromic acid anodizing (CAA) and phosphoric acid anodizing (TFSAA) are the main used anodizing processes especially for metallic bonded structures but they typically based on hazardous substances like strong acid and chromium. In order to overcome this problem, new methods are in development like sol-gel technique which will be explained in the following section.

A typical anodic oxide scheme is given in figure A.1. The main feature of the anodic oxide is its created cylindrical porosity which is just above a barrier layer. It is noted that the porous structure has a huge role of wetting of an applied primer contributing to bond strength and durability. These porous oxide layers are controllable for any given operating condition.

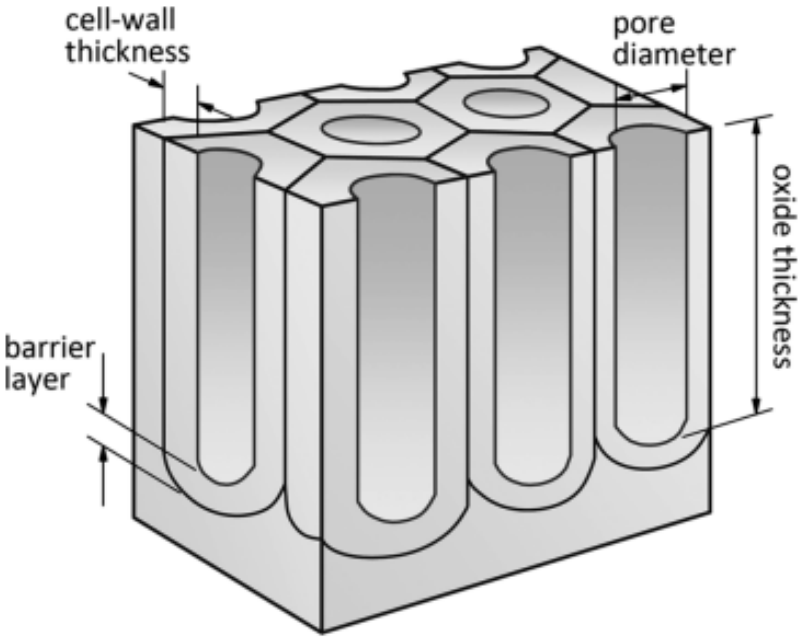

Figure A.1: Idealized anodic oxide structures.

Chromic Acid Anodization: It was developed as an efficient technique for adhesive bonding with long-term durability performance. This technique is used mostly in the European aerospace industry. The standard consists of chromic-sulphuric acid deoxidizing followed by chromic acid anodizing. Even though it has a huge durability within the corrosive environments, the use of chromate treatment processes is being restricted due to recent environmental policy.

Sulphuric Acid Anodizing: SAA, which is mostly applicable for both protective and painting purposes. Two main types of SAA exist: Type II (conventional) and Type IIB (thin film). The second type of SAA, called as thin film sulphuric acid anodizing (TFSAA), was introduced as a non-chromate alternative for adhesive bonding processes.

A.1.3 Sol-Gel Treatment

As previously mentioned, there is a need of having more environmentally friendly method for the industry. Since the sol-gel is one of them and used during the work, it's detailed in this section.

Solutiongelation (sol-gel), consists of the growth of metal-oxo polymers through both hydrolysis and a condensation reaction to form an inorganic polymer networks with a thickness range of 50 to 200 nm.

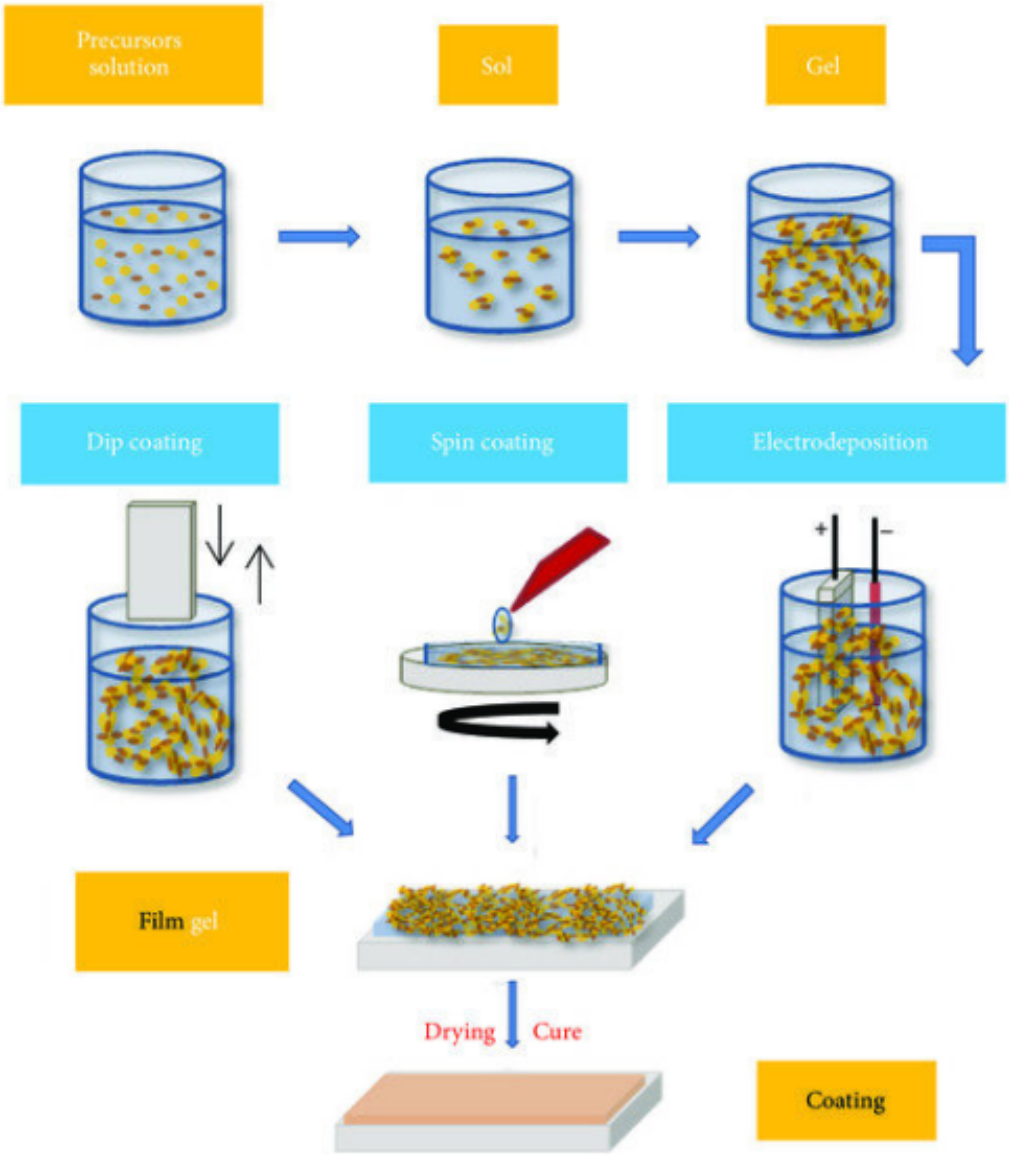

Figure A.2: Preparation of sol-gel method.

B

Appendix 2

B.1 Hugoniot & Shock Polar

B.1.1 Hugoniot Curve

The mathematical understanding of shock waves (discontinuities in pressure, density, and temperature) was developed by Rankine and Hugoniot for fluids. The equations can be easily developed by considering regions immediately ahead of and behind the shock front. As given in chapter 1, Rankine-Hugoniot relations give the conservation laws for the shock. The set of these equations for a shock discontinuity plus an equation of state, precise the shock adiabat or Hugoniot of the material.

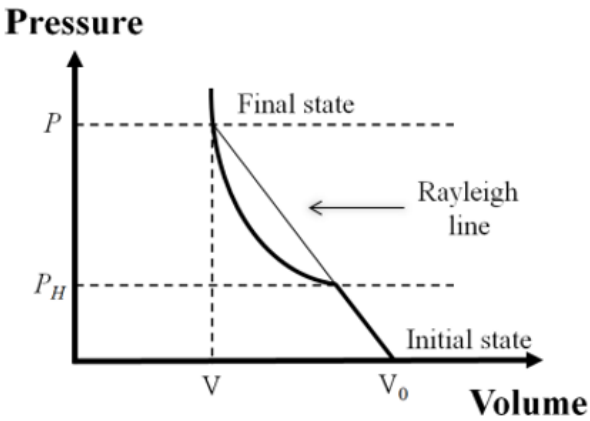

Figure B.1: Hugoniot Curve.

Figure B.1 demonstrates the Hugoniot curve. The diagram shows the possible states (P, V) of a material from an initial state which is P=P_{amb}. The curve can be divided into three parts as (i) an elastic part, (ii) a plastic wave front between the elasto-plastic limit and (iii) an hydrodynamic regime which is above the Rayleigh line.

The main purpose of the Hugoniot, which is a relationship between the parameters of states reached by shock compression, is to create the equation of state (EOS) of the

material. This equation of state is a vital step for shock-wave physics investigations. Hugoniots of many condensed materials are well defined by the following equation:

$$U = c_0 + su$$

where U is the shock velocity u is the particle velocity. In which c_0 is the sound speed at zero pressure and s is a constant factor that is in between 1 to 1.7 for most materials. Using the conservation equations, this expression for the Hugoniot can be converted to relationships between the pressure and specific volume, the pressure and particle velocity, etc.

B.1.2 Shock Polar

The shock polar of a material is the relation between the applied pressure versus particle velocity u (as seen in figure B.2).

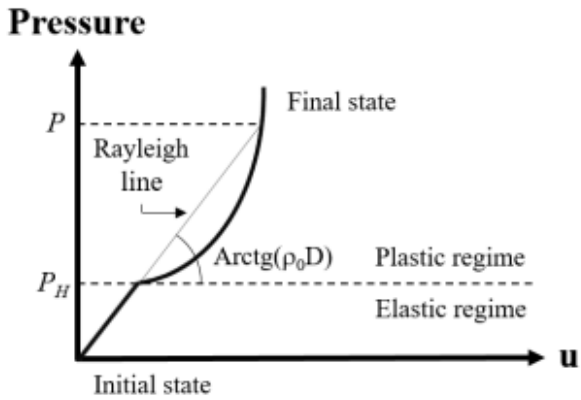

Figure B.2: Shock Polar Graph.

The shock polar equation is as given:

$$P = \rho_0(c_0 + su)u + \frac{2}{3}\sigma_{Y0}$$

where σ_{Y0} is the static elastic limit of the material. The additional part of " $\frac{2}{3}\sigma_{Y0}$ " is included due to the elasto-plastic part of the material which transfers the shock polar in the plastic regime.

Selen ÜNALDI

Test d'adhérence et procédé de décapage de la peinture par choc laser : Application aux pièces aéronautiques en alliages d'aluminium et CFRP

Résumé : Le décapage au laser est un procédé qui comprend généralement différentes formes de phénomènes d'ablation. Les travaux présentés étudient un procédé de décapage mécanique utilisant des ondes de choc induites par laser à haute pression dans un régime confiné. La densité de puissance est étudiée comme un paramètre pour le procédé de décapage de peinture sélectif au laser (LPSP) sur des échantillons et pour les adhésions de peinture. Un laser Nd:YAG pompé par une lampe flash avec une taille de spot fixe (4mm) est tiré sur une couche unique d'époxy et plusieurs couches de peinture polymérique appliquées sur AA 2024-T3 (Aluminium), AL-Li 2060 et des substrats à base de CFRP. Après le traitement laser, les échantillons sont examinés par microscopie optique, profilomètre et analyse chimique (FTIR, DSC & TGA). Les résultats montrent que le décapage sélectif au laser est possible entre différentes couches de revêtements externes d'aéronefs et sans aucun dommage visuel. De plus, le décapage de la peinture est développé du côté de la peinture des échantillons avec l'utilisation de la couche de protection thermique. Parallèlement au travail expérimental, un modèle numérique a été développé pour d'expliquer les mécanismes physiques, et réaliser une analyse détaillée des contraintes aux interface. Le développement du décapage laser de la peinture est optimisé à partir du côté de la peinture des échantillons au moyen de simulations numériques.

Mots clés : décapage de peinture au laser, tests d'adhérence, procédés de chocs laser, époxy sous taux de déformation élevé, optimisation du procédé

Résumé : Laser stripping is a process which typically includes different forms of ablation phenomena. The presented work investigates a mechanical stripping process using high pressure laser-induced shock waves in a confined regime. Power density is studied as a parameter for selective Laser Paint Stripping Process (LPSP) on specimens and for paint adhesion relations. A flashlamp-pumped Nd:YAG lasers with fixed spot size (4mm) is shot on single layer epoxy and several layers of polymeric paint applied on AA 2024-T3 (Aluminium), AL-Li 2060 and CFRP based substrates. After laser treatment, samples are investigated with optical microscopy, profilometer and chemical analysis (FTIR, DSC & TGA). The results show that selective laser stripping is possible between different layers of external aircraft coatings and without any visual damage on the substrate material. In addition, paint stripping is developed from the paint side of specimens with the usage of thermal layer for single layer of epoxy coating. In parallel to the experimental work, a numerical model has been developed to explain the background of the physical mechanisms and to evaluate the detailed stress analysis and interfacial failure simulation both for the laser stripping from the substrate side and the paint side applications.

Mots clés : laser paint stripping, adhesion tests, laser shock processes, epoxy under high strain rate, process optimization